Design and Assessment of a Battery-Supercapacitor Hybrid Energy Storage System for Remote Area Wind Power Systems

Gee, Anthony

Award date:
2012

Awarding institution:
University of Bath

Design and Assessment of a Battery-Supercapacitor Hybrid Energy Storage System for Remote Area Wind Power Systems

Anthony M Gee

A thesis submitted for the degree of Doctor of Philosophy (PhD)

University of Bath

Department of Electronic and Electrical Engineering

August 10th 2012

COPYRIGHT

Summary

Recent advances in innovative energy storage devices such as supercapacitors have made battery-supercapacitor hybrid energy storage systems technically attractive. However the field of hybrid energy storage system control is relatively new, involving the major challenge of developing control techniques optimised for improved battery-life or other performance metrics.

This thesis presents the design and analysis of an actively controlled hybrid energy storage system. Detailed information is given regarding the system implementation and dynamic controls developed as a part of the research. Novel use of the sliding-mode or hysteretic current-controlled DC/DC converter is shown to provide a versatile and robust power electronic building block for the power-control hardware implementation. Current state of the art in the field has converged around a frequency-domain approach to the overall power sharing strategy within hybrid energy storage systems employing batteries and high-power, low-energy density storage such as supercapacitors, with benefits in terms of reduced battery current maxima and an (un-quantified) increase in battery life having been reported.

This research extends previous studies by considering the frequency-domain approach in further detail and providing quantitative simulation results confirming how an estimated increase in battery cycle-life of ~18% can be achieved. A systematic simulation framework used for the development and assessment of novel hybrid energy storage system control strategies is described and demonstrated in the context of a remote wind power application. The hardware design of all systems considered is described in detail and demonstrated by experiment.

Acknowledgements

Firstly, I would like to thank my supervisor Dr R.W. Dunn for giving me this fantastic opportunity and both he and Dr F.V.P Robinson, for their advice and support.

I thank EPSRC Supergen Energy Storage Consortium for supporting this project.

My heartfelt thanks go to my parents without whose encouragement this work would never have been considered. I would like to thank my Dad whose technical expertise inspired me from an early age and my Mother for being so inspiring in every other respect.

Finally, I would like to thank Emma without whom this would not have been possible.

Contents

List of Abbreviations

Abbreviation	Description
AC	Alternating current
CRF	Capital Recovery Factor
CVCI	Constant voltage constant current
DC/DC	DC to DC
DOC	Depth of charge
DSP	Digital Signal Processing
D/A	Digital to analogue
DC	Direct current
EDLC	Electric double layer capacitor
EMI	Electro-magnetic interference
ESR	Equivalent series resistance
HCC	Hysteretic current control
HESS	Hybrid energy storage system
IP	Initial payment
IGBT	Insulated gate bipolar transistor
IC	Integrated circuit
ICC	Interrupted charge control
LCE	Levelised cost of energy
LLP	Loss of load probability
LPSP	Loss of power supply probability
LVD	Low voltage disconnect
MOSFET	Metal oxide semiconductor field effect transistor
NPC	Net present cost
FC	Fuel: Net present cost
OM	Operation and maintenance: Net present cost
NPV	Net present value
BR	Battery replacement: Net present cost
GR	Diesel-generator replacement: Net present cost
PCB	Printed circuit board
PI	Proportional plus integral (controller)
SV	Salvage value
SOC	State of charge
SMES	Superconducting magnetic energy storage
TV	Television
TI	Turbulence Intensity
VRLA	Valve regulated lead acid
WECS	Wind energy conversion system

List of Symbols

Symbol	Description	Units
A_0	Battery modelling parameter [1]	
A_{21}	Battery modelling parameter [1]	
A_{22}	Battery modelling parameter [1]	
C	Battery capacity	Ah
C_0	Supercapacitor module rated capacitance	F
C_1	Battery modelling capacitance parameter [1]	F
c_1-c_6	Wind turbine power coefficient modelling terms	
C_{bat}	Battery costs	$
C_{cell}	Cell nominal capacitance	F
C_d	Cycles to failure	
C_{float}	Battery float-level capacitance	F
C_{gen}	Generator costs	$
C_n	Battery nominal capacity	Ah
C_{n1}	Battery available capacity at current I_{n1} current	Ah
C_{nl}	Supercapacitor non-linear capacitance term	F
C_{oss}	MOSFET output capacitance	F
C_p	Wind turbine coefficient of power	
C_{sc}	Supercapacitor rated capacitance	F
$C_{snubber}$	Snubber capacitance	F
C_{wt}	Wind turbine cost	$
C_Z	Empirical battery modelling capacitance parameter	F
d	Discharge range	
d_1	Market discount rate	$
d_a	Relay amplitude	
d_t	Coefficient used in admittance function calculation	
D_{wt}	Wind turbine total frictional damping coefficient	Ns/m
e	Fuel inflation rate	$
E_{bat}	Battery energy	Wh
$E_{deficit}$	Deficit energy	Wh
E_{gen}	Wind turbine generator efficiency	%
E_{load}	Load energy	Wh

E_m	Main branch voltage in Ceraolo battery model[1]	V
E_{m0}	Nominal branch voltage in Ceraolo battery model[1] [1]	V
E_u	Unusable supercapacitor capacity	J
F_{cost}	Cost / (kw/hr) of generator fuel	$
f_{sw}	Switching frequency	Hz
h	Hysteresis-width: half-band	V
h_{wt}	Wind turbine height	m
I^*	Inductor current reference	A
I_a	Armature current	A
I_{avg}	Average battery current	A
I_{H_L}	High to low transition gate drive current	A
I_L	Inductor current	A
I_{L_H}	Low to high transition gate drive current	A
I_{leak}	Supercapacitor leakage current	A
I_{max}	Converter current limit	A
I_{out}	Converter output current	A
i_{sc}	Supercapacitor current	A
I_t	Turbulence intensity factor	
J	Wind turbine, shaft + generator total inertia	kg.m^2
K_f	Shaping filter coefficient	
k_i	Voltage control loop integral gain	
k_l	Voltage control loop current measurement gain	
k_p	Voltage control loop proportional gain	
k_v	Empirically derived differential capacitance modelling term	
k_{vgen}	Generator voltage constant	V/rpm
L_{1t}	Turbulence length scale for von Karman spectrum	m
L_a	Armature inductance	H
L_{bat}	Battery lifetime	Years
L_{proj}	Project lifetime	Years
L_t	Turbulence length scale	m
$m1$	Rational shaping filter modelling coefficient	
$m2$	Rational shaping filter modelling coefficient	
n_e	Charge number	
P_{cond_high}	Conduction loss in high-side power electronic switch	W
P_{cond_low}	Conduction loss in low-side power electronic switch	W

[1] M. Ceraolo, "New dynamical models of lead-acid batteries," *IEEE Trans. Power Syst.*, vol. 15, pp. 1184-1190, Nov. 2000.

$P_{conduction}$	Conduction loss in power electronic converter	W
P_{coss}	Power used in charging MOSFET output capacitance	W
P_{in}	Converter input power	W
P_{load}	Load power	W
P_{net}	Net power (wind power – load power)	W
P_{opt}	Optimum wind turbine output power	W
P_{out}	Converter output power	W
P_{qrr}	MOSFET body-diode reverse recovery power	W
$P_{switching}$	Total switching loss in power electronic converter	W
$P_{switching\_high}$	Switching loss in high-side power electronic switch	W
P_{wt}	Wind turbine power generated	W
Q	Reaction Quotient	C/mole
Q_e	Battery charge	C
$Q_{g(sw)}$	Gate charge required for switching	C
Q_{rr}	MOSFET body diode reverse recovery charge	C
R	Wind turbine blade radius	m
R_{00}	Battery modelling resistance parameter	Ω
R_1	Battery modelling resistance parameter	Ω
R_{10}	Battery modelling resistance parameter	Ω
R_2	Battery modelling resistance parameter	Ω
R_{20}	Battery modelling resistance parameter	Ω
R_{22}	Battery modelling resistance parameter	Ω
$R_{ds(ON)}$	Power electronic switch on-state resistance	Ω
R_{gate}	Gate internal resistance term	Ω
$R_{gatedrive}$	External gate drive resistance	Ω
R_{gen}	Number of generator replacements over project	
R_{int}	Series resistance term	Ω
R_L	Power inductor resistance	Ω
R_{leak}	Supercapacitor leakage resistance	Ω
R_{nl}	Parallel resistance term	Ω
R_s	Supercapacitor series resistance	Ω
R_Z	Empirical battery modelling resistance parameter	Ω
S_{vv}	Power spectral density	$(m/s)^2/Hz$
T	Temperature	K
t_1	Gate switching first interval	s
t_2	Gate switching second interval	s
T_{em}	Wind turbine generator electro-magnetic torque	Nm

T_f	Shaping filter coefficient	
$T_{H\text{-}L}$	High to low switching time	s
$T_{L\text{-}H}$	Low to high switching time	s
T_s	Sampling period	hr
u	Gate drive logic signal	V
V_0	Electrode-process potential	V
v_{10}	10m wind speed measurement	m/s
v_b	Battery voltage	V
V_b*	Battery reference voltage	V
V_{bat}	Battery voltage	V
V_{bmin}	Minimum battery voltage (low voltage disconnect)	V
$V_{bminhyst}$	Minimum battery voltage hysteresis	V
v_{cut_in}	Wind turbine cut-in wind speed	m/s
v_{cut_out}	Wind turbine cut-out wind speed	m/s
$v_{effective}$	Effective wind speed	m/s
V_{float}	Float voltage	V
V_{gs}	Gate to source voltage (MOSFET or IGBT)	V
v_{high}	Converter high-side voltage	V
v_{hub}	Wind speed adjusted for hub height	m/s
v_{low}	Converter low-side voltage	V
v_{mean}	Mean wind speed	m/s
V_{nom}	Supercapacitor-cell rated voltage	V
V_{oc}	Open circuit voltage	V
v_p	Battery modelling voltage parameter[2]	V
V_r	Supercapacitor rated voltage	V
V_{sc}	Supercapacitor voltage	V
V_{sc}	Supercapacitor voltage	V
V_{smax}	Maximum supercapacitor voltage	V
$V_{smaxhyst}$	Supercapacitor upper hysteresis voltage	V
V_{smin}	Minimum supercapacitor voltage	V
v_{wind}	Wind speed including turbulence	m/s
W	Battery life degradation parameter	
x_a	Process variable amplitude	
Z_0	Battery complex impedance	Ω
Z_{00}	Battery initial complex impedance	Ω

[2] M. Ceraolo, "New dynamical models of lead-acid batteries," *IEEE Trans. Power Syst.*, vol. 15, pp. 1184-1190, Nov. 2000.

z_{wt}	Height above ground used in turbulence calculation	m
z_{wt0}	Surface roughness coefficient	m

Chapter 1: Introduction

One of the key design challenges for power systems operating primarily from renewable energy sources is that the generated power profile is unlikely to match the load requirement. For this reason, much attention is focused on development of novel energy storage systems for future renewable power applications. Recent technological advances have made the employment of high power density (>4kW/kg), low energy density storage (<10Wh/kg) devices such as supercapacitors, advanced flywheel systems and superconducting-magnetic energy-storage more technologically feasible [2]. Their combined use with more traditional energy storage systems such as electro-chemical batteries (which are more suited to longer term storage, lower power/higher energy density applications) permits the key benefits of each to be employed. However, to ensure their optimal utilisation requires the development of novel control strategies and analyses. This thesis describes the development and assessment of an optimised hybrid supercapacitor/battery energy storage system for small-scale wind-energy applications by both simulation and experiment.

1.1 Motivation

This work falls under the Supergen Energy Storage Consortium initiative in Sustainable Power Generation and Supply [3]. The key motivation for this study is that distributed wind power systems and, in particular small-scale remote-area wind power systems, can provide a technically feasible option for future remote energy requirements. Concerns about the environment, sustainability and increasing energy prices have created a requirement to explore alternative, more sustainable means of energy generation such as wind power. Policy drivers promoting energy efficiency such as the Kyoto protocol and

more recent EU directives towards the reduction of CO_2 emissions by 20% and increased renewable electricity generation to 20% [4] have resulted in a policy framework in many industrialised countries for the development of sustainable generation. To help meet this requirement for increased renewable generation and reduced CO_2 emissions, in spite of an increasing world population, requires focused research and development to be applied in various disciplines including renewable energy systems.

It is anticipated that the majority of the required increase in renewable energy generation will be achieved by distributed generation units [5]. These can range in power from several kW to MW and are generally installed in the vicinity of the load they supply. In addition to meeting directives on climate change and energy production, the development of distributed, renewable remote-area power systems can be of immediate benefit to communities living isolated from national power networks by providing increased electrification, reducing generation costs and increasing sustainability.

If renewable energy sources such as wind and solar are to be utilised effectively, a need arises to store the energy produced, as load variations are not in their nature likely to coincide with available renewable supply energy variations. This is particularly apparent in systems operating in isolated, remote areas where no grid connection is available to provide power during times of low renewable energy. Communities in such areas have typically relied on diesel generators and more recent technological advances have made renewable energy or diesel-renewable hybrid systems increasingly popular. Recent studies have shown that the integration of energy storage into a distributed wind/diesel system can significantly reduce cost of operation and increase overall

system efficiency with a reduction of 38% of total costs and 53% reduction in diesel consumption having been reported [6]. The most popular energy-storage technology for renewable energy applications is currently the electro-chemical battery [7] for reasons including cost, availability and performance attributes, with the lead-acid type remaining the most popular choice [8]. Batteries and, in particular, the lead-acid type, often constitute a large proportion of the total cost associated with an off-grid renewable energy project through multiple battery replacements over the project life [9-11] due to their limited lifespan, of the order of 10^3 charging cycles [12]. In contrast, supercapacitors also known as 'electrochemical double-layer capacitors' (EDLC), "electro-chemical capacitors" or 'ultra-capacitors', store energy in the form of electrostatic charge and can offer considerably increased cycle-life (10^6 cycles) and power density but have a lower energy density [13]. Consequently, the motivation for this study has been to investigate the use of supercapacitor technology to mitigate some of the weaknesses of battery energy storage systems such as limited life, principally when operated in wind-power systems. Other hybrid energy storage combinations are possible such as with fuel cells or compressed air systems as the long-term energy storage device with flywheels or superconducting magnetic energy storage as the short-term device [14]. However, for reasons including cost, technical maturity and due to the real problem of limited battery life, this study has focussed on the use of supercapacitors with batteries in a hybrid energy storage system.

1.2 Research Overview

This study considers the hybridisation of battery and supercapacitor energy storage technologies. A combined usage of energy storage systems in a complementary configuration allows the effective use of short-term devices such as supercapacitors to deliver short-term peaks in power whilst maximising the lifetime of the long-term

energy storage device. One of the key challenges faced in the long-term operation of renewable-based distributed power systems has been mitigating reduced battery lifetime which impacts project life-cycle costs [9], [11]. For this reason, a principal problem considered in this study is the optimisation of a battery-supercapacitor composite energy storage system primarily for improved battery lifetime although other associated benefits are discussed. This has been achieved by first developing a suitable simulation environment able to realistically describe the complex and irregular power profile experienced by the battery in a remote area power system. Then the implementation of a power-electronic controlled hybrid energy storage device in hardware was considered. The power electronic converter in the hybrid energy storage system is rated at up to 50A and 600V. A test environment capable of functional real-time testing, used for ensuring the technical feasibility of the proposed solution, was also developed. Long-term simulation of the system performance (simulation intervals of one week to one year), combined with a battery cycle-life aging model, has enabled the benefits of the proposed hybridisation of the energy storage systems to be demonstrated in terms of predicted battery life. The novel simulation/hardware platforms created have also allowed new control strategies to be developed and evaluated.

1.3 Energy Storage Systems

With the proportion of electricity generated by inherently intermittent sources such as wind, wave and solar growing, the requirement to store energy is also increasing [15]. With a rising world population and increased use of electrical supply becoming the norm in areas of the world where previously it may not have been, this requirement for energy storage is likely to also increase. Some of the key benefits that energy storage systems can introduce to users are as follows:

- Increased use of intermittent renewable sources.
- Increased reliability and quality of supply.
- Improved security of supply.
- Cost reductions by shifting load to cheaper electricity tariffs or increased use of renewable generation.

However, disadvantages could also include increased initial costs and increased system complexity.

Recently, the world population living without national grid power has been estimated at over 2 billion and growing [16]. A significant growth is expected in the market for off-grid energy supply for which energy storage is often essential. Some of the main energy storage technologies currently available for use in distributed renewable energy systems are supercapacitors, fuel-cells, batteries, superconducting magnetic energy storage (SMES) and flywheel energy storage [7]. These can be roughly categorised into short-term high specific power-density devices such as flywheels, superconducting magnetic energy storage systems and supercapacitors and longer-term, lower specific power density devices such as batteries, fuel cells and hydrogen storage systems. There exists a certain synergy between these devices since their attributes are complementary. For example, most short-term, high-power devices also typically exhibit high cycle-life and efficiency whereas the long-term, high-energy devices are generally less efficient or suffer from reduced cycle-life in comparison. For this reason, a hybridised energy storage system is technically an attractive option when high-power/low-energy devices are hybridised with low-power/high-energy devices.

1.3.1 Batteries

A battery is a device that converts chemical energy directly to electrical energy. The history of the battery is a long one with the first secondary (rechargeable) lead-acid battery invented by the French physicist Gaston Planté in 1859 [17]. To this day no other cell chemistry has been able to offer a more cost effective solution suited to stationary applications. For example, recently lead-acid battery costs of 150$/kWh have been reported in comparison to 400-800$/kWh for nickel-cadmium (Ni-Cad) and 300$/kWh for lithium-ion based cells [18]. In a recent survey by the International Renewable Energy Agency, the deep-cycle lead acid cell was described as being the "de facto workhorse for commercial and industrial use" [19] and, as such, is currently the form of battery most frequently found in power applications. Shortcomings associated with the lead acid battery include a short life-span (typically <1000 cycles to failure [20]) and consequently it has been reported to be the most limiting factor in isolated power generation effectiveness [21]. For this reason, this research has focussed on the hybridisation of the lead acid battery with supercapacitor energy storage devices to improve upon its inherent limitations. Battery chemistries such as advanced lithium-based designs show good promise for future renewable applications but are currently limited in their application due to cost or technical maturity [2]. The basic principles of the techniques developed in this thesis can also be applied to the future hybridisation of other short-term, high power storage devices with future battery designs.

1.3.2 Supercapacitors

Supercapacitors are based on the double-layer capacitance concept, first described by German physicist Hermann von Helmholtz, in 1853 [22]. The first patent based on the double-layer capacitance structure was taken out by General Electric Company in 1957 [23] as a by-product of their fuel-cell research. Later, in 1966 researchers at Standard Oil Company, Cleveland, Ohio (SOHIO) developed a multi-farad device. In 1978, Nippon Electric Company (NEC) developed the first commercially-successful high capacitance device under the name ”supercapacitor”, for use in providing (low-power) backup power for computer memory systems [24]. Meanwhile, between 1975 and 1980, Brian Conway, an electro-chemist at the University of Ottawa, carried out extensive fundamental work on low-power electrochemical capacitors detailed in his work “Electrochemical supercapacitors: Scientific fundamentals and technological applications” [25]. However, the first high-power electro-chemical capacitors were developed for use in a variety of military applications by Pinnacle Research Institute (PRI) in the USA under the name “ultracapacitors” between 1982 and 1989 [26]. This then sparked interest in high-power electro-chemical capacitor systems for the electric vehicle market and, by 1990, high power electro-chemical capacitors were used for load-levelling in the drive-train of electric vehicles with improvements of ~10% in efficiency and ~10% in range increase having been reported [27].

1.4 Hybrid Energy Storage Systems (HESS)

Fig. 1.1 illustrates the relative power, energy ratings, efficiency and cycle-life characteristics of various battery cell chemistries and short-term energy storage technologies such as supercapacitors and flywheels.

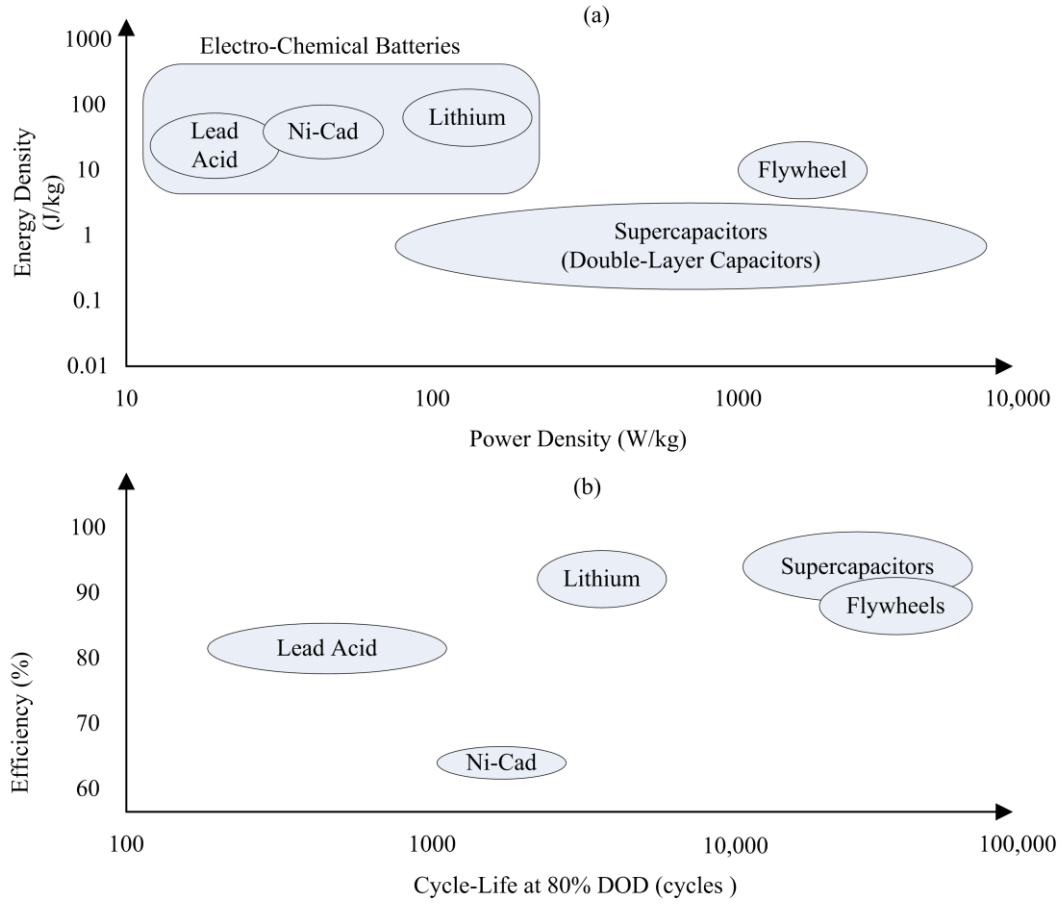

Fig. 1.1 Battery, capacitor and flywheel energy storage system attributes [28], [29] (a) Typical energy density vs. power density (b) Typical efficiency vs. cycle-life.

Combining two or more energy storage systems permits the beneficial attributes from each device to be utilised. For example, short-term, high power density energy storage technologies such as flywheel and supercapacitor energy storage systems are often hybridised with longer term, lower power density systems such as fuel cells [30], batteries [31], and compressed air energy storage [32]. Fig. 1.2 shows how a supercapacitor-battery HESS may be configured.

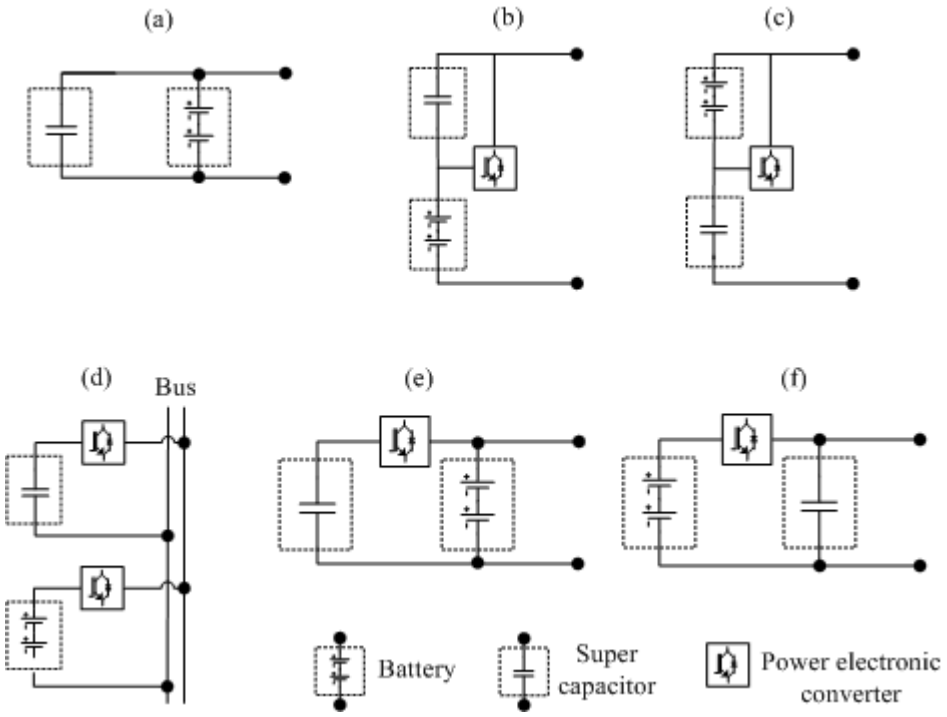

Fig. 1.2 (a) Passive parallel connection (b) and (c) active series connections (d) connection via common bus (e) active parallel connections: with battery facing load and (f) supercapacitor facing load.

Perhaps the simplest configuration is to connect the supercapacitor and battery (passively) in parallel with no active electronic interface. Research into the parallel-passive configuration has showed that the peak battery current can be reduced in applications such as automotive-traction [33], [34], automotive starting [35], [36] and wind-power [37]. However, the battery voltage range also dictates the supercapacitor usable voltage range in the passive-parallel connection and therefore limits its depth of discharge considerably. In [38], [39] the authors have provided comparison data of active and passive configurations of a relatively low energy lithium-ion cell (1.4Ah Sony 18650 series, commonly used in portable applications) and two 100F supercapacitors in series. The results show the active hybrid system has significant advantages over the passive configuration including increased power delivery

capabilities and suggest that battery life could also be extended. In [40] the authors conclude that for vehicular applications: “Optimal use of the supercapacitor requires a power controller” and that “the best control strategy is not fully developed due to challenging control issues” highlighting the need for further work in the area. The active series configuration is not well documented and the benefits of this strategy remain yet to be proven. The connection via a DC bus is also an active parallel connection, particularly of use in systems that require a DC bus interface to multiple sources and loads such as DC microgrids. In general, the current literature has shown that an active-parallel configuration has the potential to provide significantly greater performance benefits than passive or series connections for electric vehicle applications as demonstrated by Miller and Sartorelli [41] and renewable energy applications [14] as discussed by Etxeberria. For this reason, the study presented in this thesis has considered an active parallel configuration.

The two main application fields for battery/supercapacitor hybrid energy storage systems have been renewable energy and transportation. Extensive research studies in the field of electric vehicles and hybrid electric vehicles have reported the benefits of a hybrid energy storage system consisting of supercapacitor and battery energy storage systems in terms of a proposed increase in battery life due to decreased peak battery current [42], a quantified increase in battery cycle-life [43] or separate exclusive optimisations in terms of efficiency [44] or increased battery life [44]. A variety of control strategies have been proposed for the control of hybrid energy storage within vehicular based applications with most falling into the category of heuristic rule-based algorithms [45], [46] or frequency-domain filtering approaches [43], [47] although more complex alternatives such as neural network based schemes have also been reported [45]. Even though vehicle drive-cycle patterns can be considered to be irregular, there

exists a certain coupling between traction and braking events in that a major acceleration event is likely to be followed by some form of deceleration event which may well be followed by an acceleration, and so on. In this respect, traction and braking duty cycles differ from renewable energy profiles which can be significantly more erratic. Consequently the implementation of a hybrid energy storage system and power sharing controller optimised for traction applications is not necessarily optimal for a renewable energy power profile.

In renewable energy related studies, many systems have employed a power filtering or "linear filtering" [14] based control technique as a means of distributing the power between the storage devices. The low frequency power is assigned to the long-term storage device, and the rest is absorbed/supplied by the short-term storage. For example, Wei, Joos and Belanger [48], [49] have proposed a hybrid energy storage system to filter the power output of a grid-connected wind turbine. Two high pass filters with different corner frequencies are used to control the power sharing between the two sources with the supercapacitor providing the high frequency content. The authors present "hardware in the loop" results in which the battery state-of-charge fluctuations are reduced by "about 5 – 9%" in the hybrid system, resulting in a "potentially prolonged lifespan" compared with the battery-only reference system [49] with similar results reported in [48]. The implementation of the system circuit-level design is not reported in detail and a system level description is given in both studies [48], [49].

Haihua et al [28] present an energy management system for a modular supercapacitor-battery composite energy storage for renewable energy applications based on a low-pass power-filtering approach to power sharing, but do not consider battery life estimation. The system is based around a DC bus connection employing an 800Vdc bus and a series

of interleaved dual active bridge power electronic converters are used to interface to the low voltage supercapacitor (~45Vdc) from an 800Vdc bus.

Van Voorden et al. [50] have also proposed a low-pass filter derived approach to divert the high frequency content to/from the supercapacitor in a wind-energy application, with benefits of the hybridised system described in terms of reduced battery current fluctuations and reduced impact on battery life. The optimisation in terms of an energy management simulation and implementation description is at a system level.

In [51] Liu et al. present a grid connected wind-power system with hybrid energy storage. The battery power is determined by a moving average filter based control (i.e. a form of low-pass filter control) with the remaining (high frequency) content diverted to/from the supercapacitor. Reported benefits are described qualitatively in terms of smoothed battery current, enhanced efficiency and reduced battery stress (due to reduced battery current peaks). The implementation is based on a half bridge converter interface of the energy storage devices to a common DC bus. Its operation is demonstrated by simulation although the design process is not described.

Jia et al. [52-54] have described a practical-system which acts to filter the battery power for stand-alone renewable power applications. Since battery voltages typically remain relatively constant over the discharge range (1.75 – 2V/cell for lead acid cells [55]) the effect is similar to a battery power filtering technique. Hardware results are provided confirming the feasibility of the approach and the benefits are described qualitatively in terms of prolonged service life. The power electronic interface design is described in detail and is based on a half bridge DC/DC converter with the battery on the low-side and the supercapacitor on the high-side. The control system is based on controlling the battery current by use of a PI control of the converter duty ratio.

In a recent report [56], Qing et al. have proposed a hybrid energy storage system for renewable energy applications based on the power filtering approach with an additional heuristic rule based control to provide a charge strategy. The results [56] indicate that by diverting a significant proportion of the high frequency battery power profile to/from a supercapacitor, a significant improvement in battery cycle life can be expected. The authors report [56] that the supercapacitor/battery hybrid energy storage system's battery life is expected to be 4.82 times longer than the equivalent battery-only system. The authors suggest a cascaded buck and boost converter arrangement for the implementation, but do not describe the design in detail.

Abbey, Li and Joos have employed a battery-supercapacitor hybrid in a wind-diesel application also based around a modified filter-based approach to improve battery lifetime although no battery life estimation is performed [57]. In addition the optimisation and simulations are carried out at system level and the design of the converter interfaces is not documented.

Ribeiro, Cardoso, and Boccaletti [58] have described a pv-wind hybrid system with battery and supercapacitor energy storage for remote telecommunication power applications. This study has also suggested a power filtering control approach to power sharing between the two energy storage devices with the intended purpose of increasing battery life. Battery life estimation is not considered and the converter interface design is not described.

The current state of the art in the area of battery/supercapacitor hybridisation for wind-energy applications has converged around a frequency-domain based control of the power sharing between battery and supercapacitor energy storage. The underlying approach involves the control of the battery power by use of a power electronic

converter to divert the high-frequency fluctuations to/from the supercapacitor. However a review of the results presented shows little or no data available quantifying the increase in battery life that can be achieved using this technique in wind-energy applications. This indicates the need to extend previous studies by providing quantified results based on a wind-power profile. The work presented within this thesis contributes to current knowledge by describing the benefits of a battery/supercapacitor hybrid energy storage system operating under a wind-power profile both experimentally and by simulation. In addition, this work also provides a novel, systematic methodology for use in the assessment of the effectiveness of battery/hybrid energy storage systems operating under a wind-power profile.

Many studies have been carried out based on a system-level optimisation of power flows, leaving the real-time, low-level control of the power electronic converter largely unconsidered [48-50], [56-58]. The problem of control of power to/from energy storage devices such as supercapacitors presents a challenge in the field of DC/DC conversion due to the requirement for bidirectional current and operation over a wide range of operating conditions such as (supercapacitor) voltage range requirements. Since power electronic converter control strategies for the application of interfacing supercapacitor and battery energy storage systems are not well reported, this highlights the need for further consideration. The work presented in this thesis considers the problem of the real-time control of the current to/from the supercapacitor energy and battery. A novel hardware implementation of a hybrid energy storage system and its control systems are described in detail and its performance is demonstrated by experiment. With a focus of research effort in the implementation aspects of hybrid energy storage devices, the technical feasibility of future studies can be assured. In this way a consensus can be

reached regarding the optimal design of the power electronic interfaces and associated controls for future hybrid energy storage systems.

1.5 Objectives

The scope of this project is to investigate the hybridisation of battery and supercapacitor energy storage systems for remote area wind-power generation with focus on the following objectives:

1. The development of an electro-mechanical simulation platform on which the benefits of the hybrid energy storage system can be assessed. Previous studies have shown a lack of a comprehensive simulation strategy that encompasses the generation of high definition simulation power profiles with consideration for the effects of seasonal variations, turbulent variations and system sizing constraints. To be able to analyse the performance of the systems under consideration over periods longer than would be practical by experiment and long enough to be able to estimate battery cycle-life (from weeks to years), a key objective has been to develop a simulation platform capable of modelling their performance with sufficient fidelity (with one second sampling intervals).
2. An assessment of the quantitative benefits of the hybridisation of battery and supercapacitor energy storage systems operating under a realistic wind-energy resource profile. Since a review of previous work has shown little quantitative data relating the benefits of a hybridised energy storage system to a tangible increase in battery life, one of the key objectives has been to assess the performance of supercapacitor/battery hybrid systems in terms of battery life and to provide a method for doing so.

3. The majority of previous studies have concluded that a suitable power distribution strategy between short-term and long-term energy storage systems for wind-energy applications should be based on a frequency-domain, power-filtering strategy with the objective of improved battery life. So for this reason, one of the objectives of the study has been to also consider this strategy in further detail with the purpose of quantitatively validating the benefits of an increase in battery life suggested qualitatively in previous studies.
4. Since many of the previous studies in this area have suggested theoretical systems without giving detailed consideration to the implementation approach, the focus of this study has also included the design of a practical hardware system implementation. In addition, this has had the benefit of ensuring the practical feasibility of the algorithms and systems considered.
5. To develop a hardware platform on which the performance of the system can be assessed. Since a practical wind-turbine was not available for testing the systems developed, one of the objectives has been to develop a hardware test-bed for experimental validation purposes.
6. To consider the application of supercapacitor technology in a battery-supercapacitor hybrid system under novel control schemes. As part of the on-going research effort in this area, one of the objectives of this project has been to consider the benefits of novel alternative control techniques for the application of supercapacitor technology in a battery-supercapacitor hybrid energy storage system and to report the findings.

1.6 Context

The context of the system considered is that of remote area renewable power systems also known as stand-alone or isolated renewable power systems although many of the

techniques described are directly relevant in other wind-power application contexts. Remote area renewable power systems are a form of distributed generation in which there is no connection to a national power grid often due to being logistically difficult or prohibitively expensive. In such areas, where fuel transportation costs and logistics can be costly, renewable energy is emerging as an attractive power solution. Consequently typical remote area power systems can consist of renewable generation sources such as PV generators, wind-energy conversion systems and diesel generators, some form of energy storage and a load. The power rating of such systems ranges from micro-systems of a few hundred watts to large scale isolated community supplies with >>100kW power ratings. Typical loads can often be rural-domestic loads and farms in grid-isolated communities [59-66] and telecommunication loads [67-70]. A top-level schematic of a remote area power system as defined by the IEEE [71] is shown in Fig. 1.3 below.

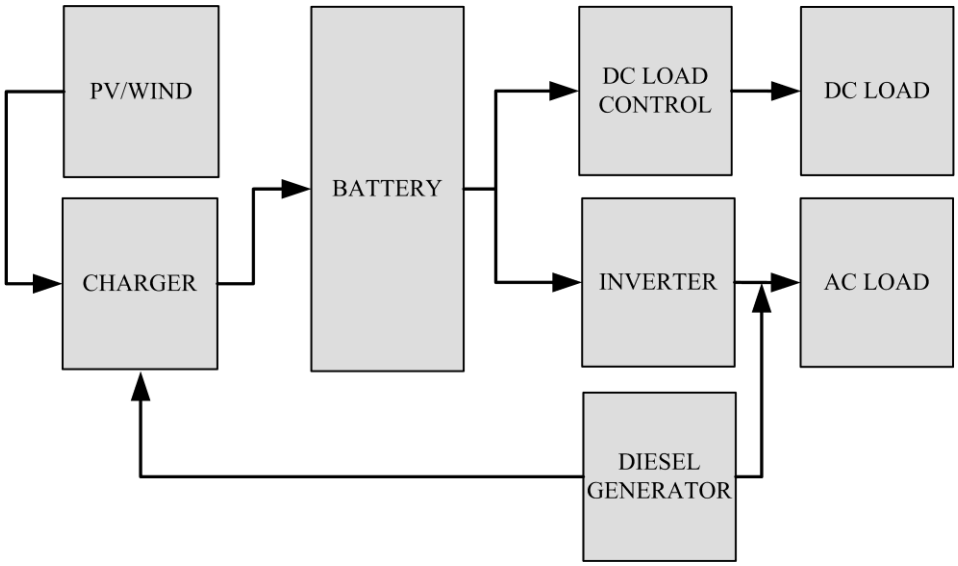

Figure 1.3 (a) Conceptual block diagram of a remote power system

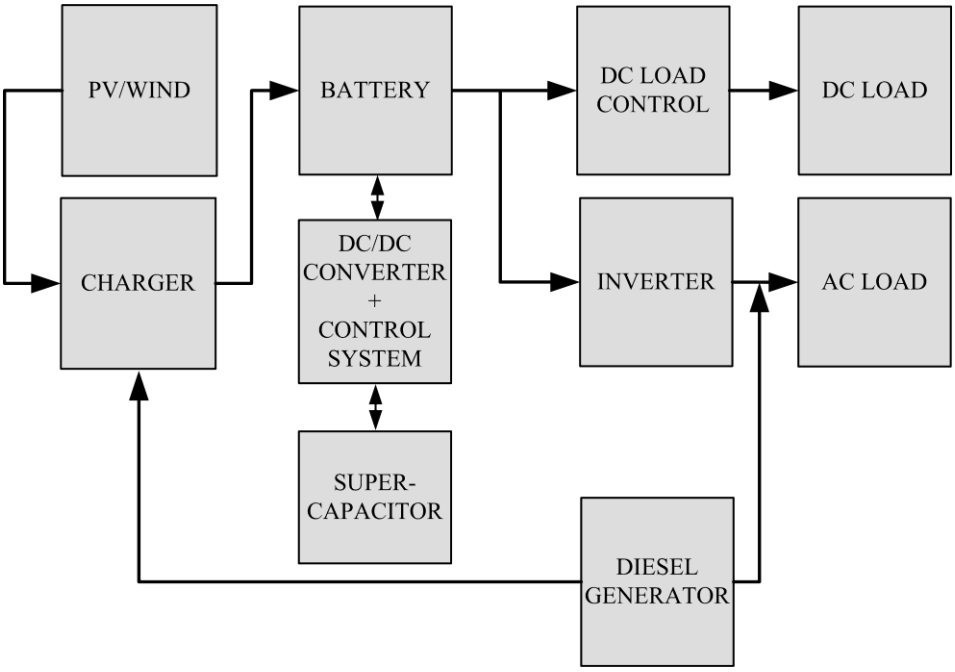

Figure 1.3 (b) Conceptual block diagram of proposed remote power system

Most renewable energy systems of this nature currently utilise lead-acid batteries [10] in spite of advances in the development of other cell chemistries, mainly due to their high availability and relatively low initial costs. High penetrations of renewable generation at real remote area power systems have been shown to reduce operation costs significantly compared with diesel-only alternatives, although battery-life has also been highlighted as a major challenge [72]. For this reason, the system implementation developed in this study has considered a lead-acid battery/supercapacitor hybrid energy storage system in the context of a remote area power system with either a high penetration of wind-generation or entirely wind-generation and no PV generation. However, the analysis presented can also be applied to grid-connected distributed generation scenarios aiming for a high level of renewable penetration such as home generation, low carbon building projects or microgrid-based systems. In addition, the general form of the modelling procedures developed can be applied in the future assessment of the other systems with only small modification to the methods presented.

1.7 Thesis Outline

Chapter 2 describes the modelling strategy used to develop a model of the wind as a resource that encompasses both long-term wind variations and short-term turbulent variations. Since long-term, low resolution (typically 1800s sampling interval data) wind speed data are readily available this chapter focuses on the simulation of the short-term or turbulent wind speed component.

Chapter 3 describes the modelling procedure used to simulate the sub-system components in the remote area power system including wind-generator, maximum power point tracking algorithm, generator-side and load-side power electronic conversion and the load itself. Models are developed from existing models or fundamental equations and optimised in the Simulink modelling environment for long-term simulation intervals.

Chapter 4 provides a theoretical background on batteries and supercapacitors and describes the modelling methodologies used to represent them. A battery model Simulink implementation, based on a commonly employed existing model is presented, some of its limitations are considered and an extension to this model is then suggested. The nature of the lead-acid cell impedance model is discussed for use in battery voltage control system design in later chapters.

Chapter 5 describes the method of battery life-time modelling employed in this study. The method is based on models developed by Manwell and McGowan who implemented them in the simulation package Hybrid2 [73]. A discussion of the limitations of the model and potential improvements is provided.

Chapter 6 describes the development of the DC/DC power electronic converters used in the active power sharing between the two energy storage devices within this study. Practical considerations relating to the design of the converter are then described, as is a Simulink model to evaluate its performance and efficiency map.

Chapter 7 presents the algorithms developed to determine a realistic configuration of wind power generation and energy storage system sizing subject to technical and techno-economic constraints.

Chapter 8 presents simulation and hardware results demonstrating a low-pass filter-based battery current control algorithm. A novel approach which employs the hysteretic current-controlled bidirectional DC/DC converter in a current filtering capacity to divert the high frequency current component to the supercapacitor is described. New results confirming the benefits of the battery power filtering approach in terms of an increase in expected battery-life are presented.

Chapter 9 presents a novel energy storage control strategy based on the use of supercapacitors to provide battery-voltage support. The theoretical derivation of the closed loop control system design, an analysis of its stability and control bandwidth limitations are given. Case study simulation results are used to show the potential benefits in terms of increased energy capture and estimated battery life. Hardware results are used to confirm the feasibility of the control strategy.

Chapter 10 provides the conclusion to this dissertation with a summary of the contributions and suggestions regarding future investigations.

1.7.1 Thesis Contributions

The main contributions from this thesis can be summarised as follows:

1. New results are presented which state the increase in battery cycle-life obtained by the use of a supercapacitor energy storage system in an active-hybridisation with batteries for battery-power smoothing in wind-energy applications. This extends previous studies which indicated the potential benefits of this control strategy but did not provide numerical results.
2. As part of the on-going research effort into the hybridisation of battery and supercapacitor energy storage systems, this study has described the novel use of an actively controlled supercapacitor under a battery-voltage based control scheme. The resulting hybrid energy storage system is capable of being charged at full-rated power across the entire state-of-charge range. This is unlike a conventional battery which typically requires some form of charge rate limitation at high states of charge. A detailed description of the control system design is given. A prototype hardware system has been developed and its operation confirmed by experiment. The potential benefits of the system operating in a remote wind-power application are shown to include increased energy capture (~29% increase when compared to typical alternative systems) and potentially increased cycle-life.
3. A detailed simulation strategy has been developed, enabling the benefits of battery-hybrid energy storage systems to be investigated. This has been achieved through the development of a high-fidelity model for the wind power as a resource coupled with a dynamic wind-energy conversion system optimised for long-term simulation intervals, a methodology for energy storage system sizing and a battery cycle-life aging model. The resulting simulation and analysis

methodology is used to present new simulation results describing the increase in battery cycle-life obtained through the use of an additional supercapacitor energy storage system, under different control strategies.

4. The novel use of a hysteretic-current controlled DC/DC converter to act as an interface between supercapacitor and battery energy storage systems has been reported and shown to have good dynamic current tracking performance. Detailed information has been given regarding the practical implementation of the converter operating under this control scheme enabling future research to build on this work. The strategy of using the hysteretic-current controlled converter as an active current filter system has been shown to significantly reduce battery charge cycling and the magnitude of battery current peaks by experiment. In addition, a system based on this converter design has been used to implement a novel hardware test-bed capable of delivering arbitrary current-profiles to the hybrid energy storage system under test.

1.7.2 Resulting Publications

Journal Papers:

A. Gee, F.V.P. Robinson, and R.W. Dunn, "Analysis of Battery lifetime Extension in an Off-Grid Wind-Energy System using Supercapacitors," IEEE Transactions on Energy Conversion.

Conference Papers:

A.M. Gee and R.W. Dunn, "Novel battery/supercapacitor hybrid energy storage control strategy for battery life extension in isolated wind-energy conversion systems," in Universities Power Engineering Conference (UPEC), 2010 45th International, Cardiff, Wales, 2010, pp. 1-6.

A. Gee, F.V.P. Robinson, and R.W. Dunn, "Sliding-mode control, dynamic assessment and practical implementation of a bidirectional buck/boost DC-to-DC converter," in *Power Electronics and Applications (EPE 2011), Proceedings of the 2011-14th European Conference on*, Birmingham, UK, 2011, pp. 1-10.

A. Gee and R.W. Dunn, "Design and analysis of a sliding-mode power electronic controlled battery/supercapacitor hybrid energy storage system for remote wind power," in Universities' Power Engineering Conference (UPEC), Proceedings of 2011 46th International, Soest, Germany, 2011, pp. 1-6.

Chapter 2: Wind Resource Modelling

2.1 Introduction

Fluctuations in the power generated by a wind turbine generator are primarily due to fluctuations in wind speed. To be able to effectively assess the performance of the energy storage systems developed in the context of a wind energy system, it was necessary to develop an accurate description of wind speed variations. This chapter describes the modelling procedure used to generate wind speed profiles used in later simulations. It is shown that wind speed variations consist of both short-term variations, typically less than a few minutes in duration, and long-term fluctuations which can vary over the course of a year more. A hybrid approach is described using real half-hourly meteorological measured data to represent the long-term or seasonal components and statistical frequency-domain techniques to model the higher frequency dynamic wind speed variations.

2.2 The Wind Resource

Winds are movements of air masses in the earth's atmosphere caused by solar radiation heating of the earth. Warmer, and therefore lighter, air rises from warmer regions of the earth's surface and moves towards the cooler poles in the higher layers of the atmosphere. At the same time, the lower layers are replaced by a return flow of air from cooler regions. The atmospheric region closest to the ground extending to a height of 100m is known as the 'surface layer'. One representation of the nature of surface layer winds is that given by Isaac Van der Hoven's spectrum shown in Fig 2.1 [74].

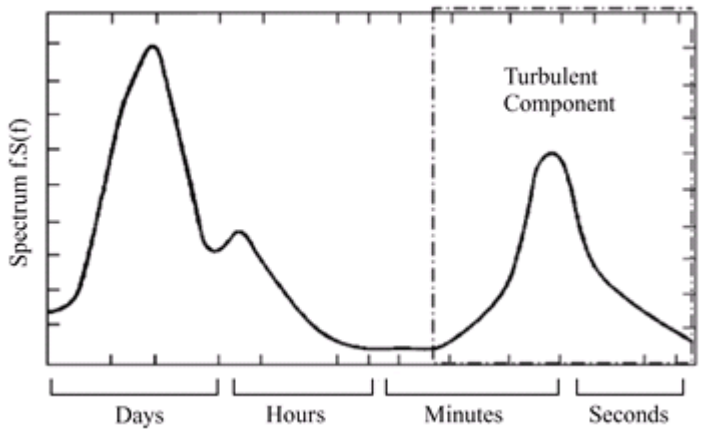

Fig. 2.1. Van der Hoven Spectrum [74].

Van der Hoven's spectral representation of the nature of wind speed variations shows two prominent peaks. This indicates that he observed two distinct frequency bands over which wind speed variations occurred more frequently in the range measured. Short-term variations of the wind speed with durations less than 10 minutes form the turbulence component and the micro-meteorological range [75]. Wind speed variations on the low frequency side of the spectrum form the macro-meteorological range [75] and a 'spectral gap' separating the short-term variations from slower variations can be seen. To characterize the lower frequency component of the wind speed spectrum, readily available real (averaged) meteorological wind-speed data taken at 1800s sampling intervals from a local weather station in Filton, Bristol were used (see Fig. 2.2) [76].

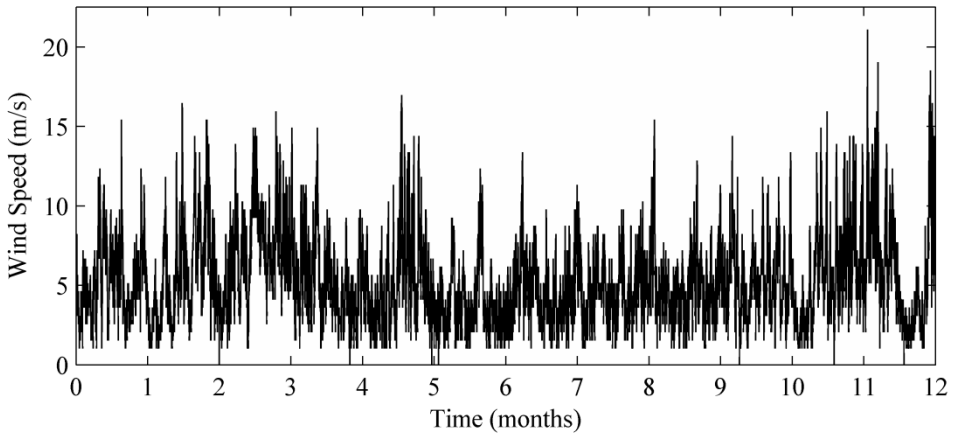

Fig. 2.2 Measured wind speeds

The measured mean wind speed can be seen to exhibit a significant variation over the year with the months 1-5 and 10–12 showing noticeably higher readings than the spring/summer months 5–10. The winds speeds shown in Fig. 2.2 are taken from an anemometer at 10m above sea level. As the installation height of the wind turbine has an effect on the energy available from the system, the 1800s mean wind-speed was corrected by a power law factor given below in Eq. (2.1) [75] with respect to the 10m wind speed reading as follows:

$$v_{hub}(h_{wt}) = v_{10}(h_{wt}/10)^{\alpha} \text{ (m/s)} \tag{2.1}$$

where $v_{hub}(h_{wt})$ is the effective wind speed (m/s) at hub height h_{wt} (m), v_{10} is the 10m wind speed reading (m/s), α = the Hellman Exponent.

α is known as the Hellman Exponent which is dependent the shape of the terrain of the local area, and the stability of the air. In [75] (p. 20) Burton states that α = 0.14 is suitable value for the Hellman exponent for relatively flat non coastal countryside.

2.3 Turbulence

‘Turbulence’ refers to rapid fluctuations in wind speed, typically arising over less than 10 minutes in duration [75] corresponding to the high frequency spectral peak in Fig.

2.1. Since there exist two distinct regions in the wind power spectrum of Fig. 2.1 separated by a spectral gap, a useful modelling assumption is to consider the wind speed as being made up of a slowly varying wind speed component and a short-term turbulence component. The slowly-varying component is determined by seasonal, synoptic and diurnal effects, with variations in the time-scale of one hour to several months and can be described by readily-available meteorological wind speed data (such as wind speed measurements taken at an 1800s sampling interval). Turbulence is a complex non-linear phenomenon which, like many weather phenomena, cannot be well defined by differential equations due to the large number of variables involved including pressure, temperature and humidity among others. Instead, the process can be thought of as stochastic [75] and it is generally a more useful modelling technique to develop statistical frequency-domain descriptions of the turbulent component of the wind speed spectrum.

2.3.1 Fixed Point Turbulence Model

Based on the assumption that turbulence is a stochastic process, the turbulent component of wind speed can be described by a spectral model of variations in the frequency-domain. Two frequency-domain representations that describe the turbulent wind component are the von Karman and Kaimal models which are defined in Eq.s 2.2 and 2.3 [75]. From the Kaimal or von Karman spectra, it can be seen that turbulent wind variations are proportional to the mean wind-speed value, whereas from the van der Hoven spectrum [74] this is not immediately apparent.

Von Karman [75]:

$$f.S_{vv}(f)/\sigma^2 = \frac{4.f.L_{1_t}/v_{mean}}{(1+70.8(f.L_{1_t}/v_{mean})^2)^{5/6}} \quad (2.2)$$

Kaimal [75]:

$$f.Svv/\sigma^2 = \frac{4.f.L_{2t}/v_{mean}}{(1+6.f.L_{2t}/v_{mean})^{5/3}} \tag{2.3}$$

where v_{mean} = mean wind speed (m/s), f = frequency (Hz), $S_{vv}(f)$ = power spectral density $(m/s)^2/Hz$, I_t = turbulence intensity factor (dimensionless). σ_w = wind speed standard deviation (m/s), L_{1t} and L_{2t} are turbulence length scales (m), see below Eq. (2.5).

Both of the above spectra have been recommended for use in the simulation of atmospheric turbulence [75]. The relative merits of the Kaimal spectrum are that it closely resembles empirical data whereas the von Karman spectrum is supported by analytical results. However, both are recognised as appropriate turbulent spectral models [75]. In Langreder's work [77], a Simulink implementation of the Kaimal spectral model is given. A similar form of implementation has been used in this thesis to describe the von Karman spectrum.

I_t is a turbulence intensity factor relative to the wind turbine location and is defined in terms of the variance and mean of the wind speed as follows:

$$I_t = \frac{\sigma_w}{v_s} \tag{2.4}$$

Typically the turbulence intensity has a value between 0 and 0.5 [78]. The effect of the turbulence variations is shown in Fig. 2.3 where it can be seen that they are greater at higher mean wind speeds.

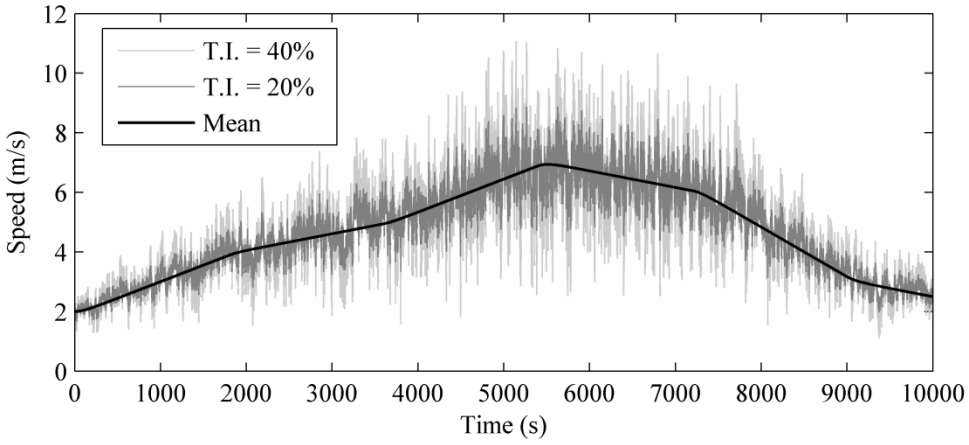

Fig. 2.3 Turbulent wind speed variations

The turbulence length scale, $L_{t,}$ and the turbulence intensity may be obtained by direct measurement or simulated according to various standards. For example, the Danish national standard DS 742 (2007) [75], [79] defines turbulence intensity and turbulent length scales as follows:

$$I_t = \frac{1}{\ln(z_{wt} / z_{wt0})} \quad L_{1t} = 150m \ \ if \ z_{wt} >= 30m \ \ L_{1t} = 5z_{wt} m \ \ if \ \ z_{wt} < 30m \tag{2.5}$$

where z_t = height in meters above ground where the wind speed is computed and z_{wt0} is the surface roughness length in meters of the terrain at the site in question.

The Danish national standard DS 742 (2007) [75], [79] does not make reference to the Von Karman spectrum but Burton [75] (p. 23) states that equivalent length scale L_{2t} $=L_{1t}/$ 2.329 can be used.

Table 2.1 shows some typical surface roughness values for different types of terrain.

TABLE 2.1: ROUGHNESS SCALES FOR DIFFERENT TYPES OF TERRAIN [75]

Terrain	Roughness Length: z_{wt0} (m)
Cities, forests	0.7
Suburbs, woodland	0.3
Villages, countryside with trees and hedges	0.1

Open farmland, some trees or buildings	0.03
Flat, grassland	0.01
Flat desert or sea	0.001

The method used to develop the turbulence model has been previously well-reported [77], [79-82]. To obtain a signal with the same spectral properties as the models described by Eqs. (2.1) and (2.3), previous work [77], [79-82] has shown that a white noise signal can be filtered such that the signal at the output of the filter has the required statistical properties. A 'shaping filter' transfer-function of the following form can be used [79], [80]:

$$H(j\omega) = \frac{K_f}{(1 + j\omega T_f)^{5/6}} \tag{2.6}$$

where K_f and T_f are computed according to Eqs. (2.7) and (2.8) ω = frequency (radians).

The non-integer order of the denominator presents some numerical difficulties when implementing the filter in this form directly in Simulink since it is not possible to directly implement fractional order transfer functions. For this reason, rational order approximations to the non-integer order spectra were developed, based on the procedure described in [79], [80] and shown in Fig. 2.4. A rational filter of this form can achieve a close approximation to the filter of Eq. (2.6). This can be used to generate the turbulence component with significantly less computational effort which is particularly useful in real-time turbulence emulation.

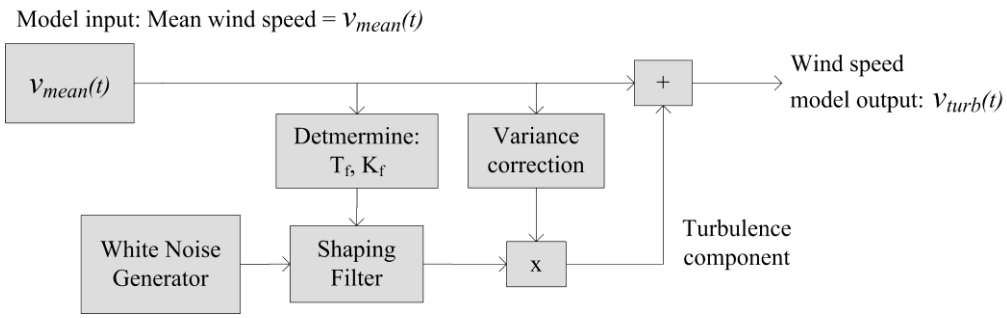

Fig. 2.4 Wind speed modelling top-level block diagram

The computations performed in each of the blocks in Fig. 2.4 are as follows. For each measured value of the mean wind speed, v_{mean} , the shaping filter coefficient, T_f and K_f are computed:

$$T_f(t) = L_{1t} / v_{mean}(t) \tag{2.7}$$

where L_{1t} is the turbulence length scale (m).

It can be shown [79], [80] that a gain K_f can be computed to obtain a unity variance at the filter output as follows:

$$K_f = \sqrt{\frac{2.\pi.T_f}{\beta(\frac{1}{2},\frac{1}{3}).T_s}} \tag{2.8}$$

where T_s is the sampling period (s) and β is the beta function [79], [80].

A second order shaping filter of the following form has been shown [79], [80] to give a good approximation to both of the spectral models of Eqs. 2.2 and 2.3:

$$H_t(s) = K_f \frac{m_1 T_1 s + 1}{(T_f s + 1)(m_2 T_f s + 1)} \tag{2.9}$$

where the constants are: $m_1 = 0.4$ and $m_2 = 0.25$ [79], [80].

The signal at the filter output has been scaled by the factor $I_t.v_{mean}$ [79], [80] to adjust the variance to that of the site in question.

To validate the shaping filter turbulence component model, the rational order and fractional-order von Karman turbulence models bode-magnitude responses were generated using the Matlab Control System Toolbox [83] with the results shown in Fig. 2.5.

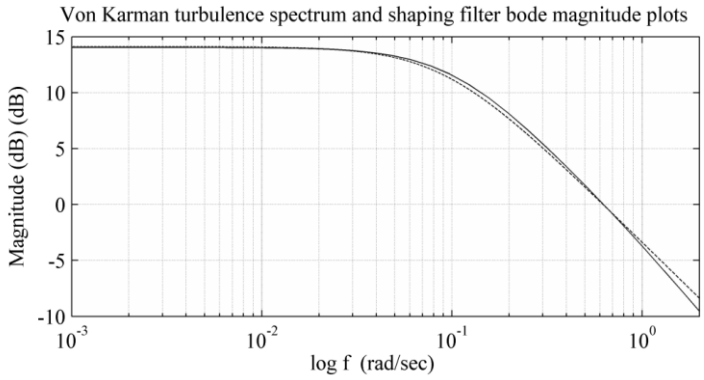

Fig. 2.5 Bode magnitude plot of von Karman fractional order shaping (dashed line) filters and rational order approximation (solid line). v_{mean} = 10m/s

The results show that the second order shaping filter output magnitude plot achieves a close approximation to the non-integer order filter magnitude response. The Simulink implementation of the von Karman turbulence generator is shown in Fig. 2.6. Since the shaping filter transfer-function coefficients from Eq. 2.7 and 2.8 are not static, the Simulink implementation involved the block diagram decomposition of the shaping filter transfer-function into separate integrator and gain blocks as shown in Fig. 2.6. This allows the filter coefficients to change dynamically during simulation time. The result is an implementation of a von Karman turbulence spectrum generator in the Simulink modelling environment.

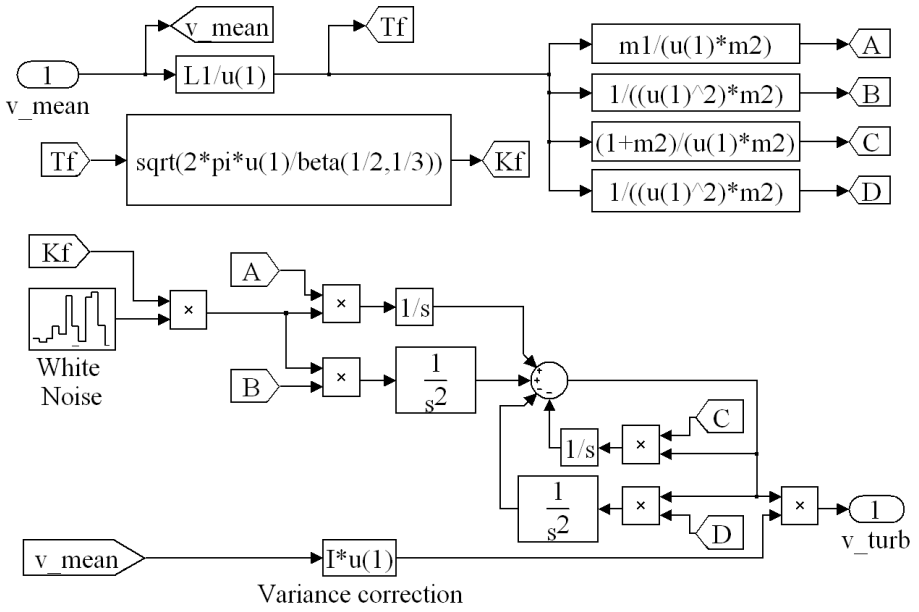

Fig. 2.6. Simulink implementation of von Karman fixed point turbulence model

The above model can generate turbulent fluctuations in real-time and consequently is a useful tool for the Simulation of turbulent wind speed for real-time hardware testing purposes.

2.3.2 Spatial turbulence model

The swept area of a wind turbine's blades can embrace a range of heights and turbulence-zones [79]. It has been shown that the power spectrum of the turbulent component of the wind acting on a wind turbine blade can be affected by its motion passing through different turbulence zones [77]. The fixed point turbulence model described in section 2.3.1 was extended to investigate the effect of rotational movement through the swept area on the effective turbulent wind speed acting on the wind turbine blades. The case study systems described in Chapter 7-9 are in a class of wind turbines with relatively small diameter radii (~5m or less). It is shown that, while the effect of the rotational movement of the blades through turbulent zones has an effect on wind turbines with larger radii (>>10m), the effect is negligible for smaller scale wind turbines (with <10m radius).

The method used to evaluate the effect of rotational movement through turbulence zones was based on that described by Langreder [77] and Sorensen [84] which involves a description of the turbulent wind field acting on the rotor in terms of a sum of harmonics of its angular velocity, ω_{wt}. Langreder [77] defines 'admittance functions' used to relate the fixed point turbulence component to that experienced by the rotating blade as it passes through the wind field. The admittance function is described as: "A weighting function to transform the fixed point spectrum into a rotational spectrum of the turbulence." [77]. Second order approximations can be used to represent the admittance functions of the 0^{th} and 3^{rd} harmonics of the wind turbine rotational velocity in transfer-function form as follows:

$$H_0(s) = \frac{0.99 + 4.79 d_1 s}{1 + 7.35 d_1 s + 7.68 (d_1 s)^2} \tag{2.10}$$

$$H_3(s) = \frac{0.0307 + 0.277 d_1 s}{1 + 1.77 d_1 s + 0.369 (d_1 s)^2} \tag{2.11}$$

where $d_1 = R/v_{mean}$ and R = wind turbine blade radius.

It has been shown [84] that only the harmonic terms, with coefficients which are multiples of 3, contribute to the effective wind speed experienced by a three-bladed wind turbine rotor. This is due to the symmetry of the rotor structure, which causes the contributions of even orders to cancel-out. Most modern wind turbines are three bladed so only harmonic terms with multiples of three were considered. Here, as per Langreder's original work [77], only the third harmonic component is included as the sixth harmonic and above components are assumed to be filtered out by the structure of the wind turbine as has been discussed by Sørensen et al. [84].

Since the admittance functions have dynamically-changing coefficients, to implement them in Simulink, block diagram reduction was used to reduce these into integrator and gain-block form as before. The third harmonic term has complex Fourier coefficients and is represented in trigonometric form so the output of the third harmonic admittance function is multiplied by the sine and cosine terms of the rotational angular velocity [77]. The overall Simulink implementation of the rotationally sampled wind field was based on the von Karman fixed point turbulent model using the technique developed by Langreder [77] and is shown in Fig. 2.7.

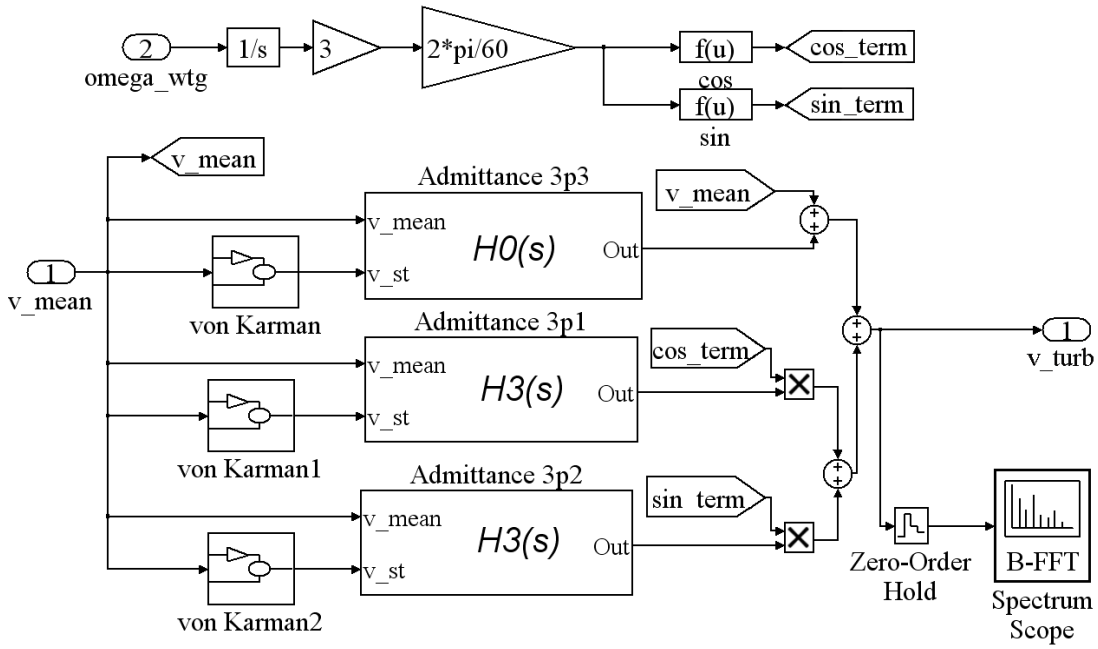

Fig. 2.7 Rotational-sampling turbulence model

To evaluate the effect of rotational sampling on the output turbulent wind-power spectral density, the Simulink spectrum-scope block [85] was connected as shown in Fig. 2.7. The output power spectrum for three different blade radii and with no rotational sampling is plotted in figs. 2.8 (a) – (d).

In Fig 2.8 (a), the effect of the rotational sampling is seen as a peak in the power spectrum at the third multiple of the rotational frequency of the machine. This

corresponds to a shift of energy to the third harmonic and, in reality, multiples of the third harmonic of the rotational frequency. Comparison of the wind-speed power spectra in Fig. 2.8 (a) – (d) shows that the effect of rotational sampling is significant in the case of the 60m wind turbine radius whereas-for wind turbines with radius <<10m it is negligible.

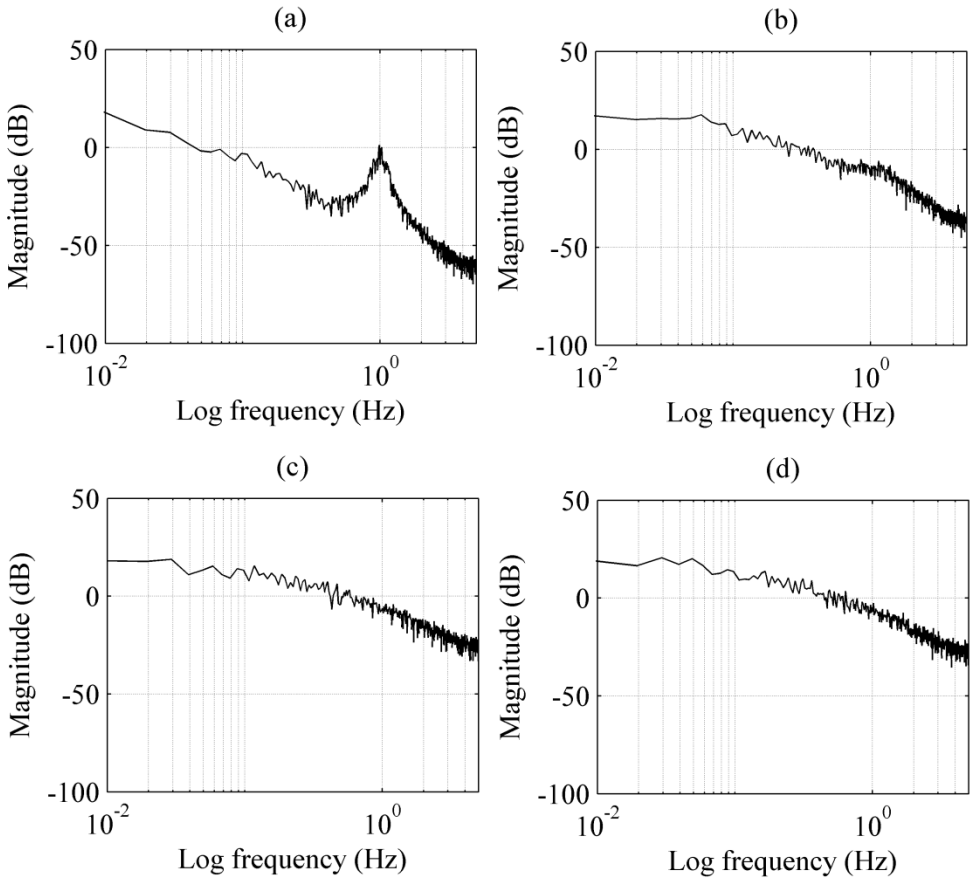

Fig. 2.8 Effective wind-speed model output power spectra (a) 60m blade-radius (b) 10m blade-radius (c) 3m blade-radius (d) no rotational sampling. Mean wind speed = 15m/s, Shaft velocity = 20rpm.

2.4 Discussion and Summary

The modelling technique presented in this chapter provides a means by which the dynamic nature of the wind can be described using a hybrid approach based on real life long term seasonal variations and a simulated turbulence spectrum model. The Simulink implementation of the model is computationally fast and allows the generation of a

dynamically varying wind field during simulation or in real-time; for use in hardware emulation of a wind turbine generator. Investigation into the correlation between the wind turbine radius and rotationally-sampled wind-power spectrum for different blade-radii has provided results confirming that the effect of rotational sampling is much greater in the case of wind turbines with larger (>10m) blade radii. This indicates that, for the class of wind turbine considered in this study, which are of relatively small blade radius (<10m), the effect of rotational sampling can be neglected from the turbulent wind-speed model. This is supported in relevant literature [79] (p. 46). Since the class of wind-turbines considered later in Chapters 7–9 fall into the category of low-power wind turbines with blade radius <10m, the fixed-point wind-speed, with no rotational sampling model has been employed in the rest of this study.

Chapter 3: Wind Energy Conversion System Modelling

3.1 Introduction

Interest in wind energy has grown considerably in recent years. This has been driven by mitigation of $C0_2$ emissions and sustainable energy generation targets in the UK and European Union. One of the biggest challenges in generating power from the wind arises due to its highly unpredictable nature, which has been shown in the previous chapter to be well represented by a stochastic process in the short-term. To assess the benefits of energy storage in the context of a wind power system, it was necessary to accurately describe the nature of the power output from a wind energy conversion system. This chapter describes the procedure used to model a representative system capable of generating electrical power from the wind. The simulation strategy is intended to capture dynamic variations primarily due to wind energy variations with electromagnetic transients and power electronic switching intervals not described. Sub-system level models for the aerodynamic power generated, the mechanical drive-train, and a generalised generator model are presented. The control of the simulated generator power output is by means of a power electronic converter based on a maximum power point tracking algorithm, also described in the model. As the consideration of the research was directed primarily towards a domestic off-grid load, an accurate domestic load profile (based on real load measurement data) is presented although the method of analysis presented later and some of the benefits of the proposed system are also valid for other typical off-grid loads.

3.2 Wind energy conversion system modelling process

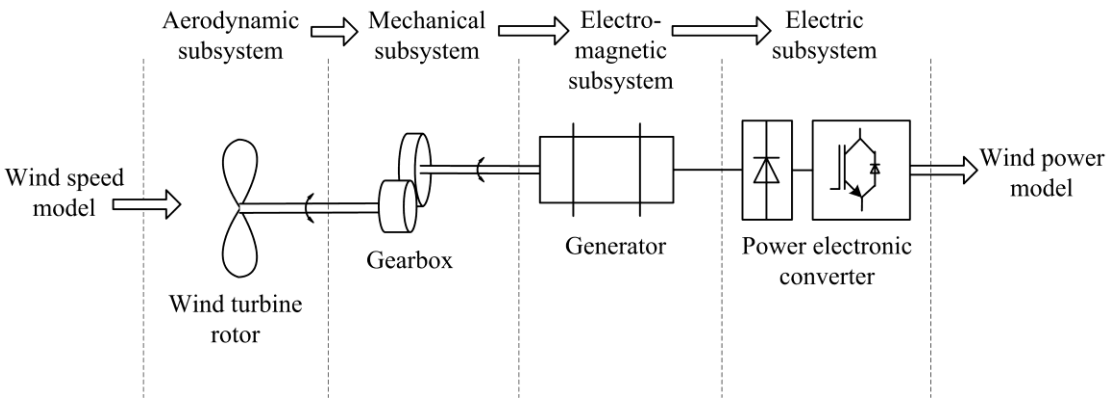

Fig. 3.1 Wind energy conversion system modelling process.

A typical wind energy conversion system as shown in Fig. 3.1 consists of the following subsystems:

- The aerodynamic subsystem, describing the aerodynamic power generated by the wind turbine blades.
- The drive-train, which transmits mechanical power from the wind turbine blades to the electrical generator.
- The electromagnetic subsystem, constituting the electric generator and associated systems.
- The electric subsystem, including power-electronic circuit elements for the conversion of electric power.

This section describes the modelling procedure used to describe these sub-systems and how they interact dynamically with each other to produce an electric power profile output dependent on input wind speed. The model includes the effects of inertias within the system, frictional damping, power regulation and maximum power point tracking

strategies. The effects of electro-magnetic transients or switching intervals were not explicitly included in the simulation to enable long term simulations of the order of one month or more to be manageably undertaken with reduced computational effort. The primary simulation objective was to capture power variations due to high frequency wind and load variations which are typically several orders of magnitude lower than power electronic switching intervals. To include such switching intervals in a Simulink model would have had the effect of increasing simulation time significantly and causing an unnecessary computational requirement.

3.2.1 Aerodynamic subsystem

The maximum theoretical efficiency which can be achieved by a wind turbine rotor can be shown to occur when the ratio of the wind-speed upstream of the wind turbine to the downstream wind speed is 1/3 [86]. In this condition, the ratio of power extracted from the moving mass of air and the total power contained in the moving mass of air is 16/27 or 0.59 which is known as Betz's limit [87]. In reality, wind turbine efficiency can only approach this value with typical values ranging from 0.3 to 0.5 [88], [89]. The power coefficient $C_p(\lambda)$ is a generally accepted way of describing the actual power extraction efficiency [75], [90], where λ denotes the ratio between the blade tip speed and the incident wind speed:

$$\lambda = R\omega_{wt} / v_{wind} \tag{3.1}$$

v_{wind} = wind speed (m/s), R = blade radius (m), ω_{wt} = shaft rotational velocity (rad/s)

The simulated power coefficient is dependent on the wind speed and shaft rotational velocity as shown in Fig. 3.1.

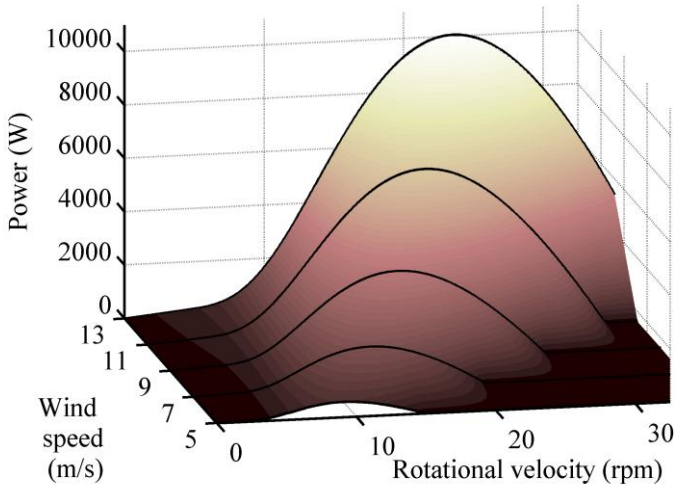

Fig. 3.2 Wind turbine output power vs. wind speed and shaft rotational velocity (Simulated results based on Eqs. 3.2 and 3.4).

To model this relationship, the coefficient of power $C_p(\lambda)$ as a function of the tip speed ratio, λ, was generated by curve fitting to manufacturer's data described by Heier [90] as follows:

$$C_p(\lambda) = c_1(c_2 - c_3\theta_p - c_4\theta_p{}^x - c_5)e^{-c_6} \tag{3.2}$$

where the results of curve fitting are [90]: c_1=5176, c_2 = 116/ λ_i, c_3 = 0.4, c_4 = 0, c_5 = 5, c_6 = 21 /λ_i, θ_p = pitch angle about its axis with respect to the hub (degrees) and x = 2 is a dimensionless modelling parameter.

and λ_i is a function of the tip speed ratio given by [90]:

$$\frac{1}{\lambda_i} = \frac{1}{\lambda + 0.089} - \frac{0.035}{\theta_p{}^3 + 1} \tag{3.3}$$

Some wind turbines employ a variable-pitch system which enables power control by varying the wind-turbine blade pitch angle θ_p. However, many small scale wind turbine

generators adopt a simpler fixed-pitch system [79]. This model considers the fixed pitch case in which $\theta_p = 0°$.

The aerodynamic power output of the wind turbine (P_{wt}) for a given wind speed can then be determined from the following equation:

$$P_{wt} = \frac{1}{2}\rho\pi R^2 v_{wind}{}^3 C_p(\lambda) \tag{3.4}$$

where ρ = density of air (kg/m), R = wind turbine radius (m), v_{wind} = wind speed (m/s)

3.2.2 Power regulation

Various strategies exist to limit power at high wind speeds such as pitch regulation, where the blade angle is varied to maintain the wind turbine output power or stall regulation where the design of the rotor blade inherently minimizes power output at higher speeds [79]. This is done to maintain the output of the wind turbine generator within a safe operating region and thereby prevent a potentially dangerous over-speed condition. For these reasons, to realistically describe power available from a typical wind turbine, it is necessary to model the method by which power is regulated at high wind speed to avoid drastically overestimating the power available.

As the study is primarily concerned with smaller scale wind turbine systems (<10m), a method often used in smaller scale designs known as ‘yaw control’ or ‘furling’ was considered [79]. This method reduces the power output of the wind turbine at high wind speeds by turning the rotor axis away from the incident wind angle as shown in Fig. 3.3.

$$P_{wt} = \frac{1}{2}\rho\pi R^2 \left[v_{wind} Cos(\theta_f)\right]^3 C_p(\lambda) \quad \text{(W)} \tag{3.5}$$

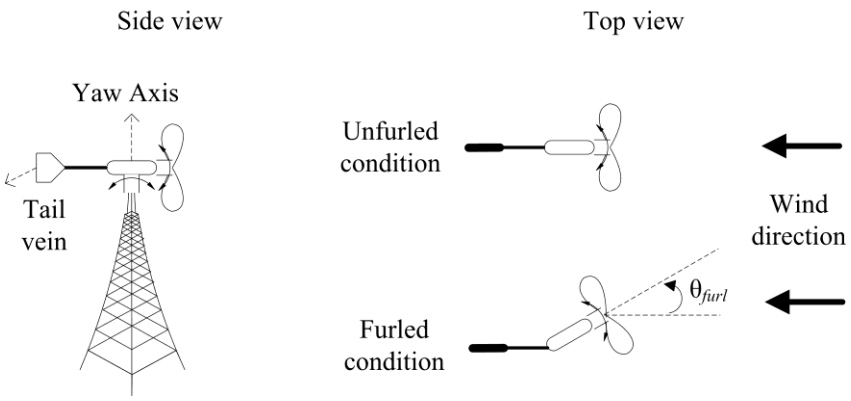

Fig. 3.3 Furling power regulation.

It has been proposed [91], [92] that an effective wind speed model during the furled condition can be derived by taking the product of the incident wind speed and the cosine of the angle between the shaft and wind direction, θ_{furl} in Fig. 3.3. The relationship between the furl angle, θ_{furl}, and incident wind speed can be determined by curve fitting [92]. A representative plot of output power vs. wind speed showing the effect of this furling mechanism model is shown in Fig. 3.4 (a).

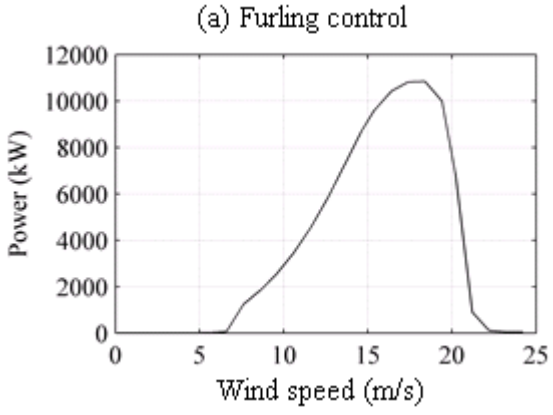

Fig. 3.4 (a) Furling power regulation model outputs. model (v_{cut_in} = 3.5 m/s, v_{rated} = 15m/s, v_{cut_out} = 19 m/s)

Since the model of Fig. 3.4 (a) has not been validated and to enable faster simulation

times, the simplified power regulation model shown in Fig. 3.4 (b) has been used in later simulations (Chapters 7 – 9). This conservatively approximates the power output of the wind turbine during power regulation by limiting the effective wind speed [93] to v_{rated}. The 'cut-in' wind speed is the wind speed below which the wind energy conversion system does not produce power. The 'cut-out' wind speed is the wind speed above which the wind energy conversion system does not produce power. To characterize this effect, the effective wind speed was set to zero if the incident was below the cut-in wind speed (typically ~3.5m/s) or above the cut-out wind speed (~20m/s). The effective wind speed can then be determined as follows:

$$v_{effective} = \begin{cases} 0 & if \quad v_{wind} > v_{cut\_out} \\ v_{rated} & if \quad v_{wind} > v_{rated} \\ 0 & if \quad v_{wind} < v_{cut\_in} \end{cases} \quad \text{(m/s)} \tag{3.6}$$

where v_{rated}, v_{cut_out} and v_{cut_in} are the rated, cut-out and cut-in wind speeds often found on wind-turbine manufacturer's datasheets.

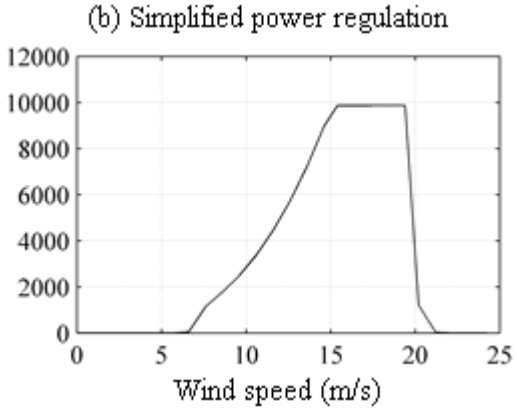

(b) Simplified power regulation model (v_{cut_in} = 3.5 m/s, v_{rated} = 15m/s, v_{cut_out} = 19 m/s)

3.2.3 Drive-train model

In general terms, the drive-train consists of the inertias associated with the system (including the turbine, rotor and generator inertia), a gear box (if present), and compliance and friction terms. The wind turbine shaft rotational velocity can be determined by resolving the resultant torque acting on the drive shaft (see Eq. 3.7). Various models were considered to describe the drive shaft mechanical sub-system. However, as the consideration turned to a relatively small diameter wind turbine of less than 10m radius, the following two-mass model with frictional damping of Eq. 3.7 was used to represent the dominant dynamics of the drive shaft with shaft stiffness neglected. The 'lumped' parameter total inertia (J) and damping (D) coefficients were used to represent the total combined inertia and damping in the wind turbine and generator. The angular velocity can be found by resolving the resultant torque acting on the shaft described by the following equation:

$$J\frac{d\omega_{wt}}{dt} = T_{wt} + T_{em} - D\omega_{wt} \quad \text{(Nm)} \tag{3.7}$$

The instantaneous wind torque is T_{wt}. The opposing electro-magnetic torque from the generator side is Tem and is determined from the electrical load applied to the generator. The above equations were implemented for the case of a wind turbine generator with a gear box in Simulink as shown in Fig. 3.5. However the wind-turbine models considered did not employ a gear box so the gear ratio was simply set to 1.

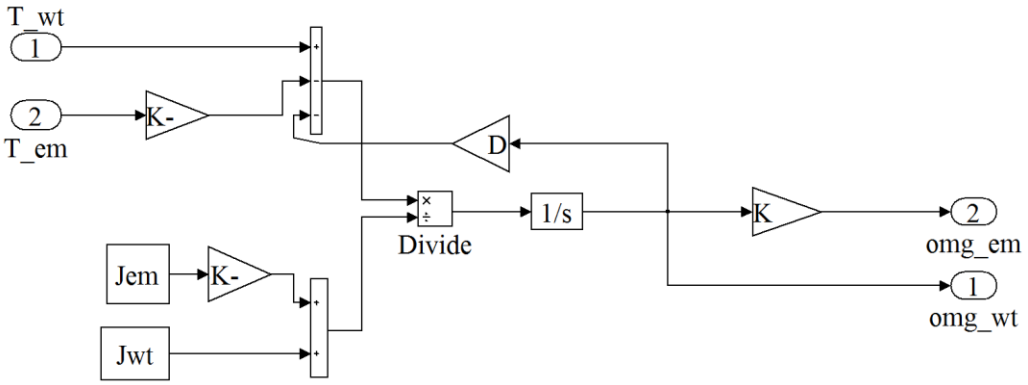

Fig. 3.5 Simulink model of rigid drive shaft with gearbox where T_{wt} = instantaneous wind torque (Nm), J_{wt} = wind turbine inertia (kgm^2), T_{em} = generator side electro-magnetic torque (Nm), J_{em} = generator side inertia (kgm^2), K = gearbox ratio.

3.2.4 Generator model

A popular choice of generator topology for stand-alone or off-grid wind energy systems is a permanent magnet synchronous generator [94]. This generator has the advantage of self-excitation meaning no electrical power is required for the generator to output power, coupled with relatively high efficiency and low maintenance requirements. The output is in the form of a variable AC voltage proportional to shaft speed. The modelling procedure will be described for the permanent magnet synchronous machine but the subsequent analysis can also apply to other generator configurations.

In the case of a permanent magnet synchronous generator, the equivalent circuit model of the permanent magnet machine shown in Fig 3.6 can be used.

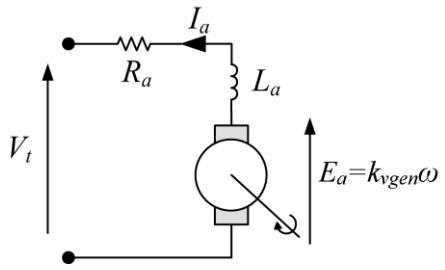

Fig. 3.6 Permanent magnet DC machine equivalent circuit where L_a = armature inductance (H), I_a = armature current (A), R_a = armature resistance (ohms), V_t = generator voltage (V), where k_{vgen} = generator voltage constant (V/rad/s), ω = generator electrical frequency (rad/s)

The governing equations for the DC machine of Fig. 3.6 are:

$$T_{em} = k_{Tgen} I_a \quad \text{(Nm)} \tag{3.8}$$

where k_{Tgen} = generator torque constant (Nm/A), I_a = armature current (A).

$$V_t = E_a - L_a \frac{dI_a}{dt} - R_a I_a \quad \text{(V)} \tag{3.9}$$

where L_a = armature inductance (H), R_a = armature resistance (ohms), V_t = generator voltage (V), I_a = armature current (A).

Initially, the above generator model was used to determine the voltage output of the generator when necessary. However, as the study turned towards the optimisation of the energy storage system over long periods of time it was necessary to make the modelling assumption that the output power of the generator (found from the product V_t x I_a) could be implicitly derived from the torque acting on its shaft using Eq 3.7.

3.2.5 Electric Subsystem

The intended output of the wind turbine electrical sub-system model is the steady state electrical output of the wind turbine generator and power electronic converter connected at the generator output. A power electronic converter is frequently connected at the

generator output terminals so that its output power can be electronically controlled according to an appropriate algorithm. To express the output power of the power electronic converter, it was necessary to consider the control regime under which it operates. It can be seen from Fig. 3.2 that for each incident wind speed, there exists a point at which the aerodynamic wind power is at a maximum. Algorithms known as "maximum power point tracking algorithms" are used to maintain the output power of the wind turbine in the near vicinity of this point as the wind speed varies. One class of algorithms known as 'perturb and observe' uses perturbation of a control variable and observes the difference in output power [79]. The position relative to the optimum power point curve is then calculated by evaluating the corresponding rate of change in output power due to the perturbation signal. Another strategy relies on a remote wind speed measurement, a rotor speed measurement and presumes knowledge of the optimum tip speed ratio λ_{opt}. Eq (3.1) is then used to control the shaft velocity such that the tip speed ratio is at or near the optimum, λ_{opt} [79]. A drawback of this system is that a real-time wind speed measurement is required and that the wind speed information measured remotely is not necessarily the same as the wind field experienced by the wind turbine's blades. An alternative method [79], [87] which does not an require additional wind speed measurement was the method implemented for use in the following simulations. This method assumes prior knowledge of the optimal tip-speed ratio λ_{opt} and that a real-time shaft velocity measurement is available. At the optimal point Eq. (3.1) becomes:

$$v_{wind} = R\omega_{wt} / \lambda_{opt} \quad \text{(m/s)} \tag{3.10}$$

Substituting (3.10) in (3.4), yields the optimal power reference as a function of shaft velocity:

$$P_{opt}(\omega) = \frac{0.5 C_p(\lambda_{opt}) \rho \pi R^5}{\lambda_{opt}^{\ 3}} \omega_{wt}^{\ 3} \quad \text{(W)} \tag{3.11}$$

To maintain operation at the maximum power point, the output power of the wind turbine generator should equal the optimum power, P_{opt}. This is achieved by controlling the electronic converter power output to control the corresponding electromagnetic torque as follows:

$$\frac{P_{opt}}{\omega_{wt}} = J \frac{d\omega_{wt}}{dt} + T_{em} + D\omega_{wt} \quad \text{(Nm)} \tag{3.12}$$

Assuming the efficiency of the power electronic converter and wind turbine generator can be represented by E_{gen}, the output power of the converter can be expressed as:

$$P_{out} = P_{opt} E_{gen} \quad \text{(W)} \tag{3.13}$$

The overall top level simulation diagram of the wind energy conversion system can then be drawn as shown in Fig. 3.7 below:

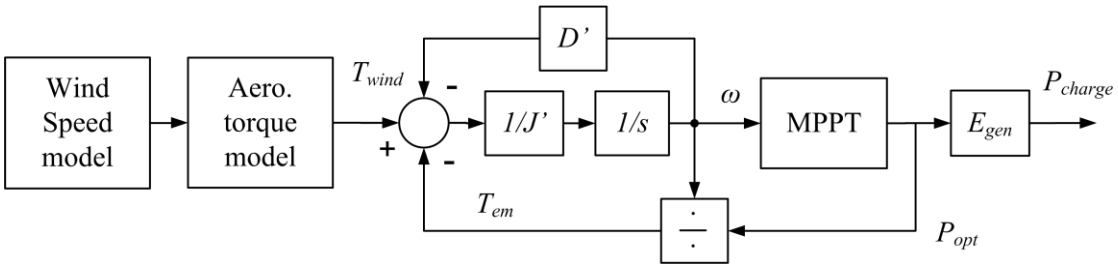

Fig 3.7 Top level simulation diagram of the wind energy conversion system.

Recent studies [95] indicate that a suitable figure for the electrical efficiency of a small generator can be >80% if the rotor speed can be maintained less at than ~350rpm. The parameter E_{gen} was used to scale the output efficiency of the wind turbine and power electronic converter in the system model to give a nominal value of 80% at rated speed.

Fig. 3.8 shows the modelling outputs from the Simulink implementation of the system in Fig. 3.7.

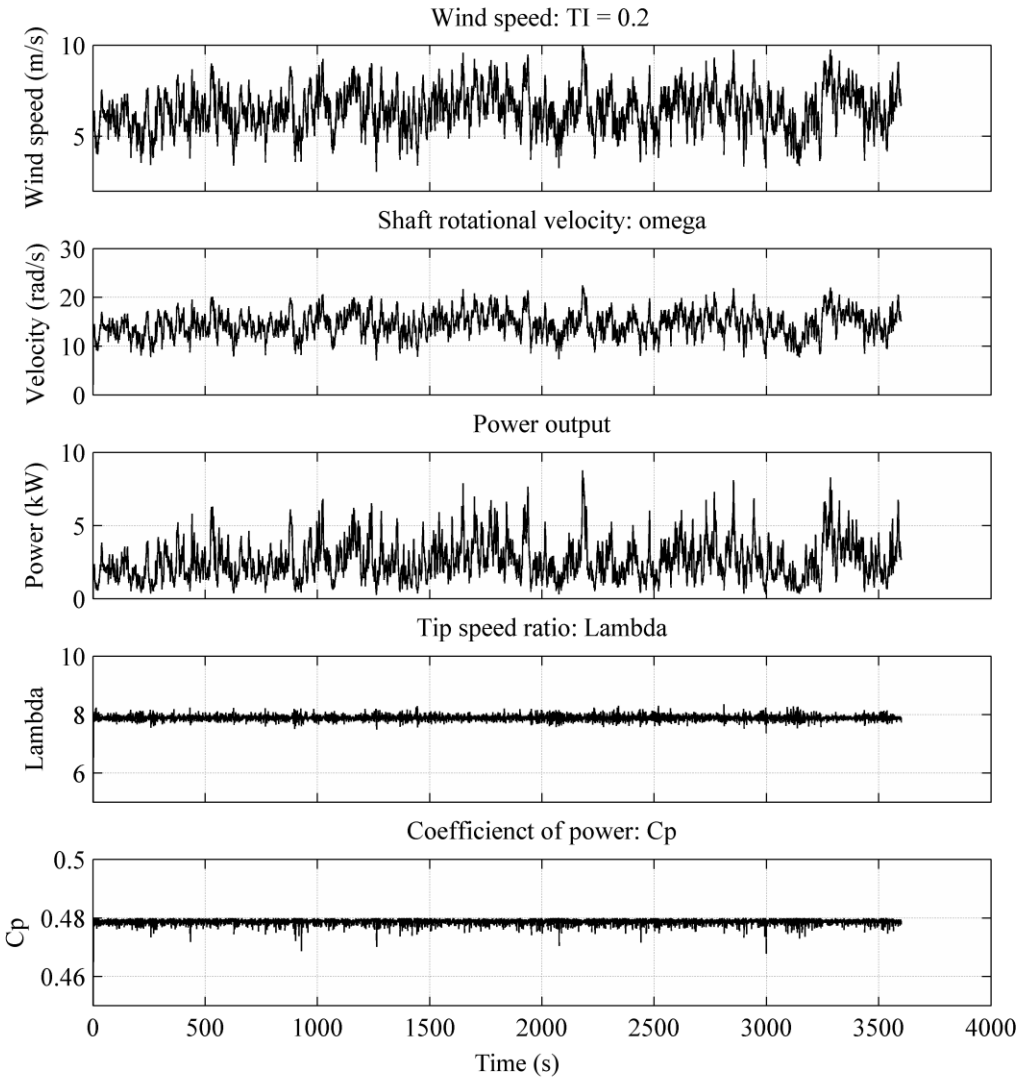

Fig 3.8 Wind energy conversion system modelling results. Wind turbine radius = 3.5m

As later analyses are performed over timescales including seasonal variations at relatively high sampling rates of the order of <1s, to improve simulation times, the assumption was made that the power electronic converter is able to control the flow of power to the load and energy storage according to the maximum power point tracking algorithms at all times that the wind speed, $v_{wind} > v_{cut\_in}$. This assumption allowed a certain level of decoupling between the above wind energy conversion system simulation and the remaining energy storage dynamic control simulation. This reduced

computational effort by allowing the output of the wind energy conversion system to be calculated for different parameter sets as a batch-process separate from the remaining energy storage control simulation. The main disadvantage of this approach is that times during which maximum power point tracking controller is not able to maintain the system on or near the maximum power point are omitted from the simulation. Such times include extreme wind events. However the general trend of the variations in wind turbine output power is still captured using this technique which was the main modelling objective.

3.3 Load model

In remote off-grid power systems, one of the main causes of variability in the power profile experienced by the battery is due to turbulent wind-speed variations. However, since the battery is subjected to the difference in power between the load and available wind power, load variations also contribute to the resultant power profile. A realistic domestic load profile was initially chosen as a load pattern representative of an off-grid system. However, other load profiles may also be relevant such as telecoms loads, remote municipal building loads such as schools and hospitals or water pumping loads. It is expected that the system proposed can provide similar benefits in such applications as well but a domestic load profile was created as described below.

3.3.1 Load Measurements

The power drawn from a local domestic load was logged at a sampling rate of 1Hz over the course of one week. This coincides with the wind turbine model which also had an output sampling rate of 1Hz. To prevent having to measure the mains voltage, the assumption was made that it was constant course of the measurement period, for safety reasons. A hall-effect current transducer was then used to measure the load current non-

intrusively. The measured alternating current signal was converted to DC using a precision rectifier, scaled to an appropriate level and logged using a National Instruments USB-6009 A/D converter and laptop for data gathering. The logging period was one week. The real power was determined from the product of the constant 230Vac voltage and measured current. The resulting power profile representing a week of recorded load data is shown in Fig. 3.9.

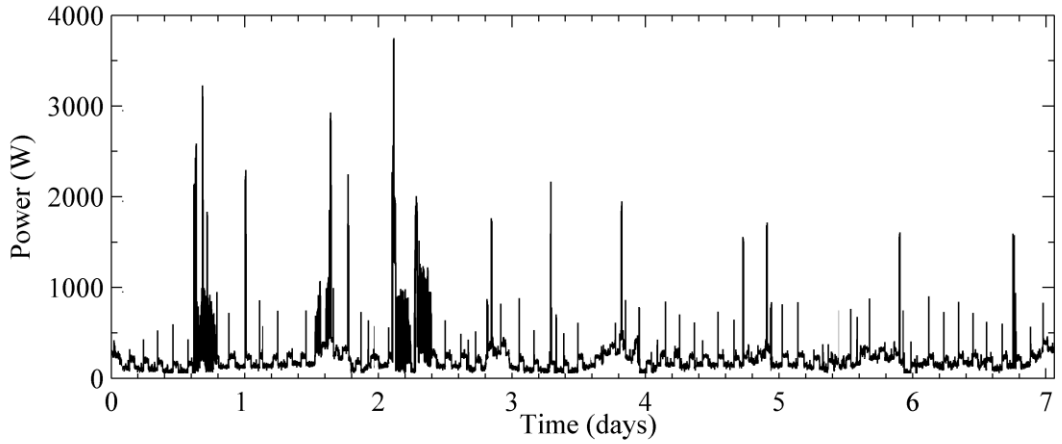

Fig 3.9 Measured 1 week domestic load profile

From the measured load profile, daily variations (with period 86400s) can be seen corresponding to daily domestic load patterns (e.g. lights and cooking in the evening). Also, large power spikes attributable to motor inrush currents such as a fridge compressor motor starting in a semi-regular pattern can be seen. The base load in this profile was due to computers operating continuously and represents significant energy consumption.

Since the availability of wind energy is not guaranteed, a rural off-grid system reliant solely on wind energy is expected to have a load pattern with lower energy and power requirements than that of Fig. 3.9. A review of reported off-grid loads shows that TV and lighting feature high on the list [59], [65] with importance being placed on refrigeration loads to keep vaccines and medicines [64]. For this reason, the large

power peaks and continuous base load may not be representative of a small off-grid remote/rural application. To generate a load which more closely resembled the expected nature of a small off-grid load, a 24 hour period of low-usage measurements was taken with the base load due to computers running intentionally disconnected. The resulting load profile consists primarily of lighting and refrigeration loads as shown in Fig. 3.10.

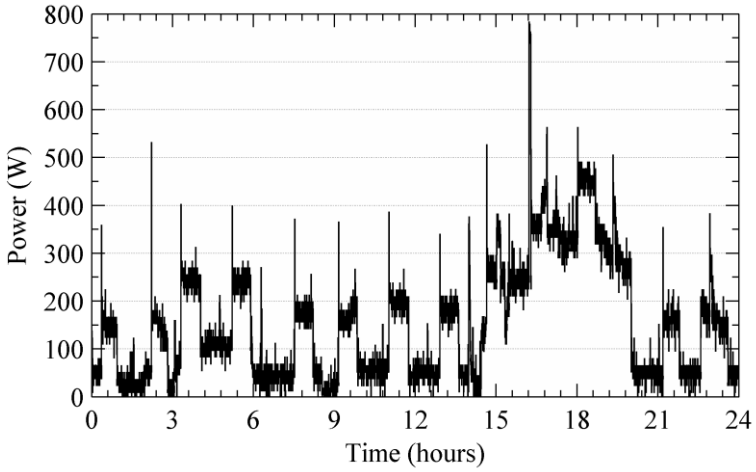

Fig 3.10 One-day reduced usage domestic load profile

3.4 Discussion and Summary

This section has described a generalised simulation model for a fixed-pitch wind energy conversion system typical of remote or off-grid wind-power applications [87]. The model is intended to represent dynamic variations in wind generator output power primarily due to turbulent wind variations subject to the dynamic effects of the wind turbine, shaft and generator inertia. The modelling assumption has been made that the output power of the wind turbine can be regulated according to the maximum power point tracking algorithm at all times. This assumption has allowed the output of the wind energy conversion system to be effectively decoupled from the remaining dynamic simulations. Later analyses are performed over timescales including seasonal variations of one year or more. Including the wind energy conversion system dynamic model in the wind-turbulence simulation model would have caused the simulation to be

excessively slow. Decoupling the simulation tasks in this way has allowed simulations over intervals of greater than 1 year at sampling resolutions of ~1 second. It is not expected to have a significantly detrimental impact on the later assessment of the control strategies considered.

Chapter 4: Energy Storage Systems

4.1 Introduction

Typically, the energy storage element in many conventional off-grid renewable energy systems is the secondary battery [8], [11]. Currently, the main commercially available cell chemistries are Lead-Acid, Nickel Cadmium (NiCad), Nickel Metal Hydride (NiMH), Lithium-Ion [10]. The attention of the research presented in this chapter is focused on modelling the lead acid battery, since this remains a popular choice for the class of wind energy conversion systems under consideration [8], [11], [71] (despite recent advances in the alternative cell chemistries). To model the lead acid battery, the well-established dynamic model developed by Ceraolo [1] was implemented in Simulink. It was found that, while this battery model was able to predict the magnitude of voltage variations at different stages of charge, the dynamic nature of these voltage variations was not well described. To be able to develop a battery voltage control system as described later in Chapter 9, Section 9.3.1 it was necessary to extend this battery model with a novel modification based on experimental findings. This allowed the nature of short term dynamic variations in voltage to be more accurately modelled.

To enable later simulations of a battery/supercapacitor hybrid energy storage configuration, it was also necessary to develop a supercapacitor model. A non-linear supercapacitor-capacitance model is presented based on experimental findings which are supported by results reported from relevant studies [96].

4.2 The Lead Acid Battery

Batteries store energy in electro-chemical form and chemical inter-conversions of the active materials within the cell take place during charge and discharge. In general terms, the lead acid cell consists of a lead oxide ($Pb0_2$) cathode and a pure-lead (Pb) anode immersed in aqueous sulphuric acid (H_2SO_4 + H_2O). The equation describing the overall reaction during charge or discharge is:

$$PbO_2+Pb+2H_2SO_4 \leftrightarrow 2PbSO_4+2H_2O \tag{4.1}$$

Here Pb and PbO_2 act as reactants and lead sulphate ($PbSO_4$) is produced by the discharge reaction at both electrodes. When a load is connected between the electrode terminals, electrons are consumed at the cathode and flow through the circuit to the anode, allowing the chemical reaction Eq. (4.1) to proceed from left to right. At the cathode, a reaction which absorbs free hydrogen ions occurs, and the lead dioxide (cathode) PbO_2 combines with the free hydrogen ions to form water (H_2O). At the same time the free Pb combines with SO_4 ions to create lead sulphate crystals ($PbSO_4$). At the pure-lead anode Pb atoms are converted to Pb_2+ ions which combine with the SO_4 ions in the electrolyte to form more lead sulphate crystals. During charge, the electrons travel in the opposite direction and the lead sulphate crystals are returned to metallic lead at the anode and lead oxide at the cathode. The concentration of the aqueous sulphuric acid is a measure of the state-of-charge of the battery [97].

4.2.1 Lead-Acid Battery Dynamic Model

Battery open circuit voltage, V_{oc}, can be described by the Nernst relation [97] which has the following form:

$$V_{oc} = V_0 + \frac{R_g T}{n_e F} \ln(Q) \quad \text{(V)} \tag{4.2}$$

where [97]:

Vo = potential of the electrode's process (V),

R_g = gas constant, 8.314

T = temperature (^oK)

n_e = number of electrons involved in electrode process

F = Faraday's charge constant, 96,487 (Coulomb/mole),

Q = Coulomb/mole

From Eq. (4.2) it can be seen that the battery open circuit voltage V_{oc} is a function of the reaction quotient, Q, which a measure of the concentration of 'electrochemical species' involved in the reaction [97]. During dynamic conditions however, the terminal voltage deviates from this idealised relation for various reasons including: ohmic volt drops in the conduction paths through the cell, activation polarisation differences due to the electrochemical reaction at the electrode surface, and concentration polarisation due to concentration differences at the electrode surface [97]. In addition, when an electrode is immersed in an electrolyte, there exists a layer of charge at the boundary between the electrode and the electrolyte known as the "electrical double layer capacitance" [97] which also affects the complex impedance of the cell. A complex fundamentally-based battery model would describe these potential differences in detail. However, due to the complexity and extreme non-linearity of the processes involved, simplified models based on the underlying fundamental processes can be applied that adequately describe the voltage response of the lead acid battery.

Some of the battery models initially considered were analytical and offer an intuitive insight into the behaviour of the cell, for example, Manwell and McGowan [98] in their kinetic battery model. After implementing this model it was found that the dynamic variations of battery voltage were not represented with sufficient accuracy over timescales of ~1s as would be required in later simulations. Instead, the approach adopted was to describe battery behaviour using equivalent electrical networks. One of the simplest of such models is the Thevenin equivalent circuit model [99] in which the battery voltage and impedance branch parameters remain constant for all states of charge. This model can lack accuracy as, in reality, lead acid battery parameter values can vary as a function of state of charge. While this modelling technique and other similarly derived models [100], [101] considered describe the slow variation of the battery voltage with respect to state-of-charge quite well, laboratory tests showed that these models did not describe short term dynamic variations or variations in battery parameters with good accuracy. Instead, a non-linear dynamic battery model was implemented based on the rate-dependent third order model described by Ceraolo [1]. This was selected as it can describe the dynamic variations in equivalent circuit parameters over the operating range and includes inefficiencies due to parasitic reactions [1]. In addition, the parameter identification procedure and implementation issues are also well documented by Barsali and Ceraolo [102] as well as measured cell parameters [1], [102].

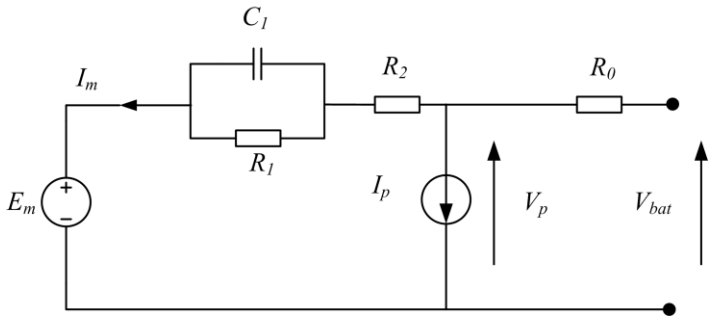

Fig. 4.1 Dynamic lead-acid battery model [1]. E_m = open-circuit voltage (V), C_1 = main branch capacitance (F), R_0 = terminal resistance (Ω) [see Eq.(4.7)], R_1 = main branch resistance 1 (Ω) [see Eq. (4.8)], R_2 = main branch resistance 2 (Ω) [see Eq. (4.9)].

The equivalent circuit shown in Fig. 4.1 represents one cell of a battery. The output voltage was scaled by the number of cells in the battery bank under the assumption that each cell in the string behaves identically. The value of each equivalent circuit element is a non-linear variable dependent on empirically determined constants as described in [1]. The governing equations of the lead-acid battery model are given below as Eqs. (4.3) to (4.12) [1].

The available capacity is a function of battery current and electrolyte temperature as follows [1]:

$$C(I,\theta) = \frac{K_c C_0 (1+\frac{\theta}{\theta_f})^{\varepsilon}}{1+(K_c-1)(I/I_n)^k} \text{ (Ah)} \tag{4.3}$$

where [1] K_c, k and ε are empirical constants defined in, θ_f is the electrolyte freezing temperature (°C), θ is the electrolyte temperature (°C), C_0 is the nominal capacity of the battery, I^* is the battery nominal current (A).

First, state-of-charge (SOC) and depth of charge (DOC) are defined as follows:

$$SOC = 1 - \frac{Q_e}{C(0,\theta)} \quad where \quad Q_e = \int_0^t I\,dt \ \text{(C)} \tag{4.4}$$

$$DOC = 1 - \frac{Q_e}{C(I_{avg},\theta)} \tag{4.5}$$

where I_{avg} is the low pass filtered battery current (Ceraolo suggests a first order low pass filter is used during run time to determine this current [1]). The capacities $C(0, \theta)$ and $C(I_{avg}, \theta)$ are calculated using Eq. 4.3 and $I = 0$ and $I = I_{avg}$ respectively. Q_e is the time-integral of current and used to determine the state of charge as defined by Eq. (4.4). Depth-of-charge varies subtly from state-of-charge in that it is a measure of the battery charge, adjusted to reflect the average discharge current, I_{avg}.

The main branch source voltage, E_m, is dependent on temperature, θ, and the logarithm of state-of-charge (SOC):

$$E_m(SOC) = E_{m0} + K_E(273+\theta)ln(SOC) \quad \text{(V)} \tag{4.6}$$

where E_{m0} is the nominal cell voltage (V) and K_E is an empirically derived term [1].

The resistive terms vary as follows:

$$R_0(SOC) = R_{00}[1 + A_0(1 - SOC)] \quad (\Omega) \tag{4.7}$$

$$R_1 = -R_{10}\,ln(DOC) \quad (\Omega) \tag{4.8}$$

$$R_2 = R_{20}\frac{exp[A_{21}(1-SOC)]}{1+exp(A_{22}I_m / I^*)} \quad (\Omega) \tag{4.9}$$

where A_0, A_{21}, A_{22}, R_{10} R_{20}, R_{22} are modelling constants as defined by Ceraolo in [1] and I* is the nominal battery current (A).

Peukert's equation [103] gives the relationship between discharging rate and effective capacity and can be rearranged in order to calculate the available capacity C_{n1} at a different discharge rate I_{n1} [103] as follows:

$$C_{n1} = C_n\left(\frac{I_n}{I_{n1}}\right)^{kp-1} \text{ (Ah)} \tag{4.10}$$

where C_n is the known cell capacity (Ah) at discharge current I_n (A) and C_{n1} is the unknown cell capacity (Ah) at discharge current I_{n1} (A)

Some criticisms of this relation Eq. (4.10) are that it predicts unfeasibly large capacities C_{n1} for low discharge currents I_{n1} and that the effects of temperature are not included [103]. An alternative relation which overcomes these issues, based on experimental results is implemented in the Ceraolo dynamic battery model [1]:

Losses due to parasitic reactions such as gassing occur during charging and are modelled by the current I_p as follows:

$$I_p = V_p G_{p0}\, exp\left[\frac{V_p}{V_{po}} + A_p\left(1 - \frac{\theta}{\theta_f}\right)\right] \text{ (A)} \tag{4.11}$$

where A_p and G_{po} are empirically derived constant for a given battery, V_{p0} is a parameter relating to the gassing model described in [1] and V_p is as in Fig. 4.1.

The above equations (4.3) – (4.12) were implemented in the Simulink modelling environment as shown in Fig 4.2 below. Losses due to self-discharge are not modelled in the model developed by Ceraolo [1]. The major input to the model is the current *(I)* and the main outputs are the battery voltage (V_{bat}) and state-of-charge (*SOC*).

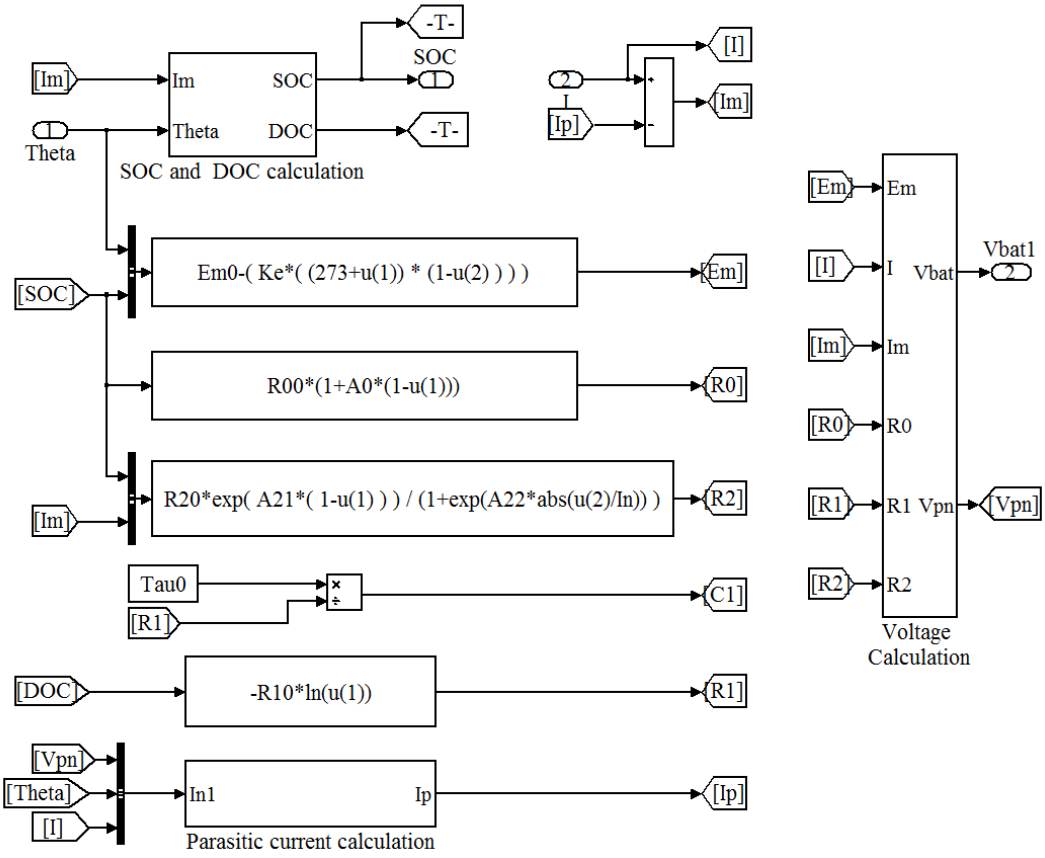

Fig. 4.2 Simulink implementation of dynamic battery model

Using the parameter identification method outlined in [102], the simulated battery voltage response to a 15A constant-current discharge can be seen in Fig. 4.3 to closely match the measured battery response. In addition, the step-response of the battery voltage can be seen at the beginning and end of the test as the constant current is connected and disconnected. The nature of the voltage step response at the end of the discharge test is significantly different from that at the end of the discharge test in that the time constant and magnitude is different. The modelled response can be seen to track the change in the nature of the response at the two different states of charge well.

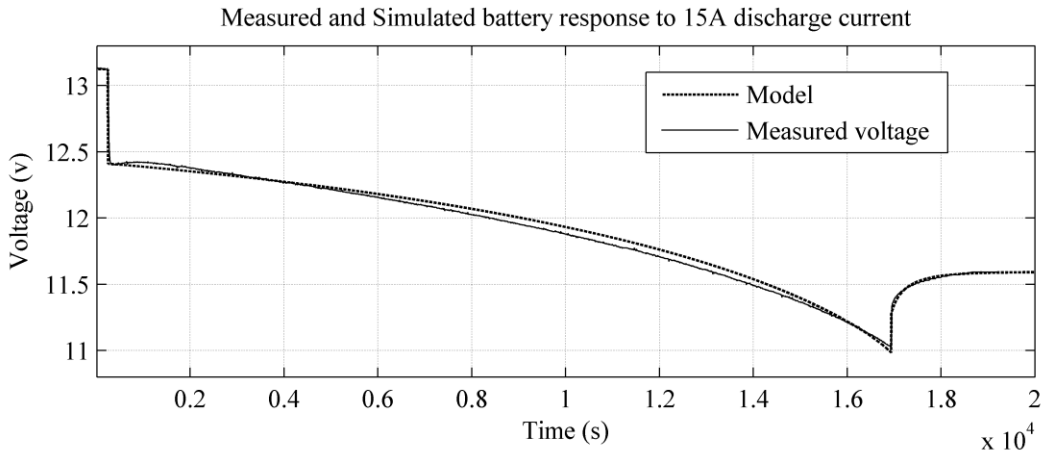

Fig. 4.3 Measured and simulated battery 15A discharge profile (Start of discharge: ~200s. End of discharge: 1.7 x 10^3s).

4.2.2 Improvements to the Dynamic Lead Acid Battery Model

Closer inspection of the initial voltage step as shown in Fig. 4.4 reveals that the Ceraolo model does not capture the dynamic characteristics of the short term voltage variation.

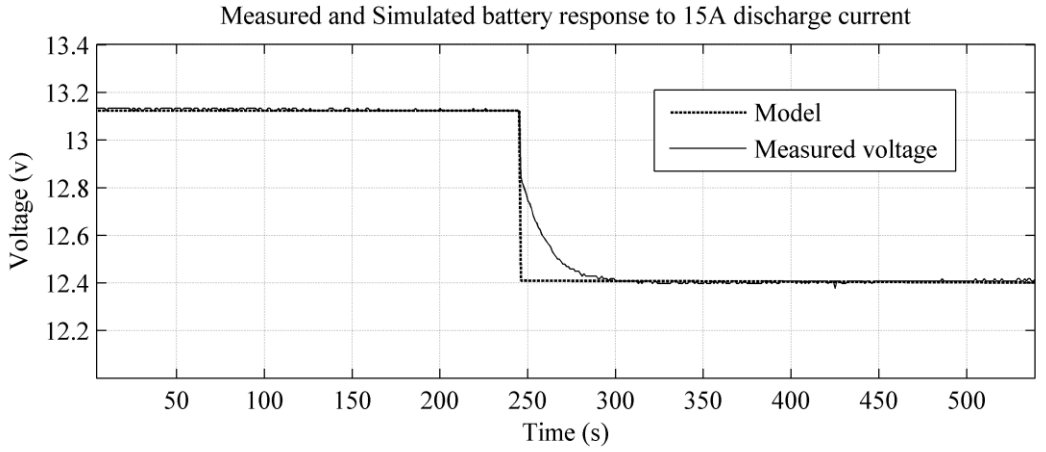

Fig. 4.4 Measured and simulated initial voltage step response to a 15A current step applied at ~ T = 250s.

For later use in battery voltage control system design, the dynamic battery model was modified as follows to accommodate the short-term dynamic variations evident from Fig. 4.4:

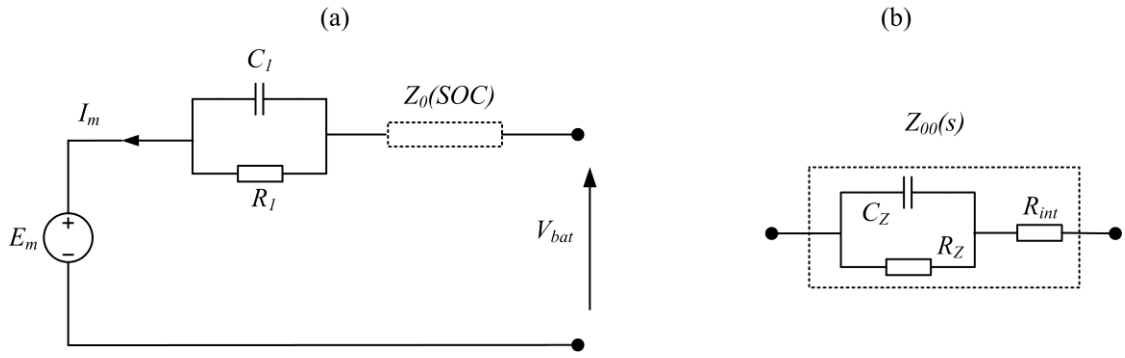

Fig. 4.5 (a) Modified dynamic battery model (b) Complex impedance term Z_{00}(s)

where Z_{00}(s) is a complex pole/zero

$$Z_{00}(s) = \frac{k_0(s+z_0)}{s+p_0} = R_{int}\frac{s+\dfrac{R_{int}+R_Z}{C_Z R_{int} R_Z}}{s+\dfrac{1}{C_Z R_Z}} \ (\Omega) \tag{4.13}$$

To estimate $Z_{00}(s)$, step current tests were applied to the battery at and the battery voltage waveform was recorded. The Matlab System Identification Toolbox was then used to identify the locations of the complex pole and zero formed by the impedance $Z_0(s)$. Since from Eq. (4.7) $R_1 = R_{10}.ln(DOC)$, the contribution of dynamic variations due to the branch formed by the parallel combination of C_1, R_1 becomes very small at high charge states, so the effect of this branch can be neglected at high states of charge during relatively short time periods.

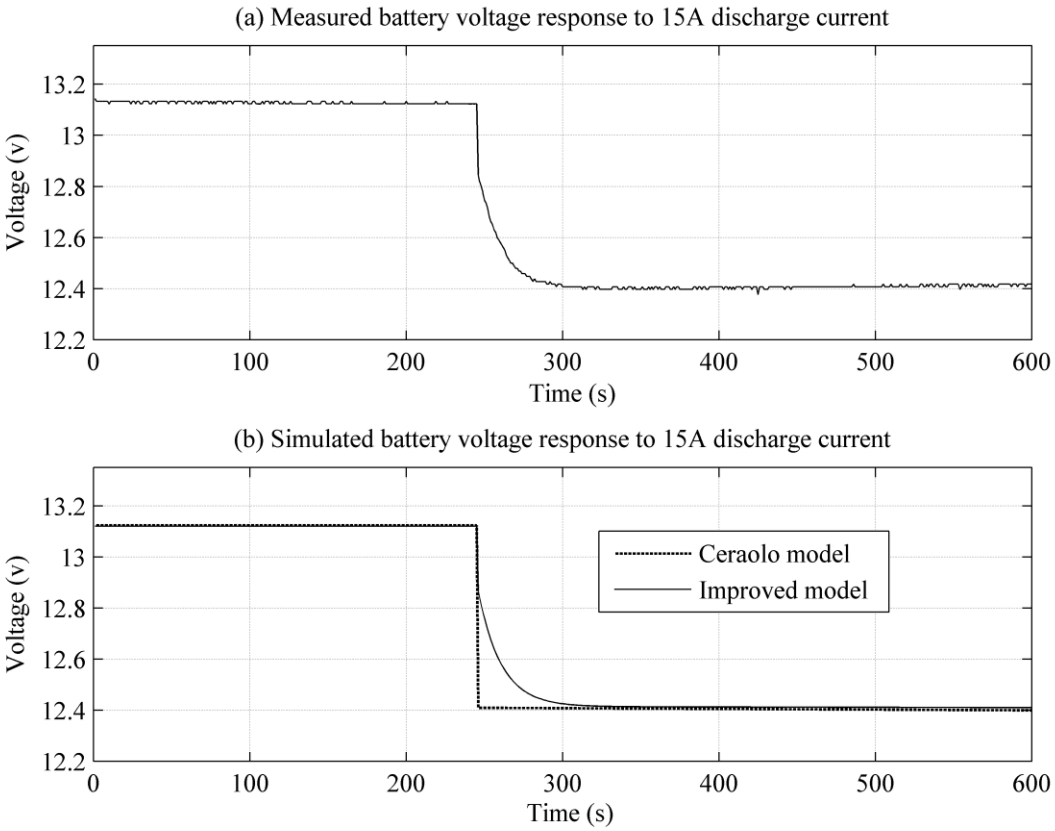

Fig. 4.6 Measured and simulated initial voltage step.

The voltage step response can be seen to reflect the measured response more accurately than the original model. The extracted parameter values for the battery impedance $Z_0(s)$ are as shown in Table 4.1.:

TABLE 4.1 IMPEDANCE PARAMETERS FOR CSB GPL1250 75AH VRLA [104].

Parameter	Description	Value
R_{int}	Series resistance term	0.0168 Ω
R_Z	Parallel resistance term	0.0302 Ω
C_Z	Parallel capacitance term	488.41 F

Defining $Z_{00}(s)$ as the value of Z_0 at a full state of charge, the complex impedance $Z_0(SOC)$ was scaled as a function of state-of-charge by modification of (4.6) as follows:

$$Z_0(SOC) = Z_{00}(s)[1 + A_0(1 - SOC)], \tag{4.12}$$

The resistor R_0 in the original model has now been replaced by the complex impedance Z_0 as shown in the Simulink implementation below in Fig. 4.7.

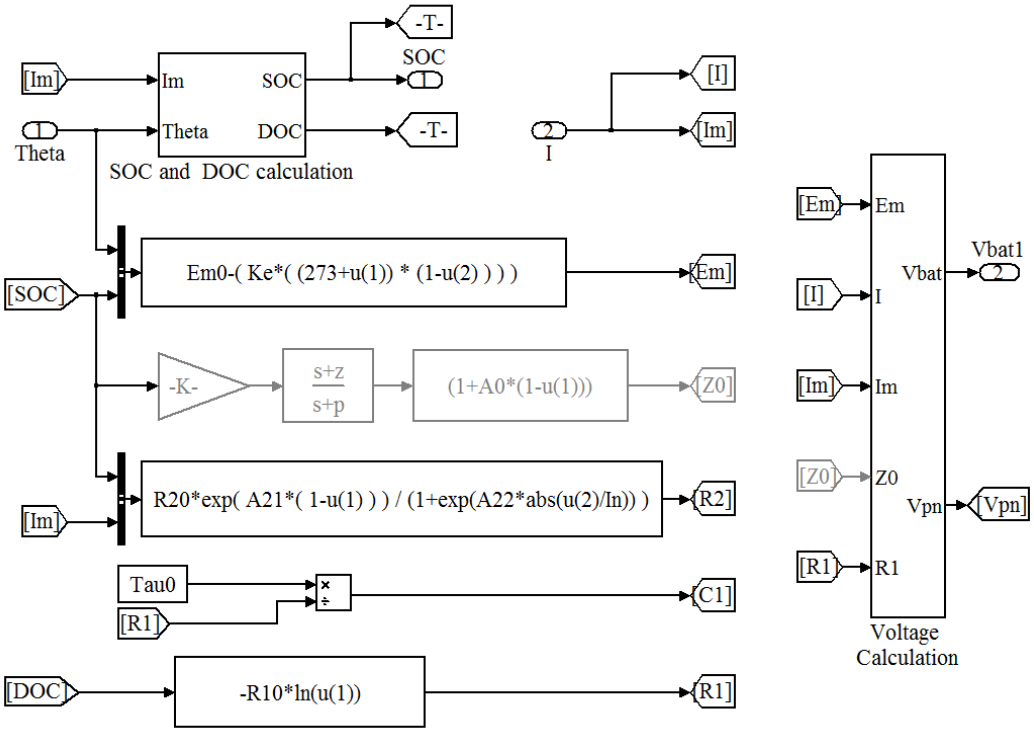

Fig. 4.7 Modified Ceraolo battery model (modification shown in grey).

This represents a novel extension of the third order battery model formulation described in [1]. Unfortunately to validate the model across all state-of-charge was beyond the scope of this project but initial tests indicated that a dynamic impedance of this nature could improve the short-term (<100s) dynamic modelling accuracy of the Ceraolo battery model.

To maintain a full-charge in a lead-acid battery, it is necessary to raise the cell potential above the fully charged cell open-circuit potential [97]. A battery raised to a potential higher than its fully charged cell open-circuit potential to mitigate the effects of self-discharge and to ensure a full charge, is often referred to as being "float charged" [105]. A distinct change in the nature of the impedance of the battery was observed during these conditions. This effect has also been reported in previous studies [106], [107]. Step current tests were used as before to reveal how the impedance characteristic changes as the cell reaches float charge polarisation in the region marked 'A' in Fig. 6-5 (b).

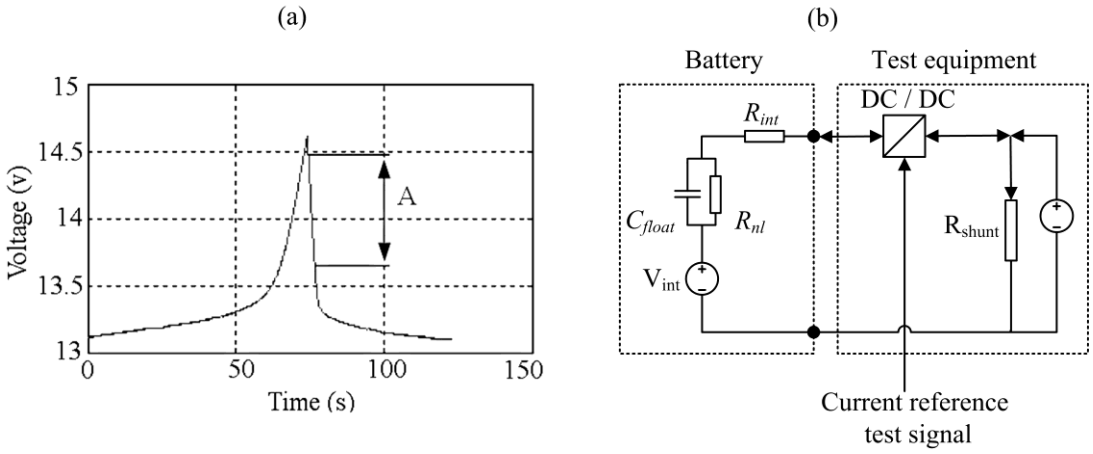

Fig. 4.8 (a) Measured battery voltage step response at float charge level. +1A at T = 0s. -1A current step input at T = 75s (b) Experimental set-up.

The response in this region can be approximated by a resistor representing the internal resistance of the battery in series with a parallel RC branch [107] as shown in Fig. 4.8 (b). To extract the time-response of the battery voltage to an arbitrary current waveform, a bidirectional current programmed DC/DC converter (please see Section 6.2 for further details regarding this converter) was used as shown in Fig. 4.8 (b). As before, by examination of the voltage response to a step current input, an estimation of the nature

of the impedance was obtained using the Matlab System Identification Toolbox [108] with results shown in Table. 4.2.

TABLE 4.2: BATTERY FLOAT IMPEDANCE PARAMETERS FOR CSB GPL1250 75AH VRLA [104]

Parameter	Description	Value
R_{nl}	Parallel resistance term	9.08 Ω
R_{int}	Series resistance term	0.01 Ω
C_{float}	Float capacitance	2.25 F
V_{float}	Float voltage	14.12 V

Having determined R_{int}, R_{nl} and C_{float}, the battery float charge impedance can then be written in zero/pole/gain form:

$$Z_b(s) = \frac{k_b(s+z_b)}{s+p_b} = R_{\text{int}} \frac{s + \dfrac{R_{\text{int}} + R_{nl}}{C_{float} R_{\text{int}} R_{nl}}}{s + \dfrac{1}{C_{float} R_{nl}}} \ (\Omega) \tag{4.14}$$

The measured and simulated voltage response to a +1 A to -1 A current pulse signal in the operating region of interest is shown in Fig. 4.9 below.

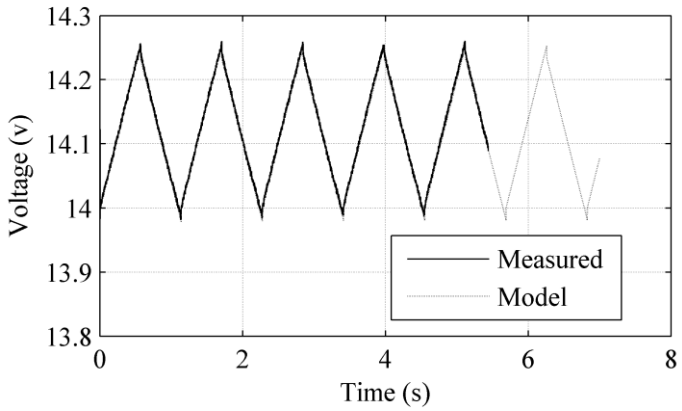

Fig. 4.9 Measured and simulated battery voltage response: +1A/-1A current steps at float charge level.

A complete dynamic model would take into account the significant changes in the effective impedance of the cell at high states of charge including voltage and state-of-charge parameter dependencies. However, the characteristics of the impedance change during the transition from less than fully charged to the float charged condition remain undefined. An accurate battery model would describe this transition smoothly. This is beyond the scope of this study but is highlighted as a potential area for future research effort.

4.3 Supercapacitor Energy Storage Systems

Unlike batteries which store charge electro-chemically, capacitors store energy as an electro-static charge within the electric field between two electrodes separated by a dielectric. Supercapacitors, [also known as “ultra-capacitors”, “electrochemical capacitors” or “electric double layer capacitors (EDLC)”] also store energy in the form of an electro-static charge. Supercapacitor electrodes are made of a porous micro-structure (typically carbon) and immersed in an electrolyte. An electrically insulating separator is inserted between the two electrodes which allows ions to pass. When a voltage is applied to the electrodes, ions in the electrolyte solution move toward the electrodes and form a layer next to the electrode surface where charge accumulates on

the solid surface, attracted by the opposing charge of the electrode. An “electric double layer capacitance” is formed; one layer being in the electrolyte and the other being just below the surface of the electrode.

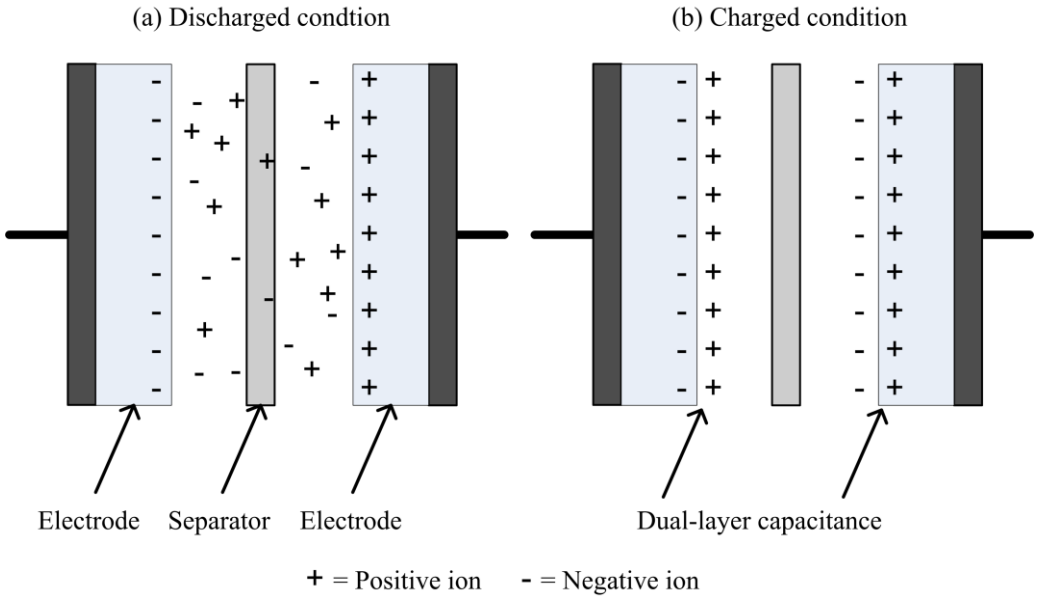

Fig. 4.10 Supercapacitor during a discharged (a) and charged condition (b).

Electrostatic charge is stored in the double layer with an effective distance between the two charge layers of the order of 1 nm [109]. The capacitance is inversely proportional to the distance between the layers and proportional to the permittivity of the dielectric and the area of the layers. Since the charge separation distance is very small and since the porous electrodes effective surface area is very high, very high capacitances can be achieved, with orders of magnitude two or three times higher than with conventional capacitors being typical. However, due to the extremely small charge separation distance, a single supercapacitor cell can operate only at considerably lower maximum rated voltages than its conventional counterpart (with cell voltages of 2.5-3V/cell being typical [110]), which is why supercapacitor modules comprised strings of series cells are frequently employed.

4.4 Supercapacitor Modelling

For the supercapacitor, various electric models have been proposed describing the behaviour of electric double layer capacitance with various levels of complexity and of approximation [96], [111], [112]. This section illustrates the models considered during this research and describes the methods used to develop them.

4.4.1 Test Procedure

A number of experimental tests were carried out to measure the behaviour of the supercapacitor module under conditions of constant current charge and discharge. A current controlled DC/DC converter (to be described in detail later in Chapter 6) developed as part of this study, was used to deliver current profiles to the supercapacitor module under test which consisted of 22 x 1800F (Maxwell BoostCap) devices made available for this research. It was found that the apparent capacitance of the supercapacitor varied with voltage in agreement with the findings reported in [96], [112]. The method used to determine this non-linear capacitance variation is as follows. First, the supercapacitor is either fully discharged or fully charged with a constant current while the terminal voltage is logged as shown in Fig. 4.11, which plots the time-current product vs. voltage.

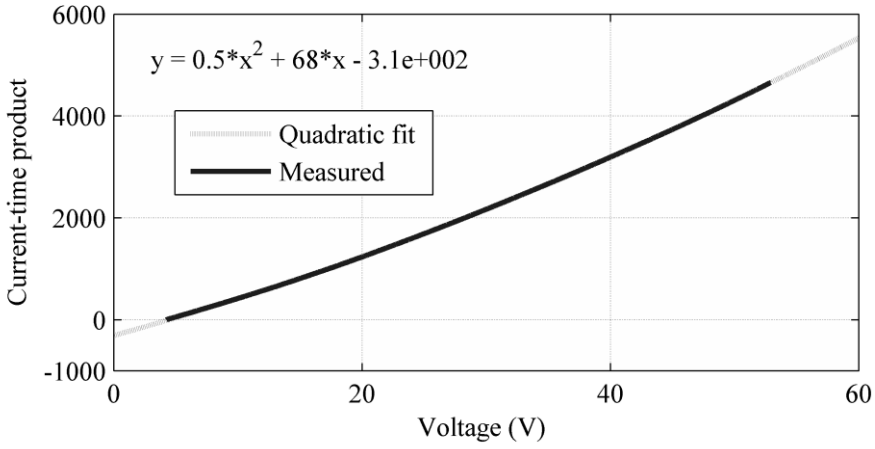

Fig 4.11 Voltage vs. current-time product.

The function relating voltage to the time-current integral can be used to determine the capacitance as follows. After the initial step due to any purely series resistive elements, the voltage response due to a the variable capacitance $C_{nl}(v)$ can be written:

$$V_{sc}(t) = \frac{1}{C_{nl}(v)} \int i dt \ \ (A) \quad or \quad V_{sc}(t) C_{nl}(v) = \int i_{sc} dt \ \ (V) \tag{4.15}$$

where V_{sc} and i_{sc} are the supercapacitor voltage and current.

A quadratic of the following form was used to fit the measured data:

$$y = ax^2 + bx + c \tag{4.16}$$

The y-axis of Fig. 4.10 represents the time-current product and since the current is constant this also represents the current time integral. The c coefficient in Eq. (4.16) represents the initial condition at time t = 0 and can be neglected for the purpose of system identification. Eq. (4.15) can then be re-written:

$$\int i dt = av^2 + bv = (k_v v + C_0) v \ \ (\mathrm{C}) \tag{4.17}$$

Here C_0 represents a linear, constant capacitance term and the product $k_v v$ represents the voltage dependent variation in capacitance. This model is based on separately obtained results [96], [112]. The non-linear effective capacitance term can be found by differentiating Eq. (4.17):

$$i = (2k_v v + C_0) \frac{dv}{dt} \ \ (\mathrm{A}) \tag{4.18}$$

$$C_{nl}(v) = (2k_v v + C_0) \text{ (F)} \tag{4.19}$$

The equivalent series resistance was determined from the step change in voltage when a constant-current load is removed or added as shown in Fig 4.12 (b) and can be compared with manufacturer's data when available [113]. The simulated and measured voltage profiles for a 10A charge/discharge test are shown below in Fig. 4.12 (a) and can be seen to represent the supercapacitor voltage variation behaviour well.

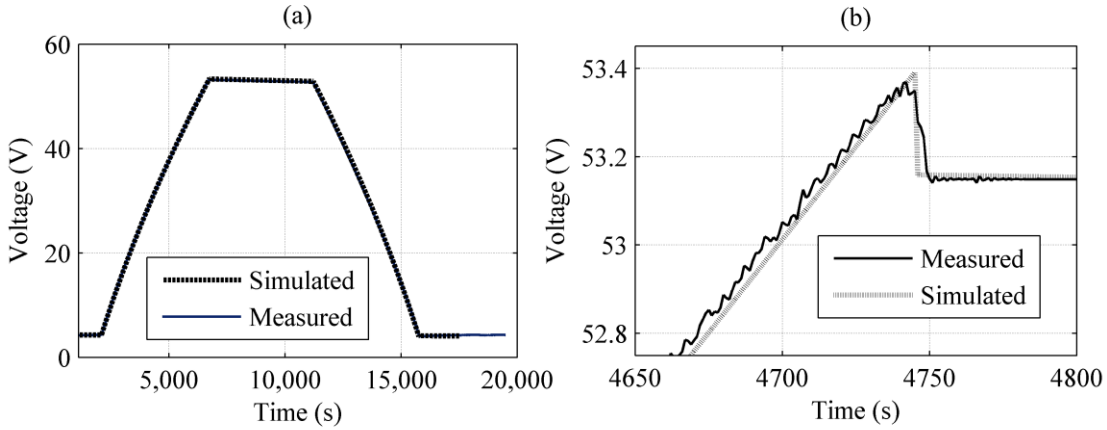

Fig 4.12 (a) Measured voltage response responses to a I=+10A charge from T=2100s to 6400s then I=-10A from 11000s to 16000s (b) Close-up of resistive volt drop.

The supercapacitor voltage can then be described by the following equation [96], [112]:

$$V_{sc}(t) = \frac{1}{(2k_v v + C_0)} \int \left(I(t) - \frac{V(t)}{R_{leak}}\right) dt + I(t)R_s \text{ (V)} \tag{4.20}$$

where R_s = series resistance (Ω), R_{leak} = leakage resistance (Ω)

4.4.2 Non-Linear Supercapacitor Model

The assumption has been made in later simulations that the apparent variation in capacitance described in Section 4.4.1 is the same during charge and discharge. The Simulink implementation of the above equations for modelling the behaviour of the supercapacitor voltage is as follows:

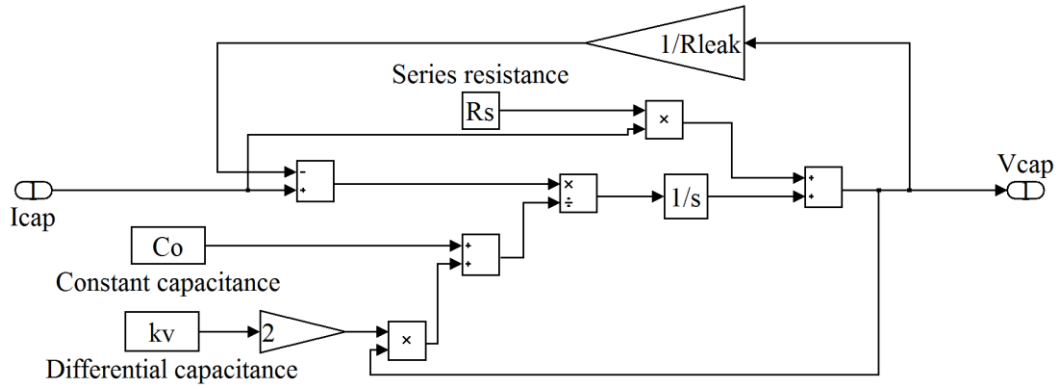

Fig. 4.13 Non-linear Simulink model of supercapacitor

In some cases, a simplified version of the above model can be acceptable as described in [114], [115], where the capacitance term is modeled as an equivalent constant capacitance term extracted from datasheet parameters or determined by measurement.

4.5 Discussion and Summary

The characteristics of the energy storage devices considered in this study have been described. The Simulink implementation of a dynamic model of the lead acid battery based on previous comprehensive research [1] has been described and the limitations of this model in terms of short-term dynamic performance have been demonstrated. A novel contribution from this chapter is a modification to the dynamic battery model considered which represents the complex dynamic impedance characteristic with a better accuracy. Experimental results have shown that this impedance exhibits a

dramatic change as the battery enters float-charge conditions. It can be concluded from this, that the design of battery voltage control systems should consider the dynamic properties of the battery impedance. Also the sudden change in impedance at float level should be considered if the battery voltage control system is required to maintain the battery voltage in this region of voltage and state of charge, as is often the case in charging applications.

The experimental results have confirmed that the proposed non-linear capacitance models of Zubieta and Rafik [96], [112] provide a good representation of the apparent quadratic nature of the voltage dependent capacitance. The procedure for determining the non-linear capacitance term has been demonstrated and simulation results have shown the representation of the supercapacitor voltage variation.

Chapter 5: Battery Lifetime Modelling

5.1 Introduction

This chapter presents a means by which battery life can be estimated based on a given usage pattern. Battery-life is one of the key metrics used in later assessments of the benefits of the supercapacitor/battery hybrid energy storage system. For this reason, it was necessary to consider a means of incorporating battery life prediction into the simulation model. The method is based on the models developed by the University of Massachusetts (UMASS) as they were successfully deployed as part of the battery model used in the commercially available simulation package Hybrid2 [73].

Unlike the semi-regular power profile that an energy storage device may undergo in an electric train or tram where a charge event due regenerative braking is usually eventually followed by a discharge event due to acceleration, the battery power profile in a wind power system is highly complex and irregular. The reason for this is primarily due to the irregular nature of the wind as a power source since it has been shown that the in the timescale of < 1 hour to 1 second the variations in the wind's speed can be well modelled as a stochastic process. So, to extract the number of irregular, overlapping charge and discharge cycles from a complex pattern of data, a modified version of the technique known as 'rain-flow counting', also used in metal fatigue estimation has been used, based on the work first presented by Downing and Socie [116]. In addition, a battery lifetime model has been developed based on battery manufacturer's datasheet information to provide an estimation of battery life using the outputs of the rain-flow cycle counting algorithm. This battery life estimation technique has been successfully employed in other research areas such as automotive electric

vehicle studies [43], locomotive applications [117] battery-only based renewable energy applications [118], [119], utility scale applications [120] and presented as part of a generic modelling framework for battery economic analysis [121].

5.2 Battery Life

Since the battery is often one of the weakest components in an off grid wind-generation system in terms of service life [8], [11], any benefit in terms of increased service life can be advantageous for cost and reliability reasons. Various studies [48-50], [56-58] have discussed the extension of battery life by the use of an actively controlled supercapacitor based system for wind energy applications without providing quantified proof. Since batteries are complicated non-linear devices whose age is a function of many parameters, accurate prediction of battery lifetime is a highly non-linear task. This task is complicated further by the complex nature of the wind charge pattern which can be seen from the results shown in Chapter 2 to have highly variable short-term and long-term components.

All secondary/rechargeable batteries degrade over time. The period that the battery remains serviceable before the capacity degrades to a predefined minimum (typically 80%) is known as the battery life. Battery end-of-life is defined as the condition in which the battery energy storage capacity has fallen to a predefined level. Battery cycle-life is defined as the number of cycles that the battery can provide before the end of life condition is met. The finite life of a battery is affected by environmental conditions such as temperature and the electrical operation of the battery in any particular application. The degradation of battery life can be due to a calendar-life ageing component or a cycling related ageing component and, in reality, is a combination of the two [97]. Battery calendar-life ageing is heavily dependent on cell chemistry, battery type and

temperature [97]. Cycle-life ageing is related to the amp hour throughput of the battery in that each charge/discharge cycle results in some degradation of the battery life. The amount by which battery life is reduced during each cycle is linked to a variety of stress factors, some of which have been highlighted for batteries operating in renewable energy systems in recent field studies as follows [11]:

- Charge factor: The ratio of amp hours charged to amp hours discharged.
- Ah throughput
- Highest discharge rate
- Time between full charges
- Time at low SOC
- Partial cycling

A complete battery lifetime model would aim to include these stress factors and calculate the battery cycle life accordingly. However, at present such a battery life model is not readily available. Instead, some of the simplified battery life estimation models that were considered, based on the key aging mechanisms are described in the next section.

5.2.1 Battery Lifetime Models

Three existing battery lifetime models were considered as a part of this project as discussed by Bindner [9]. The first, known as “the FhG model” [9] combines a performance degradation model and an ageing lifetime model. In this way, the battery performance deteriorates as the battery life is consumed. The voltage part of the model is based on the Shepherd equation (also as discussed in [122]) and modelling parameters such as internal resistance and capacity are altered during simulation time to reflect

performance degradation. This model is intended to closely describe the actual aging mechanisms experienced by the battery such as corrosion of the electrode during simulation time. The model varies significantly from the others considered due to its complexity and the need for input parameters and empirical test data [9]. In addition, this model is distinct from the other two models in that it combines a performance and lifetime deterioration model during run-time.

The next type of model to be considered was an Ah-throughput based model which can be implemented by simply determining the charge in or out of the battery. Typically, the total energy that the battery provides during a simulation interval is recorded and the assumption is made that there is a fixed amount of energy that the battery can provide before it requires replacement, regardless of the depth of discharge of individual cycles. This can be determined from manufacturers' datasheet information by reading the total battery lifetime throughput for a given depth of discharge as indicated in Fig. 5.1. The end-of-life is assumed to be reached when the total energy-throughput reaches the total energy that the battery can provide [9]. The concept of the 'life-fraction' consumed during an interval can be introduced by considering the energy delivered by the battery during that interval divided by the total energy that the battery can provide.

The total energy throughput and cycles to failure are plotted for a typical lead acid battery in Fig. 5.1 below [20].

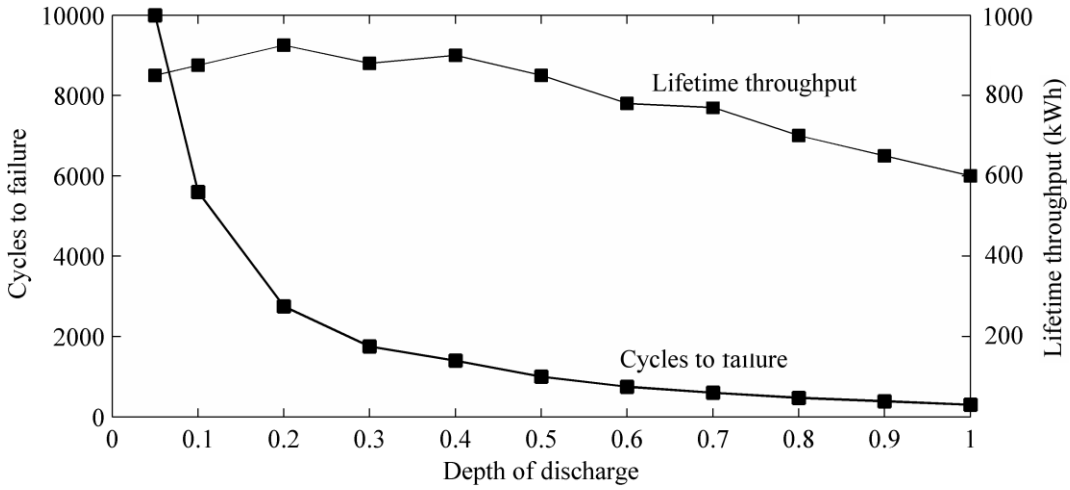

Fig. 5.1 total lifetime throughput and cycles to failure plotted for a typical lead acid battery [20].

Cycle-counting models are based on the assumption that the charge cycle amplitude determines the fraction of lifetime that is consumed based on a cycles to failure vs. depth of discharge as shown in Fig. 5.1. It can be seen that the reduction in battery lifetime can be different depending on the cycle depths of discharge. Therefore, the lifetime aging should be calculated by summation of the contribution of individual cycles charge/discharge cycles at their corresponding depths of discharge. This is the basis of the 'cycle-counting' based approach to battery lifetime estimation which was the technique employed in this study, and is explained in further detail below in section 5.2.2.

Binder has reported the results of tests with real-life batteries showing that the FhG model, when deployed with real renewable energy system data, has significantly overestimated battery lifetime [9]. Whereas the much simpler ah-throughput and cycle counting algorithms have been shown to give a closer estimation of battery lifetime [9] using the same test data. For this reason, and since a stand-alone battery lifetime

prediction method (as opposed to a run-time life model) was required, the FhG model [9] was not considered further.

It was found that one of the key advantages of a supercapacitor/battery hybrid energy storage system was achieved by the use of the supercapacitor's inherently higher cycle-life capacity to decrease the number of cycles experienced by the battery, to improve battery life. Since it provides a direct measure of the number of cycles experienced by the battery, the cycle-counting method of battery lifetime estimation was implemented to evaluate the potential benefits of the supercapacitor energy storage system in this study. In the case of a simple ah-throughput based model this information would not be directly apparent.

5.2.2 Rain-Flow Cycle-Counting

A rain-flow cycle counting algorithm was used to extract the number of cycles that the battery experienced at various depths of discharge as has previously been successfully employed in battery lifetime estimation applications such as in the renewable energy system simulation package Hybrid2 [73] and as part of Manwell and McGowan's Kinetic Battery Model [123].

Referring to Fig. 5.2, it can be seen how cycles and half-cycles are counted using the rain-flow counting technique. Corresponding half-cycles are combined to get full-cycles. Half-cycles and full-cycles within larger amplitude cycles are counted separately as smaller amplitude cycles. This method can be used to extract the number of cycles from within a complex series of charge and discharge cycles of irregular amplitudes.

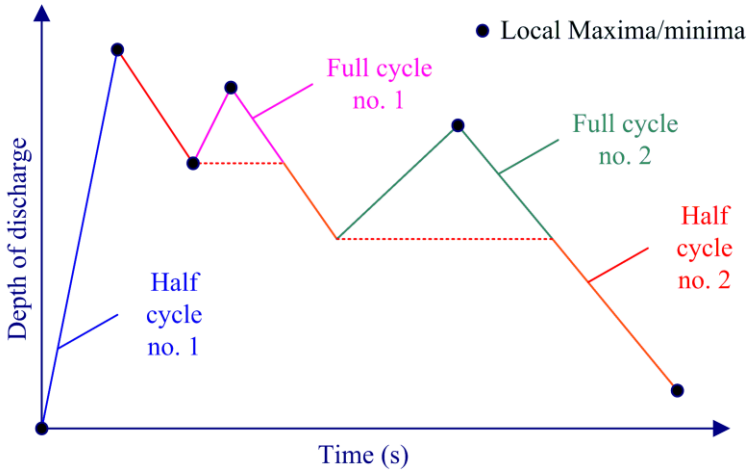

Fig. 5.2 Conceptual rain-flow cycle-counting algorithm outputs.

The implementation of the rain-flow cycle counting algorithm was done in Matlab since this is a powerful matrix and array manipulation tool and the algorithm takes an array of state-of-charge variations as the major input [116]. The state-of-charge variation data were pre-processed so that local maxima and minima were found by searching for adjacent data points with opposing gradient polarity. The local maxima and minima or "peaks and valleys" [116] are shown as black circles in Fig. 5.2.

The maxima and minima data were stored as an array, which was re-arranged to begin with the largest peak and the rainfall counting procedure was implemented according to the method originally described by Socie and Downing [116]. The range of each cycle counted was stored in a vector. These values were then used to determine their cumulative effect on battery life as described in the next section.

5.2.3 Battery Lifetime Estimation

Defining depth of discharge as the minimum state of charge (for SOC, see Eq 4.3) reached during a discharge cycle, Fig. 5.3 shows a typical plot of cycles-to-failure against depth of discharge for a typical lead-acid battery [124].

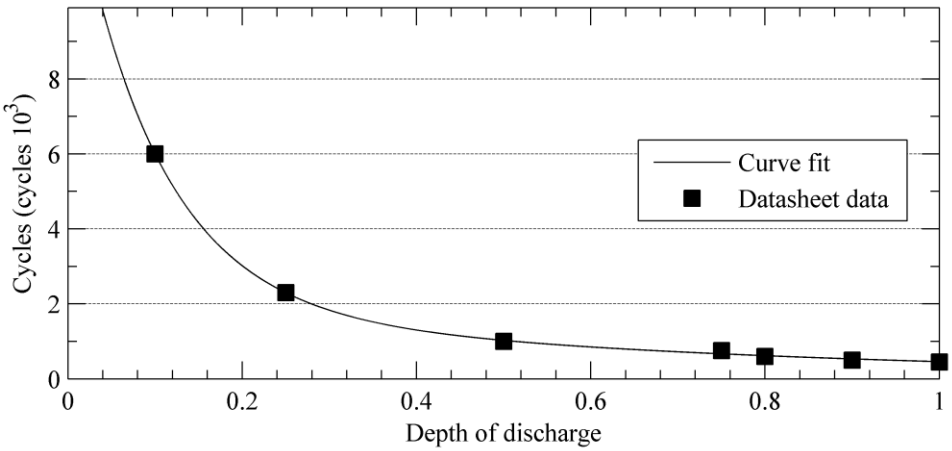

Fig. 5.3. Battery life curve from [124].

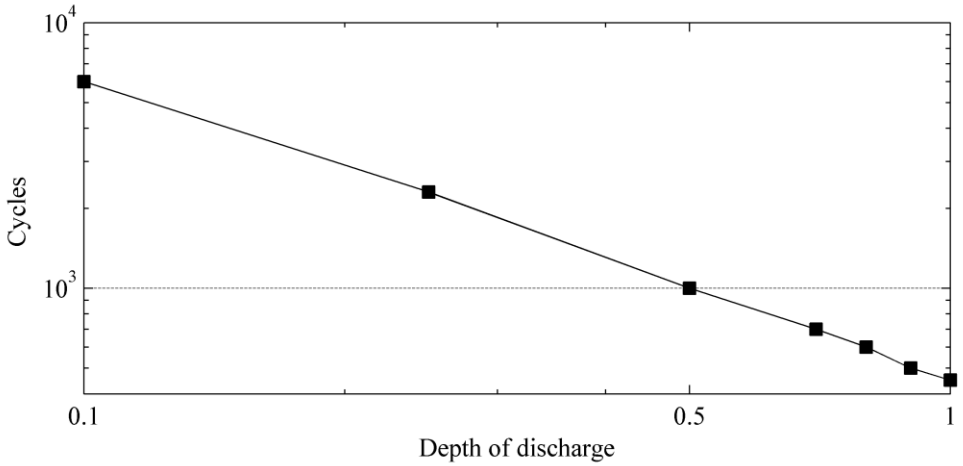

Fig. 5.4. Battery life curve from [124] plotted on a logarithmic scales.

Typically manufacturers' datasheets [124] do not contain information regarding the effect of factional discharge cycles with range less than 0.1, so it was necessary to extend the battery life curve of Fig. 5.4 so that their effect on battery lifetime could be evaluated.

It was found that the effect of turbulent wind variations with a temporal range of seconds to minutes causes a significant number of low-range battery cycles with amplitude < 0.1. Re-plotting the battery life data of Fig. 5.3 on logarithmic scales indicates the logarithmic nature of the underlying process involved.

Ruddell et al. [125] in their report on the effect of micro-cycles (short-range cycles) have stated it is a reasonable assumption that the energy throughput caused by short-range cycles can be added to the remaining battery energy throughput for the purpose of lifetime estimation. Based on this assumption, to account for additional throughput due to short-range cycles, the existing manufacturer's data was extrapolated as a straight line on a log/log scale as shown in Fig. 5.5 by using the final gradient of the curve at the last manufacturer's data point (10^{-1}) to extend to cycles with range $<10^{-3}$.

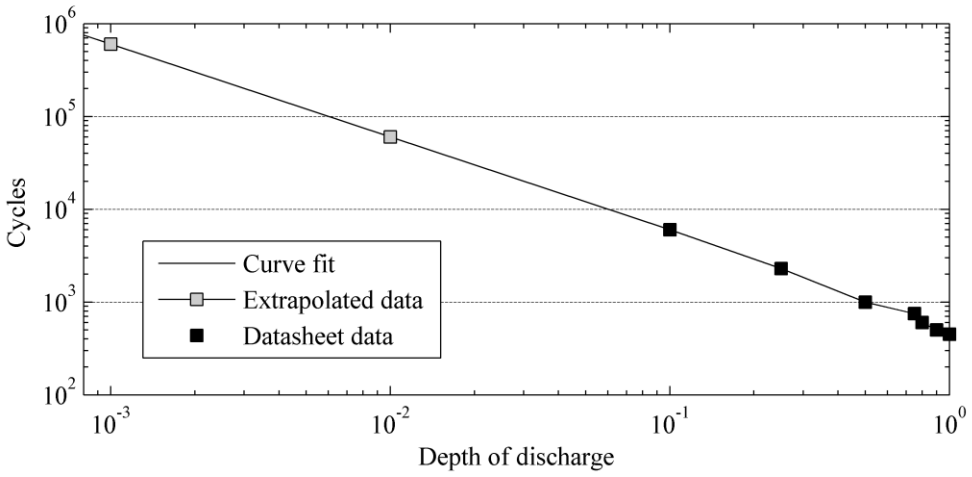

Fig. 5.5 Battery life curve with data from [124] from plotted on a logarithmic scale.

This is equivalent to assuming that cycles with depth of discharge of 10^{-2} and 10^{-3} have proportionally the same detrimental effect on battery life as cycles in the range 10^{-1}. The result of curve fitting to the extrapolated data is a logarithmic polynomial of the form:

$$C_d = a_1 d^{-4} + a_2 d^{-3} + a_3 d^{-2} + a_2 d^{-1} + a_5 \text{ (Cycles)} \tag{5.1}$$

where the number of cycles-to-failure for a depth of discharge d is C_d

and curve fitting coefficients a_1 to a_5 are:

$a_1 = -1.345 \times 10^{-12}$ $a_2 = 1.495 \times 10^{-7}$
$a_3 = -0.001507$ $a_4 = 601.5$ $a_5 = -1225$

The cumulative effect of the cycles counted using the rain-flow counting procedure can be determined as follows. If the number of cycles-to-failure for a given depth of discharge d is C_d, the amount by which the battery has aged in one full cycle of range d is then $1/C_d$ i.e. after C_d cycles of depth d the battery life is consumed. If the output of the rain-flow cycle counting algorithm is a vector of i different cycle ranges, the total battery degradation W, can be determined as follows [9]:

$$W = \sum_{i=i_{\min}}^{i=i_{\max}} \frac{1}{C_{di}} \tag{5.2}$$

If the simulation lasts N_{days} days, the expected battery lifetime, L_{bat}, can then be estimated as follows:

$$L_{bat} = \frac{N_{days}}{W} \text{ (days)} \tag{5.3}$$

5.3 Discussion and Summary

Since battery life can be one of the key metrics in assessing the benefits of a hybridised battery/supercapacitor energy storage system, it is important to be able to estimate it. Battery lifetime is a function of many non-linear variables and highly dependent on the application and usage pattern. This chapter has described a method used to obtain a simple battery cycle-life estimate based on state-of-charge variation data and readily

available battery manufacturers' data. The method used is based on analyses successfully implemented in previous similar studies which would indicate its validity [118], [119], [120]. However, this method would not be suitable to estimate a stand-by battery life or systems designed for extremely shallow and infrequent charge cycles (such as certain UPS systems, for example) since battery life in such systems could be limited by aging mechanisms not related to cycle-life. While this model does not specifically take into account some of the stress factors highlighted above such as discharge rate (see section 5.2), it remains a valid measure of the cyclic energy throughput that a battery experiences. Since the effect of the real-life stress factors described is to decrease battery life further than under laboratory condition testing, it is expected to provide an optimistic estimate of battery life in some instances. However, the battery lifetime model based on cycle-counting shows promise and in its current form can be considered as a viable means of counting the amp hour throughput to various depths of discharge which can then be used to estimate the fraction of battery life lost over a simulation period. For this reason this method has been employed in later analyses with the caveat that battery life estimations may not include a variety of known stress factors and calendar aging factors. This highlights the need for novel techniques to be developed based on manufacturer-validated test data. A good starting point for this would be if battery manufacturers were to provide battery life curves which were 'de-rated' against other stress factors such as discharge rate, for example. These could take the form of the battery life curve of Fig. 5.3 but would include also include the detrimental effect of other stress factors such as discharge rate. This would then allow a weighted-cycle counting algorithm to include their effects.

Chapter 6: DC/DC Converter Development

6.1 Introduction

This chapter describes the development of a current-controlled DC/DC converter used to empirically validate the energy storage control algorithms developed in this study. The role of the converter was primarily to control the flow of power to and from the supercapacitor although the system developed did find other uses within this study. It employs a hysteretic current control strategy and is shown to be capable of fast, bidirectional current tracking. The converter operating under this strategy has been used as a building block for the implementation of control algorithms described later, in Chapters 8 and 9. This chapter discusses the design of the converter, presents both experimental results to demonstrate its operation and a simulation model to describe its performance.

A review of previous work has revealed a predominantly system-level approach to the control of power in a hybrid energy storage device for wind power applications, leaving their implementation largely unreported. For this reason one of the objectives of this study has been to consider the implementation aspects of the hybrid energy storage system's charge-discharge circuits in greater detail. In this way the focus of research can reach a consensus regarding the implementation options available and their relative merits to validate systems practically.

6.2 Converter design

The configuration of the DC/DC converter within the hybrid energy storage system is illustrated in Fig. 6.1.

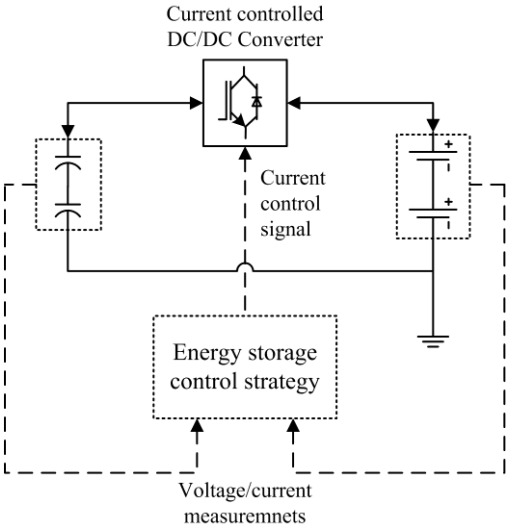

Fig. 6.1 Schematic of battery-supercapacitor hybrid energy-storage system.

Since the voltage of storage devices such as batteries and supercapacitors is often dictated by specific limitations such as state of charge, a fast and effective means of power control at a given voltage can be achieved by controlling the current to/from the energy storage device at a given voltage. For this reason, the converter used in this study was required to have fast current control and two-quadrant operation i.e. with positive input and output voltages, bipolar current control was required. After some initial research revealed that a suitable off-the-shelf unit with the required specification was not readily available, it became necessary to design and build the converter using discrete components. The control strategy used is an adapted hysteretic current control scheme as used in motor control applications [126], active power filtering [127], switched-mode audio amplifiers [128] and actuator control [129] applications.

6.2.1 Converter topology

The converter was based on a half-bridge topology which can be reconfigured to accommodate different energy storage device configurations. The synchronous buck converter and inverting buck/boost converter as shown in Fig. 6.2 were considered.

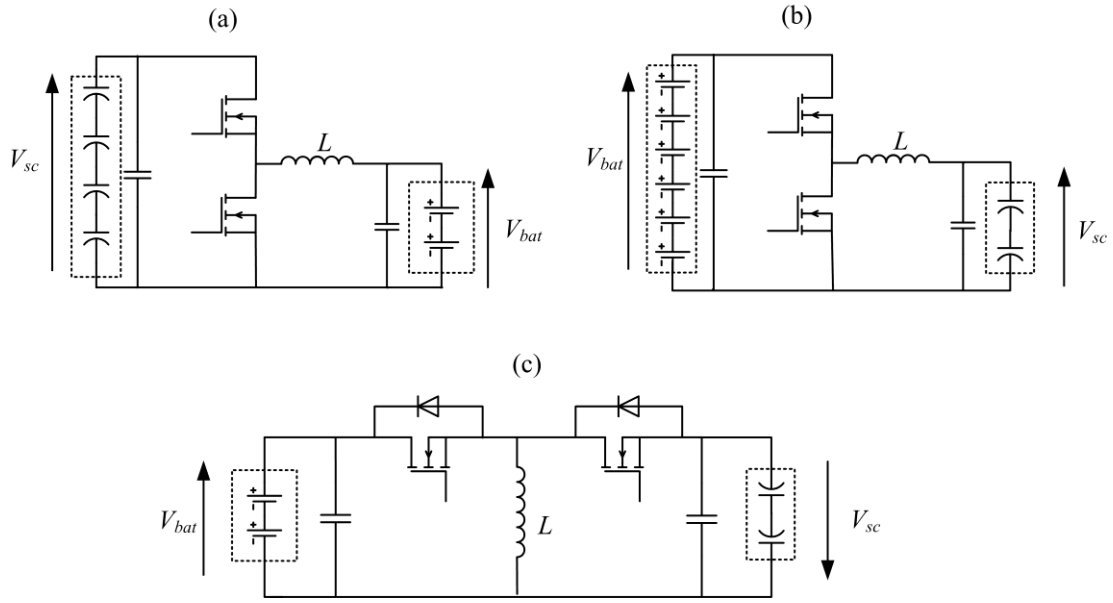

Fig. 6.2 Proposed converter configurations with operating voltage ranges of: (a) Synchronous buck for $V_{sc} > V_{bat}$ (b) Synchronous buck for $V_{sc} < V_{bat}$ (c) buck\boost $V_{sc} \geq V_{bat}$ or $V_{bat} \geq V_{sc}$

6.2.2 Hysteretic Current Control

Hysteretic current-mode control is a form of limit-cycling nonlinear feedback control [130]. This control scheme can be used to maintain tight regulation of the inductor current in DC/DC converters [131]. The reason this mode of control was chosen is that gives guaranteed stability and robust performance despite variation and uncertainty in system parameters and operating conditions [132]. Alternative schemes based on a fixed frequency PWM current-mode control suffer from sub-harmonic oscillation instability [132], [133] at duty ratios above 50% [134]. This requires the added complexity of slope-compensation to resolve [135].

Variable frequency, hysteretic current-mode control was chosen over the conventional PWM current-mode approach as it is inherently stable for all duty ratios [136]. This is advantageous in supercapacitor-interface applications due to the potentially large supercapacitor voltage swing with state of charge which could cause extreme voltage conversion ratios and therefore duty ratio requirements. In addition to stability and robustness, the hysteretic current control has the advantage of inherent, active cycle-by-cycle current-regulation, and can therefore be made resilient to input and output short circuit faults.

Jan et al. [54] have proposed a similar system to that described in this section for use in diverting high-frequency battery current fluctuations to/from a supercapacitor, with other similar systems reported in [52], [53]. The system described is based around the use of a fixed frequency PWM duty ratio control of the converter current which is unstable for duty ratios > 50% [134]. The system presented in this section extends these studies [52-54] by providing an alternative implementation, which has the operational advantage of inherent stability at duty ratios > 50% [136].

The basis of the control strategy is described below for the two main configurations in Fig. 6.2 (a) and (c), although a similar control can be developed for the configuration in Fig. 6.2 (b).

6.2.3 Synchronous Buck Converter

The converter of Fig. 6.2 (a) can be drawn in greater detail as shown in Fig 6.3:

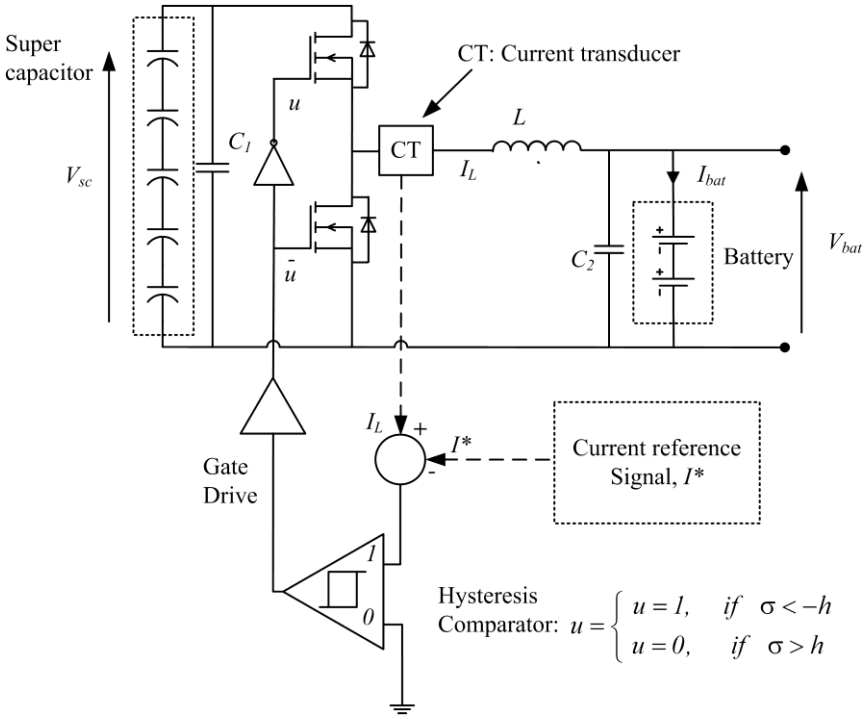

Fig. 6.3 DC/DC converter and control circuit.

Assuming ideal components in the converter of Fig. 6.3, and the necessary requirement for successful operation of the buck converter that V_{sc} is greater than V_{bat} is upheld, the equation describing inductor current variation is given by Eq. 6.1, where u is the switching logic control signal.

$$L\frac{dI_L}{dt} = V_{sc}u - V_{bat} \quad \text{(V)} \tag{6.1}$$

The control mode can be thought of as a bang-bang regulation of the inductor current although the principles of sliding-mode control theory have been applied to describe it [137]. A detailed discussion regarding sliding mode control can be found in [138] and further discussion regarding the application in DC/DC converter designs in [139]. The objective of the controller in this case is to maintain the converter output current by regulating the inductor-current I_L, such that it tracks the command reference current I^*. A control objective function $\sigma = 0$ can be defined as follows [137]:

$$\sigma = I_L - I^* = 0 \quad \text{(A)} \tag{6.2}$$

To meet the control objective, a switching strategy for the half-bridge devices control signal *u* (see Fig. 6.3) was chosen to satisfy Eq. 6.3 such that σ and its time-derivative have opposite signs. This ensures the system will converge to the state σ = *0* [137] and consequently the output current converges to the current reference, *I**:

$$\forall\ \sigma \neq 0 :\ \sigma \cdot \frac{d}{dt}\sigma < 0 \tag{6.3}$$

A switching control law which satisfies Eq. (6.3) is described by the relation (6.4), where *h* is half the width of a small constant hysteresis band lying symmetrically about the set-point value.

$$u = \begin{cases} u = 1, & if \quad \sigma < -h \\ u = 0, & if \quad \sigma > h \end{cases} \tag{6.4}$$

For later power conversion efficiency estimation, the approximate average switching frequency f_{sw} for a given set of operating conditions can be determined from the inductor rise and fall times (T_1 and T_2) in each switch position from Eq. (6.1) as follows:

$$f_{sw} = \frac{1}{T_1 + T_2} \tag{6.5}$$

$$= \frac{1}{\left(2hL \big/ (V_{sc} - V_{bat})\right) + \left(-2hL \big/ -V_{bat}\right)} \quad \text{(Hz)}$$

The above analysis can be directly applied to the converter of 6.2 (b) by swapping V_{sc} and V_{bat} and so won't be repeated.

6.2.4 Inverting Buck/Boost Converter

A similar control strategy can be applied to the inductor-current in the inverting buck/boost converter as follows.

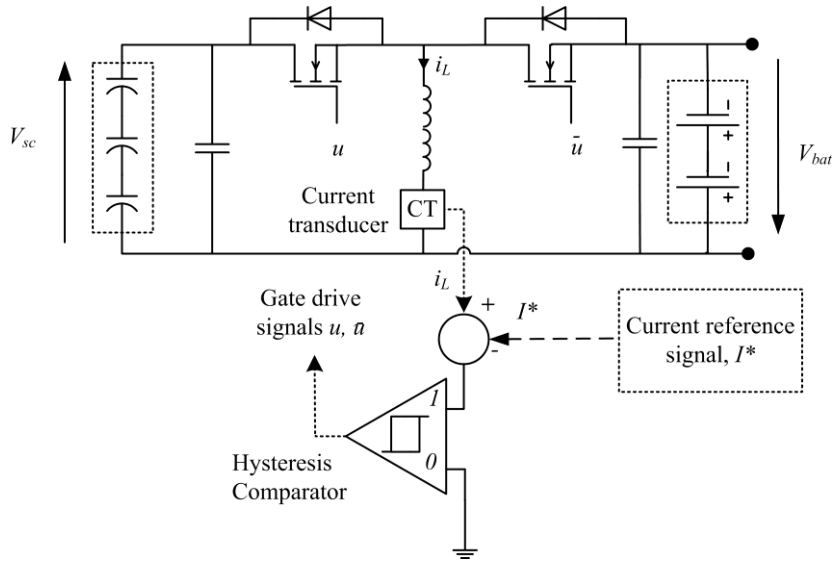

Fig. 6.4 DC/DC converter and control circuit

Assuming ideal components, the governing equation for the inductor current is:

$$L\frac{dI_L}{dt} = V_{sc}u - V_{bat}\bar{u} \tag{6.6}$$

The same switching function as Eq. (6.2) can be used for the inverting buck/boost converter as was used with the synchronous buck/boost converter:

$$\sigma = I_L - I^* = 0 \tag{6.7}$$

To ensure the system will converge to the state $\sigma = 0$ [137], the condition defined by Eq. (6.3) must be true as before. The same switching control law as Eq. (6.4) can also be chosen to satisfy Eq. (6.3) in the case of the inverting buck/boost converter as follows:

$$u = \begin{cases} u = 1, & if \quad \sigma < -h \\ u = 0, & if \quad \sigma > h \end{cases} \tag{6.8}$$

However in this instance, if V_{sc} and V_{bat} are non-zero Eq. (6.3) is met irrespective of their relative magnitudes. The constraints placed on V_{sc} and V_{bat} are therefore less stringent: $V_{sc} > 0$ and $V_{bat} > 0$.

The above control strategies have been described previously when used by Venkatarmanan [137] but only in the case of uni-directional converters employing only one power electronic switch. The work presented above in sections 6.2.3 - 6.2.4 has confirmed that the same current control applies more generally in the case of bidirectional current control using synchronous buck and inverting buck/boost converters employing two power electronic switches.

6.2.5 Practical Considerations

Since the majority of the experimental results discussed later in chapters 8 and 9 are derived from tests involving the buck configuration of Fig. 6.2 (a), practical considerations regarding the implementation of this converter configuration are discussed below. These tend to be very briefly commented on, if at all, in published accounts of power-converter implementation in this context. However, an understanding of such design detail was found to be important to the successful experimental validation of the power converters. A number of problems which are difficult to predict arise, which tend to confound experimental work and require some ingenuity to identify and address.

6.2.6 Gate Driving Circuits

The above circuits of Fig. 6.2 were implemented with IGBT (see Fig. 6.6) and then MOSFET power electronic switches. In both cases, typical gate driving voltages for these devices were 10 V to 15 V higher than the source voltage (V_{gs}). The hardware implementation of the converter for this application required a floating gate drive voltage; one that is not referenced to the ground return. Initially, a “bootstrap capacitor” was used, which was charged from the low-voltage rail during the high-side switch-off period and used to supply the high-side drive voltage. In this application, during start-up

of the buck converter, if the voltage of the energy storage device connected at the low side of the converter is higher than the gate-drive IC low voltage rail, this prevents the bootstrap capacitor from charging. To overcome this problem, a separate, floating gate-drive power-supply was implemented, using an isolated, low power DC/DC converter for both high and low side switches.

6.2.7 Output Filter

Eq. (6.5) can be used to determine the output filter inductor for a given current ripple requirement. The current ripple is determined by the hysteresis width, $2h$, and the required inductance value can be found from the required system switching frequency range. The controller in this case was designed to operate at relatively low switching frequency (<20kHz) to improve efficiency, by reduction of switching losses. The output filter capacitor was designed to minimise output voltage ripple for a given load transient slew-rate using the procedure given in [140].

6.2.8 Inductor Current Slew-Rate Limit

To achieve a high bandwidth, it is necessary to achieve a high current slew-rate. The theoretical basis for this has been derived in Appendix 1. This shows that the achievable bandwidth of a control system in which a rate-of-change limited element exists, is proportional to the rate limit and inversely proportional to the magnitude of the signal. From Eq. (6.1) it can be seen that the inductor current slew-rate is proportional to the magnitude of the inductor driving voltage and inversely proportional to the inductance. So, to maximize inductor current slew-rate (in the synchronous buck configuration) and therefore control-bandwidth, it is desirable to maintain the supercapacitor at a level sufficiently higher than that of the battery to sustain sufficient inductor driving voltage

($V_{sc} - V_{bat}$) and it is also desirable to select a suitably low inductance, L. It should be noted that the effect of maintaining the supercapacitor voltage above that of the battery is to limit the usable capacity of the supercapacitor to an extent. This is considered in further detail in Section 8.2.4.

6.2.9 Current Measurement

To implement the hysteretic current control in Section 6.2.3 it is necessary to measure the power-converter inductor current. This can be achieved at low-cost by inserting a low-value resistor in series with the inductance and amplifying the voltage drop across it. The disadvantage of this method is the power dissipation in the resistor which leads to a reduction in efficiency, and the un-isolated connection of the electronic-controller stage to the power stage provides an efficient coupling path for high-frequency switching noise which is especially disruptive to the operation of hysteretic current-control scheme. For this reason, a Hall-effect current transducer with sufficient bandwidth was used instead to measure the inductor current waveform non-intrusively.

6.2.10 Gate Drive Isolation

To provide protection for the control circuit from potentially damaging high voltage and current and further minimize switching noise coupling, the main control PCB was galvanically isolated from the gate drive and power circuits by use of opto-couplers to transmit the gate drive logic signals.

6.2.11 Snubber Network

Snubber networks are circuit networks whose function it is to protect the power electronic switches from unwanted energy spikes, typically caused by the active switching of current-carrying stray circuit inductances. Snubber networks can be of an

active or passive design. In this study, the passive approach was used which typically relies on a combination of resistors, capacitors and inductors to provide an alternate path for unwanted switching energy.

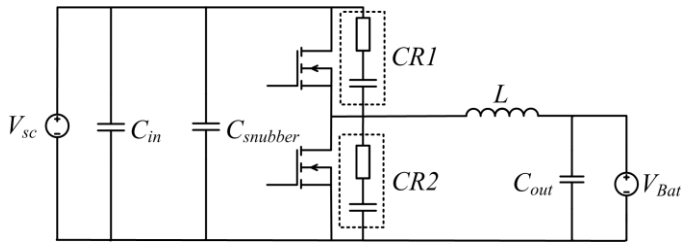

Fig. 6.5 Converter schematic with snubber components

In Fig. 6.5, two "RC snubbers" shown as *CR1* and *CR2* were used across each power electronic switch and designed according to the guidelines in [141] to control voltage overshoot and ringing that occurs when stray inductance is reset when a switch opens or a diode reverse recovers. This reduces power semiconductor avalanching and the amplitude and frequency of EMI emission which would otherwise interfere with electronic controller operation. The additional low-ESR capacitor $C_{snubber}$ was connected directly across both power electronic switches in close proximity to their terminals as in [142] to help mitigate any voltage transients occurring across both switches by providing a low impedance path which the electrolytic capacitor C_{in} may not.

6.2.12 Converter Implementation

The final component values of the principle synchronous buck converter elements used in this study are described in Appendix 3. The implementation of the DC/DC converter enclosure, control PCB and hybrid energy storage system are shown below in Fig. 6.6.

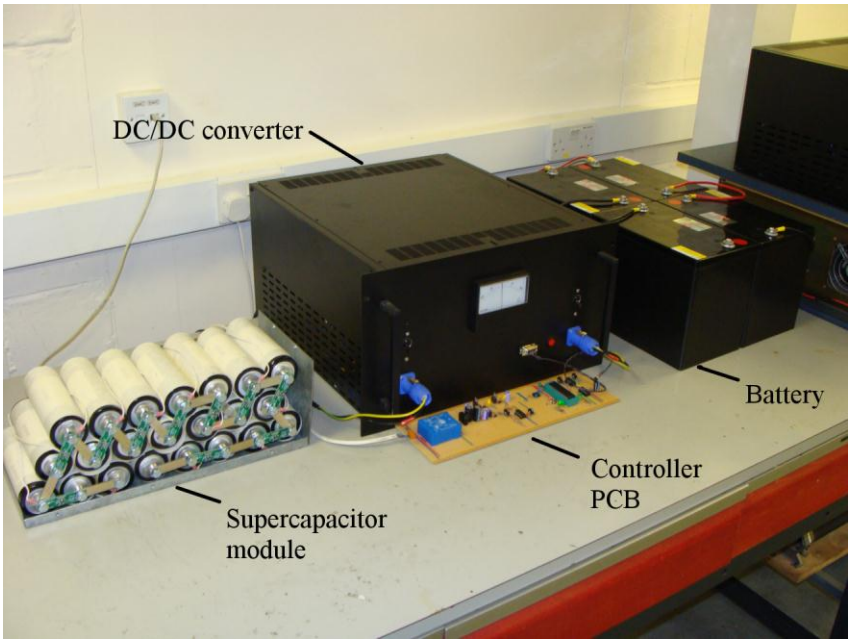

Fig. 6.6 Hybrid energy storage system

The internal arrangement of the DC/DC converter power electronic switches and electro-magnetic storage element was based around a bus-bar arrangement intended to minimise stray inductances as shown below in Fig. 6.7.

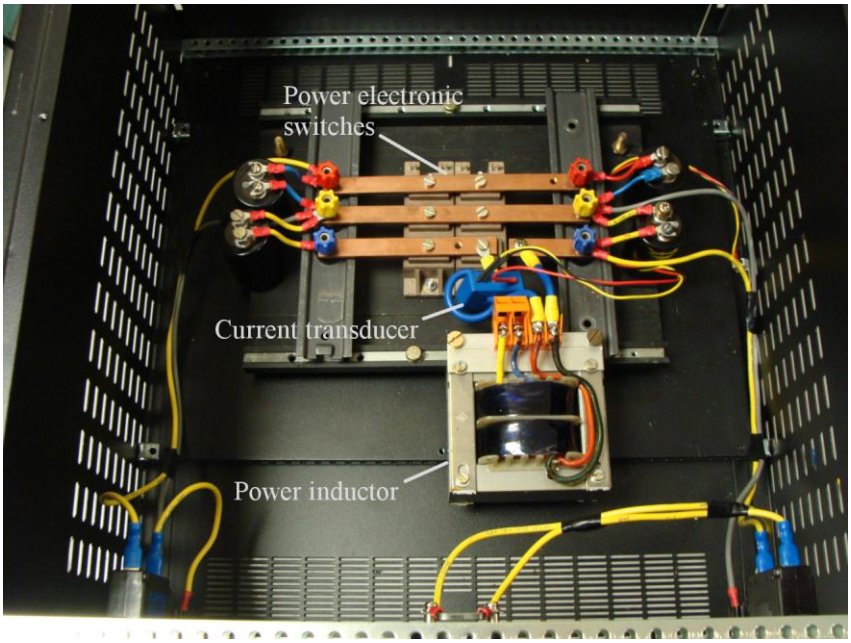

Fig. 6.7 Internal arrangement of DC/DC converter (snubber circuit elements removed).

6.3 Current Control Scheme Validation

To illustrate the performance of the converter in terms of current tracking, a bipolar 250Hz/10A square wave current reference signal was used (using a signal generator). The inductor current (blue trace) and current reference signal (yellow trace) were recorded on a digital storage oscilloscope as shown in Fig. 6.8.

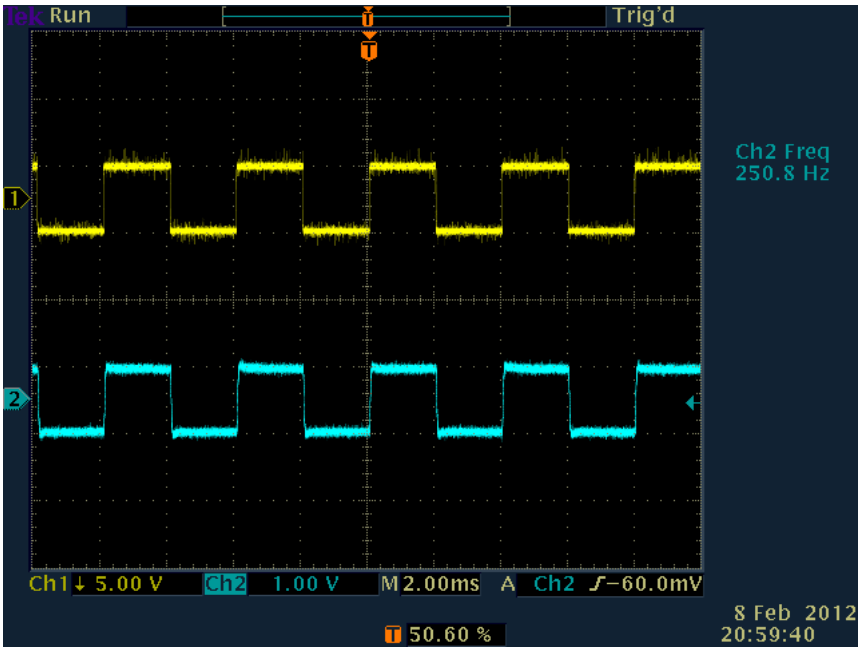

Fig. 6.8 Hysteretic current control of DC/DC converter. Yellow trace current command reference signal. Blue trace: DC/DC converter output current waveform (100mV/A)

The converter is transferring current from one energy storage device to another which in this are the battery and supercapacitor (see Appendix 3). The converter can be seen to operate with bidirectional current capability, tracking the 250Hz square wave with a good degree of accuracy. The inductor current waveform and output current were recorded over a shorter time-base as shown in Fig. 6.9.

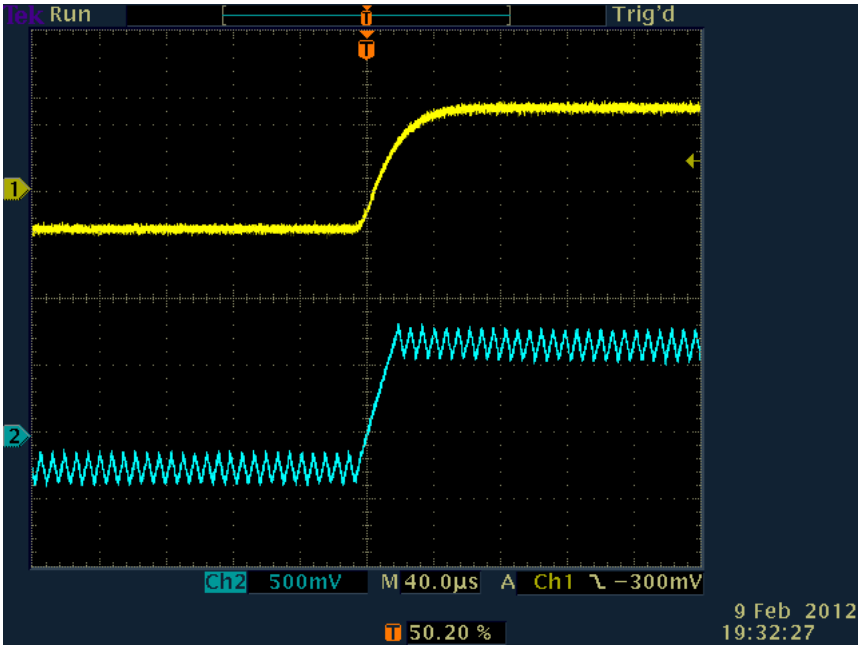

Fig. 6.9 Inductor current and output current of DC/DC converter. Yellow trace: Output current (After converter output filter [I_{bat} in Fig 6.3]). Blue trace: Inductor current waveform (100mV/A) (before converter output filter).

Fig. 6.9 shows the nature of the inductor current waveform (blue trace) and output current waveform (yellow trace). From the lower blue trace, the hysteresis effect of the inductor current waveform switching about the command reference can be seen. The upper yellow trace shows how the current ripple is significantly reduced at the converter output due to the output capacitance.

6.4 Synchronous Buck Converter Simulation

To confirm that the operation of the converter was achieved as expected, various circuit-based models of the converters described in 6.3.1 and 6.3.2 were initially developed (using Matlab/Simulink: SimpowerSystems [85]) to accurately describe the converter switching behavior with good accuracy at the expense of slow simulation times. This was useful in optimising the converter-design and component values. However, as the research effort became focused on analysis of the system over timescales of the order of

one year or more, it became necessary to develop an averaged-simulation capable of modelling the converter behavior with reduced computational effort. The model also incorporates an estimate of its steady-state efficiency map, validated by experiment and described as follows.

6.4.1 Conduction Losses

The loss-model was based on power loss equations developed in [143]. The high and low-side conduction losses in the power MOSFET can be estimated from the duty-cycle of the converter, $D = V_{out}/V_{in}$ as follows [143], if the effect of the relatively small current ripple is ignored:

$$P_{cond\_high} = I_{out}{}^2 R_{ds(on)} D \text{ (W)} \tag{6.9}$$

$$P_{cond\_low} = I_{out}{}^2 R_{ds(on)} (1-D) \text{ (W)} \tag{6.10}$$

where $R_{ds(ON)}$ represents power-MOSFET conduction resistance

Combining these terms and including resistive losses in the main inductor, the total conduction power loss, $P_{conduction}$, can be written as shown in Eq. (6.11) which shows that selection of MOSFETS with low $R_{ds(ON)}$ and a power inductor with a low DC resistance are essential for high efficiency converters.

$$P_{conduction} = I_{out}{}^2 R_{ds(on)} + I_{out}{}^2 R_L \text{ (W)} \tag{6.11}$$

where R_L represents the power inductor resistance.

6.4.2 Switching Losses

During the power-MOSFET switching interval, the drain-voltage and current-waveforms and gate-voltage under a constant gate current input condition can be represented by Fig. 6.10 [143].

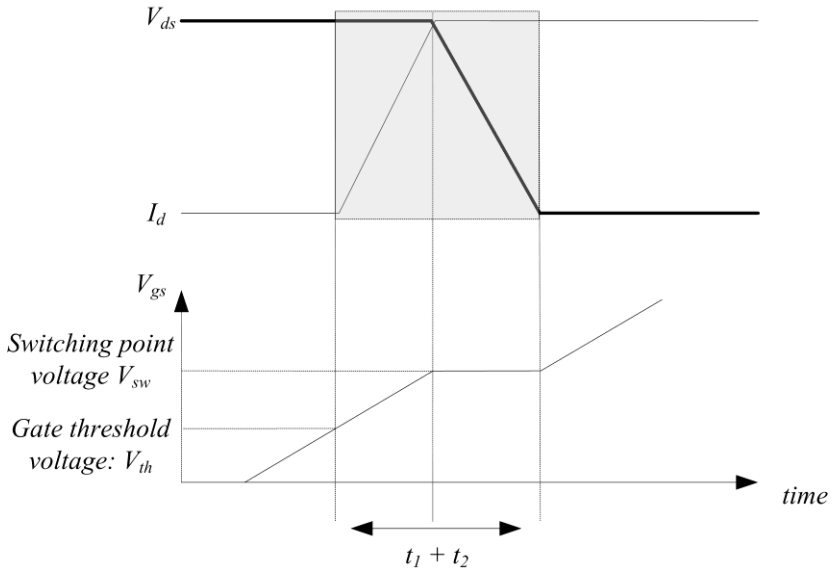

Fig 6.10 MOSFET turn-on switching waveforms

The switching loss term is an estimate of power lost due to voltage and current (V_{ds} and I_d) overlap during the rising current and falling voltage and may be estimated for the synchronous buck converter using Eq. 6.12.

$$P_{switching\_high} = 0.5 V_{sc} I_{out} (t_1 + t_2) f_{sw} \text{ (W)} \tag{6.12}$$

where V_{sc} = high side voltage (Supercapacitor voltage) (V)

The time periods $t_1 + t_2$ (Fig. 6.10) during rising and falling switching intervals can be measured or, if the MOSFET gate resistance is known (external and internal), then these times can be calculated as follows [143]:

$$I_{L\_H} = \frac{V_{dd} - V_{sw}}{R_{gatedrive} + R_{gate}} \text{ (A)} \tag{6.13}$$

where V_{dd} is the gate drive supply voltage (6.14)

$$I_{H\_L} = \frac{V_{sw}}{R_{gatedrive} + R_{gate}} \text{ (A)}$$

As shown in Fig. 6.10, V_{sw} is the gate voltage at which switching occurs and can be obtained from manufacturers' datasheets, $Q_{g(sw)}$ is defined as the gate charge required

during the MOSFET switching interval; allowing the rising (L-H) and falling (H-L) switching times to be determined as follows:

$$T_{L-H} = \frac{Q_{G(sw)}}{I_{L-H}} \text{ (s)} \tag{6.15}$$

$$T_{H-L} = \frac{Q_{G(sw)}}{I_{H\_L}} \text{ (s)} \tag{6.16}$$

Once the rising and falling switching times are determined, the switching loss may be estimated:

$$P_{switching} = 0.5 V_{sc} I_{out} (T_{L-H} + T_{H-L}) f_{sw} \text{ (W)} \tag{6.17}$$

The power loss associated with charging the MOSFET output capacitance C_{oss} can be estimated [143]:

$$P_{coss} = 0.5 C_{oss} V_{sc}^{\ 2} f_{sw} \text{ (W)} \tag{6.18}$$

where C_{oss} is the MOSFET output capacitance.

The power loss associated with the MOSFET body-diode reverse recovery charge Q_{rr} can be estimated:

$$P_{qrr} = Q_{rr} V_{sc} f_{sw} \text{ (W)} \tag{6.19}$$

where Q_{rr} is the MOSFET body diode reverse recovery charge.

Assuming that with the intrinsic diode is forward-biased, the switching losses in the power-MOSFET in parallel with the forward-biased diode are negligible, since switching takes place with a diode volt-drop potential (< 1V) across the switch, the total switching loss term may then be estimated using Eq. (6.20).

$$P_{switching} = 0.5 V_{sc} I_{out} (T_{L-H} + T_{H-L}) f_{sw} + 0.5 C_{oss} V_{sc}^{\ 2} f_{sw} + Q_{rr} V_{sc} f_{sw} \text{ (W)} \tag{6.20}$$

The first term represents power lost due to voltage/current overlap during the rising and

falling switching intervals whose rise and fall times are denoted by t_r and t_f. The second term represents the power loss associated with charging the MOSFET output capacitance $C_{oss.}$ The third term represents the loss associated with the MOSFET body-diode reverse recovery charge Q_{rr}. Many of these loss parameters are temperature dependent and a precise simulation would model these dependencies. Instead, to provide an estimation of the converter losses, the worst-case, datasheet [144] maximum values for t_r , t_f, $C_{oss,}$ and Q_{rr} were used.

The quiescent power was measured during switching operation and is included in the model below as a constant power-loss term P_q, referred to the input side. The following section describes implementation of the loss model developed in the Simulink environment.

6.4.3 Simulink Implementation

Fig. 6.11 shows the Simulink model of the synchronous buck converter including the switching and conduction loss calculations. Inputs to the Simulink model are the supercapacitor voltage (determined using the modelling procedure in Section 4.4.2) and battery voltage (determined using the modelling procedure in Section 4.2.1) and the command reference current I^* (derived from the control algorithm in use). Modelling outputs are the converter high and low side currents.

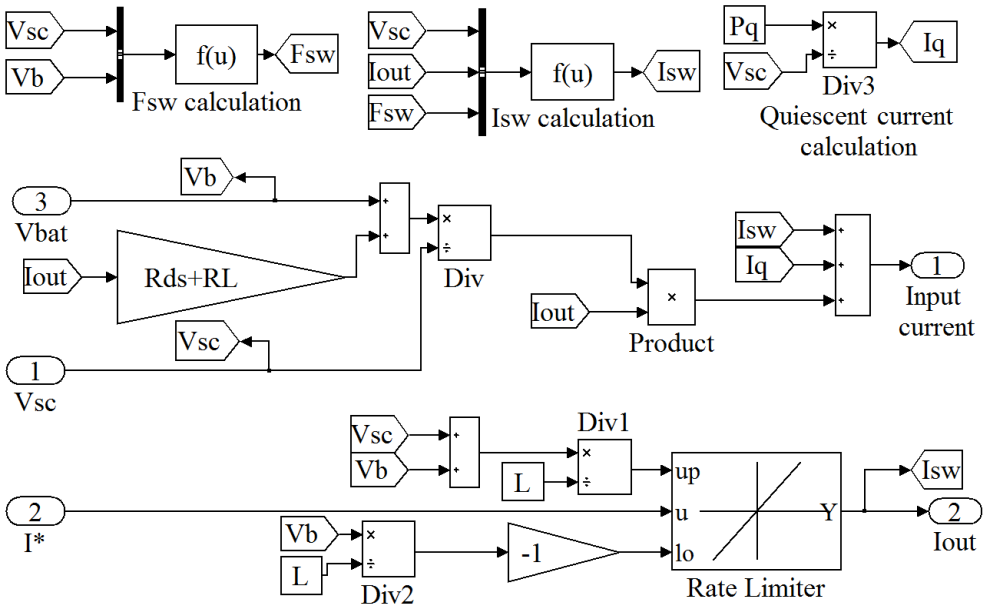

Fig. 6.11 Simulink model for hysteretic current controlled converter

The model incorporates the inductor current slew-rate limit with rise and fall slew-rates determined from Eq. (6.1) as follows:

$$\left(\frac{di}{dt}\right)_{rise} = \frac{V_{sc} - V_{bat}}{L} \quad \text{A/s} \tag{6.21}$$

$$\left(\frac{di}{dt}\right)_{fall} = \frac{-V_{bat}}{L} \quad \text{A/s} \tag{6.22}$$

The conduction losses are incorporated in the model based on Eq. (6.12) as follows:

Defining an effective duty ratio *D'*, as follows:

$$D' = \frac{V_{out} + I_{out}R_{ds(on)} + I_{out}R_L}{V_{in}} \tag{6.23}$$

This allows the effective input current to be determined using the relation:

$$I'_{in} = D' I_{out} \quad (\text{A}_{\text{rms}}) \tag{6.24}$$

The power lost due to conduction losses can be found from:

$$P'_{in} = V_{in} I_{in} \quad (\text{W}) \tag{6.25}$$

Substituting Eq.(6.23) and (6.24) into Eq. (6.25) gives:

$$
\begin{aligned}
P'_{in} &= D' I_{out} V_{in} \\
&= \frac{V_{out} + I_{out} R_{ds(on)} + I_{out} R_L}{V_{in}} I_{out} V_{in} \quad \text{(W)} \\
&= V_{out} I_{out} + I_{out}{}^2 R_{ds(on)} + I_{out}{}^2 R \\
&= P_{out} + P_{condutcion}
\end{aligned}
\tag{6.23}
$$

where P_{out} is the output power and $P_{conduction}$ as described in Eq. (6.12)

The switching frequency is determined using Eq. (6.5), allowing the switching power loss to be calculated using Eq. (6.20) which is referred to the high side input as well as a measured constant quiescent current.

The model in Fig. 6.11 was used to generate the efficiency map for the converter at various power levels and frequencies shown in Fig. 6.12. The effect of increasing the switching frequency can be seen to reduce overall efficiency due to higher switching losses.

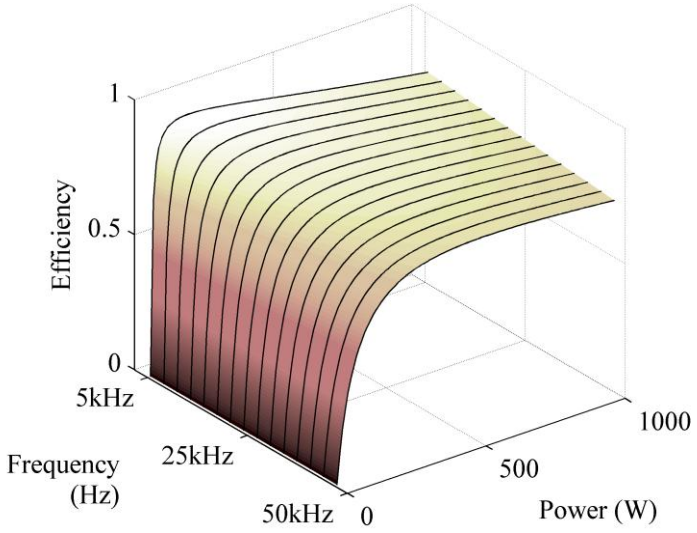

Fig. 6.12 DC/DC converter loss efficiency modelling results (see Appendix 3 for converter specification)

6.5 Efficiency Analysis

The converter efficiency was measured using a Voltech pm 1000 + power-analyser to measure the input and output power for different switching frequencies in the range

50W to 500W. Implementation of the switching-loss model based on datasheet values as described in Section 6.4 above was found empirically to underestimate the switching loss term considerably. It was found by experiment that the switching loss term $P_{switching}$ was inaccurate by a factor of ~3. The switching loss model was then empirically adjusted so that that the overall efficiency estimation closely approximated the measured efficiency as shown in Fig 6.13.

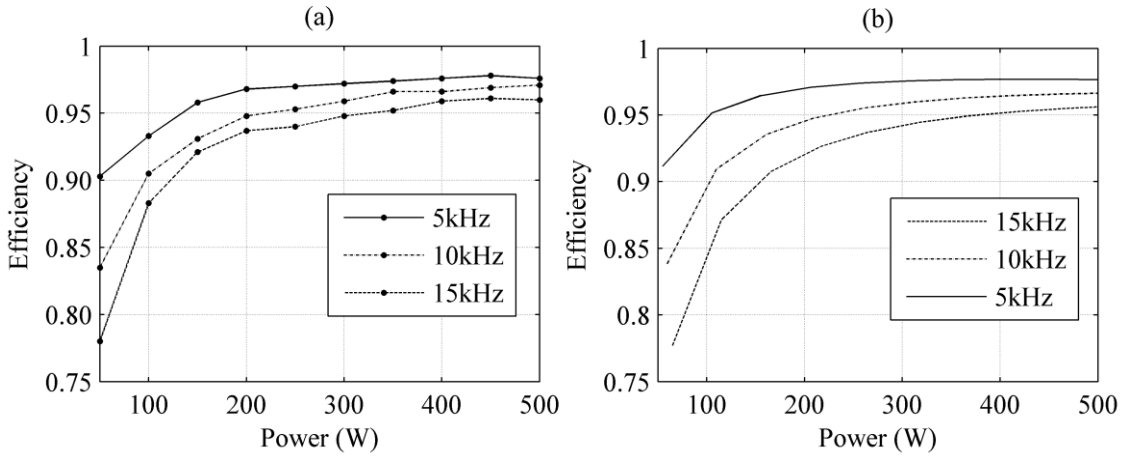

Fig. 6.13 (a) Measured efficiency values (b) Adjusted model efficiency values.

The measured peak efficiency when operating at 5kHZ was ~97% if low on-state resistance power MOSFETs are chosen (not including quiescent losses). The efficiency can be seen to decrease with increasing switching frequency due to higher switching losses. For this reason, the converter was designed to operate at a relatively low average switching frequency (<10 kHz) over the operating range.

6.6 Discussion and Summary

This chapter has described a versatile means by which current can be controlled to or from a supercapacitor or another energy storage device. Practical considerations focused on the implementation of the synchronous buck converter have been discussed.

The bidirectional current tracking performance of the converter was demonstrated experimentally by transferring power between two energy storage devices in Section 6.3. The converter was then simulated using a novel model created specifically for the purpose of long term simulation of the converter developed (>>weeks). To validate the switching loss model within the overall converter model, an experimental test was carried out using a load and a unidirectional flow of current.

A simulation strategy developed for the synchronous buck converter has provided a means by which its performance can be modeled with a frequency dependent efficiency map and reduced computational effort when compared to discrete switching models. This is desirable for long-term simulations.

The converter simulation and efficiency model have been based on a MOSFET implementation of the power electronic switches. However, since gate drive requirements for 15V MOSFET gate drives and typical IGBT gate drives are similar, both were used for functional testing. The MOSFET implementation was found to be considerably less expensive for a given current rating.

The hardware implementation of the synchronous buck converter operating under hysteretic current control has been presented and experimental results have confirmed that the strategy has good dynamic current tracking performance. The converter operating in this way represents a versatile and robust, fast-acting current-control loop and has been used as a power electronics building block for the implementation of control systems described later in Chapters 8 and 9.

Chapter 7: Energy Storage Sizing Algorithm and Introduction to Simulations

7.1 Introduction

This chapter presents the methods used to determine a configuration of wind turbine power rating and battery energy storage capacity based on given constraints. This was considered necessary to ensure that later simulations were based on a realistically configured and feasible system. First, a technique for finding the energy-storage and wind-turbine capacities for a given load, subject to reliability constraints, is presented. Secondly, a methodology for finding the energy storage and wind turbine capacity subject to economic constraints is described. This is followed by an introduction to the simulation strategies used later (in Chapters 8 and 9) and a description of the application scenarios on which they are based.

7.2 Optimisation Strategy

The problem of optimising the wind turbine and energy storage capacity for a given load can be formulated as a linear programming task with two objectives: ensuring the load is met and minimizing system costs. The constraints can take the form of reliability/performance indicators and economic/cost indicators. The “loss of power supply probability” [145] concept was chosen as a reliability-measure describing the probability that insufficient energy available to supply the load can occur. The loss-of-power-supply-probability (LPSP) is defined as the ratio of total energy deficit over the total load energy requirement [145].

$$LPSP = \frac{\sum Unmet load\ energy}{\sum Load\ energy} \tag{7.1}$$

A LPSP of 0 means the load will be always satisfied, and a LPSP of 1 means that the load will never be met by the renewable energy source. In this study, the LPSP can be considered as the probability that the load will be not be met by the wind turbine generator and battery and will be provided by an alternative energy source such as a diesel generator. Grid-connected configurations have not been considered.

The optimisation procedures were implemented in Matlab to iteratively simulate system performance over a range of combinations of battery and wind turbine ratings. Since the system optimisation algorithms are iterative in nature, it was necessary to implement simplified models of the various system components to allow faster execution times in repetitive simulations. A sampling interval of 0.5 hours, as is frequently employed in power systems analysis [146] was used to reduce computational effort compared to a shorter sampling interval. A rigorous optimisation code would simulate the system at higher resolution to capture short-term dynamic effects. However, the detailed optimistion of the sizing simulation was outside of the project scope, so a 0.5 hour simulation interval was used to indicate a plausible ratio of energy storage to wind-turbine capacity. The implementation of a higher resolution version of the procedure outlined below should be the subject of future consideration.

A simplified battery model derived from the state-of-charge equation based on the time-current interval [see Eq. (4.3)] discussed previously in Chapter 4 was implemented to determine the energy-stored by integrating incident power to the battery. In this simplified model the incident battery power is integrated to find the energy-stored (as opposed to the current) based on the assumption that the battery voltage remains

relatively constant during the sampling interval. A conceptual, top-level model of the process is shown in Fig. 7.1.

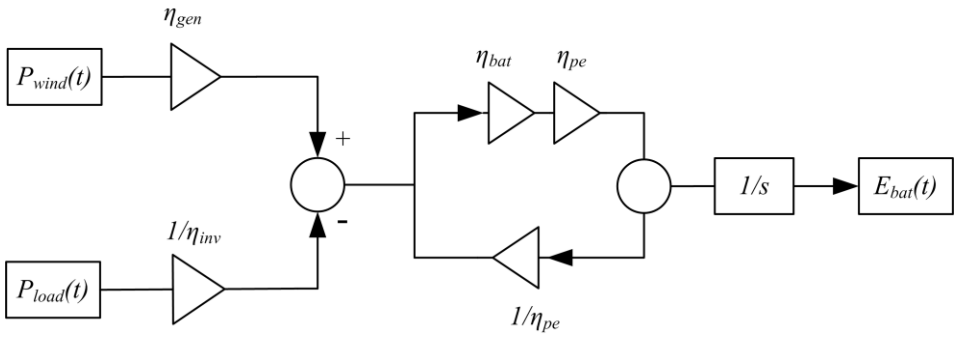

Fig. 7.1 Top-level energy storage simulation conceptual diagram.

To model battery efficiency, the simplifying assumption was made that this can be approximated by a static efficiency. The efficiencies of the DC/DC converter, load inverter and battery were also approximated by conservative static efficiency factors as shown in Table 7.1

TABLE 7.1

Parameter	Description	Value
η_{inv}	Load inverter efficiency	0.95
η_{bat}	Battery efficiency	0.85
η_{pe}	DC/DC converter efficiency	0.95
η_{gen}	Generator efficiency	0.8

To determine the power available in the wind at sampling interval, *k*, the following equation was used [79]:

$$P_{wt}(k) = \eta_{gen} \cdot \frac{1}{2} \rho \pi R^2 v_{wind}(k)^3 C_p(\lambda) \text{ (W)} \tag{7.2}$$

where η_{gen} represents the electro-mechanical efficiency of the wind turbine generator. The effective wind speed was limited to include the effects of maximum and minimum generating wind speeds as in Eq. 3.6 as follows:

$$v_{effective} = \begin{cases} 0 & if \quad v_{wind} > v_{cut\_out} \\ V_{rated} & if \quad v_{wind} > v_{rated} \\ 0 & if \quad v_{wind} < v_{cut\_in,} \end{cases} \quad \text{(m/s)} \tag{7.3}$$

where v_{rated}, v_{cut_out} and v_{cut_in} are the rated, cut-out and cut-in wind speeds often found on manufacturer's datasheets.

Next, the power to/from the battery, P_{net}, was calculated as follows:

$$P_{net}(k) = P_{wt}(k) - \frac{P_{load}(k)}{\eta_{inv}} \quad \text{(W)} \tag{7.4}$$

where $\eta_{inv} = 0.95$ represents the load inverter efficiency.

Since the simulation interval considered was typically of the order of one year or more, it was necessary to include the battery self-discharge rate. For a lead acid battery, a typical datasheet quotes the self-discharge rate as 25% over 6 months. This can be converted to a decay rate multiplication factor α_{bat} for a simulation time step of 0.5hrs as follows:

$$\begin{aligned} &25\%/6 months = 0.14\%/day \\ &= (1.4x10^{-3}/48)/0.5hour \\ &\alpha_{bat} = 1-[1.4x10^{-3}/48] = 0.99997084 \end{aligned} \tag{7.5}$$

where α_{bat} is a battery self-discharge multiplication factor

At each time step, *k*, if the available wind energy is greater than the load demand, then the energy delivered to the battery can be calculated as follows [145], [147]:

$$E_{bat}(k) = E_{bat}(k-1) \cdot \alpha_{bat} + P_{net}(k)\eta_{bat}\eta_{pe}T_s \quad \text{(Wh/2)} \tag{7.6}$$

where T_s is the sample interval (hrs).

The energy unit in this case is Wh/2 as a half hour sample time (T_s) has been used. If the available wind energy at time, *k*, is less than the load demand then the net power, P_{net}(k), is negative and the energy extracted from the battery is given by [145], [147]:

$$E_{bat}(k) = E_{bat}(k-1) \cdot \alpha_{bat} + P_{net}(k)\frac{1}{\eta_{pe}}T_s \quad \text{(Wh/2)} \tag{7.7}$$

If the sum of available wind energy and energy available from the battery is less than the load the energy requirement, the energy deficit is calculated at time *k* by [145], [147]:

$$E_{deficit}(k) = P_{net}(k)T_s - E_{bat}(k-1) \quad \text{(Wh/2)} \tag{7.8}$$

The loss of power supply probability can then be calculated:

$$LPSP = \frac{\sum_{k=0}^{k=n} E_{deficit}(k)}{\sum_{k=0}^{k=n} E_{load}(k)} \tag{7.9}$$

7.2.1 Reliability Based Optimisation

An algorithm based on previous work [145] was employed to find the required energy storage capacity for a given LPSP. The usable capacity in the optimisation was assumed to be 80% of the nominal capacity of the battery as is often the case in hybrid power systems [71]. For each wind turbine radius in the search space, a time-series simulation of the power flows and energy within the system is performed based on 1800s sampling resolution data. If the loss of power supply probability is less than the required loss of

power supply probability, LPSP*, the energy storage rating is stored and the time series analyses is repeated for the next wind turbine radius in the search space. If the LPSP is greater than the required value, the battery capacity rating is incremented and the time series simulation is repeated. Fig. 7.2 illustrates the process.

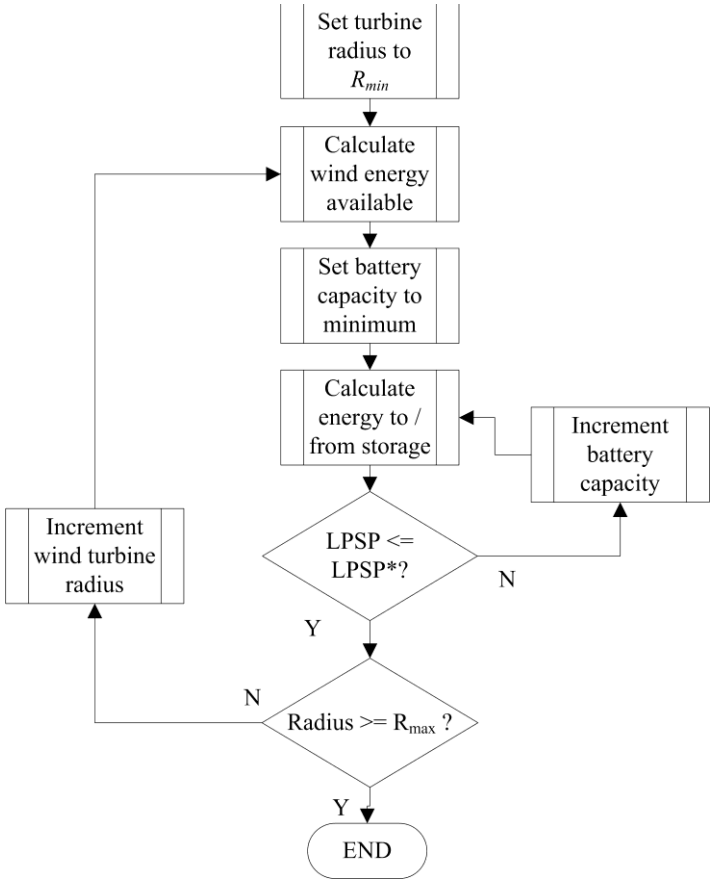

Fig. 7.2 Sizing algorithm subject to reliability constraints.

Fig. 7.3 plots the output results from the above algorithm for an autonomous system i.e. LPSP=0 with the load profile of Fig. 3.10 (re-sampled with a sample time of T_s = 0.5 hours).

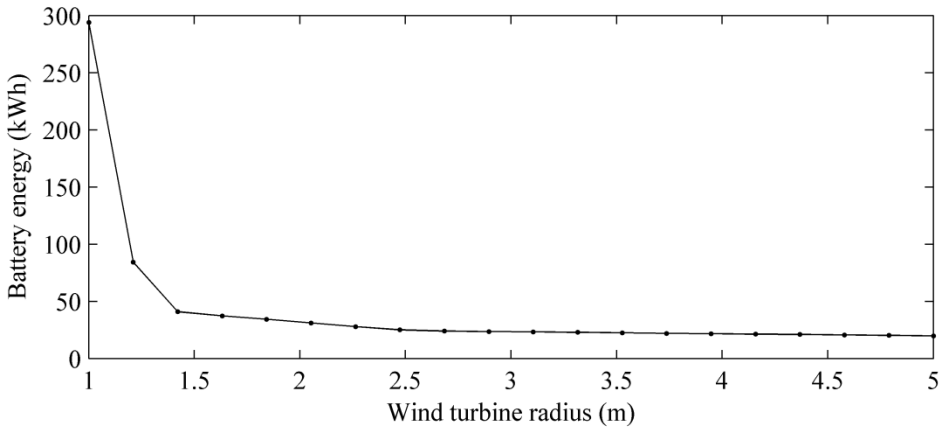

Fig.7.3 Sizing results: single-user remote off-grid load, *LPSP* = 0.

Setting the loss of power supply probability requirement *LPSP** > 0 allows a system in which the fraction of penetration of a dispatchable backup source such as a diesel generator determined by 1 - *LPSP**.

7.2.2 Techno-Economic Optimisation

From the example of Fig. 7.3 it can be seen that energy storage requirement to support the off-grid load over the course of a year with a wind turbine of 1m radius is ~300kWh. This is roughly equivalent to the energy storage capacity of two hundred and fifty 12V/100Ah batteries which, due to cost and size considerations may not be an optimal configuration. Similarly, a system with an energy storage capacity of ~20kWh requires a wind-turbine with 5m blade radius to support the load which also may not be optimal due to wind turbine cost constraints. So, to determine a realistic system configuration in terms of system cost, the algorithm described in section 7.2.2 was extended to perform an analysis of project costs (as shown in Fig. 7.4) for different combinations of wind-turbine and battery capacity capable of meeting the system reliability requirements.

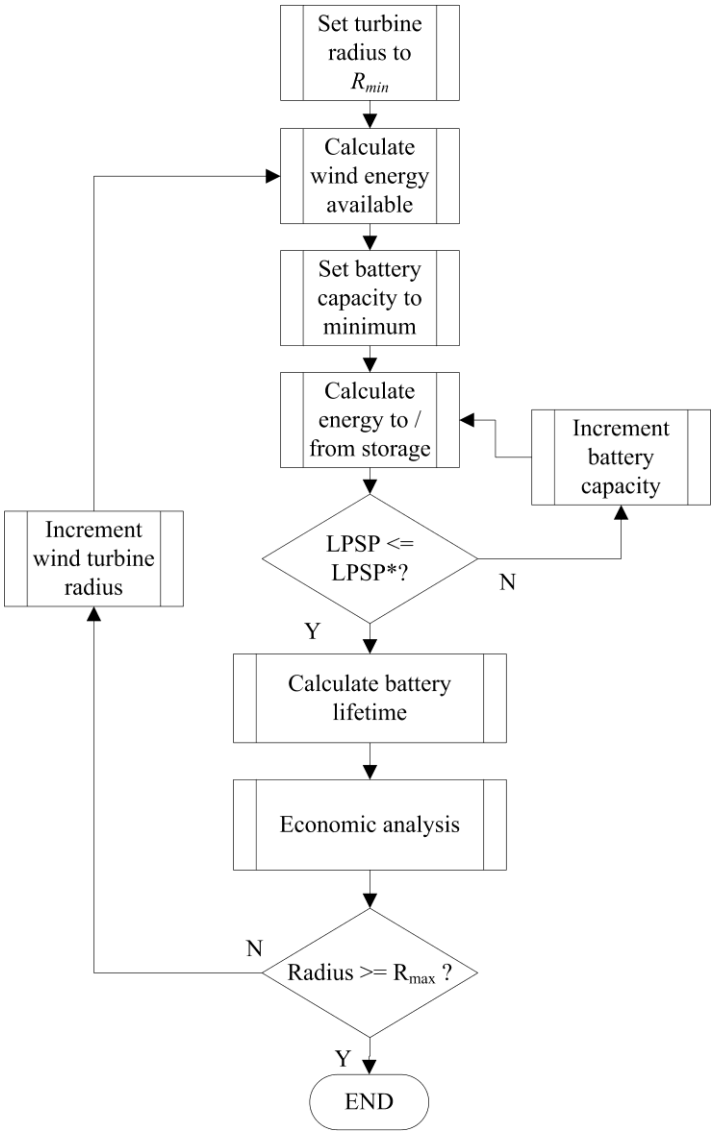

Fig. 7.4 Techno-economic optimisation algorithm

The algorithm of Fig. 7.4 finds the battery capacity required to support the load for a given wind-turbine radius and stores the energy storage state-of-charge variations in a vector. The usable capacity in the optimisation was assumed to be 80% of the nominal capacity of the battery as is often the case in hybrid power systems [71]. Battery life, L_{bat}, is then estimated based on the energy-storage state-of-charge variations using the rainflow counting lifetime model described in Chapter 5, Section 5.2.3. The number of times the batteries would require replacement over the course of a project life (in this case 25 years) allows the life-cycle costs of the battery to be determined. The main system life-cycle costs are then determined as follows.

7.2.2.1 Initial Costs

To determine the initial cost of the current wind turbine configuration in the search-space, a simplified model was developed incorporating the cost of various commercially available small (<50kW) scale wind turbine systems, using data from a recent market survey [148].

Fig. 7.4 plots the equipment cost vs. blade-radius for various commercially available wind turbine generator systems of the class under consideration.

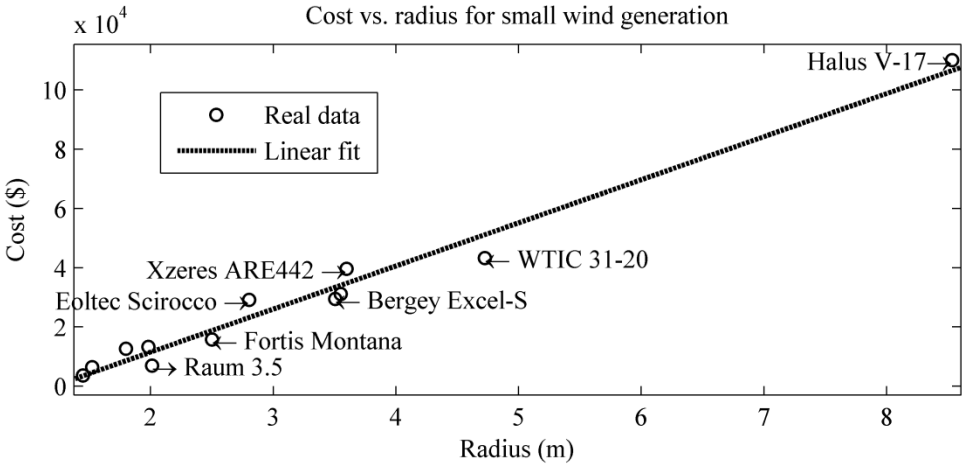

Fig. 7.5 Small wind turbines system cost vs. radius with data from a recent market survey [148].

The data points were interpolated with the resulting equation:

$$C_{wt}(r) = a \cdot r + c \quad (\$) \tag{7.10}$$

where $C_{wt}(r)$ = estimated installed wind turbine cost ($) and R = wind turbine radius (m) and linear interpolation coefficients are a = 1.454e+004 and c = -1.756e+004.

Eq. (7.11) was used to estimate wind turbine initial costs as a function of radius. To determine battery initial costs, the battery energy capacity was multiplied by the battery energy storage cost/kWh (see Table 7.2).

Systems including a diesel generator have also been considered to represent many typical real-life remote area power systems [11]. In addition, it was found that the wind to battery capacity ratio was higher for systems including diesel generation since the battery capacity requirement was lower for a given load. It has been shown [149] that systems with high wind to battery capacity ration are particularly prone to battery lifetime issues. For systems utilising a diesel backup generator, the generator was conservatively sized with power rating 25% higher than peak load power.

The initial payment was calculated as the sum of the initial costs of the wind turbine (C_{wt}), battery (C_{bat}) and diesel-generator (C_{gen}) as follows:

$$IP = C_{wt} + C_{bat} + C_{gen} \quad (\$) \tag{7.11}$$

The generator initial cost was then determined from the cost/kW reflecting current generator prices (see Table 7.2).

The procedure used to determine the costs of the system combinations under consideration was based on procedures recommended by the US Department of Energy renewable energy laboratory [150] and for use in micro-power system modelling software Homer [20] and by Hunter and Elliot [151] (p. 232 – 234) and is outlined as follows.

7.2.2.2 Net Present Cost

The total net present cost (NPC) was used to represent the life-cycle cost of the system components [151] (p. 232). The total NPC combines all costs and revenues associated with a system component into one lump-sum using the concept of present day value. In this example, NPC includes the costs of installation, fuel, replacement parts and maintenance. Revenues in this case could include income from salvage value. The net

present value for the system under consideration can be found using the following equation:

$$NPC = IP + FC + BR + GR + OM - SV \quad (\$) \tag{7.12}$$

where:

IP	= initial payment	($)
FC	= net present fuel cost	($)
BR	= net present value of battery replacement costs	($)
GR	= net present value of diesel-generator replacement costs	($)
OM	= net present operation and maintenance costs	($)
SV	= salvage value	($)

7.2.2.3 Replacement Cost

The number of times that the battery is expected to be replaced over the course of the project-life, R_{bat}, can be determined by the integer value of the project-life divided by battery-life: $R_{bat} = L_{proj} / L_{bat}$. This allows the net present cost of battery replacement to be calculated using the market discount rate, d_1 [152]:

$$BR = \sum_{n=1}^{n=R_{bat}} \frac{C_{bat}}{(1+d_1)^{R_{bat} \cdot L_{bat}}} \quad (\$) \tag{7.13}$$

A nominal diesel-generator lifetime of L_{gen} = 12.5 years was assumed. The number of generator replacements over the project-life R_{gen}, can be determined from the integer value $R_{gen} = L_{proj} / L_{gen}$ and the net present value of the generator replacement cost is then:

$$GR = \sum_{n=1}^{n=R_{gen}} \frac{C_{gen}}{(1+d_1)^{R_{gen} \cdot L_{gen}}}. \quad (\$) \tag{7.14}$$

7.2.2.4 Fuel Costs

The annual generator net present fuel cost, $FL_{n,}$ can be derived from the unmet annual load energy, $E_{deficit}$ [see Eq. (7.8)]. Defining F_{cost} as a fixed cost per kWh of generator electric energy output in terms of the fuel cost, the annual cost of generator fuel (FL_n) can then be determined as follows:

$$FL_n = E_{deficit} \cdot F_{cost} \quad (\$) \tag{7.15}$$

The net present value of fuel costs can be determined using the market discount rate, d, and fuel inflation rate, e:

$$FC = \sum_{n=1}^{n=N} \frac{(1+e)^n}{(1+d_1)^n} FL_{n,} \quad (\$) \tag{7.16}$$

where e = fuel inflation rate (%).

7.2.2. 5 Operation and maintenance costs

Annual operation and maintenance costs, OM_n, were nominally set at 5% of capital cost for the wind turbine system with net present operation and maintenance costs given by:

$$OM = \sum_{n=1}^{n=N} \frac{OM_n}{(1+d_1)^n} \quad (\$) \tag{7.17}$$

where n is the number of years over which the CRF is calculated.

7.2.2.6 Salvage revenue

A fixed salvage cost, SV, was nominally set at 20% of capital cost of the wind turbine and generator costs and 0% for the battery.

The key parameter values used in the above calculations are given in Table 7.2.

TABLE 7.2

Parameter	Description	Value
C_{bat}	Battery installed-cost [153]	\$200/kWh
C_{gen}	Generator capital cost [154]	\$1000/kW
d_1	Market discount rate	4%
e	Fuel inflation rate	5%
F_{cost}	Fuel cost / kWh [155]	0.26 \$/kWh

7.2.2.2.5 Levelised cost of energy

The "Levelised cost of energy" is often chosen as an economic feasibility indicator in renewable energy system feasibility analyses [151] (p. 234) [156]. The combinations of wind turbine and battery capacity in the search space with the lowest levelised cost of energy were chosen as system configurations for the simulations described in Chapters 8 and 9. The levelised cost of energy (LCE) can be determined as follows:

$$LCE = \frac{NPV \cdot CRF}{E_{load}} \quad (\$/\text{kWh}) \tag{7.18}$$

where E_{load} is the annual load consumption and the capital recovery factor (*CRF)* is defined [156] as follows:

$$CRF = \frac{d_1(1+d_1)^n}{(1+d_1)^n - 1} \tag{7.19}$$

Based on the above parameters, the system sizing algorithm outputs are shown below in Fig. 7.6 for a single domestic load profile configured for a 70/30%, wind/diesel generation ratio (by setting the LPSP in Section 7.2.2 to 0.3 under the assumption that the load not met by wind energy is met by the diesel generator).

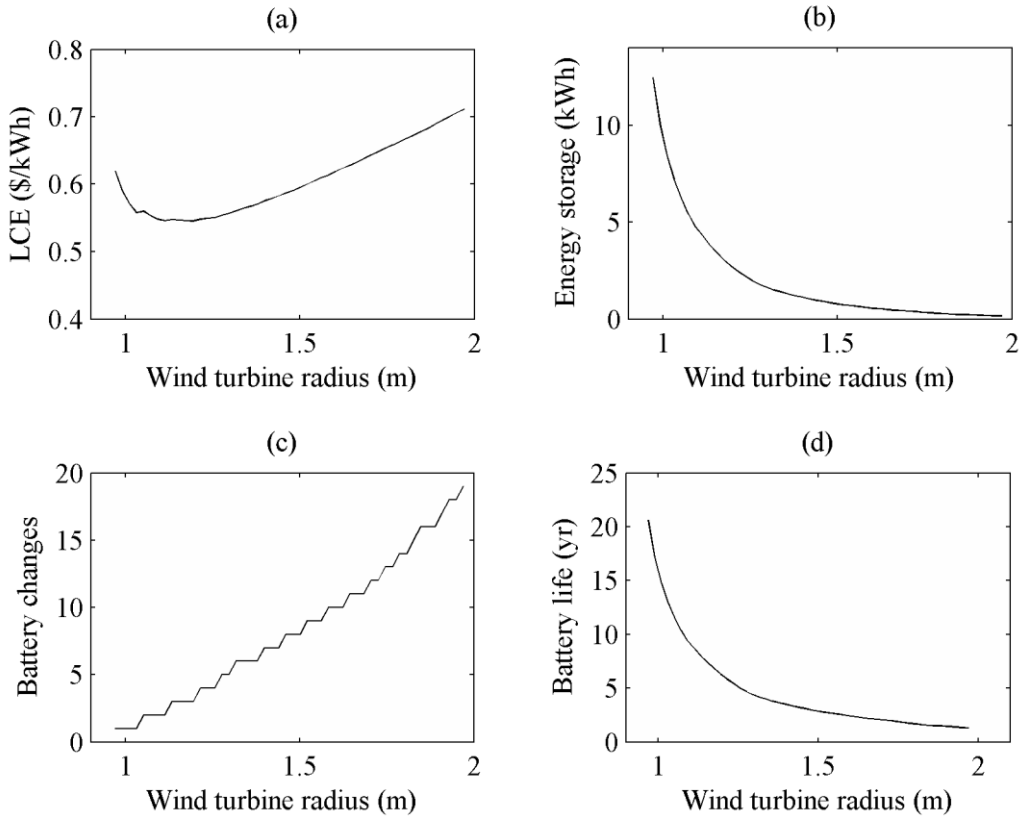

Fig. 7.6 System sizing results: (a) Levelised cost of energy (b) Required battery energy storage capacity (c) Battery changes (over the 25 year project life) (d) Estimated battery life.

Fig. 7.6 shows sample results from the techno-economic system sizing algorithm described in Fig. 7.4. The following modelling assumptions have been made:

1. A diesel generator is used to provide the energy that the wind turbine cannot provide (in this case 30% of total load).
2. The battery life modelling technique described in section 5.2 was used to estimate battery life based on the number of cycles counted.
3. The useable battery capacity was set to 80%.
4. The project life was set to 25 years.

Fig. 7.6 (a) plots the LCE vs. wind turbine radius determined using the techno-economic based optimisation algorithm (See section 7.2.2). Fig.s 7.6 (a) – (c) show sample results

from the optimisation procedure. Fig. 7.6 (b) shows the energy storage required to support the load plotted against the wind turbine radii in the search space. Fig. 7.6 (c) shows the number of battery changes required for each of the wind turbine radii in the search space and Fig. 7.6 (d) shows the results of battery life modelling using the cycle counting method described in Section 5.2. It can be seen that the energy storage requirement decreases as the wind turbine radius is increased but that the expected battery life also decreases as the wind turbine radius is increased. This is attributed to the energy storage system undergoing a higher number of cycles at higher depths of discharge as the energy storage capacity is decreased.

Fig. 7.6 (a) shows the system LCE variation with wind turbine radius for a single off-grid load configured for 70% wind energy and 30% diesel back-up generator. The optimal configuration can be found by determining the required radius from the minimum point on the LCE vs. radius graph Fig. 7.6 (a) and using the energy storage vs. radius plot Fig. 7.6 (b) to find the required battery energy storage rating. In this case, the optimal wind turbine radius (based on the combination of wind turbine capacity and battery capacity which has the lowest LCE) can be seen from Fig. 7.6 (a) to be ~1.2m. The corresponding optimal battery capacity can be found from Fig. 7.6 (d) to be approximately 7kWh.

7.3 Introduction to Simulations

Having determined an optimal combination of wind turbine and battery capacity rating using the above algorithms, to assess the long-term benefits of the energy storage systems developed, the models described in Chapters 2–6 were employed in a Matlab/Simulink simulation capable of a temporal resolution of the order of one second and simulation intervals of up to one year. The simulation run time using a 64 bit

Matlab distribution was approximately 5 minutes for a week long simulation at 1s sample resolution. This is significantly less than a corresponding switching model implemented in SimpowerSystems. These requirements came about from the need to capture short–term charge discharge cycles over which the supercapacitor energy storage was shown to be effective. It was necessary to do this over relatively long simulation periods to be able to realistically incorporate the effects of seasonal wind variations. A top level diagram of the main simulation tasks is shown in Fig. 7.7.

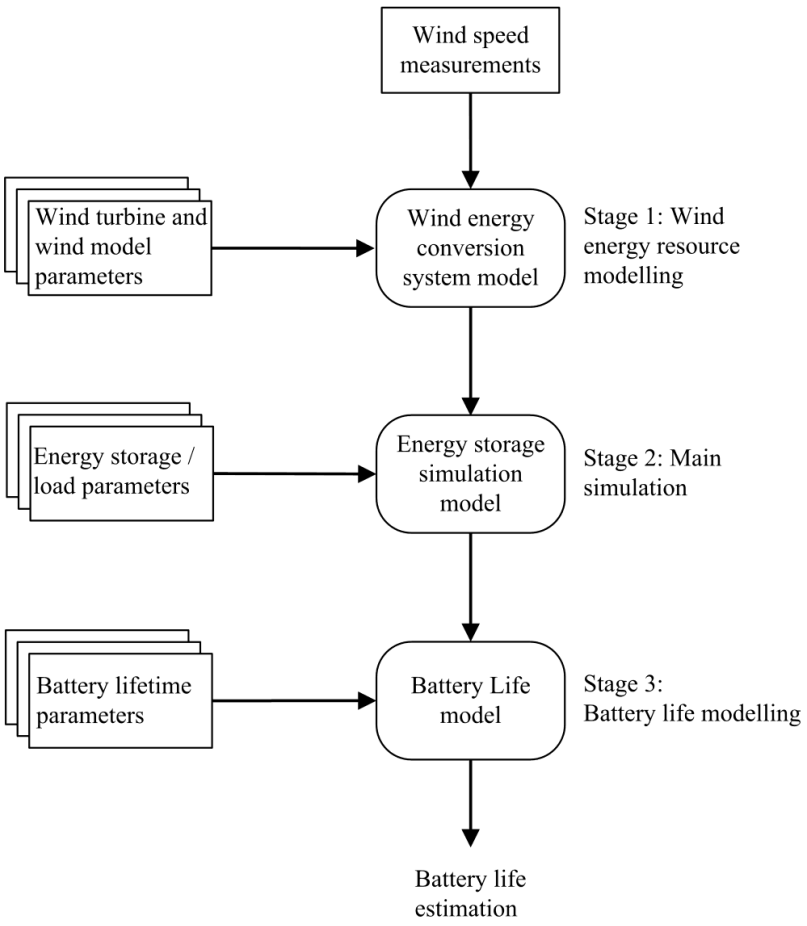

Fig. 7.7 Top level simulation system diagram

The simulation strategy consists of a pre-processing task used to determine available power in the wind over the course of the simulation period, based on the modelling procedures described in Chapters 2 and 3. The major input to this stage was a time series consisting of real meteorological wind speed data at nominal sampling intervals

of 1800s. The wind turbulence model described in Chapters 2, section 2.3.1 and the wind turbine model described in Chapter 3, section 3.2.5 were used to develop a time series of wind turbine output power. The next modelling stage shown in Fig. 7.7 consists of the main simulation stage, which was used to test and optimize the energy storage control algorithms. In this stage, the energy storage state-of-charge variations were determined by implementing the battery and supercapacitor models described in Chapter 4 sections 4.2.2 and 4.4.1 and the DC/DC model converter described in Chapter 6 section 6.4.3. The combination of these models was used to simulate battery state-of-charge variations with and without the supercapacitor energy storage system under the control strategies described in Chapters 8 and 9. Finally, the battery state-of-charge data are then passed to the third simulation stage to evaluate the performance of the algorithms developed, using the battery lifetime estimation model described in Chapter 5 section 5.2.3.

A review of previous work has indicated the potential benefits of a power-filtering control approach to the real-time management of power in the hybrid energy storage system, without providing numerical results. In addition, the implementation aspects of a system operating in this way are not well reported. For this reason, Chapter 8 demonstrates the operation of a low pass filter-based hybrid energy storage system control approach used to effectively filter the fluctuating power supply to the battery by experiment. New simulation results are then presented based on a representative week-long simulation period (of load and wind data), confirming the benefits of this strategy due to a reduction in battery charge/discharge cycles. A second, simplified simulation is then considered which demonstrates the general trend of the detrimental effects of turbulence intensity on battery life. An investigation into the degree of hybridisation with an additional supercapacitor storage device then demonstrates a relationship

between the low-pass filter controller time constant, turbulence intensity and battery life in the simplified system under consideration.

One of the objectives of the project has been to explore novel control strategies for the distribution of power between the energy storage systems within the hybridised energy storage device. In chapter 9, a review of the technical difficulties in charging lead-acid batteries in renewable power systems is presented, revealing how battery charge regulation strategies are rarely compatible with intermittent power charging. It has been shown that many real wind-energy systems of the class considered here can suffer from reduced energy capture due to turbulent wind-speed variations due to battery voltage stability effects. With this in mind, a novel control strategy was developed and is described in Chapter 9 (Section 9.3.1), employing a supercapacitor energy storage device to maintain battery voltage grid stability. Hardware results are presented confirming the operational feasibility of the approach and its performance. Simulation results are presented demonstrating benefits in terms of increased energy capture and reduced battery depth of discharge. This strategy was then extended using a real-time, dynamically re-configurable controller which combined both the voltage control and low-pass power-filter approach described in Chapter 8 which was found to increase the estimated battery life further.

7.4 Discussion and Summary

This chapter has considered optimisation of battery and wind turbine capacities, based on technical and economic constraints and has provided a systematic method for sizing the system according to these constraints. The development of an in-depth techno-economic optimisation procedure was beyond the scope of this study. However the technique presented can be used as a starting point to determine a reasonable combination of system component ratings.

The framework for the simulation and modelling strategies used to develop the control algorithms as part of this research has been introduced. This consists of a three-stage process with decoupled modelling stages for the wind-energy conversion system, energy storage systems and battery lifetime estimation.

Chapter 8: Supercapacitors for Power Filtering

8.1 Introduction

This chapter reviews the potential benefits of using a supercapacitor energy storage device to minimise the power fluctuations experienced by the storage battery in an off-grid wind-energy system. A novel hardware implementation of an actively controlled supercapacitor, optimised to mitigate high frequency current-fluctuations is described and the operational feasibility of the design confirmed by experimental results. Simulation results are then presented which demonstrate a predicted increase in battery cycle-life by use of the hybridised system under the proposed form of control.

One of the similarities between previous studies in the hybridisation of battery and supercapacitor energy storage systems for renewable energy applications [48-51], [54], [157] has been the underlying objective of an improvement in battery life without a quantifiable means by which this benefit can be proven. The results presented in this chapter extend previous studies by emphasising the benefits of the control approach in terms of a quantifiable increase battery cycle-life, by describing a method by which the cycle-life in the battery-supercapacitor hybridised system can be evaluated by simulation and a novel means by which the system can be implemented and tested in hardware.

8.1.1 Approach Outline: Active Current Control

The basis of the control strategy presented in this section is that the battery is charged/discharged with the low frequency component of the net power (wind power – load power) while the supercapacitor is used to supply the remaining high frequency component. The means by which this is achieved is based on a novel current filtering approach to distribute the respective high and low frequency components of the available system power balance to the battery and supercapacitor in real-time.

The proposed configuration is as shown in Fig. 8.1 in which the supercapacitor is connected to the battery by the hysteretic current controlled converter in an active shunt configuration. The battery voltage is used as the effective DC bus voltage as is frequently the case in small-scale off-grid applications [158-161]. The controller continuously monitors the current I_{net} and sets the converter current reference signal, I^* to cancel the high-frequency component of I_{net}. The modified battery current thus comprises the remaining low-frequency component of I_{net}. The operation of the control system and converter is similar to a shunt-connected active current filter used as is frequently employed in active power filtering for power quality applications [162-164]. In previous studies in power filtering for power quality applications, the hysteretic current control strategy has been shown to perform well in comparison with other techniques [127] and to provide active power filtering in both steady state and transient conditions [165].

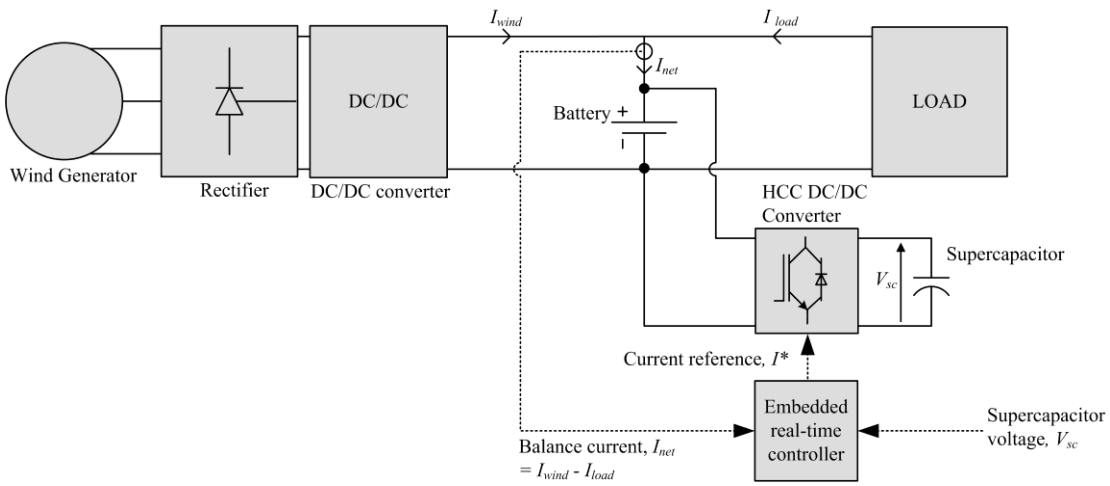

Fig 8.1 Proposed Active Current Filter Implementation

An alternative system configuration could involve the load and wind generator output converter connected to the supercapacitor terminals with the battery connected via the DC/DC converter. However, advantages of the Fig. 8.1 configuration are that the voltage at the interface to the wind charge controller and the load inverter is the battery voltage and therefore this configuration can be easily integrated into existing systems designed to operate with standard battery voltages. With the supercapacitor connected at the load, the considerably larger voltage swing of the supercapacitor may cause implementation issues limiting its application in certain situations.

Self-discharge causes the supercapacitor stored energy to decay and any further offset occurring in the power delivered can cause the supercapacitor state-of-charge and voltage to drift. Consequently, the supercapacitor voltage can drift towards zero, or toward the maximum supercapacitor rated voltage. To prevent this arising, an outer supercapacitor voltage control loop with an empirically determined, low static gain k was used to maintain the supercapacitor voltage about a nominal level, V_{sc}*. The control strategy block diagram used in this application is shown in Fig. 8.2.

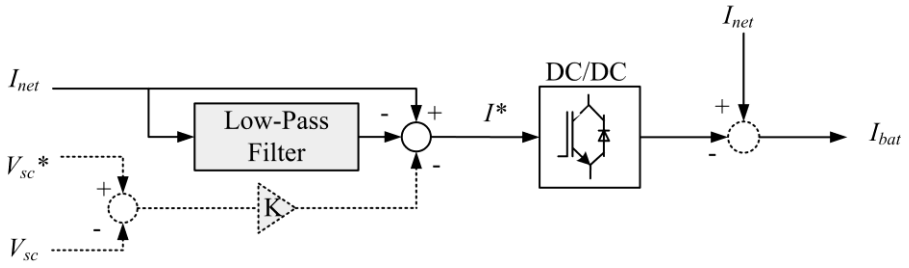

Fig 8.2 Low pass filter control algorithm

8.2 Hardware Validation

This section describes the experimental procedure used to confirm the operation of the active current-filter control strategy previously described in Section 8.1.1 under the complex duty cycles representative of an off-grid wind power system.

8.2.1 Hardware Test System Description

Since a suitable wind turbine system was not available for functional testing of the systems developed, a wind turbine and load emulator was constructed capable of delivering a pre-programmed current to the hybrid energy storage system as shown in Fig. 8.3.

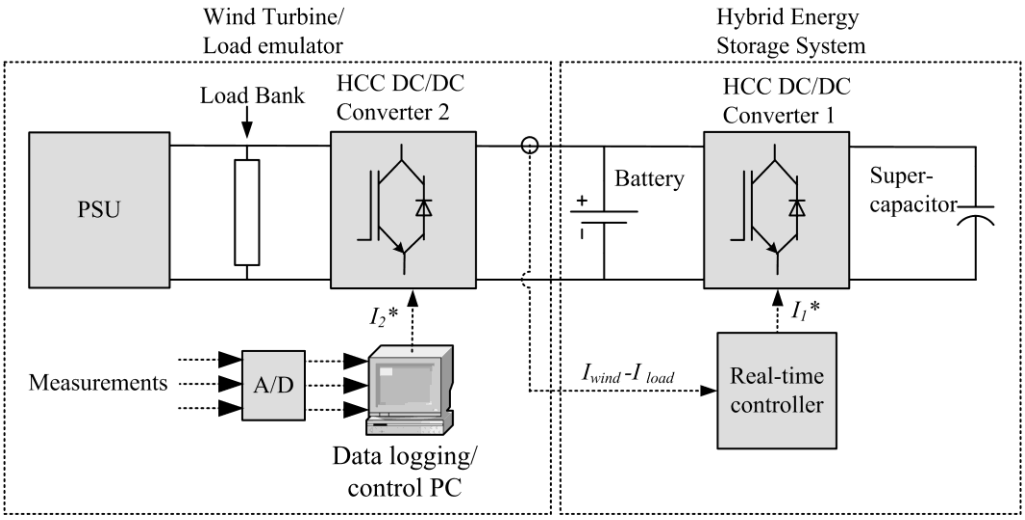

Fig. 8.3 Wind turbine emulator and hybrid energy storage laboratory test system configuration (HCC: Hysteretic current control).

The wind turbine emulator block consists of a D.C. power supply supply [166] acting as a source of power and a shunt-connected load bank acting as a power sink. Since the results presented in Section 6.4 have shown the hysteretic controlled bidirectional converter can achieve good current tracking capability, a second converter based on this design was used to control the flow of power to/from the energy hybrid energy storage system under test. A PC running National Instruments Labview/Signal Express software was used to generate the current reference signal for the second DC/DC converter based on simulated wind/load power results and to log the measurements. In this way, for testing purposes, an arbitrary bidirectional current profile could be delivered to the energy storage system.

8.2.2 Current Filter Control Implementation

To investigate the operation and performance of the converter and control algorithm, a prototype test system was constructed consisting of four CSB [104] 12V, 75Ah sealed lead-acid batteries with a 24Vdc nominal bank voltage. The supercapacitor module was made up of twenty-two Maxwell [167] 2.7V/1800F supercapacitors giving a 60Vdc maximum rated voltage.

The control algorithm was implemented using a PIC18F4520 series micro-controller [168] to monitor the net current profile using a LA 100-P/SP13 current transducer (from manufacturer LEM [169]) rated at 100A, and then to calculate the required converter reference current in real-time. The controller program implementation uses an interrupt-driven sub-routine to sample the net charge current and calculate the low frequency content of the signal using a digital realisation of a first order low pass filter. Various low pass filter time constants were used in the range 10s – 500s. The difference between the current low-pass filtered value of the net current signal and the actual net current

value is calculated at each sample interval and represents the converter reference current signal. In this way, the converter current reference is set to cancel the high frequency component of the battery current in real-time. The analogue output of the D/A is then converted from a single ended, unipolar signal to a bipolar signal using operational amplifiers and is then used as the bidirectional converter reference current, I^* (see Fig. 8.1).

This implementation provided an easily re-configurable hardware platform for testing the current-filter control-scheme functionality and is shown below in Section 8.2.3 to be functional. However, areas of ongoing and future work include improving sampling resolution by use of a dedicated digital signal processing (DSP) controller and also a purely analogue implementation of the controller. The reason that a purely analogue implementation of the controller is considered as a potential area for future work is that it may prove to perform as well as a digital controller and cost significantly less.

8.2.3 Measured Results

Figs. 8.4 and 8.5 show the recorded experimental results of functional system testing of the hybrid energy storage system. In Fig. 8.4, the blue trace shows the net current, which represents the current-time profile that the battery would experience in a system employing only battery energy storage. The white trace shows the modified battery current in the hybrid system, which can be seen to follow the low-frequency component of the current profile and to contain significantly fewer current polarity reversals (charge/discharge cycles). In addition, the magnitude of the battery current peaks are considerably reduced by use of the proposed current filtering control.

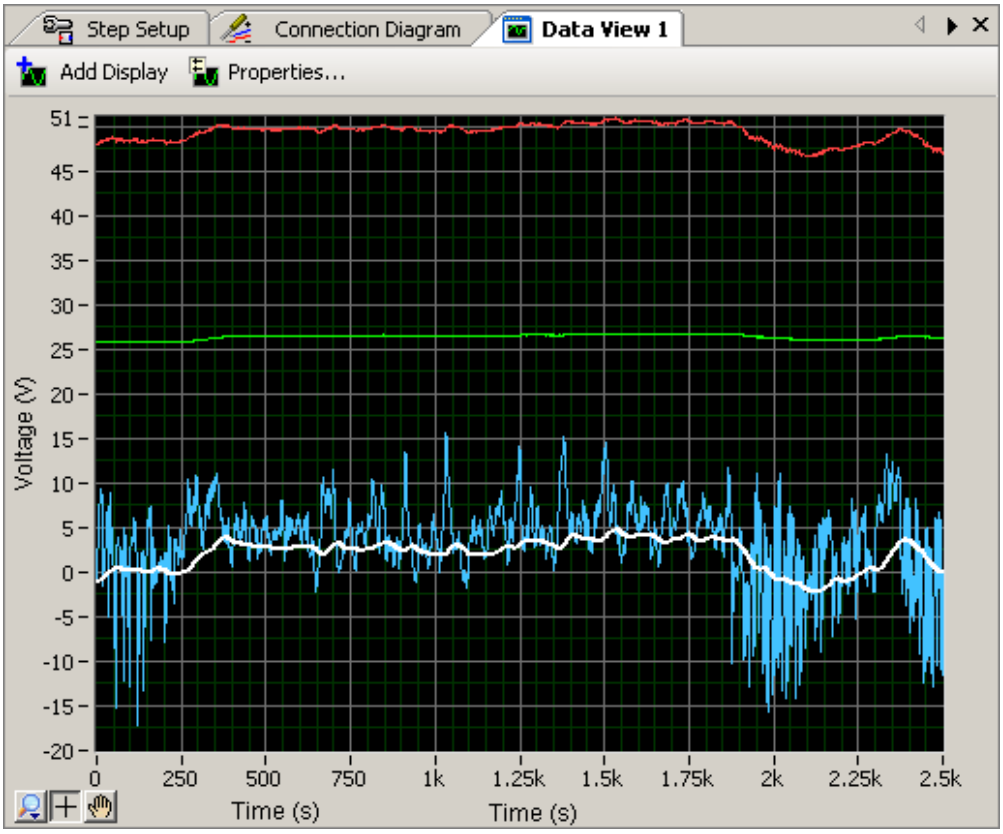

Fig. 8.4 Measured results vs time: Red trace: Supercapacitor voltage. Green trace: Battery voltage. Blue trace: Net current. White trace: Battery current (1V/Amp). Low pass filter time constant = 100s. Initial conditions: Supercapacitor SOC: 0.65. Battery SOC: 0.8. Positive current is charge polarity.

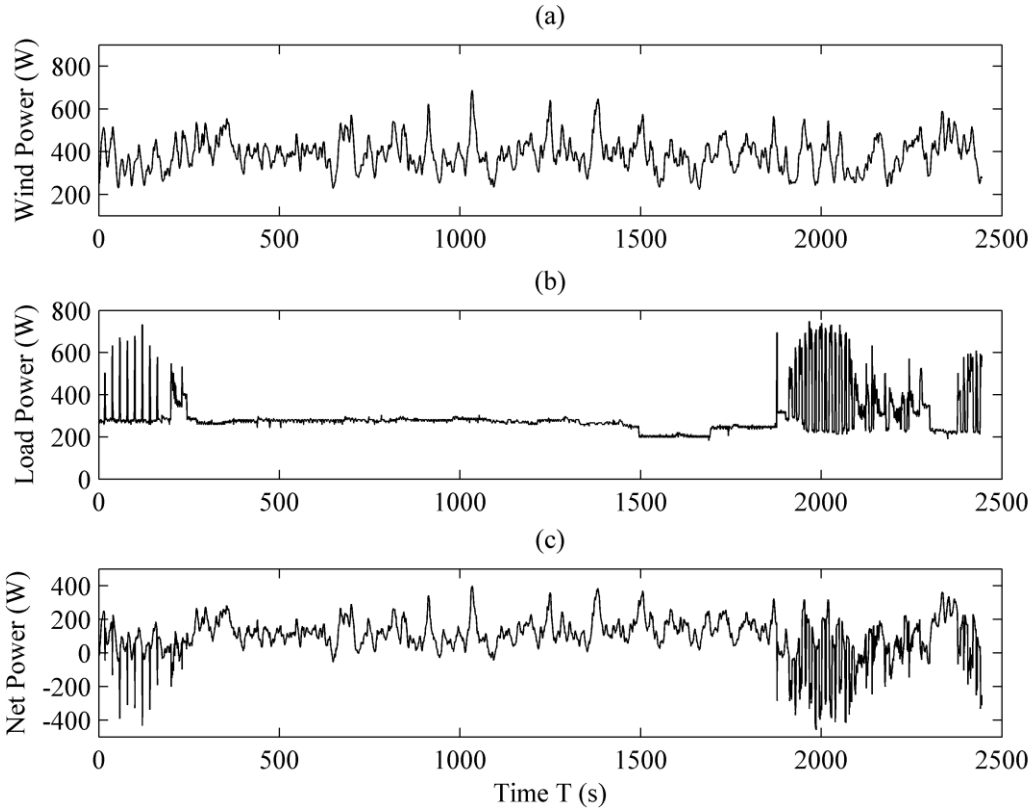

Fig. 8.5 Test inputs plotted vs. Time: (a) Wind power (b) Load power (c) Net power vs. Time

The relevant battery input data sets for the test in Figs. 8.4 are plotted in Fig 8.5. The simulated load profile Fig 8.5 (b) contains a series of current peaks intended to test the ability of the system to reject real-life dynamic current variations taken from recorded domestic load data. The turbulence intensity of the corresponding wind profile in Fig 8.5 (a) was set to 0.1.

8.2.4 Limitations of the Active Current Filter Approach

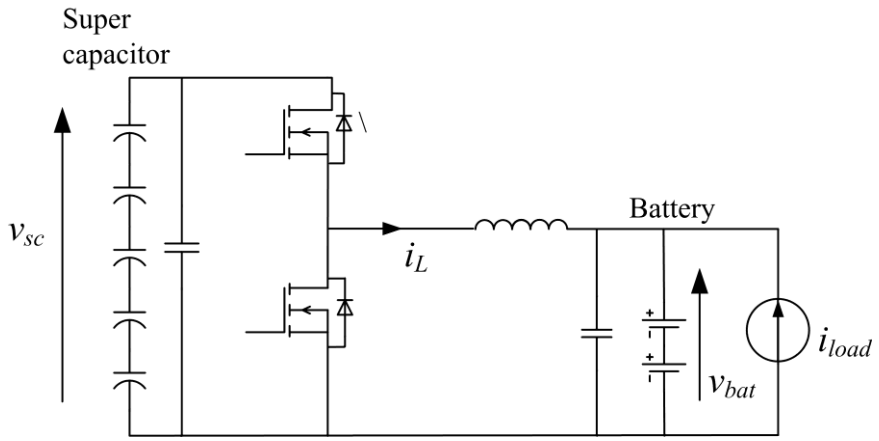

Fig. 8.6 Down-convert supercapacitor/battery interface

The main limitation of the use of a buck-derived topology in this case is that the supercapacitor voltage (on the high side) must be higher than the battery voltage (on the low side) for the converter to function. This limits direct application of the system to configurations in which the supercapacitor voltage can be maintained higher than the battery voltage. This also results in some unusable supercapacitor capacity as the supercapacitor can be discharged only until its voltage equals that of the battery. The following example demonstrates how the effects of this may be limited. Considering a system with a 120Vdc maximum supercapacitor bank voltage and nominal capacitance, C_{sc}, hybridised with a 24Vdc battery. The potential operating range of the supercapacitor is 24Vdc–120Vdc. In this example, the percentage un-usable supercapacitor energy, E_u, can be determined as follows:

$$E_u = \frac{\frac{1}{2}C_{sc} \cdot 24^2}{\frac{1}{2}C_{sc}120^2} \cdot 100 = 4\% \tag{8.1}$$

Here, the unusable supercapacitor capacity is 4% whereas in the case of a 48Vdc battery it would be 16%. A review of some recently published studies employing supercapacitor energy storage revealed the following supercapacitor operating voltage ranges have been used:

TABLE 8.1 SUPERCAPACITOR OPERATING VOLTAGES USED IN RECENT STUDIES.

Reference:	Supercapacitor operating voltage range
[170] C.M. Krishna.	0.75 - 2.75 V/cell
[171] Murray et al.	125 – 250 V
[172] Brouji et al.	0.5 - 2.5 V/cell
[173] Lu, Zhu and Tian.	160 - 320 V
[174] Tan et al.	190 – 320 V
[175] Bae et al.	105V – 125 V

A restricted operating range, limited at the lower end is common to all of the above examples and, in most cases, the limitation is more restrictive than in the example system [Eq (8.1)].

Realistically, the choice of a buck-derived converter limits direct application of this system to low voltage battery grids, to prevent the unusable supercapacitor capacity from becoming too high. Direct application areas include in small-scale distributed generation systems applications [158-161] and remote telecoms applications [68-70] which typically employ 48Vdc networks [68], [69].

To address this limitation the proposed system was reconfigured to allow battery grid voltages higher than that of the supercapacitor bank, thus allowing higher power applications to be considered for a given current rating. The proposed control system

was re-designed such that the battery could be connected on the high side and the supercapacitor on the low-side as described below in section 8.2.5.

8.2.5 Current Filter Control for Higher Power Applications

Section 6.2 has shown how the inductor current can be tightly regulated using hysteretic current control. To control the output current on the high side of the half bridge converter as shown in Fig. 8.7 by means of the inductor current, the inductor current to output current relationship must be considered.

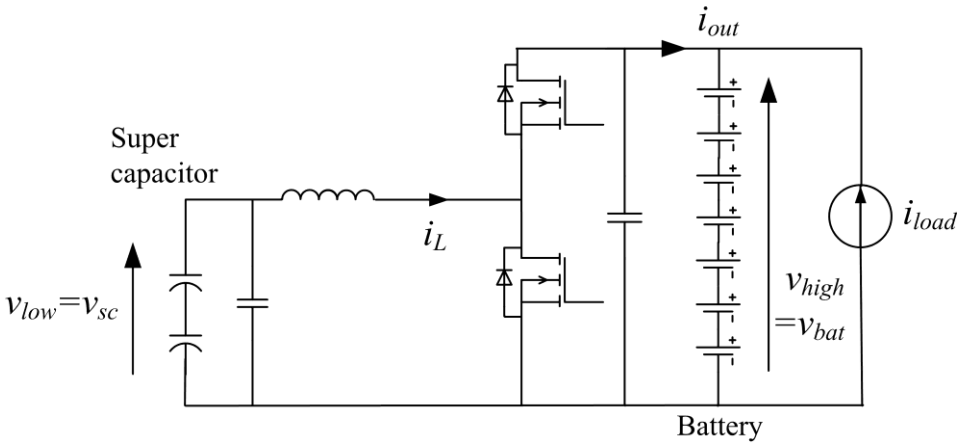

Fig. 8.7 Up-convert supercapacitor/battery interface

Erickson has shown that under steady state conditions the inductor current to output current relationship can be expressed as follows [176]:

$$i_{out} = i_L \frac{v_{low}}{v_{high}} \eta = i_L D' \eta \ \text{(A)} \tag{8.2}$$

where η is the efficiency of the converter and *D'* is the reciprocal of the voltage conversion ratio.

Initially, attempts were made to control the output based on an estimation of the ratio *D'* and the efficiency η product then setting the required inductor current according to Eq.

(8.2). However, Sections 6.5 has shown how the converter efficiency varies with frequency. In addition, this efficiency term is highly non-linear and dependent on temperature making its determination difficult in real-time for control purposes. So a suggested control approach is to use a feed-forward estimate of the required inductor current based on Eq. (8.2) and to use a feedback compensator such as a PI controller to remove any residual error as shown in Fig. 8.7 (a).

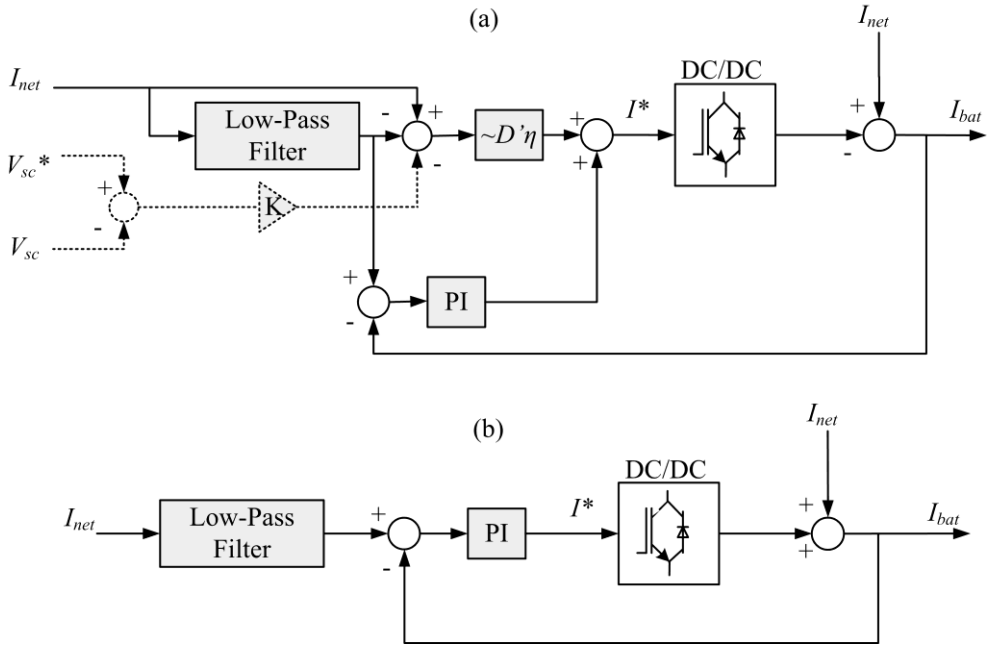

Fig. 8.8 (a) Suggested output current control (b) Implemented output current control

To validate the principle of operation of the system in Fig. 8.7, the simplified control of Fig. 8.8 (b) was used for functional testing as the feed-forward design in Fig. 8.8 (a) could not be implemented due to time constraints. The results of high-power testing using a 96Vdc nominal battery bank on the high side and the same (<60Vdc) supercapacitor module used in Sections 8.2.2-8.2.3 connected on the low side are shown below in Fig. 8.9.

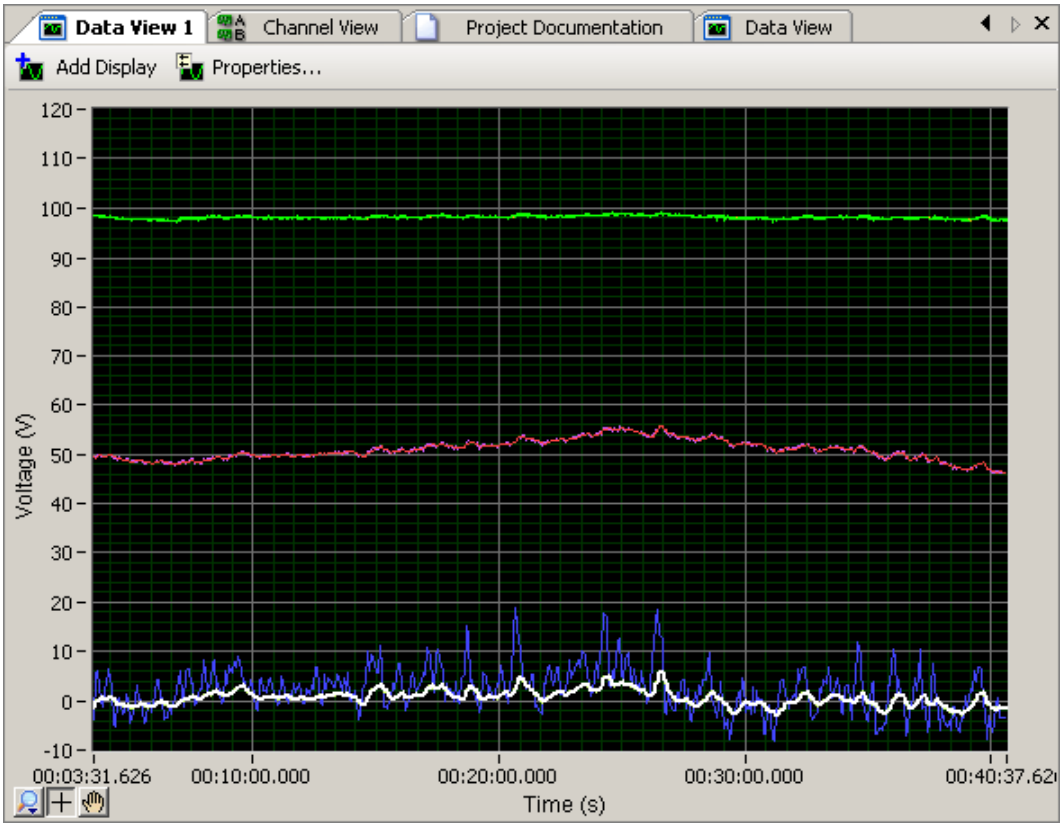

Fig. 8.9 Results of current filter control with battery bank on the converter high-side. Low pass filter time constant = 100s. Green trace: battery voltage. Red trace: Supercapacitor voltage. Blue trace: Net current measurement (1V/Amp) White trace: Battery current measurement (1V/Amp). Supercapacitor SOC: 0.69. Battery SOC: 0.85. Positive current is charge polarity.

The battery voltage was configured to be 96Vdc nominal and the system current rating was limited to approximately 20A as before. By doing this the test system power rating was increased by a factor of 4. To design the PI controller in this case the assumption was made that for frequencies well below the switching frequency (~20kHz) the inductor current tracks the reference current perfectly as has previously been made by the authors in [177]. Olivier [178] has shown that for this approximation to be effective, the switching regulator switching frequency must be considerably higher than the system dynamics. With this in mind, the control bandwidth was designed to be very much lower than the minimum expected switching frequency [calculated using Eq. (6.5)]. In addition, the inductor current slew-rate limits the achievable bandwidth as shown in Appendix 1, so the control bandwidth was designed to be less than this limit

also. A more rigorous analysis of the characteristics of the control systems in Fig. 8.8 and an investigation of the relative merits of the feed-forward approach in Fig. 8.8 (a) over the system in Fig. 8.8 (b) will be the subject of future work as time constraints prevented further analysis in this area.

8.3 Single Domestic Off-Grid Load Simulation

The first simulation carried out was based on the case study of a single off-grid load operating solely from wind-energy. This section describes the system and results obtained.

8.3.1 System Description

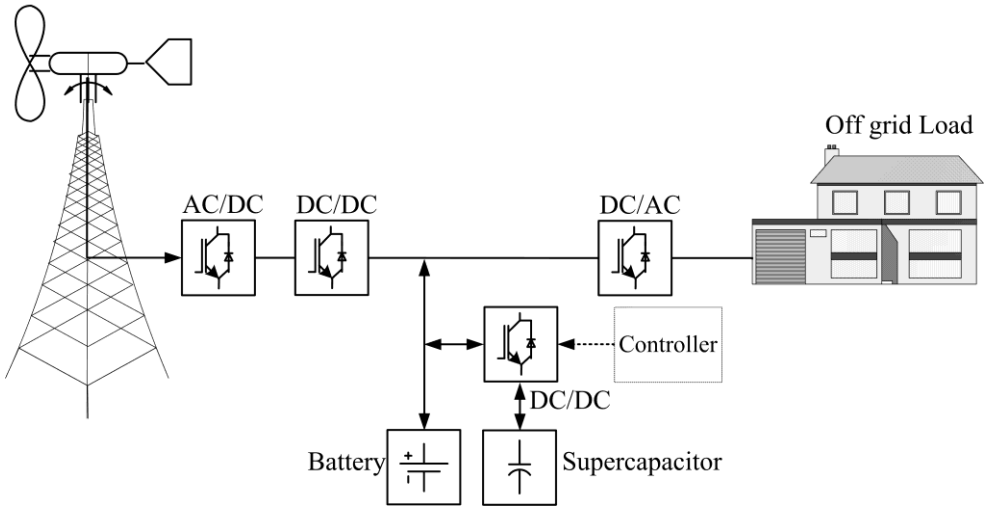

Fig. 8.10 Case study 1: Single domestic off-grid load

To determine the performance of the proposed system by simulation, a low power (<5kW) wind energy conversion simulation system as shown in Fig. 8.10 has been implemented using the models described in Chapters 2-4. The AC voltage generated by the wind turbine is rectified and fed to the battery and load via a DC/DC converter under maximum-power-point tracking control such as described by de Broe et al [87]

(see Section 3.2.5). A DC/AC power converter is used to the convert the battery DC voltage to single-phase AC in the case of an AC load. The battery voltage has been assumed to be 24Vdc nominal and connected on the low-side of the converter. Relevant application areas include small-scale distributed generation systems [158-161] and remote telecoms applications [68-70].

Conventional simulations employing mean data (measured at 10min–1hr intervals) for renewable resource patterns have been shown to cause short-term fluctuations and associated charge/discharge cycles to be ignored, resulting in underestimation of battery throughput and associated wear as pointed out by Ruddell et al. [125]. For this reason, the simulation was carried with higher sampling rates of >1Hz using a week of representative wind and load data. The load profile was based on the single-user domestic load profile described in Section 3.3.1. The wind turbine model was based on a commercially available unit as described by Sambatra et al [179] and the corresponding wind turbine generator parameters are shown in Table 8.2.

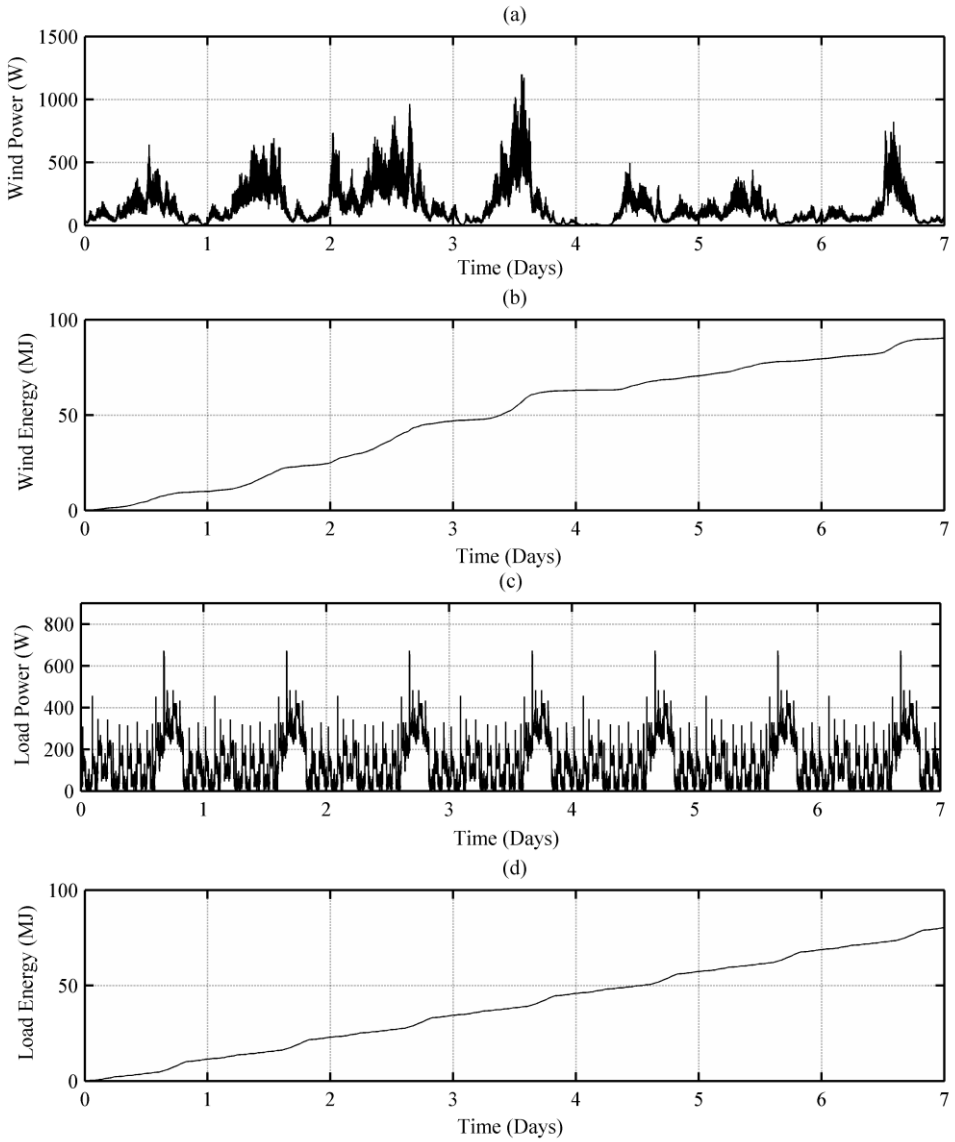

Fig 8.11 Case study 1: (a) Wind-power profile (b) Wind Energy (c) Load-power profile (d) Load Energy

Table 8.2: Wind turbine model parameters [179].

Parameter	Description	Value
R	Blade radius	1.3m
J_{wt}	Turbine rotor moment of inertia	1.5kg/m^2
J_{elec}	Generator moment of inertia	0.5kg/ms^2
D'	Damping coefficient	0.00035 Nm/rad/s

The required battery capacity was determined from the optimisation method described in Section 7.2.2. The battery parameters are given in Table 8.3 and are equivalent to a

series string of twelve 2v cells whose parameters have been determined and reported by Ceraolo [1]. The cell nominal capacity has been slightly modified to meet the battery sizing requirement. However it is not expected that this small change in cell nominal capacity would drastically change the remaining cell modelling parameters.

Table 8.3 Case study 1: Battery system modelling parameters [1].

Parameter	Description	Value
K_c	Empirical constant	1.177
ε	Temperature coefficient	1.29
θ_f	Electrolyte freezing temp.	-40 °C
δ	Empirical constant	1.4
E_{m0}	Full-charge rest voltage	25.62
R_{10}	R1 value at 100% SOC	8.4mΩ
R_{00}	R0 value at 100% SOC	24mΩ
Ke	Empirical constant	70.58 mV/°C
I^*	Reference current	49A
A_0	Empirical constant	-0.3
τ_b	RC branch time constant	5000s
C_0	Nominal capacity	280Ah

8.3.2 Simulation Results

A Simulink schematic of the simulation including the previously described models for the supercapacitor (Section 4.3.3), battery (Section 4.2.1), hysteretic-current controlled converter (Section 6.5.3) and proposed current-filtering controller (Section 8.1.2) is shown below.

To demonstrate the improvement in battery life achievable by use of the current filtering supercapacitor control strategy, the low pass filter time constant was set to 3600s initially. This is significantly higher than was used in the experimental results shown in Section 8.2 as the supercapacitor rating required to support a low pass filter time constant of 3600s was greater than the supercapacitor bank available for experimental tests.

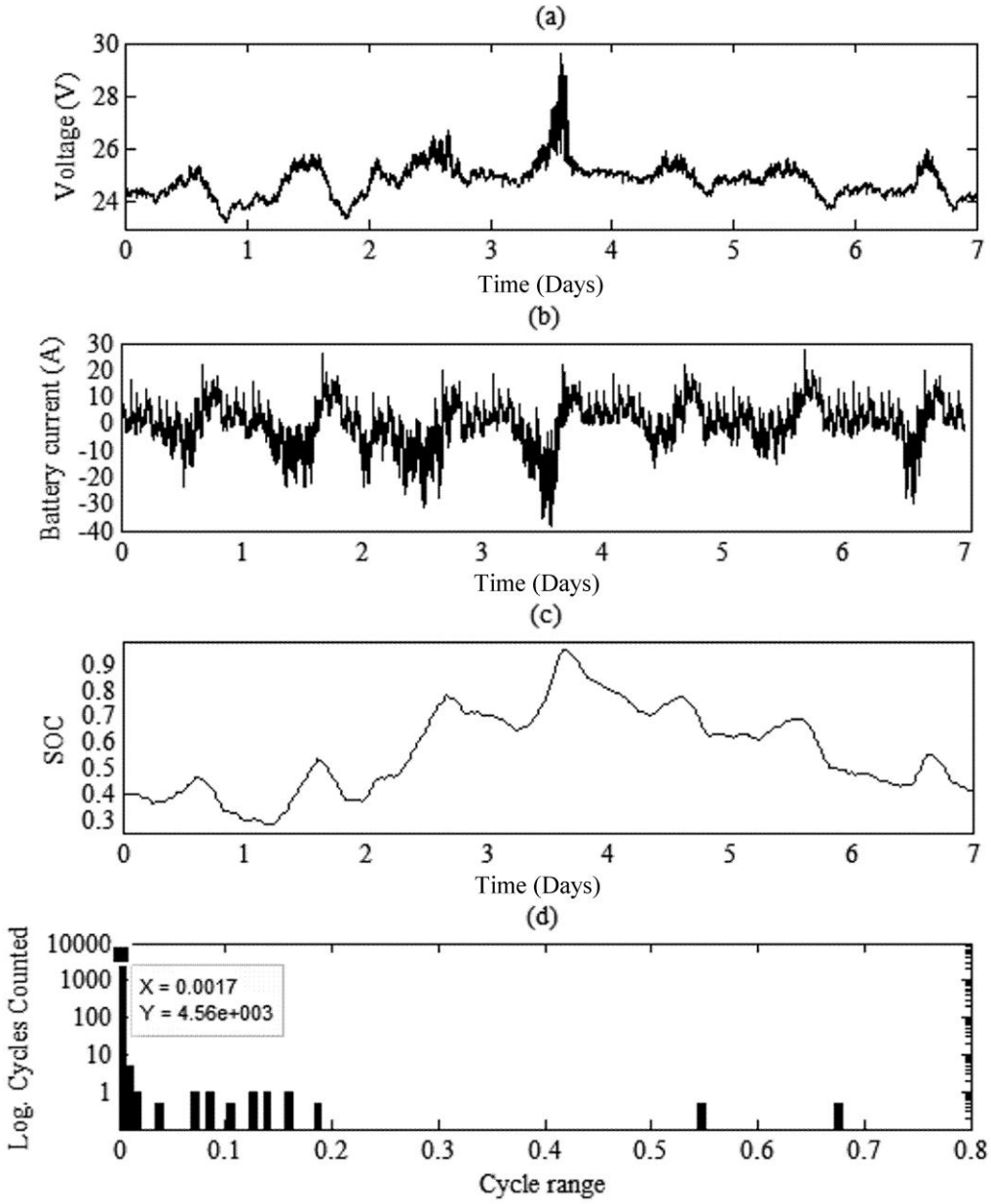

Fig. 8.12 Battery only system results: (a) Battery voltage (b) Battery current (c) Battery state-of-charge (d) Histogram of rain-flow cycles

Fig. 8.12 shows the results from the battery-only test case simulation. The simulation was then repeated with the actively-controlled battery/supercapacitor hybrid energy storage system, as shown in Fig. 8.13.

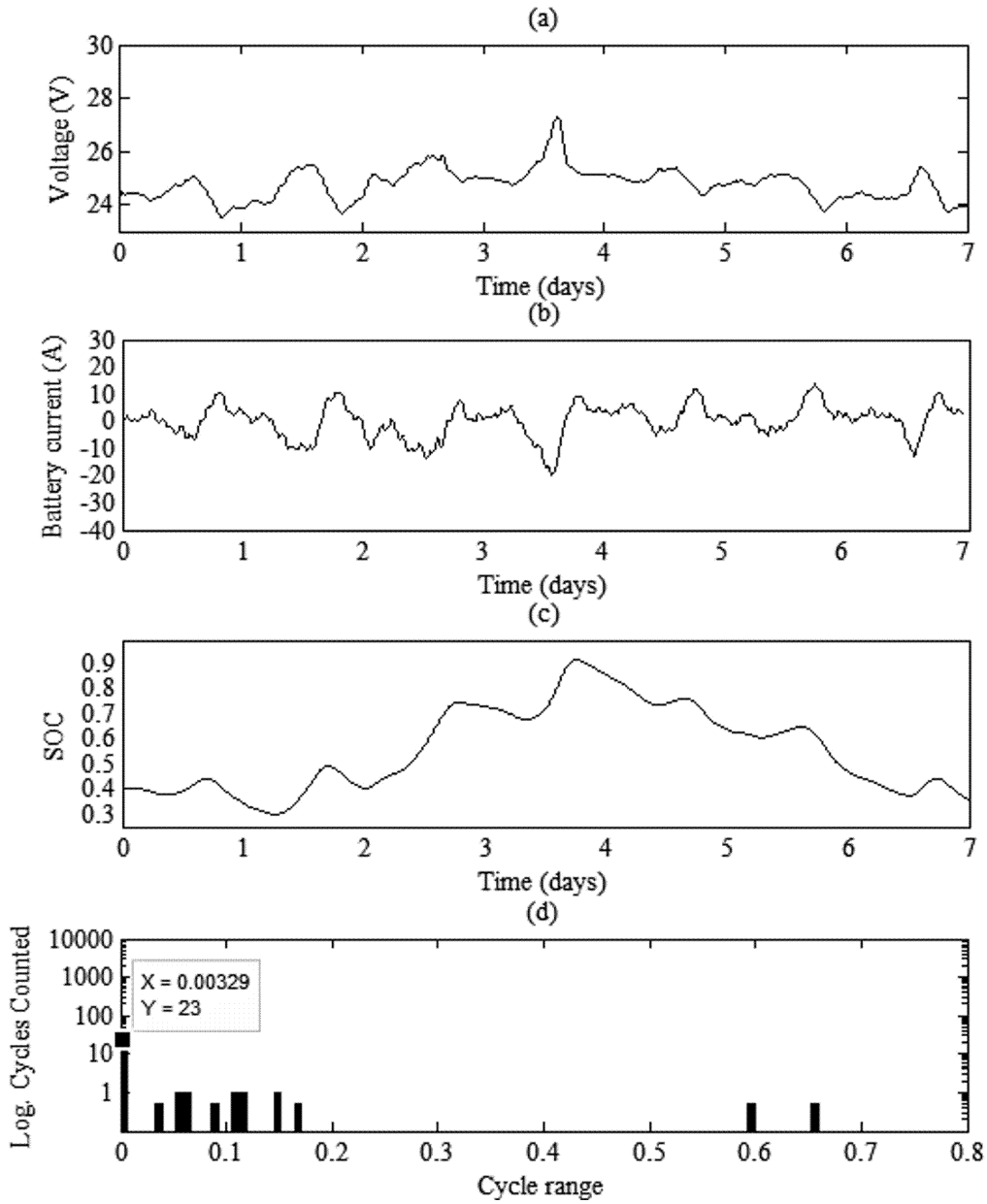

Fig. 8.13. Hybrid system results with low pass filter time constant = 3600s (a) Battery voltage (b) Battery current (c) Battery state-of-charge (d) Histogram of rainflow cycles.

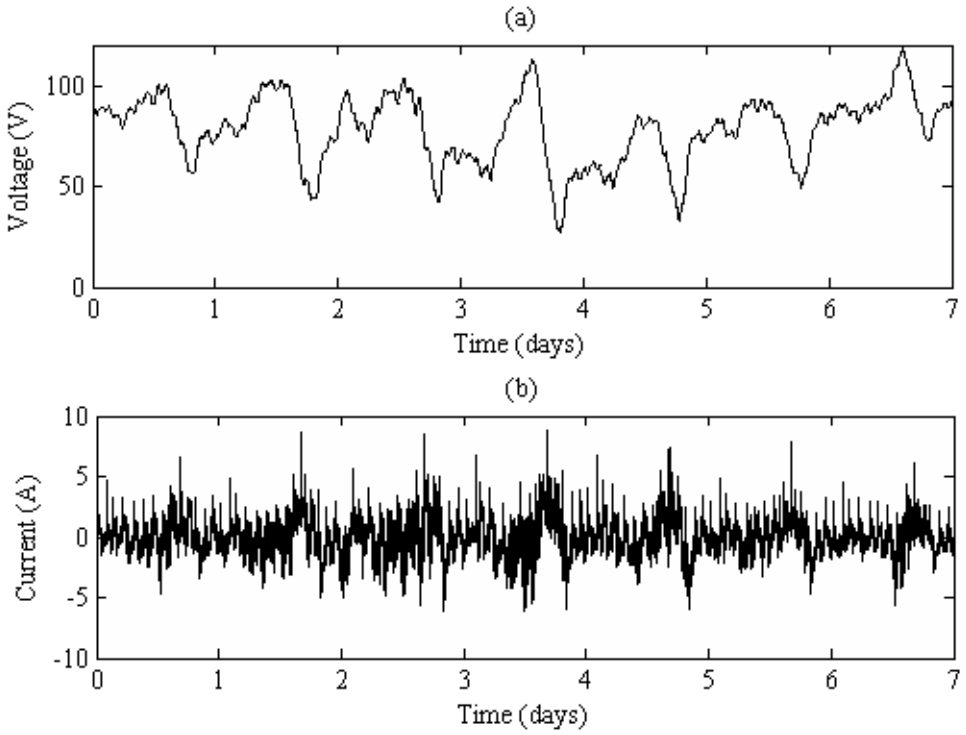

Fig. 8.14. Hybrid system results with low pass filter time constant = 3600s (a) Supercapacitor voltage (b) Supercapacitor current

The required supercapacitor capacity was found by integrating the simulated supercapacitor power signal over time and taking the peak to peak variation of the integrated energy signal to determine the required energy storage capacity. The commercially available supercapacitor cell [113] parameters shown in Table 8.4 were considered and configured to make up the required supercapacitor module capacity. For the above example in Fig.s 8.13 and 8.14, the required energy rating of the supercapacitor module was found to be 803 Wh or 160 cells of the type described in in Table 8.4.

TABLE 8.4 SUPERCAPACITOR CELL PARAMETERS [113]

Parameter	Description	Value
C_{cell}	Cell nominal capacitance	5000F
R_s	Series resistance (total)	0.33mΩ
R_{leak}	Leakage resistance	351.85Ω
V_{nom}	Rated cell voltage	2.7Vd.c.

8.3.3 Battery Cycle-Life Improvement

The battery current results in the hybrid system of Fig. 8.1 can be seen to undergo significantly fewer polarity reversals than in the conventional system results shown in Fig. 8.12. This is displayed in Fig. 8.15 below which overlays the battery currents in the battery-only [Fig. 8.12 (b)] and battery-supercapacitor [Fig. 8.13 (b)] for direct comparison.

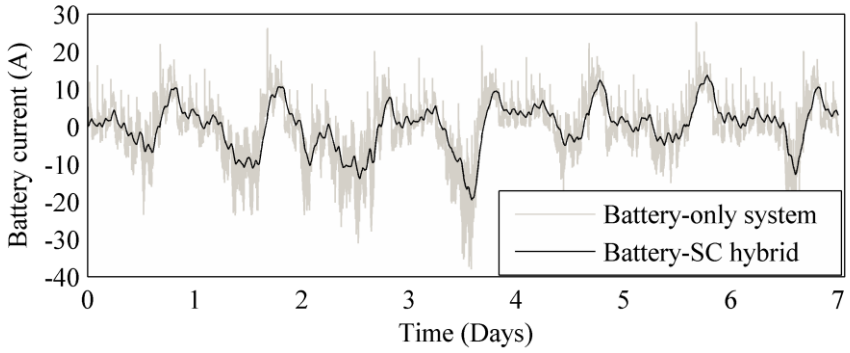

Fig. 8.15. Comparison of battery currents from the conventional battery-only system: Fig. 8.12 (b) and battery-supercapacitor system: Fig. 8.13 (b).

The results of rain-flow cycle counting show [see Fig. 8.12 (d) and Fig. 8.13 (d)] that the hybrid system undergoes extensively fewer short-range cycles in the proposed system: 23 as opposed to 4560 in the conventional system. The battery life estimation method described in Section 5.2.3 was used to determine the expected battery lifetime based on the results of rain-flow cycle counting. In the case of the battery-only system, the expected battery lifetime estimate is 7.4 years whereas in the case of the supercapacitor/battery hybrid system is 8.7 years with low-pass filter controller time constant set to 3600s. This corresponds to an increase in battery lifetime of ~18%. To achieve this, the required energy rating of the supercapacitor module in the simulation was found to be 803 Wh or 160 cells of the type described in Table 8.4 [113]. The

resulting battery cycle-life estimate is plotted for various other low-pass filter time-constant values as shown in Fig 8.16.

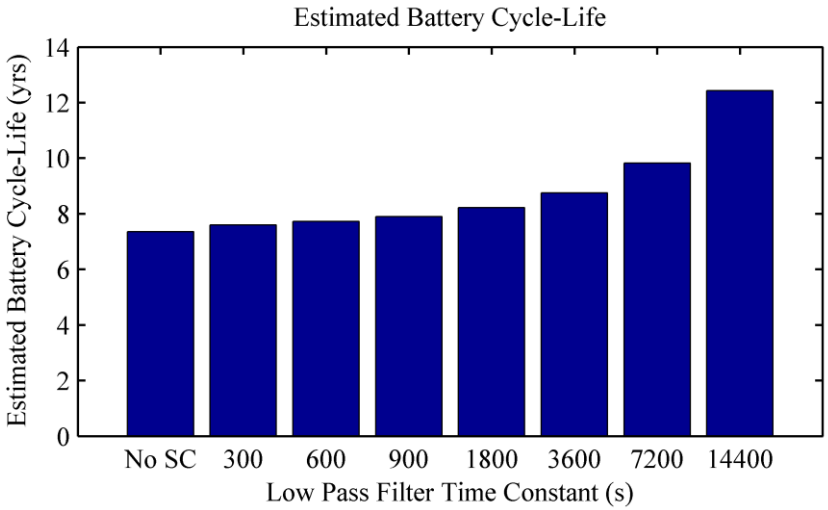

Fig. 8.16 Estimated Battery Cycle-life vs. Low Pass Filter Time Constant

8.3.4 Battery Current Peak Reduction

Comparison of the peak battery current in the hybrid system in Fig. 8.13 (b) with the peak battery current in the conventional battery-only system Fig. 8.12 (b) shows that another significant benefit of the proposed system is a reduction in peak battery discharge current. This decrease in current maxima has an un-modeled benefit in terms of further reducing battery-stress as high-current cycling has been shown to increase battery failure rates [54], [180].

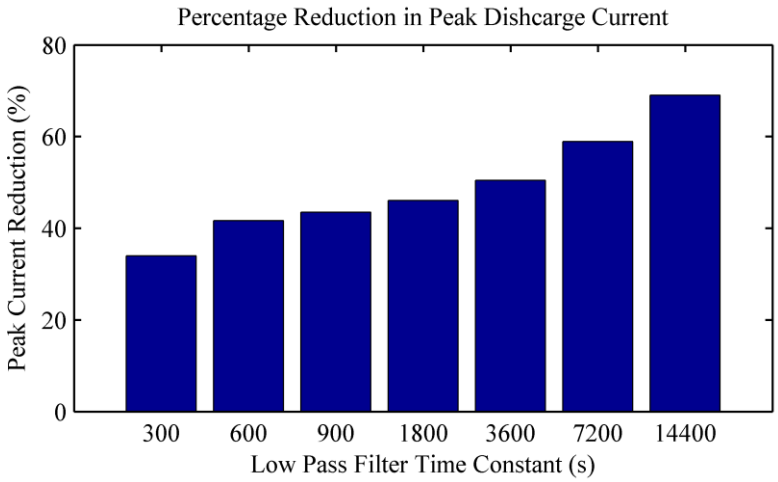

Fig. 8.17 Percentage reduction in Peak Currents

8.3.5 Power Loss Analysis

The increase in simulated battery-life is at the expense of a decrease in overall energy storage efficiency. Although the supercapacitor itself is a higher efficiency device than most current battery technologies as stated in [181], in this application, the energy stored in the supercapacitor must pass through a power electronic interface each way during a cycle with consequent losses. In addition, the self-discharge rate of the supercapacitor (from Table 8.4) is significantly higher than that of the battery [from Eq.7.5)] causing a further decrease in the supercapacitor energy-storage efficiency.

In contrast, with a battery-only energy storage system, losses are primarily due to series resistance (I^2R losses) and parasitic reactions within the cell such as gassing. The total energy loss in the battery-only energy storage system was found to be 610.5Wh or 2.4% of the energy generated. The losses associated with the battery, converter and supercapacitor in the hybrid system employing a 3600s time constant low-pass filter controller were found to be 1036.7Wh or 4.1% of the energy generated. Fig. 8.19 shows how the losses are distributed within the hybrid energy storage system.

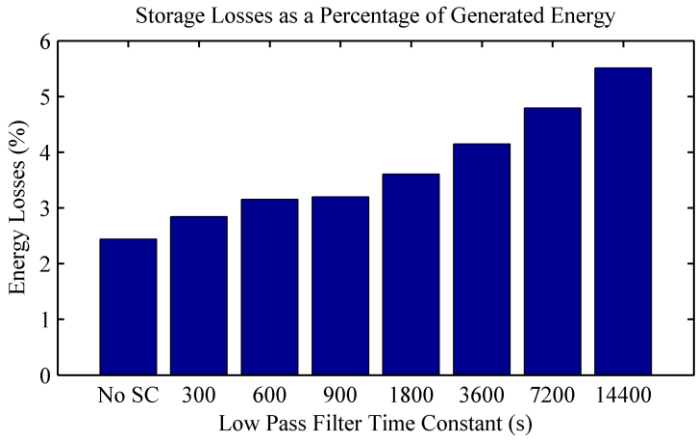

Fig. 8.18 Battery/Supercapacitor hybrid system losses

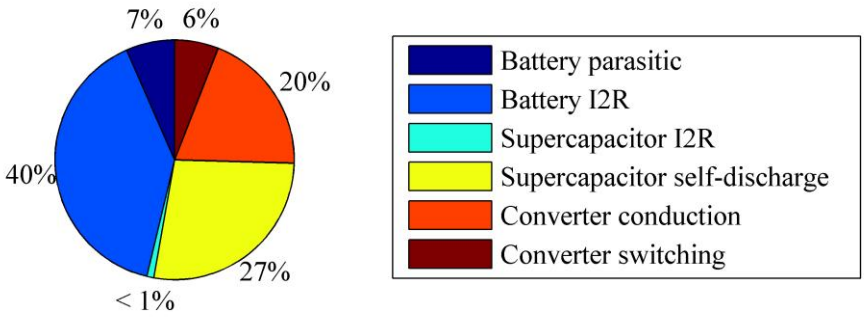

Fig. 8.19 Battery/Supercapacitor hybrid system losses. Time Constant = 3600s.

Quiescent power loss makes up a significant fraction of the total power losses. This quiescent loss estimation was based on the measurements from the prototype converter and it is expected that this could be improved by re-design of the converter gate drive. Optimisation of the gate drive circuit and control circuit of the DC/DC converter to reduce quiescent current losses remains the subject of ongoing work.

8.3.6 Required Supercapacitor Rating

In a recent article, Ball [43] has reported the cost per Farad and Joule of supercapacitors in recent years and these data have been converted to kWh and plotted as shown in Fig. 8.20.

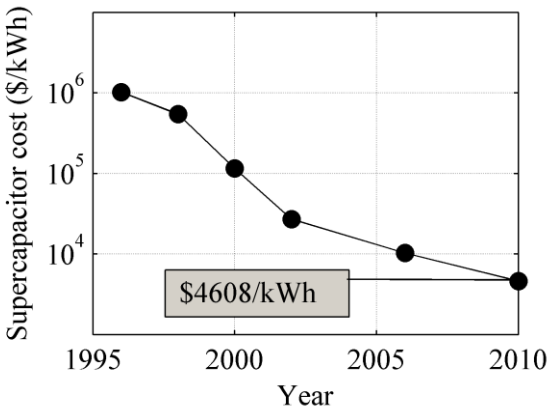

Fig. 8.20 Supercapacitor cost/kWh [182].

Increasing the low-pass filter time-constant of the current filter controller results in

greater supercapacitor energy variation and consequently the supercapacitor energy storage capacity must also be increased. The required rating and resulting cost of the supercapacitor energy storage, determined from Fig. 8.20 are plotted below in Fig. 8.21.

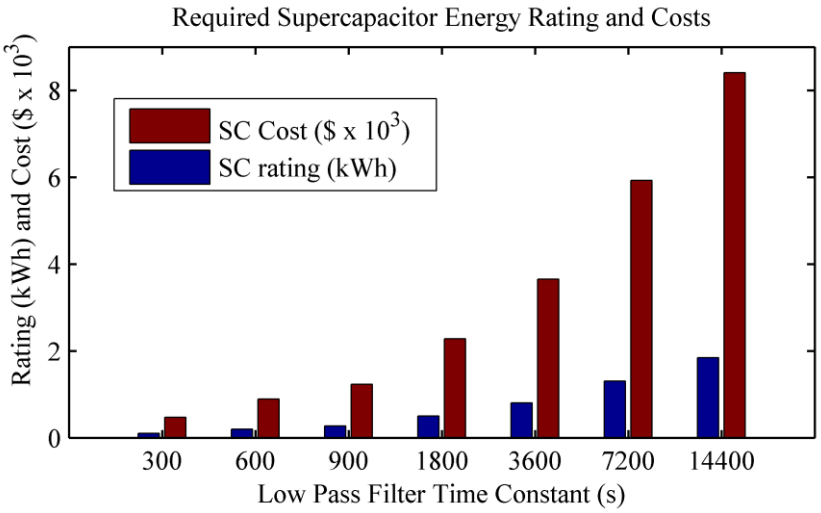

Fig. 8.21 Required Supercapacitor Rating and Cost.

From Fig. 8.21, the estimated savings due to the installation of the supercapacitor system can be calculated by determining the number of battery changes over the course of the project life of 25 years, nominally. The cycle-life of the supercapacitor was considered in each case from the supercapacitor energy throughput for the simulation period. The cycles-to-failure rating for cells of the type considered in this example is 500,000 cycles of 75% of the usable energy, equivalent to 50% of the usable voltage range. This can be used to determine the total-life energy throughput that the supercapacitor can provide by multiplying this figure by the rated usable energy of the supercapacitor. An estimation of supercapacitor life-fraction used in the simulation period was calculated by dividing the supercapacitor energy throughput over the simulation period total-life energy throughput. This allows an estimation of the cycle-life to be obtained as the reciprocal of the life-fraction multiplied by the simulation period length. In each case, the predicted cycle-life was significantly higher than the

design project life of 25 years. Assuming the supercapacitor and power electronic interface do not need replacement over the project life, and a simplified model for the cost of battery-ownership in which the battery-cost is simply the present-day initial cost and no salvage value is possible, then the potential savings can be considered as shown below.

Table 8.5 Case Study 1 Cost-Benefits Analysis

Time Constant (s)	Battery Changes	Battery Savings ($)	Supercapacitor Cost ($)	DC/DC Converter ($)
Battery-only system	3	0	0	0
300	3	0	2266	500
600	3	0	2800	500
900	3	0	3648	500
1800	3	0	4697	500
3600	2	1434	5928	500
7200	2	1434	8404	500
14400	2	1434	8892	500

In Table 8.5, it can be seen that configurations with 3600s, 7200s and 14400s low pas filter time constants result in one less battery change than the configurations with time constants: 300s, 600s, 900s, 1800s and the battery only system. The battery cost was calculated from the battery capacity (from Table 8.3) and the price/kWh of battery storage of 200$/kWh (see Table 7.2). The cost of the supercapacitor was taken as 4608$/kWh based on 2010 supercapacitor prices (see Fig. 8.18).

This simplified cost-analysis has not considered true life-cycle costs of the system components in detail due to time constraints and considers only initial component costs. Based on this, the system would be un-economical with 2010 supercapacitor prices as the expected battery savings are not greater than the expenditure on the supercapacitor and DC/DC converter. This may change if supercapacitor prices continue to drop as the trend in Fig. 8.20 indicates. The battery cycle-life benefit demonstrated in Section 8.3.3 can still become an economic advantage based on the cost-benefit figures in Table 8.5

in remote applications such as remote telecoms sites or remote rural communities where the cost of battery replacement is significantly higher than the battery cost/kWh, if access to the site is costly.

The above example has presented an analysis of a system operating at a relatively low turbulence intensity level of 0.1 in a scale of 0 to 0.5. If the site under consideration was at a location where the topographical and climatic conditions caused a higher general turbulence intensity level, then the number of charge/discharge cycles experienced by the battery is expected be higher. Recalling that Eq. (2.4) shows that turbulence intensity is a measure of the standard deviation of the wind speed, the implication of this is, that with a higher turbulence intensity, the resulting wind power will also exhibit more fluctuations and therefore cause more charge/discharge cycles when used to support a given load pattern. The system-level analysis in Section 8.4 has considered the effects of turbulence intensity on battery cycle-life in further detail.

8.4 Effect of Turbulence on Battery Cycle-Life

To consider the effect of turbulent wind variations on battery life, the following case study system-simulation was carried out based on the general case of a system in which the incident power to the battery is filtered by means of an additional actively controlled supercapacitor device, optimised to remove the high frequency content from the battery power profile. This approach has been proposed in a number of recent studies [28], [48-51], [54], [157] but the effects of the turbulence intensity on the battery/supercapacitor hybrid energy storage system have not been considered. For this reason the following section presents an analysis of the effects of turbulence intensity on battery cycle-life and presents results quantifying how an actively-controlled supercapacitor can mitigate the detrimental effects of turbulence on battery cycle-life.

8.4.1 System Description

The previous section illustrated the potential benefits of the hybrid energy storage system over the course of a representative week long simulation period. To evaluate possible benefits of the proposed super capacitor/battery hybrid energy storage system in the presence of seasonal wind variations, the simulation interval considered was one year. A case-study scenario was considered of a small microgrid as shown in Fig. 8.22 in which the load is supported by an alternative dispatchable power source such as a diesel generator during times of low wind power.

The load was assumed to consist of 8 relatively similar low-usage domestic loads. A simple aggregated load-model was developed by assuming that each daily load-cycle started at times staggered by 15 minutes within 2 hours of each other. The corresponding load-profile is shown in Fig. 8.23 (b) over the course of a week.

The techno-economic system sizing procedure described in Section 7.2.2 was used to configure the system for a 70% penetration of wind energy with the remaining energy requirement supported by a dispatchable diesel generator. The permissible battery state-of-charge operating-range was set from 1 (full) to 0.2 (80% depth of discharge) and the simplifying assumption was made that the generator does not charge the battery. The configuration with the lowest cost over the 25 year project life was determined to be a 3.13m radius wind turbine with a 33.2 kWh capacity storage battery. The wind-turbine model-parameters were based on the commercially- available Bergey Excel wind-turbine of similar radius as discussed in [183], [184] and which are given in Table 8.6 below.

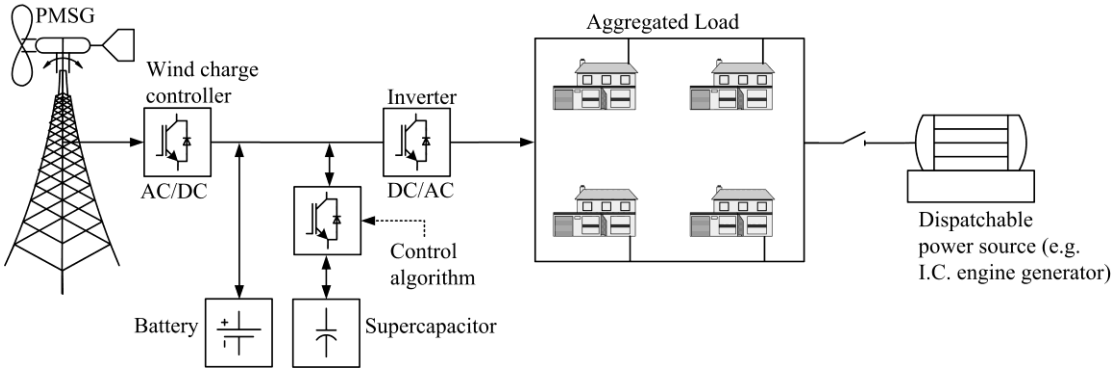

Fig. 8.22 Microgrid Case Study System.

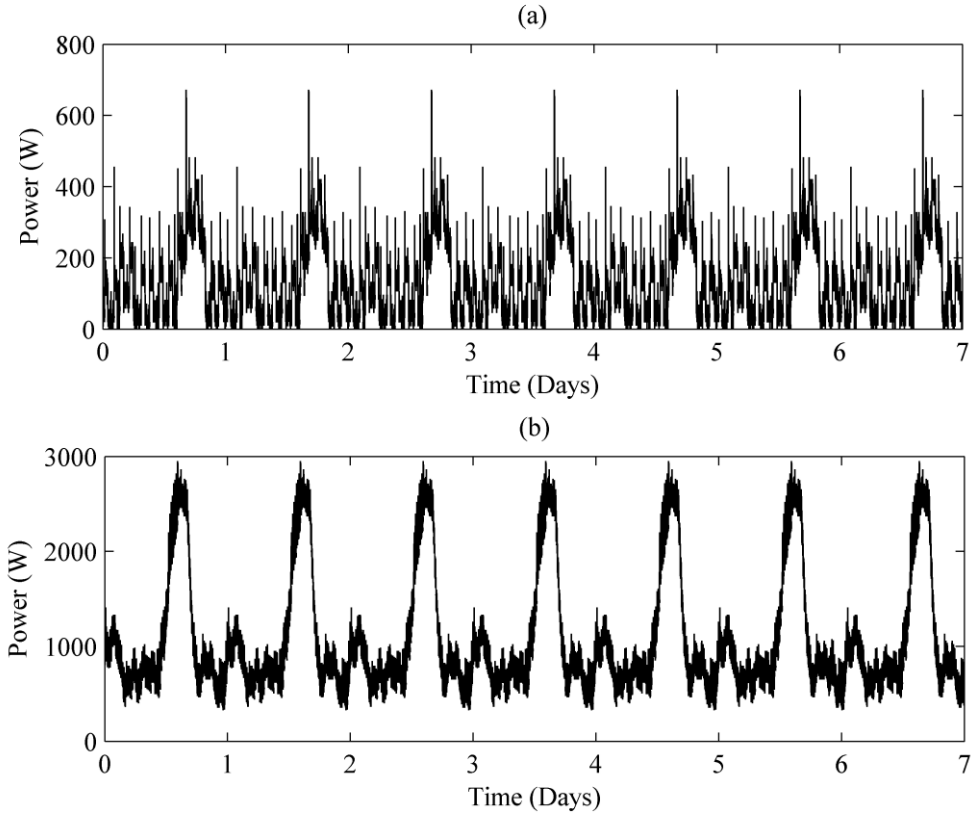

Fig. 8.23 (a) Single domestic low-usage profile (b) Aggregated load model.

Table 8.6: Wind turbine model parameters [184].

Parameter	Description	Value
R	Blade radius	3.13m
J_{wt}	Turbine rotor moment of inertia	2.5kg/m^2
J_{elec}	Generator moment of inertia	1.5kg/ms^2
D_{wt}	Damping coefficient	0.025 Nm/rad/s
ω_r	Rated wind speed	15m/s

8.4.2 Simplified System-Level Simulation

At this stage in the research, simulations were carried out using a 32-bit version of Matlab/Simulink. The detailed simulation of the system as used in Section 8.3 were found to cause “out of memory errors” when carried out over year-long simulation intervals on a 32-bit platform using a 1s sampling period. So, to analyse the performance of the battery-power filtering supercapacitor control-strategy over periods long enough to include seasonal variations using the 32-bit system, the following underlying simplifying assumptions were made:

1. Battery voltage variations can be neglected.
2. The battery and supercapacitor states-of-charge can be determined by integration of the net power delivered.
3. Battery and supercapacitor efficiency can be modeled using static one-way values as is commonly employed in top-level power system simulations [145], [185-187].
4. The efficiency of the power electronic converter can be modeled using a static value.

The Simulink block diagram used to implement this simplified model is shown below in Fig. 8.24.

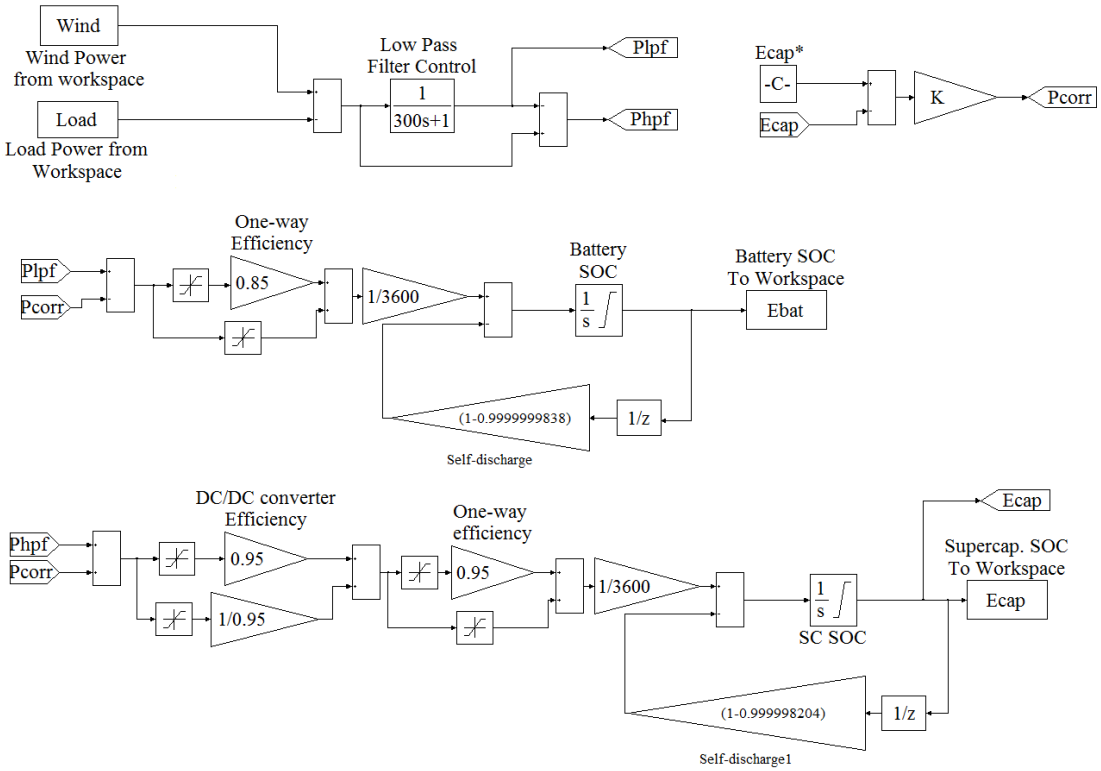

Fig. 8.24 Simplified Long-Term Low-Pass-Filter Based Control Simulation

The decay of energy stored in the supercapacitor and battery have been included in this long-term simulation as follows. For the supercapacitor, the leakage current and rated voltage [113] are used to obtain an equivalent leakage resistance term:

$$R_{leak} = \frac{V_r}{I_{leak}} \tag{8.2}$$

where V_r is the supercapacitor rated voltage and I_{leak} is datasheet-quoted leakage current [113].

The rate of decay of the supercapacitor voltage can be found from the *RC* time- constant as:

$$V = V_0 e^{-t/(R_{leak}C_0)} \tag{8.3}$$

where C_0 and V_0 are the rated capacitance and voltage of the supercapacitor bank, respectively.

The rate of decay of energy stored can then be found:

$$E = \frac{1}{2}.C_0\left(V_0 e^{-t/(R_{leak}C_0)}\right)^2 = \frac{1}{2}.C_0 {V_0}^2 e^{-t2/(R_{leak}C_0)} \tag{8.4}$$

Eq. 8.4 has the exponential time constant:

$$\tau = \frac{C_0 R_{leak}}{2} \tag{8.5}$$

From Eq. (8.5), the energy loss per second can be found and converted to a multiplication factor as shown in Fig. 8.22. Similarly a typical battery manufacturer-quoted self-discharge rate is 25% over 6 months [104] which has also been converted to a discrete self-discharge factor and used in the above simulation in Fig. 8.22.

8.4.3 Effect of Turbulence on Battery Life

The effects of different turbulence intensities on predicted battery cycle-life were considered by running the simulation in Fig. 8.24 with the supercapacitor system omitted. The rain-flow counting algorithm was then used to estimate the battery life for turbulence intensity levels in the range 0 (no turbulence) to 0.5 (maximum turbulence intensity) with the results plotted in Fig. 8.25.

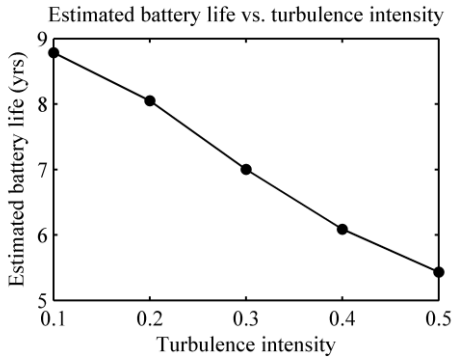

Fig. 8.25 Case study 2 battery-only simulation results: Battery life vs. turbulence intensity

The results presented in Fig. 8.25 show how expected battery cycle-life is inversely proportional to the turbulence intensity for a given load.

8.4.4 Effect of Supercapacitor Energy Storage System on Battery Cycle-Life

Fig 8.26 demonstrates the effect of adding the supercapacitor energy-storage and under the proposed power-filtering control scheme with the low-pass filter time constant set to 3600s. The results show that the proposed supercapacitor system can significantly decrease the number of charge/discharge cycles experienced by the battery.

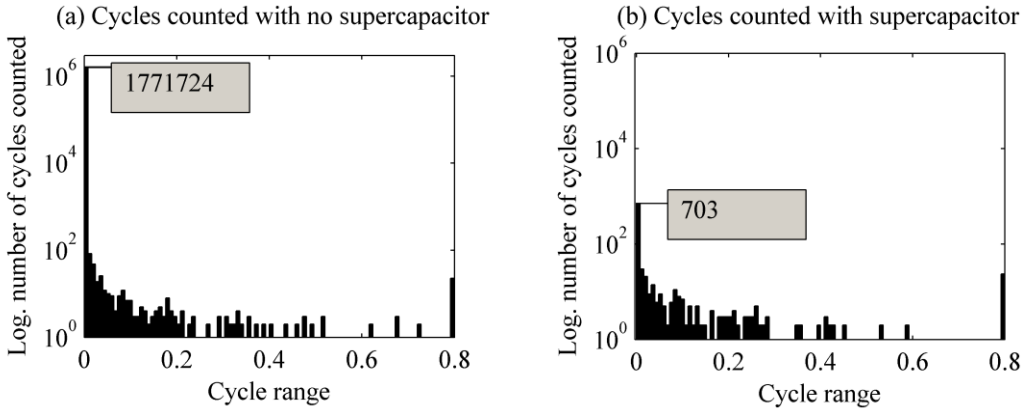

Fig. 8.26 Case study 1. Battery rain-flow cycle counting results. Turbulence intensity = 0.3. Low pass filter time constant = 3600s.

To assess the effect of varying the low-pass filter time-constant, the simulation was repeated with the low-pass filter time-constant incremented over the range 15s to 7200s. Battery state-of-charge variations were logged and used to determine resulting battery life prediction using the rain-flow counting algorithm described in Section 5.2.2. The required supercapacitor energy rating was calculated from the maximum peak-to- peak supercapacitor energy variation.

Fig. 8.25 has shown the relationship between battery cycle-life and turbulence intensity level. Fig. 8.27 indicates the general trend of how adding a supercapacitor energy storage system under the current-filtering control scheme can mitigate the decrease in battery life due to increased turbulence levels.

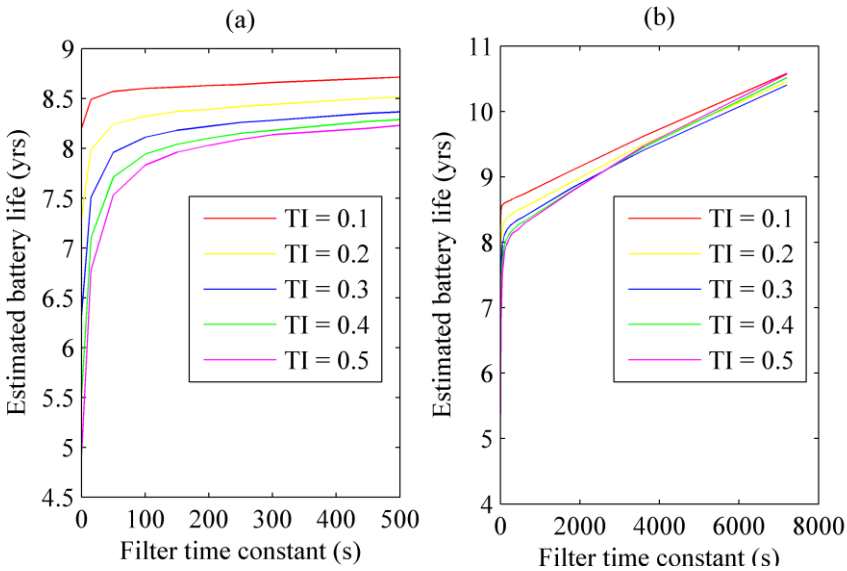

Fig. 8.27 (a) Expected battery life vs. low-pass filter time-constant and turbulence intensity: Low value time constants (0-500s). (b) Expected battery life vs. low-pass filter time-constant and turbulence intensity: Full range time constants (0-2000s).

From Fig. 8.27, it can be seen that predicted battery life curve rises rapidly as the low pass filter time constant is increased until ~1000s after which the battery life estimation increases approximately linearly.

Fig. 8.28 shows the required supercapacitor capacity rating for each low-pass filter time-constant and turbulence intensity level combination. It should be noted that some of the supercapacitor energy capacity ratings considered in Fig 8.26 are unrealistic from a current cost perspective when compared to the current cost of the remaining system components.

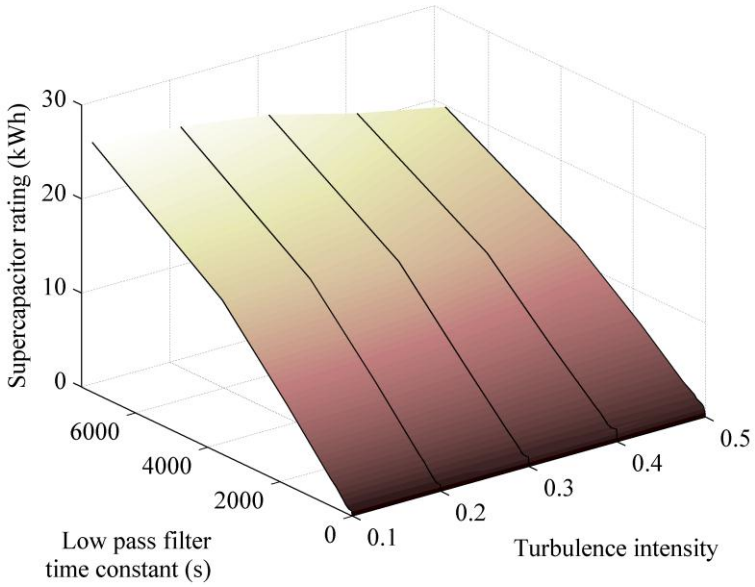

Fig. 8.28 Required supercapacitor rating vs. low-pass filter time-constant and turbulence intensity

8.5 Summary and Discussion

This chapter has considered the potential benefits of using an actively controlled supercapacitor energy storage system to reduce short-term battery power cycles in the context of an off-grid wind energy conversion application. New results obtained have shown how, with increased turbulence intensity in systems employing battery storage alone, battery cycle-life is reduced. The simulation results obtained also show how the degree of hybridisation of the battery energy storage system with an additional supercapacitor storage element (under a power filtering approach) can mitigate the

effects of decreased cycle-life at high turbulence intensity levels. In terms of battery life, the greatest benefit of the proposed system, can be achieved at high turbulence intensity-levels as the increased battery cycle-life is proportionally higher at lower turbulence intensity levels for a given supercapacitor capacity rating. These results also indicate that the optimum combination of supercapacitor, battery and time constant can be found for a given turbulence intensity site. A cost minimisation procedure can be used to calculate the relative costs of the combinations of battery and supercapacitor based on estimated battery life over the project. This has potential to be the subject of future work.

The key contributions from this chapter can be summarised as follows:

- A novel hardware implementation of an actively-controlled supercapacitor device, optimised to mitigate high frequency current fluctuations, has been presented and its functionality confirmed.
- Experimental and simulation results have shown how the proposed system is capable of reducing battery current cycles and current maxima.
- Simulation results have indicated the benefits of the proposed system in terms of increased battery cycle-life.
- New simulation results have been presented showing the relationship between turbulence intensity and battery cycle life. The benefits of an actively controlled supercapacitor under a power-filtering control-strategy have been shown to improve battery cycle-life under highly turbulent wind conditions.

The results in Fig. 8.17 have shown a significant reduction in battery discharge current-maxima due to hybridisation. Since discharge current magnitude has been directly connected to premature battery failure, it is expected that the power filtering mode of

control has a significant un-modeled benefit in terms of battery life. The inclusion of this effect in the modelling procedure is a subject of potential future work. Binder reports that investigations were made into a modified rain-flow counting algorithm which can “allow charge or discharge rates to be accounted for” [9] but goes on to state that the work hasn’t been completed. Such a battery life model would enable novel strategies for the optimisation of the system specifically to reduce discharge current to be evaluated in future work, highlighting the need for further research in the area.

One of the assumptions made has been that a battery voltage control system can be omitted from the simulations in this chapter. While this may be the case for continuous operation at states-of-charge significantly less than one, it may also be desirable to operate the battery at a high state-of-charge for extended periods of time, depending on the optimum wind to battery capacity-ratio. For these reasons, in reality some form of battery voltage control is typically included in a practical wind-energy system to prevent overcharge [188]. Based on this operational requirement, Chapter 9 considers the use of an actively controlled supercapacitor system to help prevent battery overcharge.

Chapter 9: Supercapacitors for Battery Voltage Support

9.1 Introduction

This chapter describes a novel approach to supercapacitor/battery hybrid energy storage system control developed as part of this research. The control system is designed to prevent overcharge by regulation of the battery voltage in the presence of a varying wind power profile. One of the difficulties faced in charging battery energy storage systems from a wind energy supply is the potential for overcharge during wind power peaks. Typically the solution is to defer excess power to a dump-load resistor to prevent over-charge and generator over-speed. Many studies in automotive and railway vehicle dynamic braking systems have demonstrated how short-term, high power energy storage systems can be used to capture dynamic braking energy which would otherwise be wasted as heat in a resistive grid or in friction braking ([189], for example). The technique presented in this chapter has drawn from such results and used the supercapacitor system to reduce the use of a resistive dump-load in a wind energy system.

9.2 Battery Voltage Stability in Wind Energy Systems

Section 7.1-7.2 has shown that an optimal energy storage configuration in terms of cost and reliability metrics may not be one which is able to store all the available wind power throughout the year. The consequence of this in an autonomous off-grid application is that when the energy storage is at maximum state of charge, excess power must be diverted away from the energy storage system. In the case of PV off-grid generation, the solar generator can be simply disconnected from the battery without any undesirable effects [190]. With wind energy conversion systems it is desirable to

operate the generator under some form of load at all times to prevent an over-speed condition [191]. The excess wind power that the battery cannot accept is typically diverted to a dump-load to prevent generator over-speed and battery overcharge [66], [149], [192-198]. This method of over-speed control is designed to operate when the wind to load power ratio and battery state-of-charge is high, in conjunction with the 'furling' over-speed control mechanism described in Section 3.2.2, which is designed to operate at extreme wind speeds [191]. Field test reports have shown a significant reduction in usable wind-energy output from remote-off grid wind energy systems due to excessive power dissipated in the dump-load [66], [149], [192], [194], [197] with losses ranging from 75% [149], [192] to 59% [66] and 18% [194] having been reported. The mechanism by which this occurs has been highlighted as being due to battery voltage variations under wind-charging conditions causing battery overcharge protection circuits to divert a significant proportion of the available wind energy to the dump load [149], [192]. Simply increasing the number of parallel connected batteries could potentially improve battery voltage stability by reducing the effective impedance of the battery bank. However, the battery would then operate at a reduced state-of-charge which has been highlighted as a direct battery ageing factor [11]. For this reason, the focus of the research presented in this chapter was directed at investigating the development of a battery/supercapacitor hybrid energy storage system control optimised for operation under peak power charging conditions at high states of charge. The resulting novel hybrid energy storage device can be charged at full-rated current until end-of-charge (in contrast to a battery which would generally require some form of charge rate reduction at high states of charge).

9.2.1 Charge Control Strategy

A proper charge control strategy is important to obtain optimum performance from a secondary battery [97]. Various strategies exist for recharging stationary lead acid batteries [199], depending on the application. In stand-by applications (for example telecom and UPS systems) batteries are discharged infrequently under generally only emergency conditions [199] and charging is from a reliable utility power source [200], [201], and relatively straight-forward [200]. In contrast, for batteries in cycling applications such as remote power and distributed energy systems (and electric vehicles applications) the implementation of a charge control strategy is less straightforward due to the intermittent nature of the available charging supply.

Some of the most common charging strategies include constant voltage, constant current (CVCI), intermittent charging and interrupted charge control. Of these, the most common to be employed in cycling applications are regimes based on the CVCI approach and the intermittent charge control approach. Intermittent charge controllers (ICC) charge the battery with current proportional to the available charge power initially, then when an upper voltage threshold is reached, charge power is disconnected until the battery voltage has fallen to a lower threshold. This process repeats intermittently with battery voltage oscillating between upper and lower thresholds. The ICC is one of the most commonly employed techniques used by commercial photovoltaic charge regulators [202] and has a tendency to undercharge the battery [199]. Interrupted charge control is an extension of the intermittent charging strategy and consists of four modes of operation [203]: During stage one, the battery is charged using a constant current until an upper voltage threshold is reached. In stage 2, a rest period is activated during which the battery is left open-circuit. When the battery voltage has fallen to a lower voltage threshold, a third stage of (low) constant current

charge pulses is activated. Finally stage four terminates the charge by disconnecting the battery when the terminal voltage reaches an upper limit during pulsed charging. This technique has been shown to be most suitable in stand-by applications [203]. A more common and generally accepted technique (particularly in cycling applications) is based on the constant-current/constant-voltage technique also known as 'CICV charging'. Relevant studies to use this form of charge control can be found in the field of wind-battery systems [188], [195], [196], [204], stand-alone photo-voltaic systems [202], [205-207], distributed generation [208] and micro-grid applications [209].

An example of two typical CVCI-based charging regimes for the lead-acid battery is shown in Fig. 9.1 below [199].

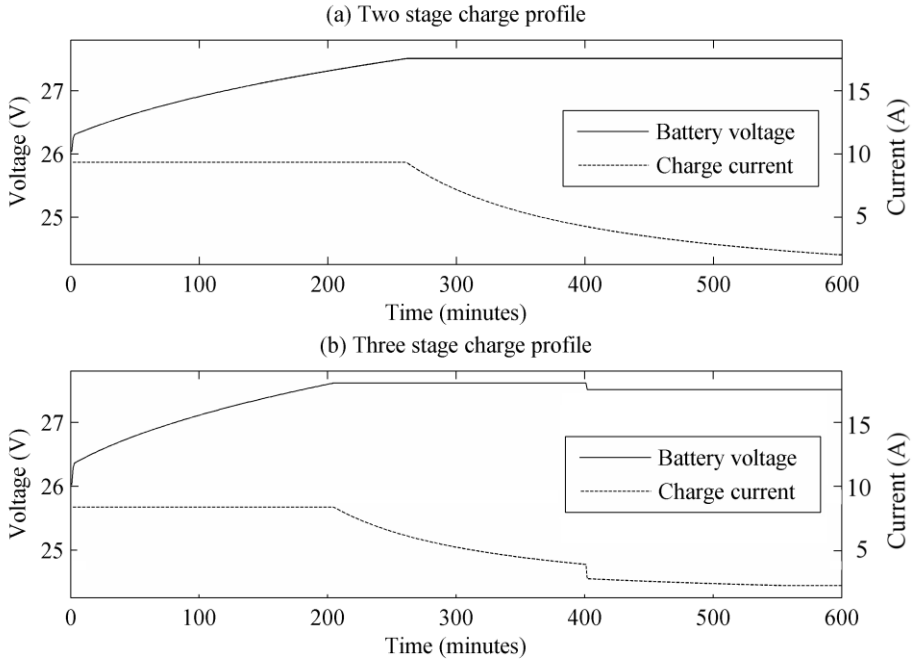

Fig. 9.1 Typical lead-acid battery charge profiles (a) Two stage approach (b) Three stage approach.

In both of the charge strategies in Fig. 9.1, the battery is first charged using constant current until a voltage set-point is reached. The voltage is then regulated at this point

until the battery reaches a full state-of-charge [199] in the two-stage implementation of Fig. 9.1 (a). Whereas, in the three stage implementation of the CVCI charge regime shown in Fig. 9.1 (b), an additional lower voltage stage is added to maintain the battery state-of-charge indefinitely, sometimes known as the float charge stage [210], [211].

Although various charge control approaches have been suggested including intermittent charging [202], [212], [213] and interrupted charge control [202], [203], CVCI techniques remain widely regarded as appropriate for charging lead-acid cells in renewable energy and cycling applications by the IEEE [71], [210], battery manufacturers [214] and in recent studies [211]. CVCI-based techniques are also employed in charging lithium-ion cells [215], [216] although voltage regulation, cell balancing and thermal management tolerances must be much tighter. As a result, a derivative of the proposed hybridisation approach may also be applicable to lithium based cell chemistries and considered in future studies.

One of the challenges faced in charging any battery from renewable power sources is that the power profile dictated by the balance of power available is unlikely to match a defined battery charge profile. For this reason, the constant-current/constant-voltage charge profile is not often directly implemented in the exact form of Fig. 9.1 in renewable energy applications. Instead, the method frequently adopted is a current-limited, constant-voltage approach as recommended in "IEEE Guide for Optimizing the Performance and Life of Lead-Acid Batteries in Remote Hybrid Power Systems" [71], the “IEEE Guide for Application and Management of Stationary Batteries Used in Cycling Service” [210] and implemented in recent studies [188], [204]. In this variant of the CVCI strategy, the battery is charged during stage one with power according to the power available from the renewable source (often dictated by a maximum power point

tracking algorithm in wind and solar applications) and limited by the maximum system charge current. Then, as the battery voltage approaches the constant-voltage charging set point value, the charge controller changes to some form of voltage-based control, allowing the battery charge current to diminish exponentially. Typical charging voltage set point values lie in the range 2.3-2.4V/cell for lead-acid cells depending on the cell model [97] (page 24.17) and are generally specified in manufacturers' datasheets. Many systems employ the two stage approach shown in Fig. 9.1 (a) as batteries often do not reach the float charge state (stage 3) for extended periods of time in highly cyclic applications [210], [211].

It can be seen from Fig. 9.1 that the battery charge current falls to a low level during voltage regulated charging. This has the effect of reducing the ability of the battery energy storage system to absorb excess power effectively when a charge regulator is in place. In wind-charging applications, excess wind power that cannot be absorbed by the battery is typically diverted to a dump-load [66], [149], [192-198] to prevent over-charge and generator over-speed. Unless the energy diverted to the dump load can be used in a productive capacity such as to heat water or for water pumping, then it is typically wasted as heat in a dump load resistor. Field test reports have shown that this can lead to a considerable reduction in energy yield [66], [149], [192], [194], [197]. To help mitigate this issue, a novel supercapacitor/battery hybrid energy storage device operating under a battery-voltage control strategy was designed and implemented as described in this chapter in Sections 9.3 - 9.4 and reported in [217] which enables the hybrid energy storage system to be charged at full rated current over the entire state-of-charge range. This is unlike the un-hybridised battery which is charged with an ultimately diminishing current (see Fig. 9.1).

9.3 Battery Voltage Control Scheme

This section describes the control system designed to divert excess wind-power to the supercapacitor module to maintain the battery voltage at an appropriate constant-voltage charge level. This has the benefit of allowing the energy stored in the supercapacitor to be re-used which would otherwise be dissipated in a resistive dump load.

Voltage control is achieved by an outer voltage control loop optimised for, but not limited to the synchronous buck DC/DC converter described in Section 6.2. An alternative novel control approach implementation was also developed and described in [218] as part of this research, which allows voltage control of the battery using a non-linear control optimised for the inverting buck/boost converter.

9.3.1 Battery Voltage Control System Design

This battery voltage control strategy is effectively based on a proportional and integral (PI) control of the output current of the synchronous buck converter and, as is shown below, can be analysed using variable structure control techniques.

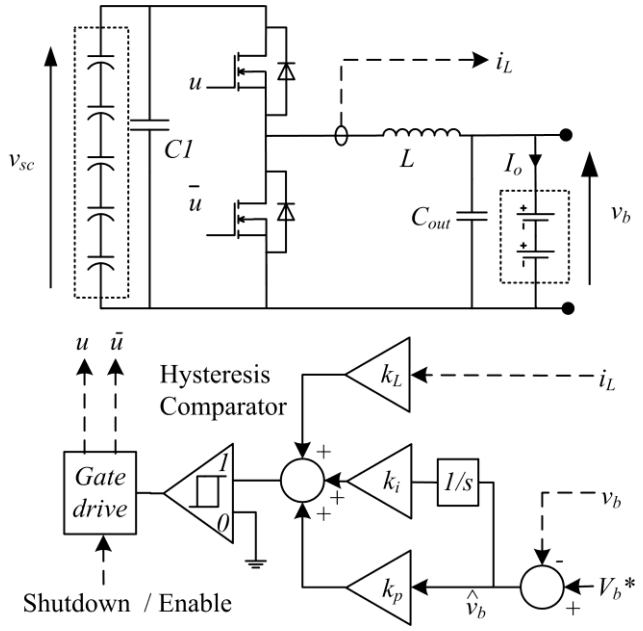

Fig. 9.2 Bidirectional synchronous buck converter.

Variable structure control originated in the Soviet Union in the 1960's and is now a well-established technique for robust control of non-linear systems. A variable structure control system is typically characterised by a series of control laws and a switching function [219]. Sliding mode control is a type of variable structure control in which the system trajectory is driven to the vicinity of a desired operating point by choice of an appropriate switching function. One of the major advantages of this approach is low sensitivity to parameter variation and disturbances [219].

The proposed voltage control scheme in Fig. 9.2 is shown below to be well approximated by proportional plus integral control action on the converter output current. The switching action of the power electronic converter allows the system to be modelled as a variable structure system [219] (p 265) and the proposed control can be analysed using variable structure control theory. The following section presents the procedure used to analyse the nature of the control system in Fig. 9.2 using these techniques.

The controlled variable is the battery voltage v_b, and V_b* represents the command reference voltage, which in this case is also an appropriate charge regulation voltage. v_{sc}, represents the supercapacitor voltage. Defining u and $\bar{u}$ as the gate drive signals for the electronic switches, the equations describing this switched system are:

$$L\frac{di_L}{dt} = v_{sc}u - v_b \quad \text{(V)} \tag{9.1}$$

$$C\frac{d\hat{v}_b}{dt} = i_L - I_O \quad \text{(A)} \tag{9.2}$$

The output voltage can be written in terms of a steady state voltage (indicated by *) and an error term (indicated by ^):

$$v_b = V_b^* + \hat{v}_b \quad \text{(V)} \tag{9.3}$$

To control the output voltage and ensure zero steady-state error, a switching function, σ, can be defined in terms of the output voltage error term, its integral and the inductor current as follows:

$$\sigma = -k_L i_L + k_p \hat{v}_b + k_i \int \hat{v}_b = 0 \tag{9.4}$$

where k_L is an inductor current measurement gain.

To ensure that the system reaches the sliding surface $\sigma = 0$ in a finite time, the following condition must be true and $d\sigma/dt$ must be bounded away from zero [219]:

$$\sigma \cdot \frac{d\sigma}{dt} < 0 \forall \neq 0 \tag{9.5}$$

By substitution in Eq. (9.4) with Eqs. (9.1) and (9.2) an expression for the derivative $d\sigma/dt$ can be found as follows:

$$\frac{d\sigma}{dt} = -k_L \frac{1}{L}(v_{sc} u - v_b) + k_p \frac{1}{C}(i_L - I_o) + k_i \hat{v}_b = 0 \tag{9.6}$$

The following control law can satisfy the necessary conditions for reaching the surface defined by Eq. (9.5) [138]:

$$u = \begin{cases} 0, & if \quad \sigma < 0 \\ 1, & if \quad \sigma > 0 \end{cases} \tag{9.7}$$

For Eq. (9.5) to be true with the control law of Eq. (9.7) the most stringent requirement is that v_{sc} be greater than v_b which is also a requirement for the operation of the buck converter. The L and C parameter values and gain values k_i, k_v and k_L must be chosen such that the condition Eq. (9.5) remains valid over the operating range.

The actual implementation of the sliding mode controller incorporated a modification to limit output current. The modified sliding line is made up of three straight lines, and can be expressed as follows:

$$\begin{aligned} \sigma^* &= k_L I_L - I_{\max} = 0 && \text{If } i_l > i_{\max} \\ \sigma^* &= k_L I_L - k_v \hat{v}_o - k_i \int \hat{v}_o = 0 && \text{If } -i_{\max} \le i_l \le i_{\max} \\ \sigma^* &= k_L I_L + I_{\max} - = 0 && \text{If } i_l < -i_{\max} \end{aligned} \tag{9.8}$$

This is done as, at start-up, voltage error and error-integral terms are high causing a high initial current. Also, with this modification to the sliding line, the bidirectional converter has the beneficial feature of input and output overcurrent protection. In the current limited region, the controller regulates the current in the same manner as described in Section 6.2.3. The effect of adding start-up current limitation is demonstrated in Fig. 9.3.

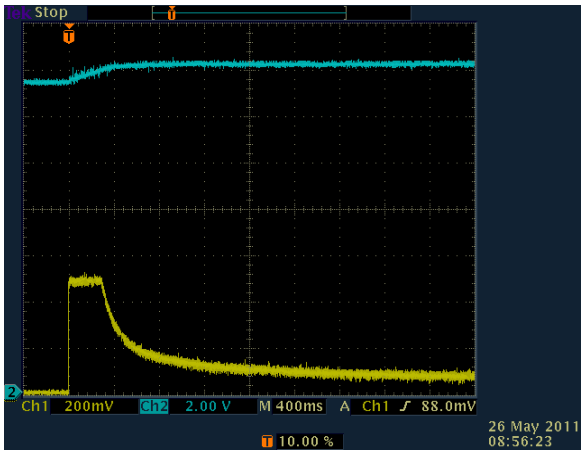

Fig. 9.3. Inductor current (yellow trace, 50mV/A) and output voltage (cyan trace) at start up with current limiting.

Re-arranging Eq. (9.4) and transforming to the Laplace domain gives the following relationship:

$$i_L(s) = \hat{v}_b(s)\left(\frac{k_p}{k_L} + \frac{k_i}{k_L s}\right) \tag{9.9}$$

By inspection, Eq. (9.9) can be seen to be equivalent to proportional-plus-integral action on the voltage error term.

While the system remains in sliding mode control and for frequencies well below the switching frequency, the control system model can now be approximated by the equivalent linear PI controller $G_c(s)$ in Eq. (9.10) and Fig. 9.3. This has the advantage of enabling the use of linear frequency-domain analysis techniques while this is the case.

$$G_C(s)=\left(\frac{k_p}{k_L}+\frac{k_i}{k_L s}\right)=\left(k_p'+\frac{k_i'}{s}\right) \tag{9.10}$$

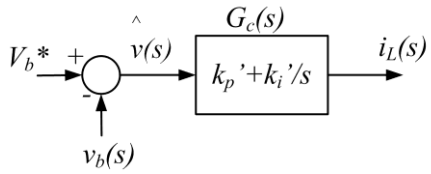

Fig. 9.4 Proportional plus integral action on voltage error term.

To complete the control-loop, the impedance of the battery and converter are considered next. It was shown in Section 4.2 the battery impedance can be modelled by a complex impedance term of the form:

$$Z_b(s)=\frac{k_b(s+z_b)}{s+p_b} \tag{9.11}$$

The total parallel combination impedance of the battery and output capacitor of the converter, C_{out} (see Fig. 9.2) is:

$$Z_{out}(s)=\frac{k_b(s+z_b)}{(k_bC_{out})s^2+(k_bC_{out}z_b+1)s+p_b} \tag{9.12}$$

The model of the control system operating in sliding mode control can be represented as shown in Fig. 9.5.

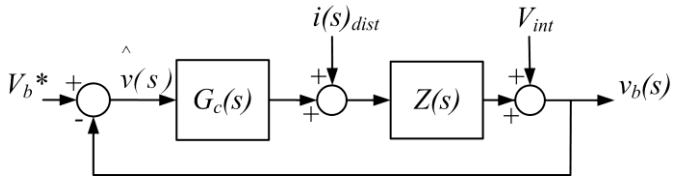

Fig. 9.5 Voltage control system under sliding mode control

The effect of including a typically sized output capacitor of the order of 10^{-3} Farads is to add a high frequency pole to Eq. (9.11) several orders of magnitude greater than the dominant dynamics of the battery impedance. So to design the overall time response of the system, the impedance term *Z(s)* was approximated by the dominant pole/zero of the battery impedance Eq. (9.9). The simplified closed-loop and disturbance transfer functions of the system in Fig. 9.4 are then:

$$G_{cl}(s)=\frac{k_b(k_i'+k_p's)(s+z_b)}{s^2(1+k_p'k_b)+s((k_bk_p'z+k_bk_i')+p)+k_bk_i'z_b} \tag{9.13}$$

$$G_{dist}(s)=\frac{k_bs(s+z_b)}{s^2(1+k_p'k_b)+s((k_bk_p'z+k_bk_i')+p)+k_bk_i'z_b} \tag{9.14}$$

9.3.2 Battery Impedance Variation

A typical fully-charged open-circuit voltage for a (VRLA) lead-acid battery is ~2.10V/cell [97] (page 24.16) whereas a suitable charge voltage regulation set point is ~2.3 - 2.4 V/cell [97] (page 24.17). Depending on the state of the charge of the battery and disturbance current magnitude it can be possible for the battery terminal voltage to reach the regulation voltage at both a partial and full state of charge. For this reason, the control system performance must be considered at both full and high-partial states of charge. The results in Section 4.2 have shown that the battery impedance exhibits a significant change when a fully-charged or float condition is approached, a result which has also been reported in previous studies [106], [107]. The system closed-loop

response was designed for operation at partial state-of-charge and its response was verified to be acceptable at a full state of charge.

Based on the impedance model parameters in table 4.1 and table 4.2 (Section 4.2) the PI voltage controller was designed to have a non-oscillatory response and nominal response time of <0.05 seconds at both partial and full state-of-charge operation. The controller was designed using the Matlab Control System Toolbox SISO design tool [83] as follows:

$$G_c(s) = \frac{21.8(s + 6549)}{s} \tag{9.15}$$

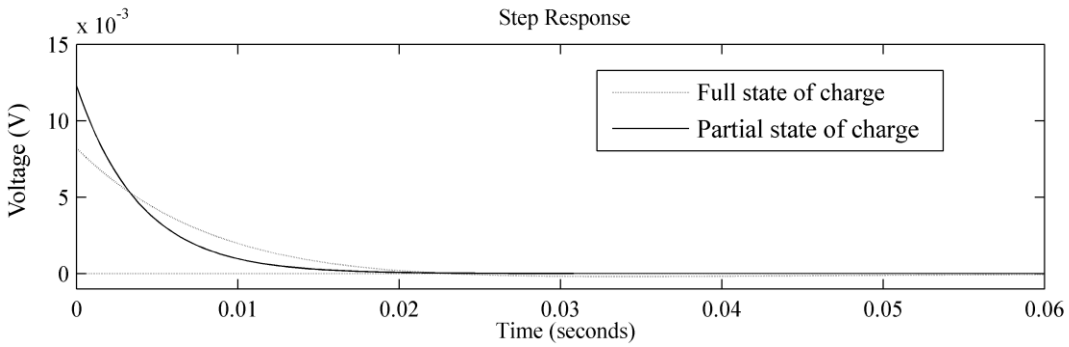

Fig. 9.6 Battery voltage response to a unit step current disturbance at plant input under partial state-of-charge and full-charge conditions.

The local stability of this system and performance was ensured by designing the closed loop transfer-function to have negative real poles. To examine the global stability of the system, the switching action of the converter within the control loop was modelled as described in Section 9.3.3.

9.3.3 Stability Analysis

The above analysis in Section 9.3.1 was based on the assumption that the dynamic response of the system can be well approximated by an equivalent linear-system response. This description of the system is valid for trajectories along the sliding surface and for frequencies well below the switching frequency [178]. This Section describes the method used to assess the global stability of the system, by modelling the switching action of the power electronic converter as a relay with hysteresis in the control loop [130], [178].

The describing function was used to predict if a limit-cycle oscillation would occur under the developed control regime and to examine its stability. The describing function technique is a widely used method to study the frequency response of nonlinear systems [220-223]. The underlying approach of this technique is to replace the nonlinear element(s) with a descriptor known as the describing function whose gain can be a function of input amplitude and/or frequency [224]. This is advantageous in this case, as other modelling techniques such as state space averaging [225], cannot be easily applied to relay-feedback systems employing hysteresis modulation switching control laws [178].

The system of Fig. 9.5 can be re-drawn as shown in Fig. 9.7 (a) to include the switching relay with hysteresis, the DC resistance of the inductor, R_L and the total parallel combination impedance of the battery and output capacitor $Z_{out(s)}$, Eq. 9.11.

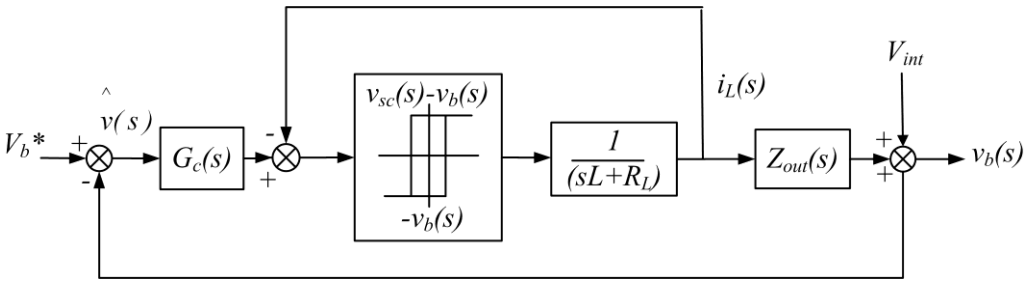

Fig. 9.7 Control system block diagram including relay with hysteresis representation of the switching converter

Fig. 9.7 can be re-drawn with the relay element replaced by the descriptor, *N(x)*, as shown in Fig. 9.8.

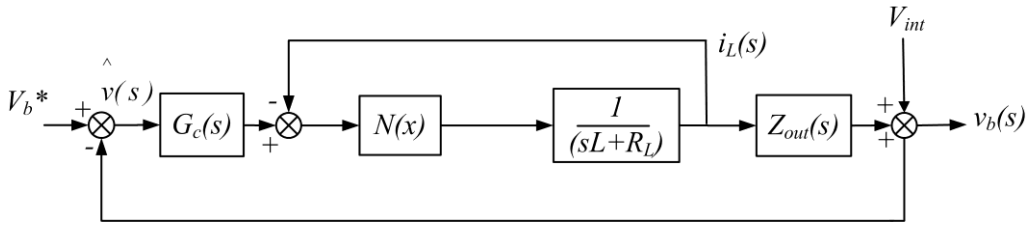

Fig. 9.8 System block diagram with non-linear elements shown in describing function form.

Since Fig. 9.8 contains a nested loop, to analyse the system stability using the technique described in [224] (p. 115) the system was reduced to an equivalent single loop form shown in Fig. 9.9 (see Appendix 2).

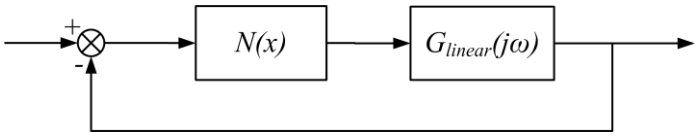

Fig 9.9 Non-linear term cascaded with linear system

Here $G_{linear}(j\omega)$ represents an equivalent transfer-function representing the linear terms of the system in Fig. 9.8 as determined in Appendix 2.

The describing function for a relay with hysteresis is [224] (p.121):

$$N(x) = \frac{4d_a}{\pi\sqrt{x^2 - \varepsilon^2} + j\pi\varepsilon} \tag{9.27}$$

where ε is the relay hysteresis, d_a is the relay amplitude, x_a is the amplitude of the oscillation of the process variable.

By plotting the Nyquist locus of $G_{eq}(j\omega)$ and observing the intersection with the locus of the term $-1/N(x)$, the presence of a limit cycle can be detected and an assessment of its stability can be obtained [224] (p. 119).

The loci of $G_{eq}(j\omega)$ and $-1/N(x)$ are plotted below under typical operating conditions:

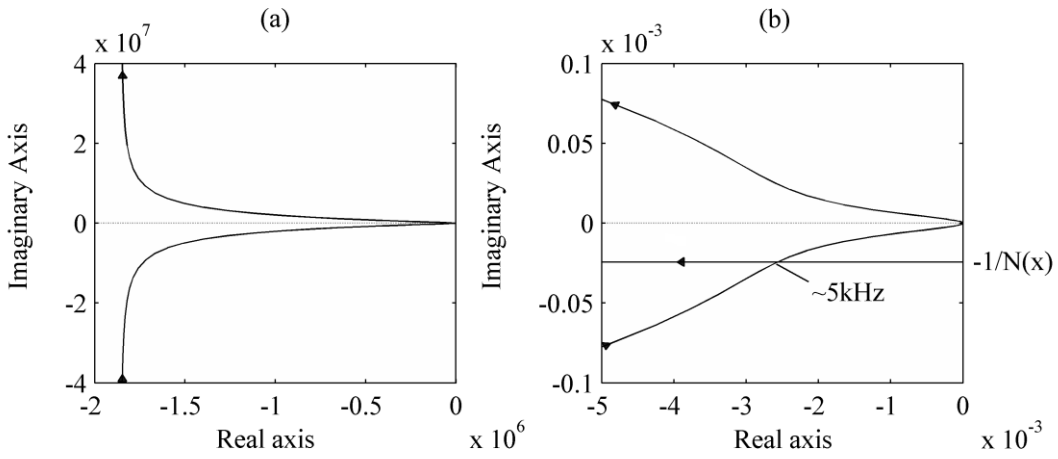

Fig 9.10 (a) Nyquist plot of G_{eq}(s) (b) Nyquist plot of G_{eq}(s) zoomed in to show intersection with locus of $N(x)$. Operating conditions: Input voltage of Vsc = 48Vdc, Output voltage $Vbat$ = 24Vdc, hysteresis width ε = 200mV (Direction of increasing amplitude/frequency marked).

The point of intersection of the two loci is analogous to the critical point of stability on the Nyquist chart used in linear control system theory [226]. If a small increase in the amplitude of the oscillation causes the locus of the linear subsystem to encircle this point, then an unstable limit cycle is predicted [224] (p. 118). If the opposite is true as can be seen to be the case in this system in Fig. 9.11 (b), then a stable limit cycle is

predicted. The frequency of the limit cycle can also be predicted by the frequency at the point of intersection of the two loci.

9.3.4 Control Bandwidth

In the ideal case, the sliding mode system would switch at infinite frequency about the sliding surface [138]. For the sliding mode model of the system to be valid, the practical implementation of the system should approximate this behaviour by design such that the switching frequency is significantly higher than the fastest dynamics of the system trajectory along the sliding surface [178]. For this reason, it was necessary to ensure that the control bandwidth corner frequency was significantly lower than the lowest switching frequency of the converter, dependent on operating conditions and component selection [determined from Eq. 6.5 (Section 6.2.3)]. In addition the control bandwidth is limited by the inductor current slew-rate-limit as described in Appendix 1.

9.4 Hardware Implementation of the Voltage Based Controller

The voltage control loop was originally implemented in the digital domain initially using a PIC18 series microcontroller [168] to be able to easily alter control parameters in firmware. However, it was found that the fidelity could be significantly improved using an analogue op-amp implementation of the control loop (see Fig. 9.2). This was due to the limited resolution of the PIC A/D converter. For this reason the voltage control loop was implemented using OP-AMPs as shown in Appendix 4.

The voltage error was typically in the range of mV which makes observation of the shape of the disturbance response difficult due to noise. So to observe the characteristics of the response more clearly, the inductor current response to a step disturbance current was measured and also plotted in Matlab as shown in Fig. 9.7.

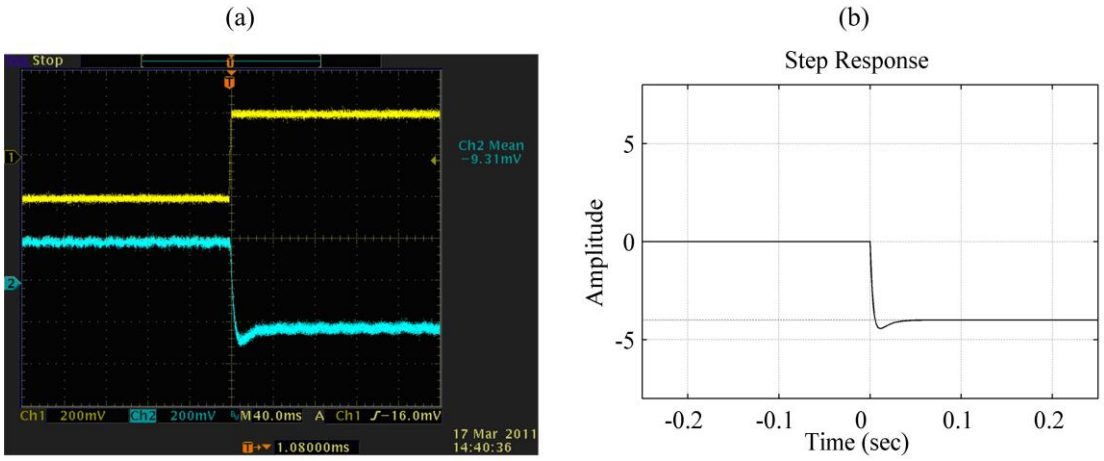

Fig. 9.11 Measured inductor current step response at float conditions (a) Yellow trace: disturbance current. Cyan trace: Inductor current (50 mV/A) (b) Simulated inductor current response.

A good agreement between the measured and theoretical low-frequency approximation of the response plotted in Matlab using Eq. (9.14) can be seen. The small overshoot is due to the effect of zeros in the disturbance-to-output closed-loop transfer-function Eq. (9.14).

To show the overall performance of the voltage control strategy, a single 12V battery was subjected to +10A/-10A step current disturbance as shown in Fig. 9.12. The experimental set-up is shown in Fig. 9.12 (c). This is comprised of a first hysteretic current controlled DC/DC converter used to deliver the test profile to the hybrid energy storage system while. The test profile current reference signal was generated by a PC running National Instruments Labview software which was also used for data logging.

In 9.12 (a), at time = 12s the converter gate drive is enabled and the converter briefly enters a current limited mode of operation with current limited to 12.5A in this example. After a short period of constant-current operation, the voltage error is reduced and the system enters the voltage-controlled mode of operation regulating the battery voltage at ~14V. The converter then provides the battery charge current which diminishes

exponentially until time = 58s, when the step disturbance current shown in Fig. 9.12 (b) is applied at the battery terminals. The operation of the converter under the proposed control strategy can be seen to counteract the disturbance current by generating an opposing current while also maintaining the battery voltage at the regulation set point.

Fig. 9.12 below shows the results of an initial experiment to demonstrate the performance of the voltage control system to a step disturbance current at the battery terminals. The supercapacitor can be seen to discharge as the energy stored is being used to maintain the battery voltage at the command set-point level.

This constitutes an energy storage device which can be charged at a significantly higher rate across the entire range of battery states of charge than the lead-acid battery alone. The measured results in Fig. 9.13 demonstrate this. In this experiment, a relatively low-capacity lead-acid battery (7Ah) [227] was used for demonstration within the same experimental configuration as shown in Fig. 9.12 (c). The hybrid energy storage system was subjected to constant current charge/discharge test using a second current-controlled converter.

(a)

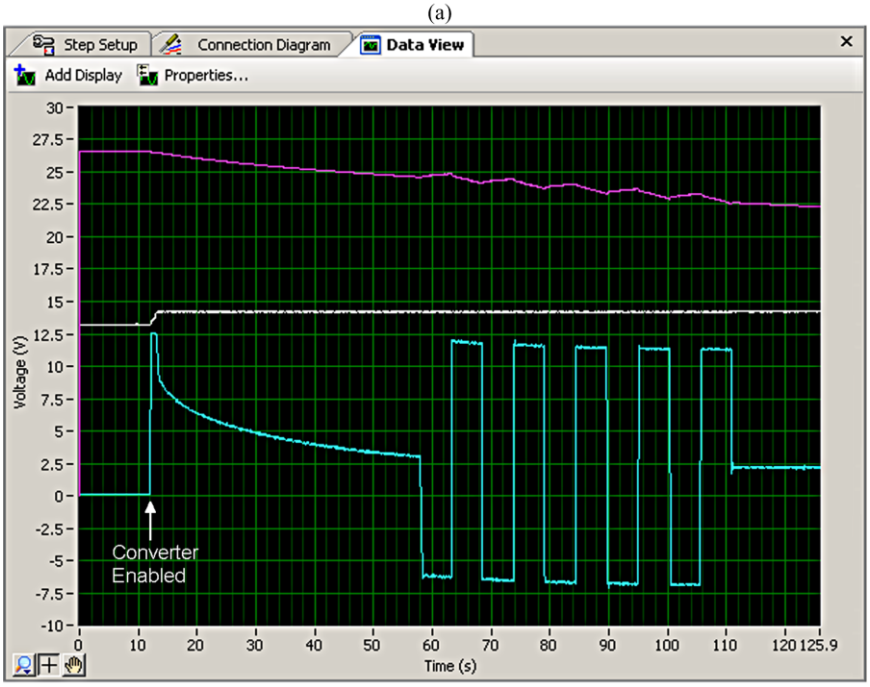

(b)

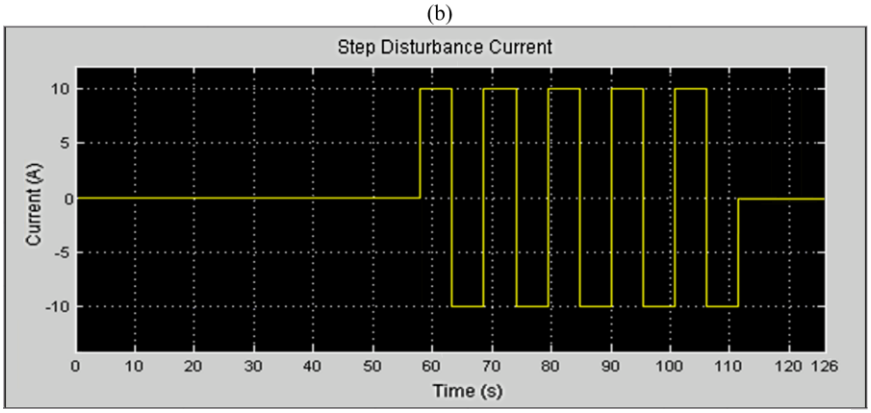

(c)

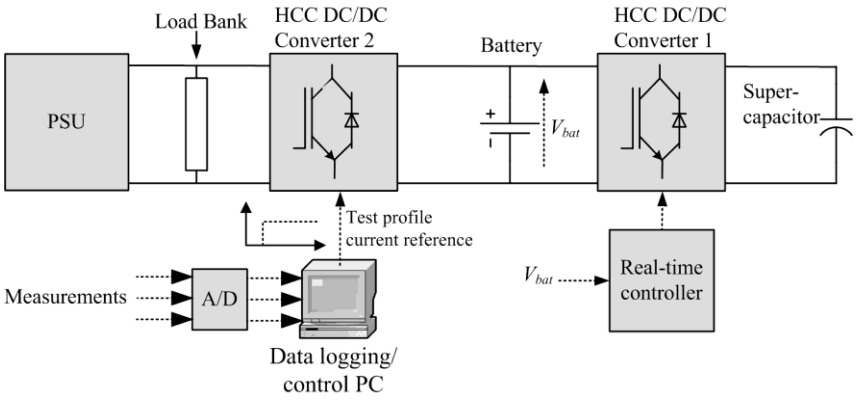

Fig. 9.12 (a) Voltage controller test results. Voltage set point: 14Vdc. White trace: battery voltage. Cyan trace: converter current (1V/A). Purple trace: Supercapacitor voltage. (b) Disturbance current input. (c) Test set-up.

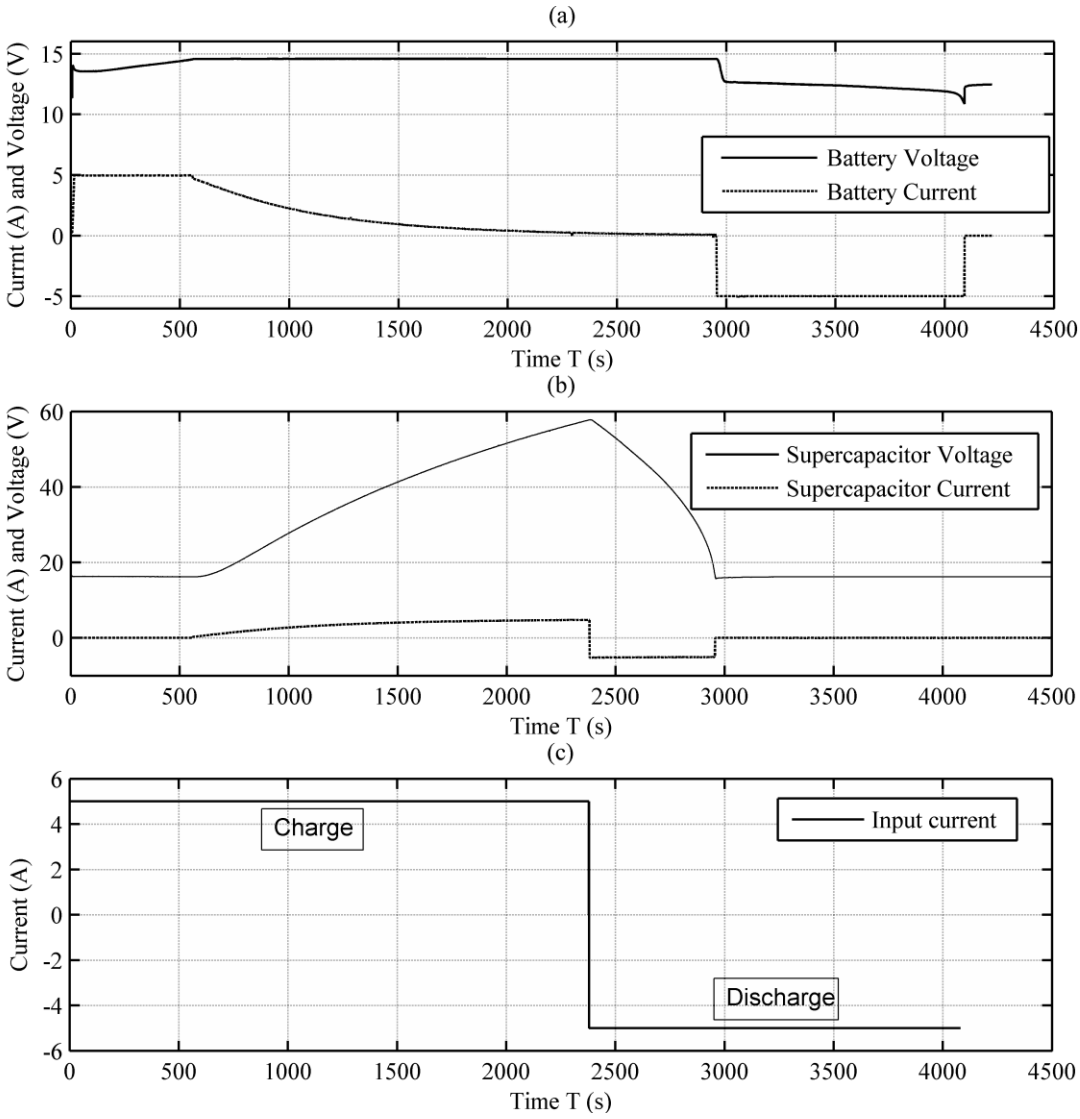

Fig. 9.13 Measured results: Voltage controlled hybrid storage system charge/discharge test (a) Battery current and voltage (b) Supercapacitor voltage and current (c) Test input current.

Fig. 9.13 (a) shows the battery voltage rise during charging until the reaching the charge regulation set point at T=600s approx. At this point, the supercapacitor voltage can be seen to rise in Fig. 9.13 (b) as the battery voltage has been effectively clamped at the regulation set-point by diverting the excess power to the supercapacitor. At T=2400s the input current is changed to a constant-current discharge and the supercapacitor voltage can be seen to fall, while the battery charge regulation voltage is maintained. When the

supercapacitor has been discharged at T=2900s (approx.), the battery then provides the discharge current until the end of the test.

9.5 Existing Battery Voltage Control Techniques

The following section first illustrates the operation of typical existing methods of battery charge control in wind energy applications, and then two novel strategies are described based on the control system described above in Section 9.3.

The system sizing algorithm defined in Section 7.2.2 was used to configure a system based on the commercially available wind turbine/generator system with the following main modelling parameters taken from [179]. A 70% penetration of renewable generation was assumed with the remaining power supplied by a diesel generator set.

TABLE 9.1: VOLTAGE CONTROL SIMULATION MODELLING PARAMETERS [179]

Parameter	Description	Value
R	Blade radius	1.1m
J_{wt}	Combined moment of inertia	1.05kg/m^2
D_{wt}	Damping coefficient	0.001 Nm/rad/s
E_{gen}	Generator efficiency	0.8

An 8.23kWh battery was determined to be optimal based on the results of the optimisation procedure shown in Section 7.2.2 (Fig. 7.5), allowing an 80% depth of discharge. In this simulation, the Ceraolo battery model was used with parameters as determined by Ceraolo [1] and used previously Section 8.3.1 with the cell capacity adjusted to reflect the energy storage requirement. The suggested improvements to the model described in section 4.2.2 was not used in this case due to not having been validated over the entire state of charge range.

TABLE 9.2: CASE STUDY 3 ENERGY STORAGE SYSTEM RATINGS

ICC Conventional System	CVCI Conventional System	Voltage-Based Control	Voltage-Current Hybrid Control
Battery:8.23kWh (310Ah/24Vdc)	Battery: 8.23kWh (310Ah/24Vdc)	Battery: 5.65kWh (215Ah/24Vdc) Supercapacitor: 2.583kW	Battery:5.65kWh (215Ah/24Vdc) Supercapacitor: 2.583kW

The wind speed, generated wind power and load profile are shown in Fig. 9.14.

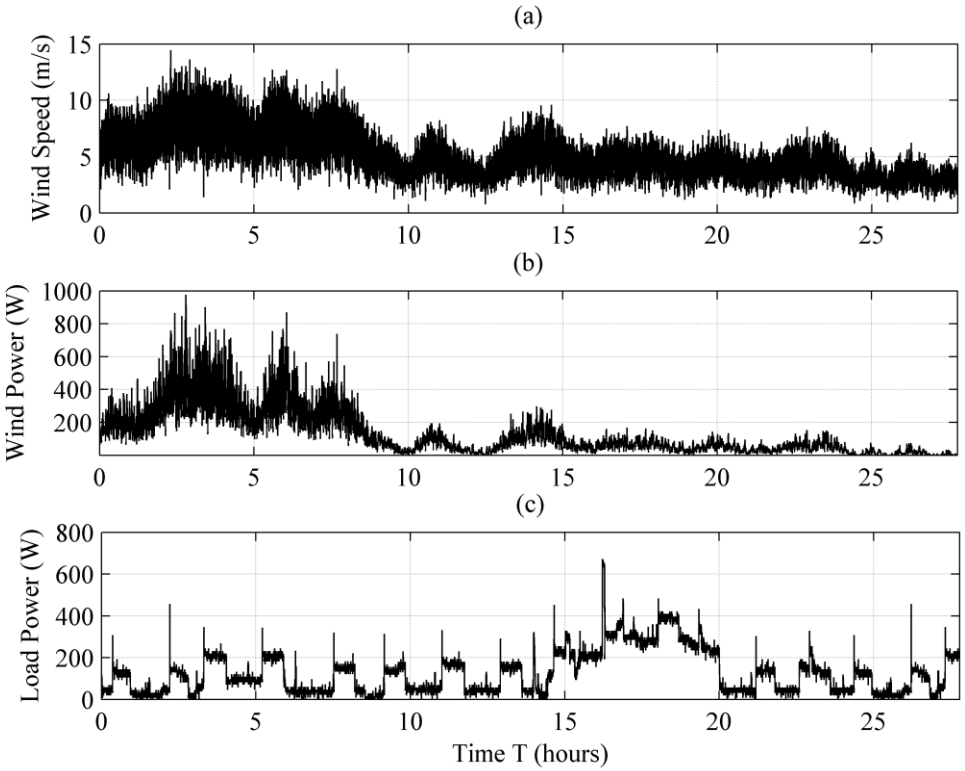

Fig. 9.14 Simulation Inputs: (a) wind speed, (b) generated wind power and (c) load profile

To enable a direct comparison between the hybrid energy storage system and the battery-only based alternatives, the total energy storage rating of the supercapacitor and battery in the hybrid system was set to equal the energy storage rating of the battery only systems. Studies have indicated [228] that lead acid batteries reach the voltage controlled stage in a CVCI charge regime at 70% state-of-charge. So the supercapacitor

to battery energy capacity ratio was set in this example to 30%. The energy storage system ratings used in this simulation have been summarised above in Table 9.2.

9.5.1 Existing System 1: Intermittent Charge Control

In this example, the battery is charged according the output of the renewable generator until an upper voltage threshold is reached. At this point the battery is disconnected from the power source until a lower voltage set point is reached. This method of charge control has been typically used in photo-voltaic systems [202] but examples can be found in in wind/solar-hybrid systems [67], [229] and wind energy systems [230].

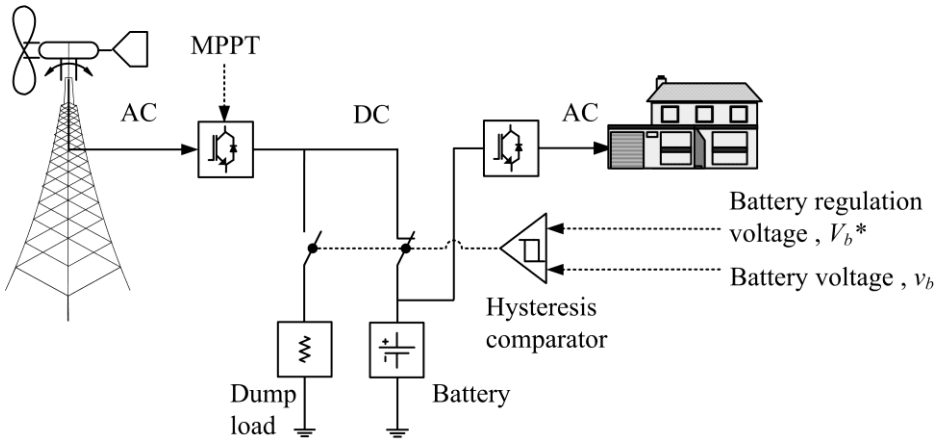

Fig. 9.15 Intermittent charge control with relay controlled dump-load.

To prevent frequent switching of the power to the battery, upper and lower hysteresis limits are used to disconnect the charge power to the battery when a regulation set point (V_{batmax} = 27.5Vdc) is reached and to re-connect the charge power at a lower voltage set-point (V_{bmax} - $V_{bmaxhyst}$ = 25.5Vdc) [230]. Similarly, the control system also protects the battery from over-discharge by disconnecting the load when a lower battery voltage is reached (V_{bmin} = 23.5) and reconnecting it after the battery voltage has risen (V_{bmin} + $V_{bminhyst}$ = 24.5), as has been commonly employed in relevant studies [190], [231], [232]. This is typically referred to as a low-voltage-disconnect (LVD).

A state diagram describing the intermittent charge control system process is shown in Fig. 9.16 below.

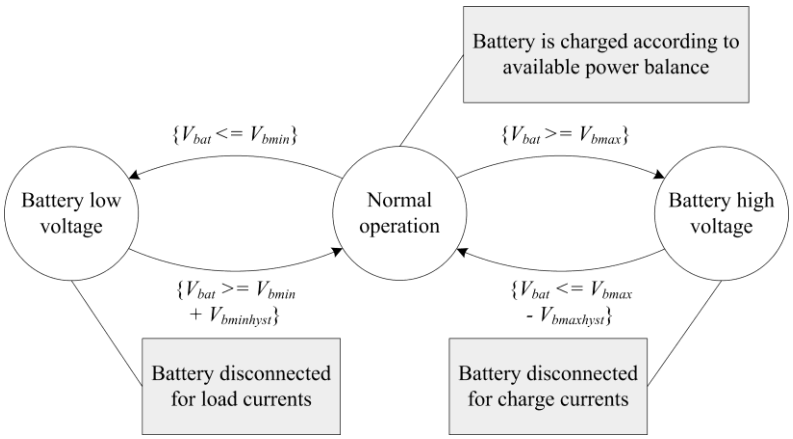

Fig. 9.16 Simulation state diagram representing the hysteresis control of battery voltage

Fig. 9.19 demonstrates the performance of the intermittent charge control system over a representative period during which the battery approaches a full state-of-charge.

9.5.2 Existing System 2: CVCI Charge Control

A commonly employed approach to battery charge regulation in wind-based systems is to utilise a power electronic converter under PWM control to regulate the battery voltage by diverting excess power to a controlled dump load [195], [196] according to a CVCI charge profile [188], [195], [196], [204].

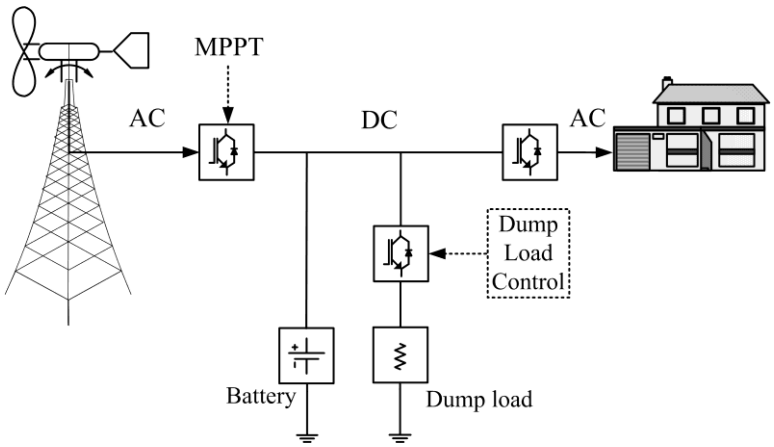

Fig. 9.17 CVCI charge control with PWM controlled dump load

To model the operation of such a system, it was assumed that a unidirectional current controlled converter of the type described in Section 6.5.3 could be employed to control the battery voltage at the charge regulation set point voltage by means of a voltage control loop which diverts power to the dump load. The voltage control loop in this case was nominally implemented based on the assumption that a unidirectional control of converter output current is possible. The system process including over-discharge protection is illustrated in Fig. 9.18. The performance of a nominal system with modelling parameters given in Table 9.1 and the simulation inputs shown in Fig. 9.14 is shown in Fig. 9.20.

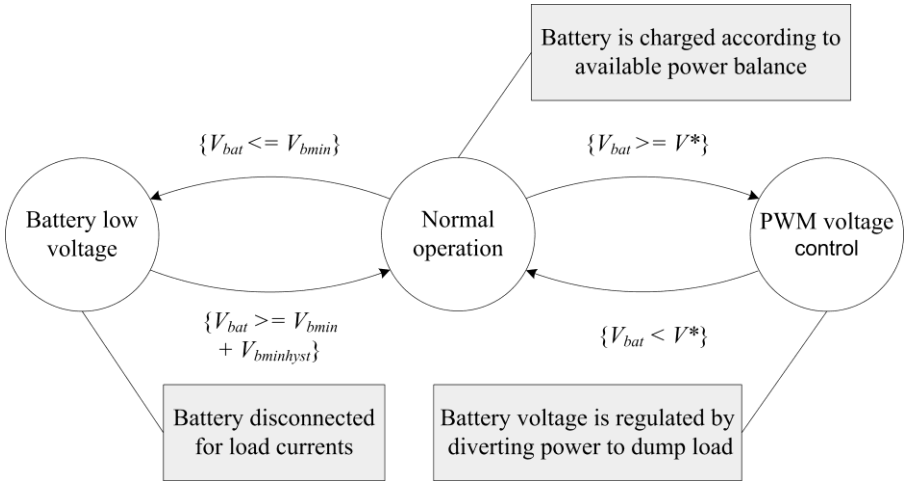

Fig. 9.18 Simulation state diagram representing the hysteresis control of battery voltage

9.5.3 Simulation Results

The operation of the conventional battery voltage control schemes is shown in Figs. 9.19 and 9.20.

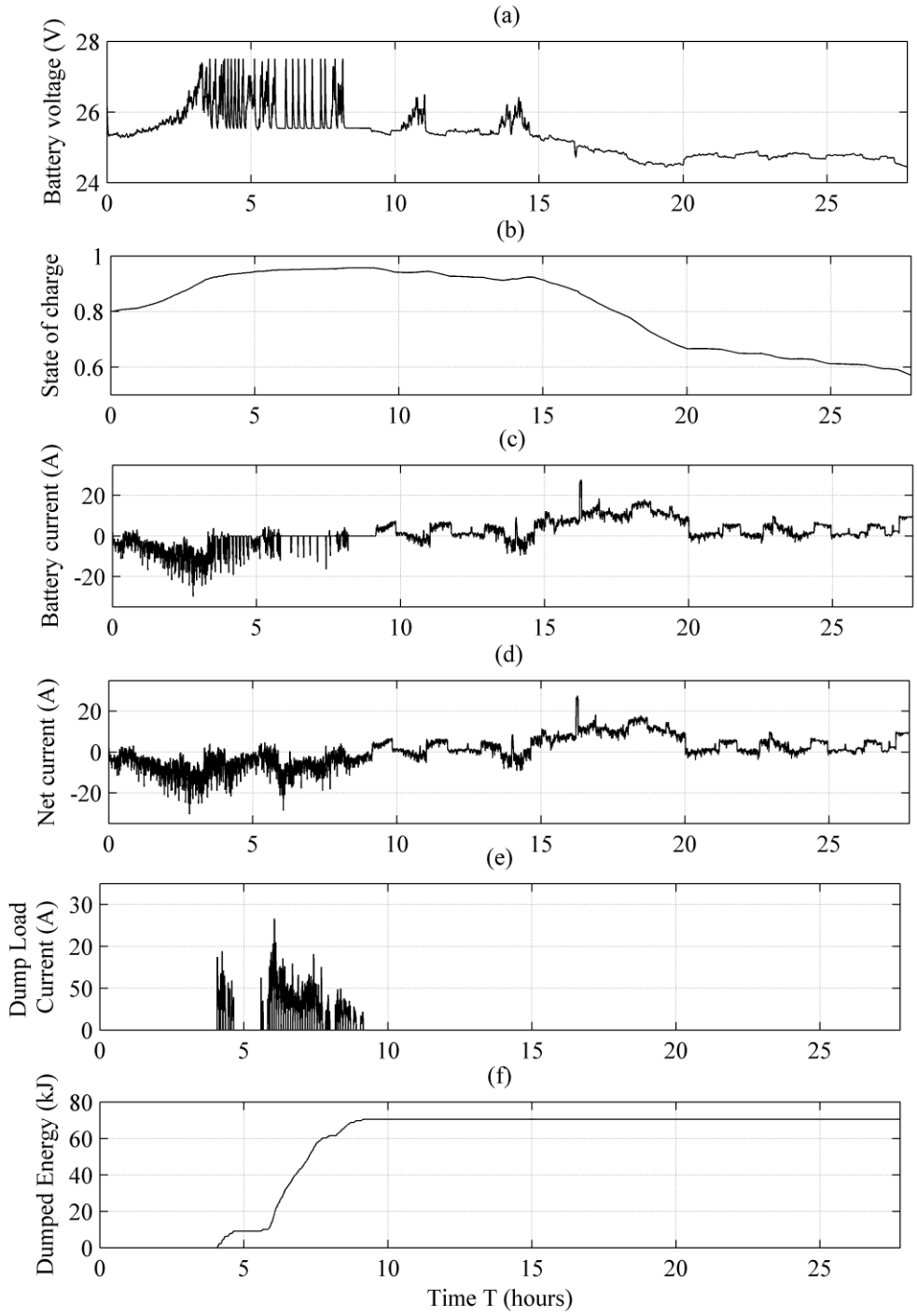

Fig. 9.19 Intermittent charge controller performance (a) Battery voltage (b) Battery state-of-charge (c) Battery current.

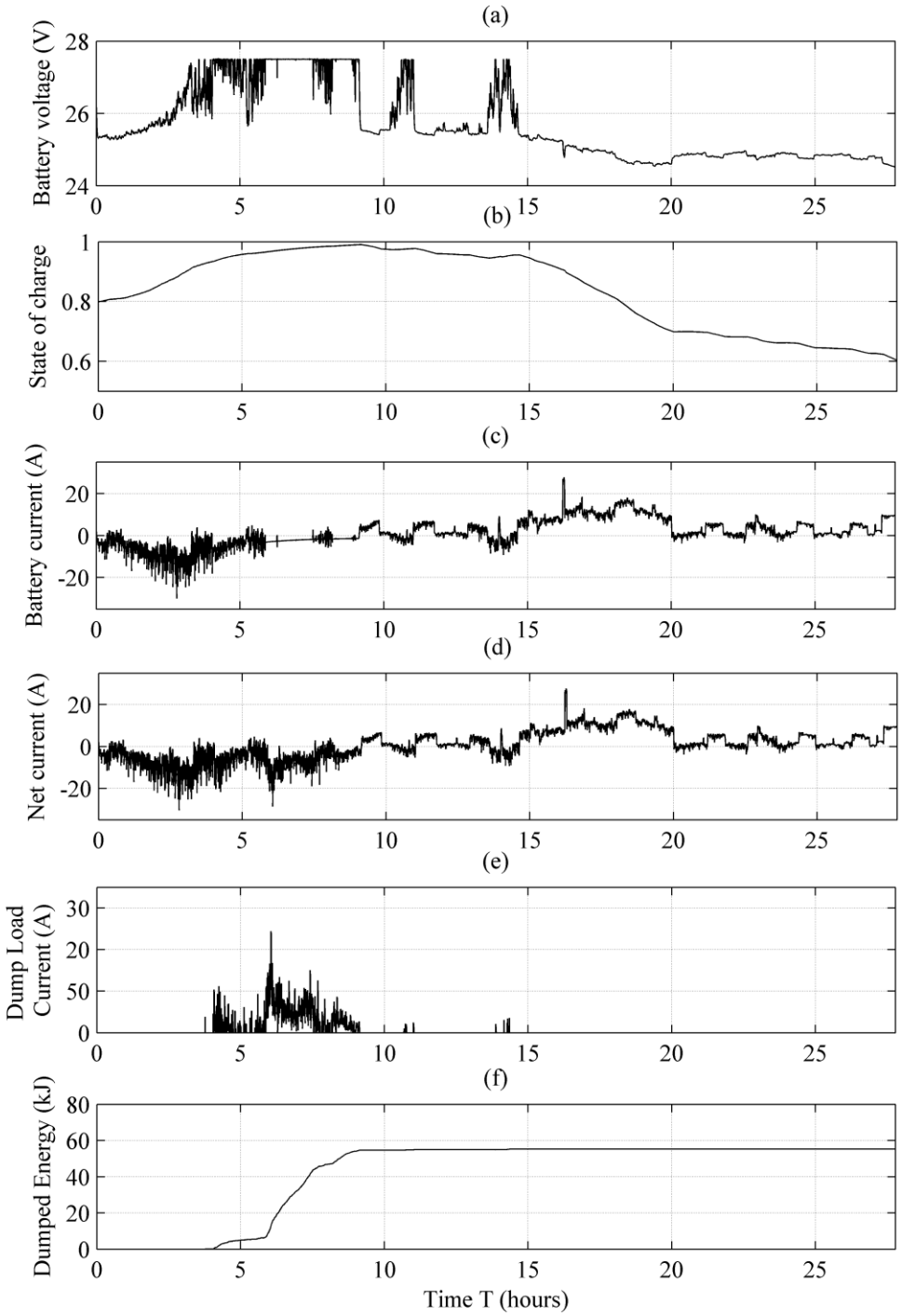

Fig. 9.20 CVCI dump-load controller performance (a) Battery voltage (b) Battery state-of-charge (c) Battery current.

9.6 Supercapacitor/Battery Hybrid Energy Storage Systems

The system shown in Fig. 9.21 employs a battery/supercapacitor hybrid energy storage control system based on the controller design described above in Section 9.3. The

operation is analogous to an energy storage device used to capture energy regenerative braking in vehicular applications which would otherwise be wasted as heat in friction braking. A dump-load has also been included to maintain the operation of the wind-turbine at times during which the battery and the supercapacitor are both unable to accept charge.

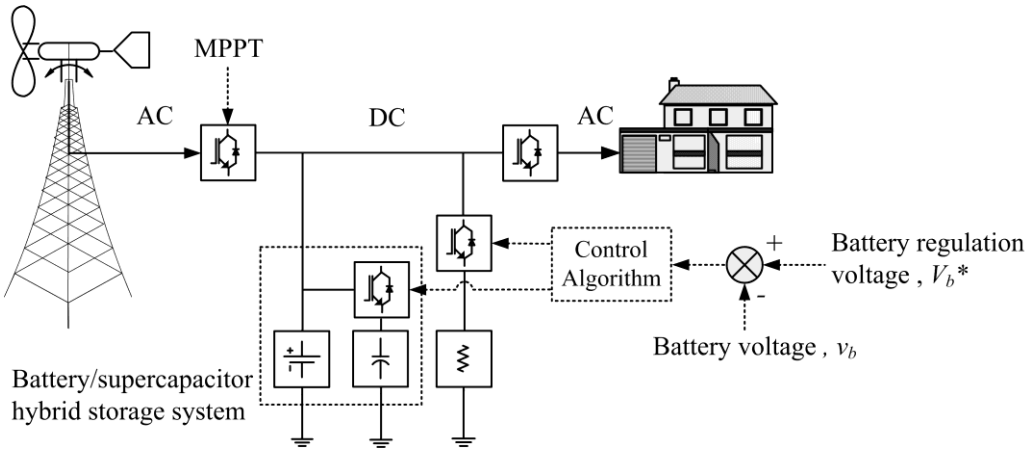

Fig. 9.21 Hybrid energy storage system configuration

Two strategies were developed to control the hybrid energy storage system in Fig. 9.21. The first, described below in Section 9.6.1 is based on a purely voltage based control approach, employing the controller design described in Section 9.3. The controller was designed using the procedure outlined in Section 9.3 and using the battery partial state-of-charge impedance model described in Section 4.2.2. The second, described in Section 9.6.2, is based on a hybrid control loop which uses a priority-based scheduling algorithm to switch between the voltage based control and the active current-filtering strategy outlined in Section 8.1.2 in real-time, depending on the battery and supercapacitor voltage levels.

The system parameters used in the following simulations in Sections 9.6.1 and 9.6.2 are as given in Table 9.2 with the supercapacitor made up from series/parallel combinations

of commercially-available supercapacitor cells described in [113] to achieve the required energy and voltage ratings.

9.6.1 Proposed System 1: Battery Voltage-Based Control System

A state diagram describing the operation of the voltage-based control algorithm is shown below.

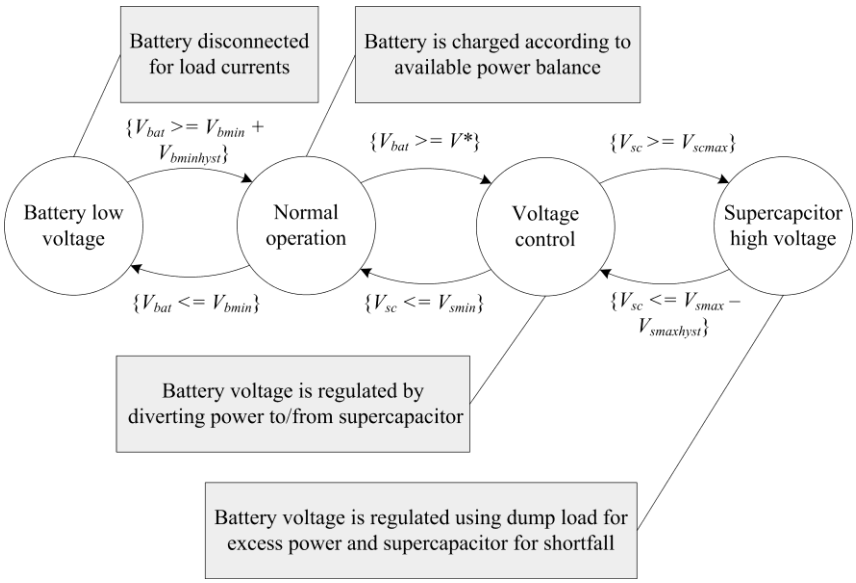

Fig. 9.22 Voltage-based hybrid energy storage control state diagram

During the "normal operation" state, the battery voltage level is within the upper and lower boundaries (V_{bmin} and V*) and receives the available net charge-power according to wind and load variations. If the battery voltage rises to the upper regulation set point, V*, the system enters the "voltage controlled" state and the battery voltage is maintained at that level. This continues until either: the supercapacitor voltage has fallen to a predefined minimum level, V_{smin} (indicating that the supercapacitor energy has discharged into the battery) or if the supercapacitor voltage rises to an upper threshold V_{smax} (indicating that the supercapacitor is unable to accept further charge). In this case, the system regulates the battery voltage by use the of the dump load to absorb excess

power and the supercapacitor to provide any shortfall. This continues until the supercapacitor voltage has fallen by a predefined amount $V_{smaxhyst}$.

9.6.2 Proposed System 2: Battery Voltage/Current Filter Hybrid Control

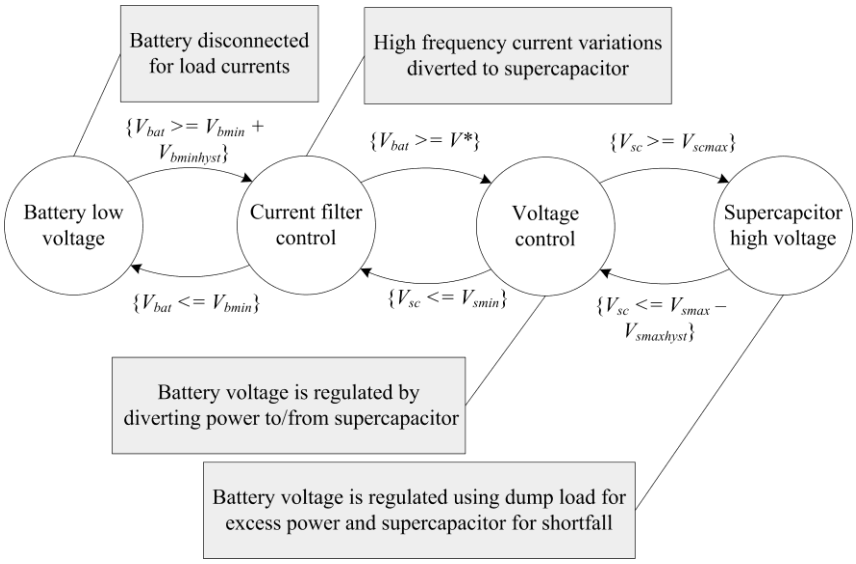

Fig. 9.23 Voltage control/current filter hybrid energy storage control state diagram

Chapter 8 has showed how, by implementation of a low pass filter current-based algorithm to direct the high frequency current content away from the battery, the estimated battery cycle-life can be extended. Comparison of Figs. 9.20 (a) and 9.24(a) (below) shows that by controlling the battery voltage using a bidirectional converter and a supercapacitor, the battery can be charged at a suitable level for longer periods [Fig. 9.24(a)] than would be possible with a typical dump-load-based control scheme [Fig. 9.20(a)]. Based on these two sets of results, a novel control strategy which combines the benefits of both the current-filtering approach and the voltage-control approach was developed. The state diagram, Fig. 9.23, illustrates the process.

Fig. 9.23 represents a novel, dynamically re-configurable control system in which the mode of control is dependent on external stimuli such as battery and supercapacitor

voltage levels. This control strategy operates in a similar manner as the system described in Section 9.6.1 except that the “Normal operation” state is replaced with the “Current-filter control” state in which the system employs the current-filtering mode of control described in Section 8.1.2.

9.6.3 Simulation Results

Simulation results showing the operation of the battery-supercapacitor hybrid energy storage systems under a voltage based control scheme are shown in Figs. 9.24 and 9.25 (below) under the same example wind and load conditions shown in Fig. 9.14 and the main modelling parameters given in Table 9.1 and 9.2

As the battery voltage reaches the charge regulation set point of 27.5V in Fig 9.24(a) (below), the system regulates the battery voltage by charging the supercapacitor with the power that the battery is not able to store. Then, the battery voltage is maintained at the set point level of 27.5V until the stored energy in the supercapacitor has been transferred into the battery. In this way, the energy which the battery cannot accept is temporarily stored in the supercapacitor then transferred to the battery by charging at a suitable charging voltage level as shown in Fig 9.24(a). In this example the dump load is not used in contrast to the existing system’s performance shown in Figs. 9.20 (f) and 9.17 (f).

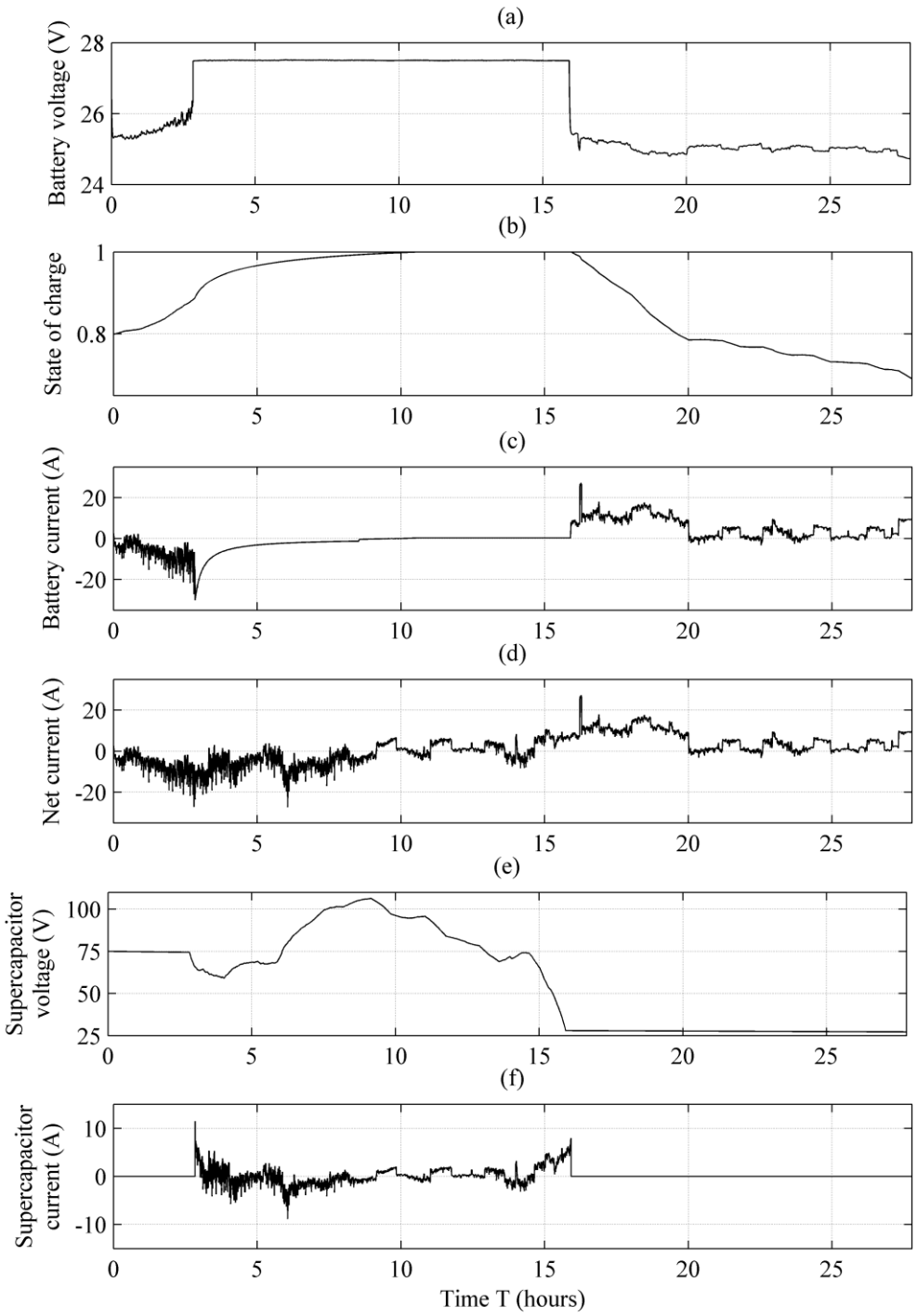

Fig 9.24 Voltage based control algorithm system simulation outputs under a wind-charging regime at high state of charge. Low-pass filter time constant = 3600.

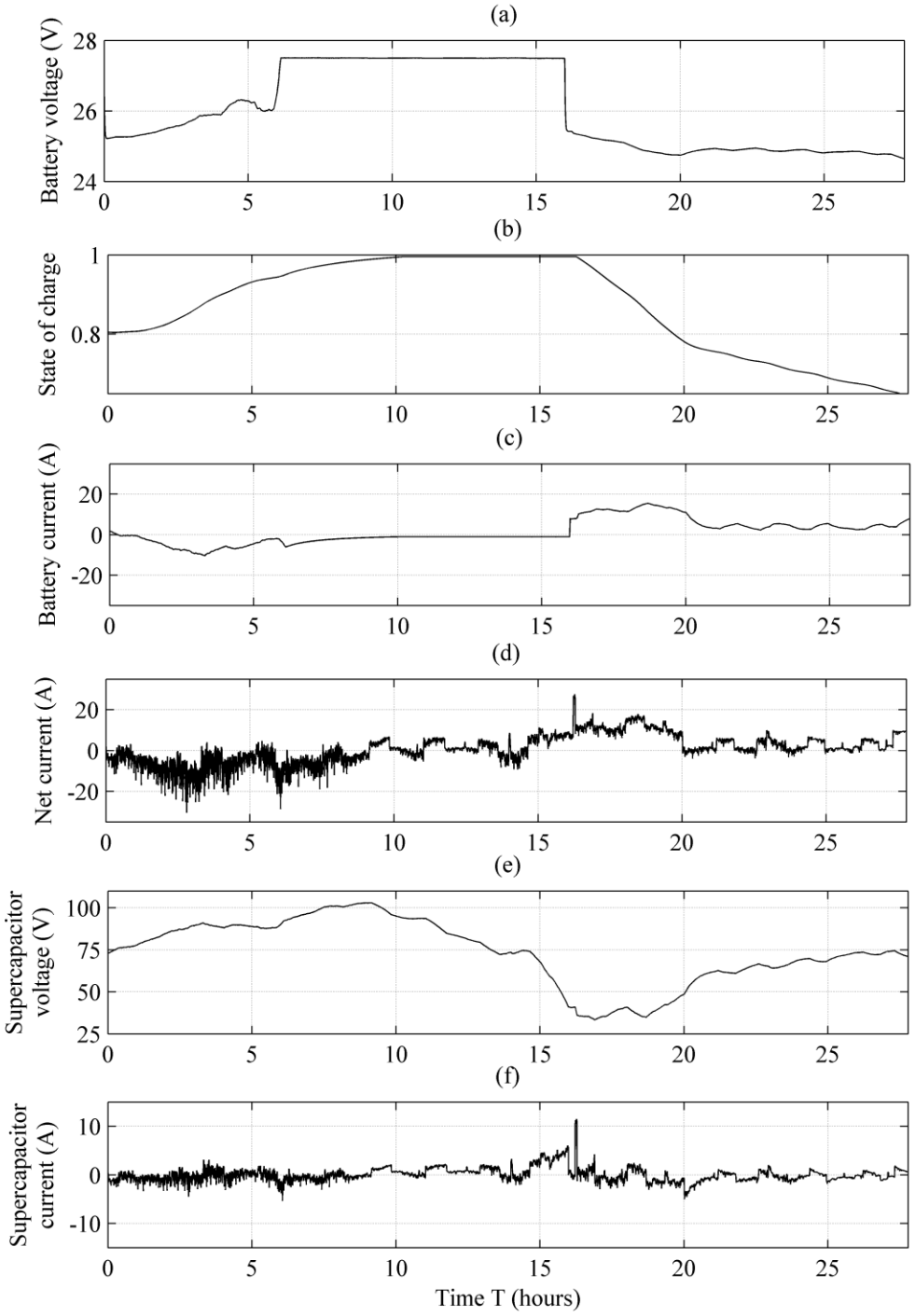

Fig 9.25 Voltage/low-pass filter hybrid control algorithm system simulation outputs under a wind-charging regime at high state of charge. Low-pass filter time constant = 3600.

The sample simulation results of Fig. 9.25 show the system is in the "Current filter control" state initially as the battery voltage is within the upper and lower threshold limits (V^* and V_{bmin}). In this state, the high frequency content of the net current

waveform is diverted to/from the supercapacitor. When the battery voltage reaches the regulation level, V^* at approximately time: T=6 hours, the system enters the "Voltage control" state. The system remains in this state until T=16 hours (approx.) when the supercapacitor energy has been discharged and its voltage has then fallen to a pre-set level (V_{smin}). At this stage, the control loop switches back to the "Current filter control" state.

This example has been used to illustrate the potential performance benefits of the dynamically re-configurable controller in terms of reduced current polarity reversals implying reduced state-of-charge fluctuations and therefore increased cycle-life in addition to a reduction in dumped energy compared with the existing alternative systems shown in Figs. 9.20 and 9.19.

9.7 Comparison of Battery Voltage Control Schemes

Sections 9.5 and 9.6 have illustrated the performance of the systems under examination over a relatively short period of 26 hrs. To compare their relative performances, the effect of the different charge control strategies on the state-of-charge and dumped energy over a representative period of 12 days (approx.) has been considered. The wind turbine and energy storage simulation parameters have been kept the same as in Sections 9.5 and 9.6. Fig. 9.26 plots the simulated battery state-of-charge and dumped energy over this period.

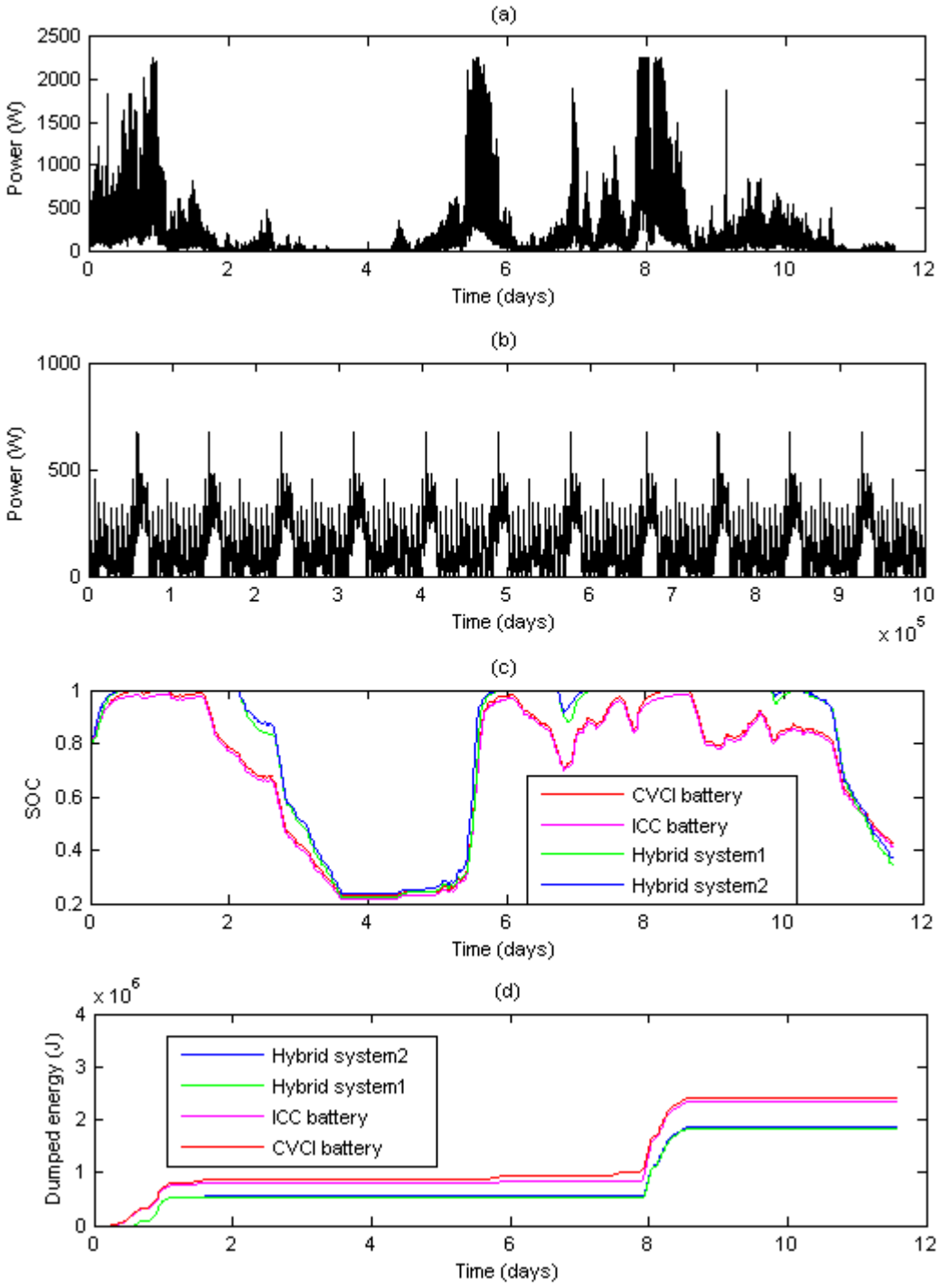

Fig 9.26 (a) Wind power profile: Turbulence intensity = 0.2 (b) Repeated one-day domestic load profile (c) Battery state-of-charge (d) Dumped energy. (Hybrid system1 is the voltage-based control scheme. Hybrid system 2 is the voltage/current-filter control scheme)

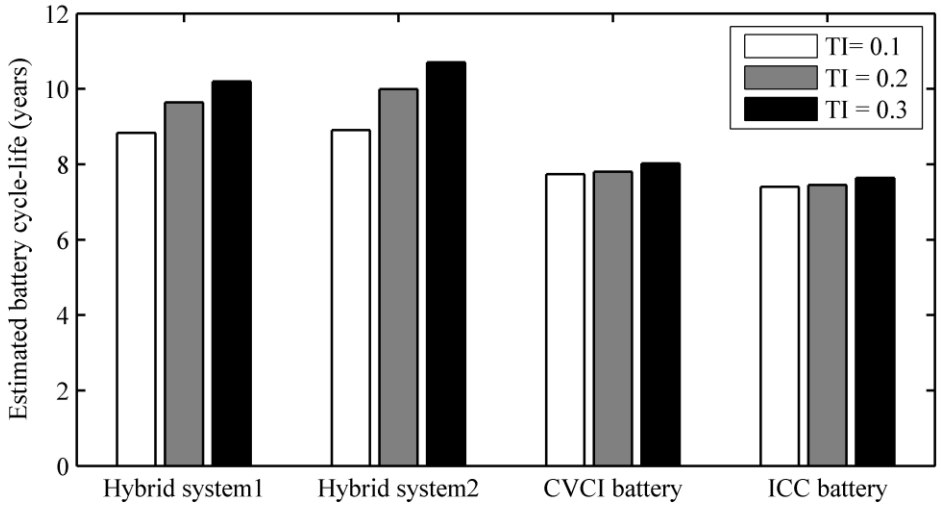

Fig 9.27 Estimated cycle-life at different turbulence intensities. (Hybrid system1 is the voltage-based control scheme. Hybrid system 2 is the voltage/current-filter control scheme)

Fig. 9.26 (a) shows the battery state of charge over the course of the simulation interval. The benefit of the proposed hybrid systems in terms of energy capture can be seen from Fig. 9.26 (b). At times of high battery state of charge [see Fig. 9.26 (a)] the energy dissipated in the dump load in the conventional systems can be seen to be greater than the in the proposed hybrid systems. The reason for this is that excess energy is stored in the supercapacitor module for re-use which would otherwise be dumped in the conventional systems. It should be noted that all systems started with the same initial energy.

The state-of-charge variations in the conventional systems can be seen to be greater over the course of this simulation period in Fig. 9.26 (a). The effect of this is to reduce the expected cycle-life as shown in Fig. 9.27 under different levels of turbulence intensity in the range 0.1 -0.3.

The effect of the reduction in dumped energy by use of the proposed control schemes is that the battery can be maintained at a higher state-of-charge over the course of the

simulation with a reduction in battery charge/discharge cycle range. This in turn has the effect of increasing the estimated battery cycle life, based on this simulation interval, as the major discharge cycles have a lower range in the hybridised systems.

9.8 Hardware Validation of Hybrid Control Strategy

In this test, the same energy storage components as used in Section 8.2.2 were used consisting of four 75Ah sealed lead-acid batteries [12] with a 24Vdc nominal bank voltage and twenty-two 2.7V/1800F supercapacitors [13] connected in series. To confirm the operation of the hybrid control scheme, the proposed battery/supercapacitor was subjected to a representative (wind-load) power profile as shown in Figs. 9.29 and 9.29 below.

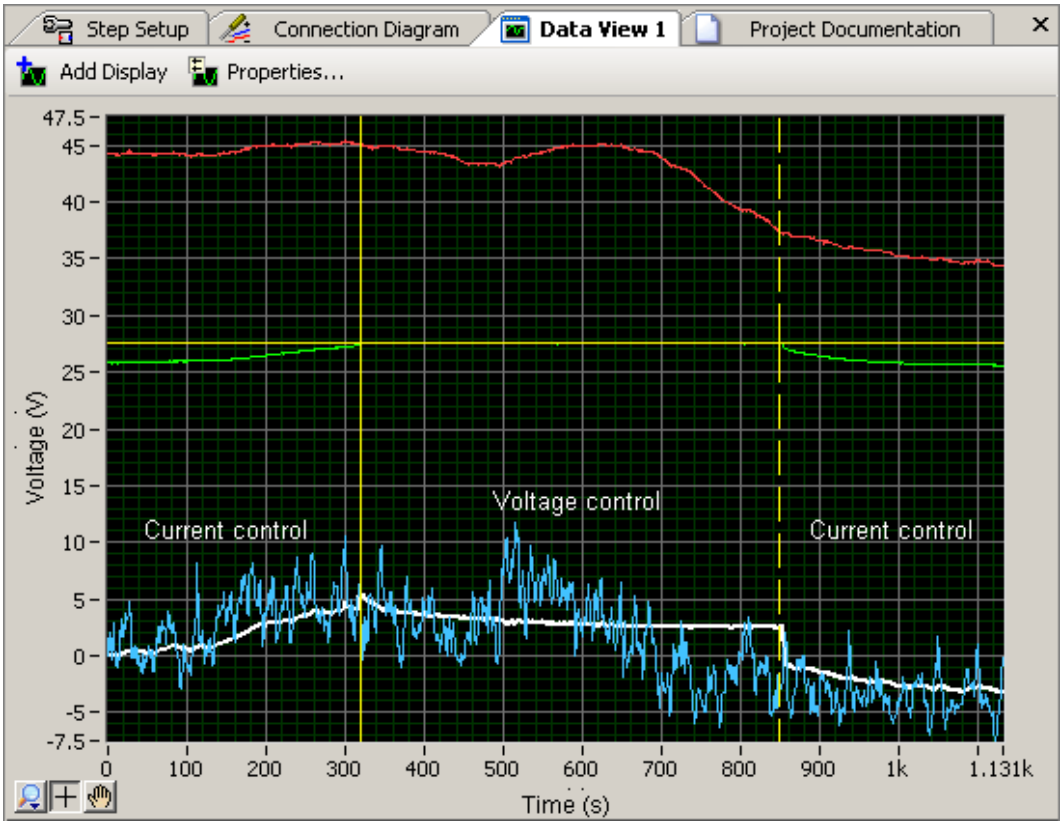

Fig. 9.28 Measured results: Red trace: Supercapacitor voltage. Green trace: Battery voltage. Blue trace: Net current. White trace: Battery current (1V/Amp).

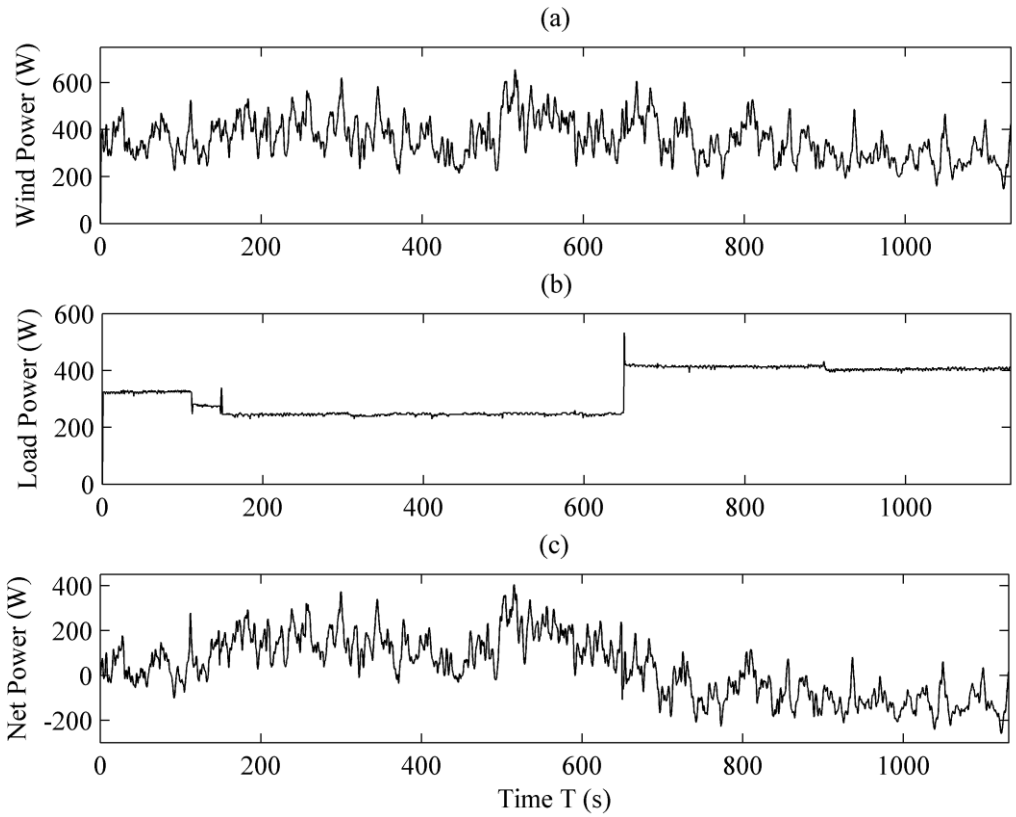

Fig. 9.29 Test inputs for simulation in Fig. 9.27: (a) Wind power (b) Load power (c) Net power

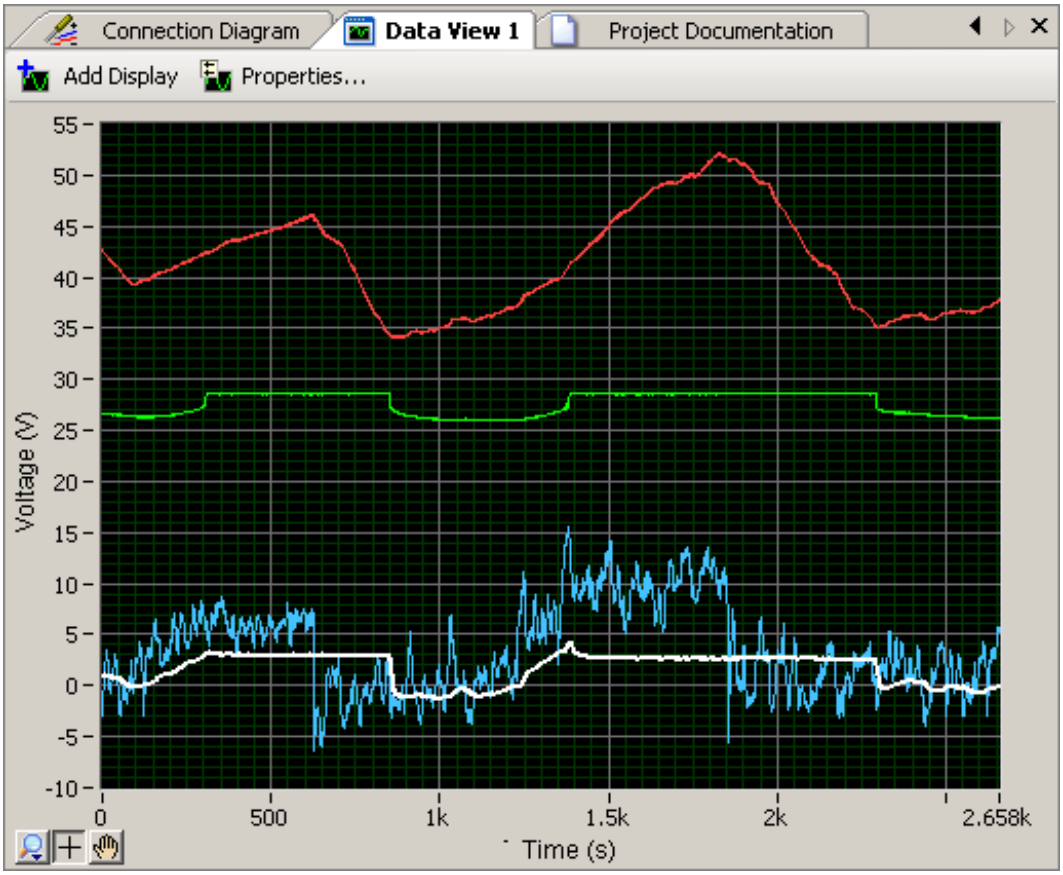

Fig. 9.30 Measured results: Red: Supercapacitor voltage. Green: Battery voltage. Blue trace: Net current. White trace: Battery current (1V/Amp).

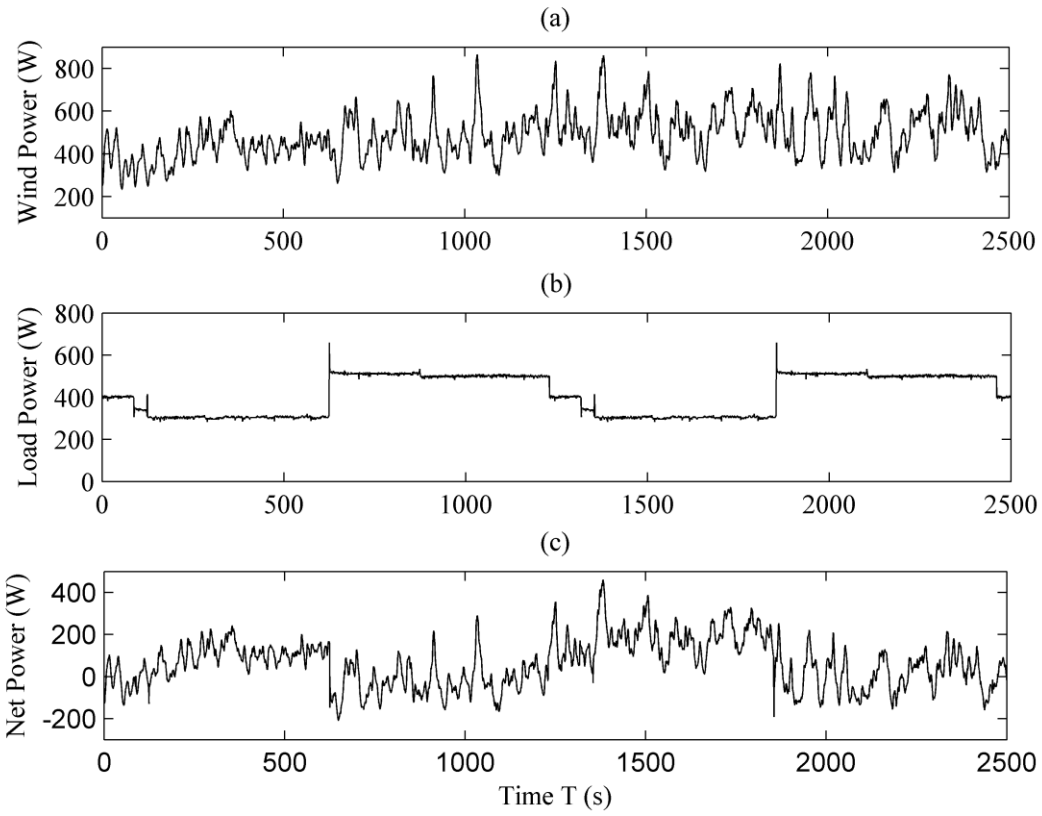

Fig. 9.31 Test inputs for Fig. 9.29: (a) Wind power (b) Load power (c) Net power.

9.9 Summary and Discussion

This chapter has considered one of the shortcomings of battery energy-storage systems in wind-charging applications, that the wind power-profile seldom matches a defined charging-strategy. Charging strategies usually require that the rate of charge is reduced at high states of charge therefore limiting the power that the battery can absorb. This chapter has presented a novel, actively controlled supercapacitor/battery hybrid energy system which has been shown to improve the overall performance of the energy storage system in terms of charge power acceptance at high states of charge.

A control system design has been presented which is used to maintain battery voltage stability at high states of charge by diverting power to/from a supercapacitor energy storage system. The design process has been described and the stability of the switched non-linear system has been considered. The operation and feasibility of the control system has been demonstrated by simulation and experiment. This voltage control strategy has been extended to combine the current-filtering control scheme described previously in Section 8.1.2 as part of a novel, dynamically–reconfigurable controller. The proposed strategies can be seen to improve battery voltage stability, decrease dumped energy and an improvement in battery cycle-life has been estimated.

A similar control approach can be used to design a voltage control loop for the boost converter where the voltage on the high side is controlled. However, with this configuration, the performance of the achievable response is limited by the presence of the well documented [233-235] right-half-plane zero in the control to output voltage transfer function. To help mitigate this issue a sliding-mode alternative control for the bidirectional inverting buck/boost converter was proposed and evaluated as described [218] (a publication resulting from this research) to be able to control the battery voltage

in battery grids whose voltage can be higher or lower than the supercapacitor bank voltage. This controller has the advantage of global stability whereas control of the half-bridge boost converter (or inverting buck/boost converter) output high side voltage by conventional (linear) methods cannot, at present, guarantee global stability.

One of the limitations of the proposed system in this chapter is prohibitive cost. Since the supercapacitor energy rating has been set to 20-30% of the battery rating, this would amount to a significantly more expensive device than any estimated savings. However, the principle of use can still apply in systems employing a significantly lower supercapacitor to battery capacity ratio. In addition, if the price of supercapacitors continues to fall as the trend in Fig. 8.20 would appear to indicate there may come a time when a cost benefit analysis would prove more favourable.

Chapter 10: Conclusions

10.1 Introduction

This thesis has presented the design, simulation, implementation and analysis of an active hybrid system consisting of battery and supercapacitor energy storage devices for wind-power applications. Chapters 1–5 describe the methodologies used to develop a software platform capable of simulating its performance over a representative period. Chapter 6 describes the hardware development for a hysteretic current controlled DC/DC converter used to control the flow of power to and from the supercapacitor. Chapter 7 has described the approach used to determine the optimal supercapacitor/battery energy storage system sizing ratio.

Chapter 8 has shown new results which quantify the increase in battery cycle-life that can be achieved using a power-filtering control strategy to the distribution of power between the supercapacitor and the battery. In addition, the relationship between the controller low-pass filter time-constant setting, battery life and supercapacitor rating requirement has been illustrated. A novel concept was introduced of using the hysteretic-current controlled DC/DC converter in an active filtering application by diverting high frequency current variations to the supercapacitor energy storage system. The system performance has been shown to be functional by experiment.

Power systems simulations often do not consider the effects of a charge regulation strategy [236]. Typically, practical systems include a means by which the power to the battery can be regulated at high states of charge (a charge regulation strategy) which can cause a significant reduction in wind-energy capture. To consider this, Chapter 9 has described a novel control approach which uses the supercapacitor energy storage device

to support battery-voltage as part of a constant-current/constant-voltage charge regulation strategy. In doing so, it is shown that the system provides a means by which the battery-charge is regulated at high states of charge according to an appropriate charge strategy whilst also increasing the ability of the storage system to accept charge. The design of the control strategy is described in detail, its functionality proven by experiment and its performance benefits are demonstrated by simulation. After this, the hardware system developed in Chapter 9 was then modified so that the mode of operation of the real-time embedded controller could switch between active-current filtering control and a voltage-based control scheme, combining the benefits of both strategies.

Chapters 1 to 7 represent the development of a simulation environment including a high-definition turbulent wind-speed generator, dynamic mechanical modelling of the wind turbine drive-train, averaged converter models and methodologies for estimating an optimal wind/battery capacity ratio and battery cycle-life. This is in line with Objective 1 (Section 1.6).

10.2 Supercapacitors for Power Filtering

A review of previous studies revealed a lack of quantifiable data to prove the benefits of a power-filtering supercapacitor control strategy for increased battery life-time in wind energy applications. The present study has demonstrated the benefits of such a strategy by presenting new results which quantify the advantages numerically, by satisfying the outcomes of Objectives 2 and 3 (Section 1.6). Battery cycle-life increase of 18% is predicted based on a representative week-long simulation profile employing a 3600s low-pass filter controller time-constant. The results also indicate a direct correlation between the low-pass filter controller time-constant and increase in battery cycle-life,

previously not reported.

A basic system-level simulation has also been carried out to assess the effect of wind turbulence intensity level on battery cycle-life over the course of a year-long simulation interval. Novel results have shown that the estimated battery cycle-life is inversely proportional to turbulence intensity in systems employing only battery storage. The study has gone on to show how the degree of hybridisation of the battery energy storage system with additional supercapacitor storage (under a power filtering approach) can mitigate the effects of increased turbulence intensity in decreasing battery cycle-life.

The key contributions from Chapter 8 can be summarised as follows:

- Novel hardware implementation of an actively-controlled supercapacitor device, optimised to mitigate high-frequency current fluctuations, has been presented and its functionality confirmed (Objective 4, Contribution 4, Chapter 1).
- Benefits of increased battery cycle-life and decreased battery discharge current have been quantified in the proposed system using a week-long simulation (Objective 3, Contribution 3, Chapter 1).
- Operation of the proposed system in terms of battery peak-current reduction and charge/discharge cycles has been demonstrated by experiment (Objective 4, Contribution 4, Chapter 1).
- New simulation results have been presented showing quantitative results which indicate the benefit of the hybridisation of supercapacitor and battery energy storage systems and the methods for doing this have been described. (Objective 2, Contribution 1, Chapter 1).
- The effect of different low pass filter time-constants has been evaluated by simulation and shown to be proportional to increased battery cycle-life and

supercapacitor rating requirement (Objective 2, Contribution 3, Chapter 1).

- A hardware test-bed has been implemented and described which is capable of functional testing of the systems under consideration by experiment (meeting Objective 5, Contribution 4, Chapter 1).

10.3 Supercapacitors for Battery Voltage Support

Power system simulations rarely include the effects of a charge-control strategy on energy capture. Real field-test reports have shown that the energy capture of remote wind-power systems operating in the field can be significantly reduced due to the operation of charge control systems, primarily due to battery voltage fluctuations under turbulent wind conditions [66], [149], [192], [194], [197]. This thesis has considered the use of an additional supercapacitor under a battery voltage control scheme to mitigate this reduction in energy capture. The key results from Chapter 9 fall in line with Objective 6 (see Section 1.5) and can be summarised as follows:

- Use of the battery/supercapacitor combination under the proposed control scheme results in a well-defined battery voltage control capable of holding the battery voltage at an appropriate level for constant voltage charging in the presence of typical wind/load disturbance variations (Contribution 2, Chapter 1).
- Use of the proposed control has been shown to reduce the use of a dump-load in a remote wind-power system to dissipate excess power that the battery cannot store due to charge regulation, under the test conditions presented (Contribution 2, Chapter 1).
- A reduction in dumped energy in the proposed system has been shown by simulation to contribute to maintaining the battery at a higher state-of-charge than in the case of the battery–alone systems. This in turn has been shown to

have a beneficial effect in the reduction of the battery charge-cycle amplitude. Cycle-life aging estimation results have indicated that an increase in battery life can be achieved by use of this control (Contribution 2, Chapter 1).

The hybrid energy storage system employing the voltage-based control has been evaluated in terms of a typical wind-energy application. However, there may be other application-areas in which this system could be of benefit by maintaining the battery state-of-charge at a higher level than would be possible with a battery alone.

10.4 Future Work

One of the limitations of connecting the supercapacitor on the high-side of a synchronous buck-converter acting as the interface between the two energy storage systems is that the supercapacitor must be maintained at a voltage higher than that of the battery. A system employing the converter in this configuration is directly relevant to low-voltage battery grid distributed generation systems [158-161] and renewable telecoms applications, which typically use 48Vdc systems [68], [69]. Section 8.2.5 has demonstrated by experiment how the hysteretic mode of current control can be used in a power filtering application with the battery on the high-side of the synchronous buck converter and the supercapacitor on the low-side. This enables its application with battery grid voltages which are higher than the available supercapacitor bank voltage. However, due to time-constraints, the development of this strategy was limited to proof of the concept. A novel feed-forward control approach has been suggested for this circuit topology and an area of future work will be to develop this configuration and control system further and in greater detail.

The optimisation procedure developed in Section 7.2.2 was based around the use of half hourly data for the wind resource. However, the results in Section 8.5.3 have shown

how battery-life is related to turbulence intensity. Since the optimisation procedure accounts for battery life, it may only be accurate at sites with a low turbulence intensity. As such, the existing procedure has provided a good starting point in the optimisation of the wind/energy storage capacity ratio to minimize life-cycle costs in a wind or wind/diesel system. However an obvious improvement for a future implementation of this procedure will be to include the effects of turbulence in the system sizing algorithm if not computationally too intensive.

The hardware implementations of the systems considered have been demonstrated using a relatively low-computing power real-time controller. While this has been adequate to for demonstration purposes a more optimal approach will be to use a dedicated DSP-based controller for higher accuracy, resolution, sampling rate and to enable more complex controls. In addition, it may be technically advantageous to implement some of the control systems proposed in OP-AMP/analogue form or a digital/analogue mixed signal implementation to further improve control fidelity by removing quantisation error at a reduced cost. This remains an area for future investigation.

The optimal management of hybrid energy storage systems to mitigate the intermittency in renewable energy and, in particular, wind-energy systems is a complex and non-linear task. Currently the lack of unified test procedures and performance metrics may be hindering the objective comparison of hybrid energy storage system controller performance. This is, in part, due to lack of accurate battery life modelling data, highlighting the need for further research in this field. A starting point would be to provide battery life-curve data which reflects the effects of battery stress factors experienced by batteries operating in the field.

This study has provided a systematic means for assessment of hybrid energy storage systems in the context of a wind power application. Previous works [48-50], [56-58] in this area have shown that a low-pass filter based control strategy to provide a good starting point for the distribution of power between the hybridised energy storage systems. The work presented in this thesis has confirmed this by providing novel numerical results. In addition, the problem of charge regulation in autonomous renewable systems has been considered and a hybrid control approach has been shown to combine the benefits of the power filtering approach with increased energy capture. An area for future work will be the development of energy management strategies to build on the real-time controls and analysis presented in this thesis.

References

[1] M. Ceraolo, "New dynamical models of lead-acid batteries," *IEEE Trans. Power Syst.*, vol. 15, pp. 1184-1190, Nov. 2000, DOI: 10.1109/59.898088

[2] M.S. Whittingham, "History, Evolution, and Future Status of Energy Storage," *Proc. IEEE*, vol. 100, pp. 1518-1534, May 2012, DOI: 10.1109/jproc.2012.2190170

[3] *"RCUK Energy Programme: What the Energy Programme funds." Research Councils UK, Polaris House, North Star Ave, Swindon, SN2 1ET*, [Online], Access date: Jul. 2012, Available: http://www.rcuk.ac.uk/research/xrcprogrammes/energy/EnergyResearch/Pages/SUPERGEN.aspx

[4] M. Venables, "Closing in on 2020," *Engineering & Technology*, vol. 7, pp. 28-31, Feb. 2012

[5] B. De Wachter. *"Connecting Distributed Generation (DG) units to the network." Leonardo Energy, London, Jul., 2008.*, [Online], Access date: Jul. 2012, Available: http://www.leonardo-energy.org/connecting-distributed-generation-dg-units-network

[6] M.R. Student, R. Hidalgo, C. Abbey, and G. Joos, "An Expert System for optimal scheduling of a diesel - wind - energy storage isolated power system," *Industrial Electronics, 2009. IECON '09. 35th Annual Conference of IEEE*, Porto, Portugal, 2009, pp. 4293-4298.

[7] G. Coppez, S. Chowdhury, and S.P. Chowdhury, "The importance of energy storage in Renewable Power Generation: A review," *Universities Power Engineering Conference (UPEC), 2010 45th International*, Cardiff, Wales, 2010, pp. 1-5.

[8] G. Coppez, S. Chowdhury, and S.P. Chowdhury, "South African renewable energy hybrid power system storage needs, challenges and opportunities," *Power and Energy Society General Meeting, 2011 IEEE*, Detroit, MI, 2011, pp. 1-9.

[9] H. Bindner, T. Cronin, P. Lundsager, J.F. Manwell, U. Abdulwahid, and I. Baring-Gould, "Lifetime modelling of lead acid batteries," Risø Nat. Lab., Roskilde, Denmark, Apr. 2005.

[10] N. Garimella and N.K.C. Nair, "Assessment of battery energy storage systems for small-scale renewable energy integration," *TENCON 2009 - 2009 IEEE Region 10 Conference*, Singapore, 2009, pp. 1-6.

[11] V. Svoboda, Wenzl, H., Kaiser, R., Jossen, A., Baring-Gould, I., Manwell, J., Lundsager, P., Bindner, H., Cronin, T., Nørgård, P., Ruddell, A., Perujo, A., Douglas, K., Rodrigues, C., Joyce, A., Tselepis, S., van der Borg, N., Nieuwenhout, F., Wilmot, N., Mattera, F., and D. Sauer, "Operating conditions of batteries in off-grid renewable energy systems," *Solar Energy*, vol. 81, pp. 1409-1425, 2007

[12] N. Kularatna, "Rechargeable batteries and their management," *IEEE Instrum. Meas. Mag.*, vol. 14, pp. 20-33, April 2011, DOI: 10.1109/mim.2011.5735252

[13] L. Peiwen, "Energy storage is the core of renewable technologies," *Nanotechnol. Mag.*, vol. 2, pp. 13-18, Dec. 2008, DOI: 10.1109/MNANO.2009.932032

[14] A. Etxeberria, I. Vechiu, H. Camblong, and J.M. Vinassa, "Hybrid Energy Storage Systems for renewable Energy Sources Integration in microgrids: A review," *International Power and Energy Conference, IPEC, 2010 Conference Proceedings*, Singapore, 2010, pp. 532-537.

[15] B.R. Alamri and A.R. Alamri, "Technical review of energy storage technologies when integrated with intermittent renewable energy," *Sustainable Power Generation and Supply, 2009. SUPERGEN '09. International Conference on*, Nanjing, China, 2009, pp. 1-5.
[16] P.J. Hall and E.J. Bain, "Energy-storage technologies and electricity generation," *Energy Policy*, vol. 36, pp. 4352-4355, Oct. 2008, DOI: 10.1016/j.enpol.2008.09.037
[17] G. Plante, *The Storage of Electrical Energy*. Whitefish, MT Publisher Kessinger Publishing, 2007 1859 ISBN: 9781154857726
[18] R. Sebastian and R. Pena-Alzola, "Study and simulation of a battery based energy storage system for wind diesel hybrid systems," *Energy Conference and Exhibition (ENERGYCON), 2012 IEEE International*, Florence, Italy 2012, pp. 563-568.
[19] D. Gielen, "Electricity Storage and Renewables for Island Power: A Guide for Decision Makers," ed: IRENA (International Renewable Energy Agency), 2012.
[20] T. Lambert, P. Gilman, and P. Lilienthal, "Micropower system modeling with HOMER," *Integration of Alternative Sources of Energy* ed New York: John Wiley & Sons, 2006.
[21] G. Coppez, S. Chowdhury, and S.P. Chowdhury, "Review of battery storage optimisation in Distributed Generation," *Power Electronics, Drives and Energy Systems (PEDES) & 2010 Power India, 2010 Joint International Conference on*, New Delhi, India, 2010, pp. 1-6.
[22] V. Musolino, L. Piegari, and E. Tironi, "New full frequency range supercapacitor model with easy identification procedure," *IEEE Trans. Ind. Electron.*, vol. PP, pp. 1-1, Aug. 2012, DOI: 10.1109/tie.2012.2187412
[23] H.I. Becker, "Low voltage electrolytic capacitor " United States Patent US patent 2800616, 23 July 1957.
[24] J. Schindall, "The Charge of the Ultracapacitors," *IEEE Spectr.*, vol. 44, pp. 42-46, 2007, DOI: 10.1109/mspec.2007.4378458
[25] B.E. Conway, *Electrochemical supercapacitors : scientific fundamentals and technological applications*. New York: Plenum Press, 1999. ISBN: 9780306457364
[26] G.L. Bullard, H.B. Sierra-Alcazar, H.L. Lee, and J.L. Morris, "Operating principles of the ultracapacitor," *IEEE Trans. Magn*, vol. 25, pp. 102-106, Jan. 1989, DOI: 10.1109/20.22515
[27] A.F. Burke, J.E. Hardin, and E.J. Dowgiallo, "Application of ultracapacitors in electric vehicle propulsion systems," *Power Sources Symposium, 1990., Proceedings of the 34th International*, Cherry Hill, NJ, 1990, pp. 328-333.
[28] Z. Haihua, T. Bhattacharya, T. Duong, T.S.T. Siew, and A.M. Khambadkone, "Composite Energy Storage System Involving Battery and Ultracapacitor With Dynamic Energy Management in Microgrid Applications," *IEEE Trans. Power Electron.*, vol. 26, pp. 923-930, Mar. 2011, DOI: 10.1109/IPEC.2010.5543543
[29] S. Vazquez, S.M. Lukic, E. Galvan, L.G. Franquelo, and J.M. Carrasco, "Energy Storage Systems for Transport and Grid Applications," *IEEE Trans. Ind. Electron.*, vol. 57, pp. 3881-3895, Dec. 2010, DOI: 10.1109/tie.2010.2076414
[30] H. Tai-Sik, M.J. Tarca, and P. Sung-Yeul, "Dynamic Response Analysis of DC-DC Converter With Supercapacitor for Direct Borohydride Fuel Cell Power Conditioning System," *IEEE Trans. Power Electron.*, vol. 27, pp. 3605-3615, 2012, DOI: 10.1109/tpel.2012.2185711

[31] P.H. Mellor, N. Schofield, and D. Howe, "Flywheel and supercapacitor peak power buffer technologies," *Electric, Hybrid and Fuel Cell Vehicles (Ref. No. 2000/050), IEE Seminar*, 2000, pp. 8/1-8/5.

[32] S. Lemofouet and A. Rufer, "A Hybrid Energy Storage System Based on Compressed Air and Supercapacitors With Maximum Efficiency Point Tracking (MEPT)," *IEEE Trans. Ind. Electron.*, vol. 53, pp. 1105-1115, 2006, DOI: 10.1109/tie.2006.878323

[33] P. Bentley and D.A. Stone, "The parallel combination of a valve regulated lead acid cell and supercapacitor for use as a hybrid vehicle peak power buffer," *Power Electronics and Applications, 2005 European Conference on*, Dresden, Germany, 2005, pp. 10 pp.-P.10.

[34] P. Bentley, D.A. Stone, and N. Schofield, "The parallel combination of a VRLA cell and supercapacitor for use as a hybrid vehicle peak power buffer," *J. Power Sources*, vol. 147, pp. 288-294, 2005, DOI: 10.1016/j.jpowsour.2005.01.016

[35] V. Brslica, "Supercapacitor for engine cranking," *MECHATRONIKA, 2010 13th International Symposium*, Teplice, Slovakia, 2010, pp. 14-15.

[36] L. Hanmin, W. Zhixin, Q. Shutong, and L. Yunhai, "Improvement of engine cold start capability using supercapacitor and lead-acid battery hybrid," *Applied Power Electronics Conference and Exposition, 2008. APEC 2008. Twenty-Third Annual IEEE*, Austin, TX, 2008, pp. 668-675.

[37] G. Wenzhong, W. Xiaoyu, and E. Muljadi, "Power capacity specification for energy storage in wind application using probability- based method," *Energy Conversion Congress and Exposition (ECCE), 2011 IEEE*, 2011, pp. 2125-2132.

[38] G. Lijun, R.A. Dougal, and L. Shengyi, "Power enhancement of an actively controlled battery/ultracapacitor hybrid," *Power Electronics, IEEE Transactions on*, vol. 20, pp. 236-243, 2005, DOI: 10.1109/tpel.2004.839784(410) 20

[39] L. Gao, R.A. Dougal, and S. Liu, "Active power sharing in hybrid battery/capacitor power sources," *Applied Power Electronics Conference and Exposition, 2003. APEC '03. Eighteenth Annual IEEE*, Miami, 2003, pp. 497-503 vol.1.

[40] S. Pay and Y. Baghzouz, "Effectiveness of battery-supercapacitor combination in electric vehicles," *Power Tech Conference Proceedings, 2003 IEEE Bologna*, Bologna, Italy, 2003.

[41] J.M. Miller and G. Sartorelli, "Battery and ultracapacitor combinations - Where should the converter go?," *Vehicle Power and Propulsion Conference (VPPC), 2010 IEEE*, Lille, France, 2010, pp. 1-7.

[42] A.C. Baisden and A. Emadi, "Advisor-based model of a battery and an ultra-capacitor energy source for hybrid electric vehicles," *IEEE Trans. Veh. Technol.*, vol. 53, pp. 199-205, 2004, DOI: 10.1109/TVT.2003.822004

[43] E. Schaltz, A. Khaligh, and P.O. Rasmussen, "Influence of Battery/Ultracapacitor Energy-Storage Sizing on Battery Lifetime in a Fuel Cell Hybrid Electric Vehicle," *IEEE Trans. Veh. Technol.*, vol. 58, pp. 3882-3891, Oct. 2009, DOI: 10.1109/tvt.2009.2027909

[44] R. Carter, A. Cruden, and P.J. Hall, "Optimizing for Efficiency or Battery Life in a Battery/Supercapacitor Electric Vehicle," *IEEE Trans. Veh. Technol.*, vol. 61, pp. 1526-1533, May 2012, DOI: 10.1109/tvt.2012.2188551

[45] M. Ortuzar, J. Moreno, and J. Dixon, "Ultracapacitor-Based Auxiliary Energy System for an Electric Vehicle: Implementation and Evaluation," *IEEE Trans. Ind. Electron.*, vol. 54, pp. 2147-2156, Aug. 2007, DOI: 10.1109/tie.2007.894713

[46] P. Thounthong, V. Chunkag, P. Sethakul, B. Davat, and M. Hinaje, "Comparative Study of Fuel-Cell Vehicle Hybridization with Battery or Supercapacitor Storage Device," *IEEE Trans. Veh. Technol.*, vol. 58, pp. 3892-3904, Oct. 2009, DOI: 10.1109/TVT.2009.2028571

[47] J.J. Awerbuch and C.R. Sullivan, "Control of Ultracapacitor-Battery Hybrid Power Source for Vehicular Applications," *Energy 2030 Conference, 2008. ENERGY 2008. IEEE*, Atlanta, GA, 2008, pp. 1-7.

[48] L. Wei and G. Joos, "A power electronic interface for a battery supercapacitor hybrid energy storage system for wind applications," *Proc. IEEE Power Electronics Specialists Conference 2008.*, Rhodes, Greece, 2008, pp. 1762-1768.

[49] L. Wei, G. Joos, and J. Belanger, "Real-Time Simulation of a Wind Turbine Generator Coupled With a Battery Supercapacitor Energy Storage System," *IEEE Trans. Ind. Electron.*, vol. 57, pp. 1137-1145, Apr. 2010, DOI: 10.1109/TIE.2009.2037103

[50] A.M. van Voorden, L.M.R. Elizondo, G.C. Paap, J. Verboomen, and L. van der Sluis, "The Application of Super Capacitors to relieve Battery-storage systems in Autonomous Renewable Energy Systems," *Proc. IEEE Power Tech 2007*, Lausanne, Switzerland, Jul. 2007, pp. 479-484.

[51] F. Liu, J. Liu, and L. Zhou, "A novel control strategy for hybrid energy storage system to relieve battery stress," *Power Electronics for Distributed Generation Systems (PEDG), 2010 2nd IEEE International Symposium on*, Hefei, China, 2010, pp. 929-934.

[52] J. Yan, Oti, K., Yamamura, N., and M. Ishida, "A Study on Electric Power Smoothing System for Lead-acid Battery of Stand-alone Natural Energy Power System Using EDLC," *Power Conversion Conference - Nagoya, 2007. PCC '07*, Nagoya, Japan 2007, pp. 236-242.

[53] J. Yan, K. Oti, N. Yamamura, M. Ishida, and R. Shibata, "Characteristics of Smoothed-power Output Topology of Stand-alone Renewable Power System Using EDLC," *Power Electronics Specialists Conference, 2006. PESC '06. 37th IEEE*, Jeju, South Korea, 2006, pp. 1-7.

[54] J. Yan, R. Shibata, N. Yamamura, and M. Ishida, "A Control Method of Prolonging the Service Life of Battery in Stand-alone Renewable Energy System using Electric Double Layer Capacitor (EDLC)," *Proc. Int. Conf. Power Electronics and Drives Systems 2005*, Kuala Lumpur, Malaysia, 2005, pp. 228-233.

[55] R. Islam, S. Anwar, A.T. Kamal, S.N. Rahman, H.M. Faraby, H. Imtiaz, M.S. Jahan, and F.S. Tulip, "Battery Chemistry Detection Algorithm Implementable with Intelligent Systems: A Step towards the Development of a Novel Charger Applicable for Multi-Chemistry Environment," *Intelligent Information Technology Application, 2008. IITA '08. Second International Symposium on*, Shanghai, China, 2008, pp. 805-810.

[56] X. Qing, L. Xue, W. Yanzhi, M. Pedram, S. Donghwa, and C. Naehyuck, "State of health aware charge management in hybrid electrical energy storage systems," *Design, Automation & Test in Europe Conference & Exhibition (DATE), 2012*, Dresden, Germany, 2012, pp. 1060-1065.

[57] C. Abbey, L. Wei, and G. Joos, "An Online Control Algorithm for Application of a Hybrid ESS to a Wind/Diesel System," *IEEE Trans. Ind. Electron.*, vol. 57, pp. 3896-3904, Dec. 2010, DOI: 10.1109/tie.2010.2051392

[58] E. Ribeiro, A.J.M. Cardoso, and C. Boccaletti, "Power conditioning and energy management in a renewable energy based hybrid system for

telecommunications," *Telecommunications Energy Conference (INTELEC), 2011 IEEE 33rd International*, Amsterdam, Netherlands, 2011, pp. 1-9.
[59] A. Doig, "Off-grid electricity for developing countries," *IEE Review*, vol. 45, pp. 25-28, 1999, DOI: 10.1049/ir:19990104
[60] C. Abbey and G. Joos, "A Stochastic Optimization Approach to Rating of Energy Storage Systems in Wind-Diesel Isolated Grids," *IEEE Trans. Power Syst.*, vol. 24, pp. 418-426, Feb. 2009, DOI: 10.1109/tpwrs.2008.2004840
[61] A.H. Al-Badi and H. Bourdoucen, "Economic analysis of hybrid power system for rural electrification in Oman," *Adaptive Science & Technology, 2009. ICAST 2009. 2nd International Conference on*, Accra, Ghana, 2009, pp. 284-289.
[62] F.A. Bhuiyan and A. Yazdani, "Reliability assessment of a wind-power system with integrated energy storage," *Renewable Power Generation, IET*, vol. 4, pp. 211-220, May. 2010, DOI: 10.1049/iet-rpg.2009.0070
[63] L. Flowers and I. Baring-Gould, "Lessons learned by NREL's village power and rural energy program," *Power Engineering Society General Meeting, 2004. IEEE*, Colorado, USA, 2004, pp. 2093-2097 Vol.2.
[64] J. Gutierrez-Vera, "Renewables for sustainable village power supply," *Power Engineering Society Winter Meeting, 2000. IEEE*, Singapore, 2000, pp. 628-633 vol.1.
[65] F.B. Howard, "A practical analysis of the economic justification for small RAPS systems [remote area power supply]," *Small Wind Power Systems (Digest No. 1996/175), IEE Colloquium on*, 1996, pp. 5/1-5/3.
[66] A.J. Bowen, N. Zakay, and R.L. Ives, "The field performance of a remote 10 kW wind turbine," *Renewable Energy*, vol. 28, pp. 13-33, 2003, DOI: Doi: 10.1016/s0960-1481(02)00011-3
[67] C. Coleman, "Hybrid power system for a remote microwave repeater site in the Dominican Republic," *Telecommunications Energy Conference, 1992. INTELEC '92., 14th International*, Washington, D.C., 1992, pp. 389-391.
[68] G. Fabbri, A.J.M. Cardoso, C. Boccaletti, and A. Girimonte, "Control and optimisation of power consumption in Radio Base stations," *Telecommunications Energy Conference (INTELEC), 2011 IEEE 33rd International*, Amsterdam, The Netherlands, 2011, pp. 1-6.
[69] G. Rami, T. Tran-Quoc, N. Hadjsaid, and J.L. Mertz, "Energy supply for remote base transceiver stations of telecommunication," *Power Engineering Society General Meeting, 2004. IEEE*, Denver, CO, 2004, pp. 1916-1921.
[70] G. Schmitt, "The Green Base Station," *Telecommunication - Energy Special Conference (TELESCON), 2009 4th International Conference on*, Vienna, Austria, 2009, pp. 1-6.
[71] "IEEE Guide for Optimizing the Performance and Life of Lead-Acid Batteries in Remote Hybrid Power Systems," *IEEE Standards Coordinating Committee 21 on Fuel Cells, Photovoltaics, Dispersed Generation, and Energy Storage*, ed. New York, NY: IEEE, 2008, pp. C1-25.
[72] P.T. Moseley, "Energy storage in remote area power supply (RAPS) systems," *J. Power Sources*, vol. 155, pp. 83-87, Aug. 2006, DOI: 10.1016/j.jpowsour.2004.10.036
[73] J.F. Manwell, A. Rogers, G. Hayman, C. Avelar, and J.G. McGowan, "Hybrid2 Theory Manual," Dept. of Mechanical Engineering, University of Massachusetts, Amherst, MA, USA, 1998.

[74] I. Van der Hoven, "Power Spectrum of horizontal wind speed in the frequency range 0.0007 to 900 cycles per hour," *J. Atmospheric Sciences*, vol. 14, pp. 160-164, April 01, 1957 1957, DOI: 10.1175/1520-0469(1957)014<0160:PSOHWS>2.0.CO;2

[75] T. Burton, Sharpe, D., Jenkins, N., Bossanyi, E., *Wind energy handbook*. New-York NY: John Wiley, 2001. ISBN: 978-0470699751

[76] *Available data sets, The Met. Office, FitzRoy Road, Exeter, Devon, EX1 3PB, United Kingdom*, [Online], Access date: Jan. 2008, Available: http://www.metoffice.gov.uk/climatechange/science/monitoring/ukcp09/available/index.html

[77] W. Langreder, "Models for Variable Speed Wind Turbines," M.Sc. Thesis, CREST and Risø Nat. Lab., Loughborough University, Loughborough, 1996.

[78] C. Eisenhut, F. Krug, C. Schram, and B. Klockl, "Wind-Turbine Model for System Simulations Near Cut-In Wind Speed," *IEEE Trans. Energy Convers.*, vol. 22, pp. 414-420, Jun. 2007, DOI: 10.1109/tec.2006.875473

[79] I. Munteanu, Bratcu, A.I., Cutululis, N.A., and E. Ceanga, *Optimal Control of Wind Energy Systems - Towards a Global Approach*. London: Springer-Verlag 2008. ISBN: 978-1849967242

[80] A.D. Diop, E. Ceanga, J. Rétiveau, J. Méthot, and A. Ilinca, "Real-time three-dimensional wind simulation for windmill rig tests," *Renew. Energ.*, vol. 32, pp. 2268-2290, Oct. 2007

[81] C. Nichita, D. Luca, B. Dakyo, and E. Ceanga, "Large band simulation of the wind speed for real time wind turbine simulators," *IEEE Trans. Energy Convers.*, vol. 17, pp. 523-529, Dec. 2002, DOI: 10.1109/TEC.2002.805216

[82] E. Welfonder, Neifer, R. and M. Spanner, "Development and experimental identification of dynamic models for wind turbines," *Control Engineering Practice*, vol. 5, pp. 63-73, 1997, DOI: 10.1016/S0967-0661(96)00208-0

[83] "Matlab Control System Toolbox R012a," ed. Natick, MA: The MathWorks Inc., 2012.

[84] P. Sørensen, Hansen, A., Janosi, L., Bech, J. and B. Bak-Jensen, "Simulation of Interaction between Wind Farm and Power System," Risø National Laboratory, Roskilde2001.

[85] "MATLAB r2011b," ed. Natick, MA: The MathWorks Inc., 2011.

[86] J.W. Kolar, T. Friedli, F. Krismer, A. Looser, M. Schweizer, P. Steimer, and J. Bevirt, "Conceptualization and multi-objective optimization of the electric system of an Airborne Wind Turbine," *Industrial Electronics (ISIE), 2011 IEEE International Symposium on*, Orlando, Fl, 2011, pp. 32-55.

[87] A.M. De Broe, S. Drouilhet, and V. Gevorgian, "A peak power tracker for small wind turbines in battery charging applications," *IEEE Trans. Energy Convers.*, vol. 14, pp. 1630-1635, Dec. 1999, DOI: 10.1109/60.815116

[88] Y. Errami, M. Maaroufi, and M. Ouassaid, "Modelling and control strategy of PMSG based variable speed wind energy conversion system," *Multimedia Computing and Systems (ICMCS), 2011 International Conference on*, Chennai, India, 2011, pp. 1-6.

[89] J.A. Baroudi, V. Dinavahi, and A.M. Knight, "A review of power converter topologies for wind generators," *Electric Machines and Drives, 2005 IEEE International Conference on*, San Antonio, Texas, 2005, pp. 458-465.

[90] S. Heier *Grid Integration of Wind Energy Conversion Systems*. Chichester, UK: John Wiley 1998. ISBN: 978-0-470-86899-7

[91] M. Arifujjaman, "Modeling, simulation and control of grid connected Permanent Magnet Generator (PMG)-based small wind energy conversion system," *Electric Power and Energy Conference (EPEC), 2010 IEEE*, Halifax, NS, Canada, 2010, pp. 1-6.

[92] J.T. Bialasiewicz, "Furling control for small wind turbine power regulation," *Industrial Electronics, 2003. ISIE '03. 2003 IEEE International Symposium on*, 2003, pp. 804-809 vol. 2.

[93] R. Karki, H. Po, and R. Billinton, "A simplified wind power generation model for reliability evaluation," *IEEE Trans. Energy Convers.*, vol. 21, pp. 533-540, Jun. 2006, DOI: 10.1109/tec.2006.874233

[94] S. Sayeef, N. Mendis, K. Muttaqi, and S. Perera, "Enhanced reactive power support of a PMSG based wind turbine for a Remote Area Power system," *Universities Power Engineering Conference (AUPEC), 2010 20th Australasian*, Christchurch, New Zealand, 2010, pp. 1-5.

[95] J. Martínez, A. Morales, O. Probst, A. Llamas, and C. Rodríguez, "Analysis and simulation of a wind-electric battery charging system," *Int. J. of Energy Research*, vol. 30, pp. 633-646, Jan. 2006, DOI: 10.1002/er.1175

[96] F. Rafik, H. Gualous, R. Gallay, A. Crausaz, and A. Berthon, "Frequency, thermal and voltage supercapacitor characterization and modeling," *J. Power Sources*, vol. 165, pp. 928-934, Mar. 2007, DOI: 10.1016/j.jpowsour.2006.12.021

[97] D. Linden and T.B. Reddy, *Handbook of Batteries (3rd edition)*. New York, NY: McGraw-Hill, 2002. ISBN: 0-07-135978-8

[98] J.F. Manwell, McGowan, J.G., "Lead acid battery storage model for hybrid energy systems," *J. Solar Energy*, vol. 50, pp. 399-405, May 1993, DOI: 10.1016/0038-092X(93)90060-2

[99] Z.M.C. Salameh, M. A. and W.A. Lynch, "A mathematical model for lead-acid batteries," *IEEE Trans. Energy Convers.*, vol. 7, pp. 93-98, 1992, DOI: 10.1109/60.124547

[100] J.R. Bumby, P.H. Clarke, and I. Forster, "Computer modelling of the automotive energy requirements for internal combustion engine and battery electric-powered vehicles," *Physical Science, Measurement and Instrumentation, Management and Education - Reviews, IEE Proceedings A*, vol. 132, pp. 265-279, Sept. 1985, DOI: 10.1049/ip-a-1:19850059

[101] O. Tremblay, L.A. Dessaint, and A.I. Dekkiche, "A Generic Battery Model for the Dynamic Simulation of Hybrid Electric Vehicles," *Vehicle Power and Propulsion Conference, 2007. VPPC 2007. IEEE*, Arlington, TX 2007, pp. 284-289.

[102] S. Barsali and M. Ceraolo, "Dynamical models of lead-acid batteries: implementation issues," *IEEE Trans. Energy Convers.*, vol. 17, pp. 16-23, Mar. 2002, DOI: 10.1109/60.986432

[103] D. Doerffel and A.S. Suleiman, "A critical review of using the Peukert equation for determining the remaining capacity of lead-acid and lithium-ion batteries," *J. Power Sources*, vol. 155, pp. 395-400, Jun. 2006, DOI: 10.1016/j.jpowsour.2005.04.030

[104] *"CSB Battery: GPL12750 datasheet," CSB Battery Co. Ltd, 11F, No. 150, Sec. 4, Chengde Rd., Shilin Dist., Taipei City 11167, Taiwan.* , [Online], Access date: Jul. 2012, Available: www.csb-battery.com/upfiles/dow01245131622.pdf

[105] H. Giess, "The operation of VRLA monoblocs with an on/off float charge regime," *Telecommunications Energy Conference, 2001. INTELEC 2001. Twenty-Third International*, Edinburgh, UK, 2001, pp. 116-120.
[106] J.M. Hawkins and L.O. Barling, "Some aspects of battery impedance characteristics," *Telecommunications Energy Conference, 1995. INTELEC '95., 17th International*, The Hague, The Netherlands, 1995, pp. 271-276.
[107] P.M. Hunter and A.H. Anbuky, "VRLA Battery Virtual Reference Electrode: Battery Float Charge Analysis," *IEEE Trans. Energy Convers.*, vol. 23, pp. 879-886, Sept. 2008, DOI: 10.1109/tec.2008.926041
[108] L. Lennart, "Matlab System Identification Toolbox 2012a User's Guide," ed. Natick, MA: The MathWorks Inc., 2012.
[109] L. Collins. (2007, June-July 2007) If the Cap Fits. *Electronics, IEEE*. 18-21.
[110] H. Ibrahim, A. Ilinca, and J. Perron, "Energy storage systems—Characteristics and comparisons," *Renewable and Sustainable Energy Reviews*, vol. 12, pp. 1221-1250, 2008, DOI: 10.1016/j.rser.2007.01.023
[111] C. Yonghua, "Assessments of Energy Capacity and Energy Losses of Supercapacitors in Fast Charging–Discharging Cycles," *Energy Conversion, IEEE Transactions on*, vol. 25, pp. 253-261, Mar. 2010, DOI: 10.1109/tec.2009.2032619
[112] L. Zubieta and R. Bonert, "Characterization of double-layer capacitors (DLCs) for power electronics applications," *Industry Applications Conference, 1998. Thirty-Third IAS Annual Meeting. The 1998 IEEE*, 1998, pp. 1149-1154 vol.2.
[113] "Title," unpublished|.
[114] P. Thounthong, S. Rael, and B. Davat, "Analysis of Supercapacitor as Second Source Based on Fuel Cell Power Generation," *IEEE Trans. Energy Convers.*, vol. 24, pp. 247-255, Mar. 2009, DOI: 10.1109/TEC.2008.2003216
[115] C. Yonghua, "Assessments of Energy Capacity and Energy Losses of Supercapacitors in Fast Charging-Discharging Cycles," *IEEE Trans. Energy Convers.* , vol. 25, pp. 253-261, Mar. 2010, DOI: 10.1109/TEC.2009.2032619
[116] S.D. Downing and D.F. Socie, "Simple rainflow counting algorithms," *Int. J. of Fatigue*, vol. 4, pp. 31-40, 1982, DOI: 10.1016/0142-1123(82)90018-4
[117] A. Jaafar, B. Sareni, X. Roboam, and M. Thiounn-Guermeur, "Sizing of a hybrid locomotive based on accumulators and ultracapacitors," *Vehicle Power and Propulsion Conference (VPPC), 2010 IEEE*, Lille, France, 2010, pp. 1-6.
[118] H. Beltran, M. Swierczynski, N. Aparicio, E. Belenguer, R. Teodorescu, and P. Rodriguez, "Lithium ion batteries ageing analysis when used in a PV power plant," *Industrial Electronics (ISIE), 2012 IEEE International Symposium on*, Hangzhou, China, 2012, pp. 1604-1609.
[119] J.F. Manwell and J.G. MbGowan, "Developments in battery storage for wind/diesel systems," *Battery Conference on Applications and Advances, 1991. Proceedings of the Sixth Annual*, Long Beach, CA 1991, pp. 49-57.
[120] M. Chawla, R. Naik, R. Burra, and H. Wiegman, "Utility energy storage life degradation estimation method," *Innovative Technologies for an Efficient and Reliable Electricity Supply (CITRES), 2010 IEEE Conference on*, Waltham, MA, 2010, pp. 302-308.
[121] S. You and C.N. Rasmussen, "Generic modelling framework for economic analysis of Battery Systems," *Renewable Power Generation (RPG 2011), IET Conference on*, Edinburgh, UK, 2011, pp. 1-6.
[122] B. Pattipati, C. Sankavaram, and K. Pattipati, "System Identification and Estimation Framework for Pivotal Automotive Battery Management System

Characteristics," *Systems, Man, and Cybernetics, Part C: Applications and Reviews, IEEE Transactions on,* vol. 41, pp. 869-884, Nov. 2011, DOI: 10.1109/tsmcc.2010.2089979

[123] J. Manwell, J.G. McGowan, U. Abdulwahid, and K. Wu, "Improvements to the Hybrid2 Battery Model," presented at the Windpower 2005 Conference, Washington, DC, 2005.

[124] *"Deep-Cycle Gel Battery Datasheet." Trojan Battery Co., Santa Fe Springs, Trojan Battery Co., Santa Fe Springs, CA., Apr., 2008 (Apr. ed.),* [Online], Access date: Jul. 2012, Available: http://www.trojanbattery.com/pdf/GEL_SS_Web.pdf

[125] A.J. Ruddell, A.G. Dutton, H. Wenzl, C. Ropeter, D.U. Sauer, J. Merten, C. Orfanogiannis, J.W. Twidell, and P. Vezin, "Analysis of battery current microcycles in autonomous renewable energy systems," *J. Power Sources,* vol. 112, pp. 531-546, Aug. 2002, DOI: 10.1016/s0378-7753(02)00457-3

[126] G. Chen and J. Kang, "Simulation and Analysis of Hysteresis Current Controller in Motor Control," *Electrical and Control Engineering (ICECE), 2010 International Conference on,* Dhaka, Bangladesh 2010, pp. 4196-4199.

[127] S. Buso, L. Malesani, and P. Mattavelli, "Comparison of current control techniques for active filter applications," *IEEE Trans. Ind. Electron.,* vol. 45, pp. 722-729, Oct. 1998, DOI: 10.1109/41.720328

[128] C. Jiann-Jong, H. Yuh-Shyan, L. Wen-Ta, L. Chien-Tsung, and S. Juing-Huei, "Hysteresis-Current-Controlled Class-D Amplifier with Active Current Sensing Techniques," *Communications, Circuits and Systems Proceedings, 2006 International Conference on,* Guilin , China 2006, pp. 2737-2740.

[129] O. Gomis-Bellmunt, J. Rafecas-Sabate, D. Montesinos-Miracle, J.M. Fernandez-Mola, and J. Bergas-Jane, "Design and control of a half-bridge converter to drive piezoelectric actuators," *Power Electronics and Motion Control Conference, 2008. EPE-PEMC 2008. 13th,* Poznan, Poland, 2008, pp. 731-733.

[130] I. Boiko, "Input-output analysis of limit cycling relay feedback control systems," *American Control Conference, 1999. Proceedings of the 1999,* San Diego, CA, 1999, pp. 542-546 vol.1.

[131] T. Szepesi, "Stabilizing the Frequency of Hysteretic Current-Mode DC/DC Converters," *IEEE Trans. Power Electron.,* vol. 2, pp. 302-312, Oct. 1987, DOI: 10.1109/tpel.1987.4307865

[132] M. Castilla, J.M. Guerrero, J. Matas, J. Miret, and J. Sosa, "Comparative study of hysteretic controllers for single-phase voltage regulators," *IET Power Electron.,* vol. 1, pp. 132-143, Mar. 2008, DOI: 10.1049/iet-pel:20070151

[133] O. Trescases, A. Prodic, and N. Wai Tung, "Digitally Controlled Current-Mode DC-DC Converter IC," *IEEE Trans. Circuits Syst.* , vol. 58, pp. 219-231, Jan. 2011, DOI: 10.1109/TCSI.2010.2071490

[134] A.S. Kislovski, "Current-mode control: a unified model for open-loop instability," *Applied Power Electronics Conference and Exposition, 1991. APEC '91. Conference Proceedings, 1991., Sixth Annual,* Dallas, TX, 1991, pp. 459-465.

[135] R.B. Ridley, "A new, continuous-time model for current-mode control [power convertors]," *IEEE Trans. Power Electron.,* vol. 6, pp. 271-280, Apr. 1991, DOI: 10.1109/63.76813

[136] H. Daniyal, E. Lam, L.J. Borle, and H.H.C. Iu, "Comparing current control methods using an active power filter application as the benchmark," *Power*

Engineering Conference, 2008. AUPEC '08. Australasian Universities, Sydney, Australia 2008, pp. 1-6.

[137] R. Venkataramanan, Sabanovic, A. and S. Cuk, "Sliding-mode control of power converters," *J. of Indian Ins. of Science.*, vol. 69, pp. 193-211, 1989, DOI: oclc/47058135

[138] V. Utkin, *Sliding modes in control and optimization*. Berlin: Springer-Verlag, 1992. ISBN: 978-0387535166

[139] T. Siew-Chong, Y.M. Lai, and C.K. Tse, "General Design Issues of Sliding-Mode Controllers in DC-DC Converters," *IEEE Trans. Ind. Electron.*, vol. 55, pp. 1160-1174, Mar. 2008, DOI: 10.1109/TIE.2007.909058

[140] Y. Panov and M.N. Jovanovic, "Design considerations for 12-V/1.5-V, 50-A voltage regulator modules," *Applied Power Electronics Conference and Exposition, 2000. APEC 2000. Fifteenth Annual IEEE*, New Orleans, LA, 2000, pp. 39-46 vol.1.

[141] *"Application Guide Snubber Capacitors.", CDE Cornell Dubilier, 1605 E. Rodney French Blvd., New Bedford, MA* [Online], Access date: Jul. 2012, Available: www.cde.com/catalogs/igbtAPPguide.pdf

[142] J. Lamp. *"Application Note IGBT Peak Voltage Measurement and Snubber Capacitor Specification." SEMIKRON INTERNATIONAL GmbH, P.O. Box 820251, 90253 Nürnberg, Deutschland,* [Online], Access date: Jul. 2012, Available: http://www.semikron.com/skcompub/en/AN-7006_IGBT_PeakVoltage_Snubber_juli_2011.pdf

[143] J. Klein. *"AN-6005 Synchronous buck MOSFET loss calculations with Excel model", Fairchild Semiconductor Corp., San Jose, CA,* [Online], Access date, Available: http://www.fairchildsemi.com/an/AN/AN-6005.pdf

[144] *"PolarTM Power MOSFET IXFN140N30P datasheet", Ixys Corp., Milpitas, CA, May. 2008.*, [Online], Access date: Jul. 2012, Available: http://ixapps.ixys.com/DataSheet/DS99571F(IXFN140N30P).pdf

[145] B.S. Borowy and Z.M. Salameh, "Methodology for optimally sizing the combination of a battery bank and PV array in a wind/PV hybrid system," *IEEE Trans. Energy Convers.*, vol. 11, pp. 367-375, 1996, DOI: 10.1109/60.507648

[146] S.C.E. Jupe, P.C. Taylor, and A. Michiorri, "Coordinated output control of multiple distributed generation schemes," *Renewable Power Generation, IET,* vol. 4, pp. 283-297, May. 2010, DOI: 10.1049/iet-rpg.2009.0142

[147] S. Diaf, D. Diaf, M. Belhamel, M. Haddadi, and A. Louche, "A methodology for optimal sizing of autonomous hybrid PV/wind system," *Energy Policy,* vol. 35, pp. 5708-5718, 2007, DOI: DOI: 10.1016/j.enpol.2007.06.020

[148] I. Woofenden and M. Sagrillo. *"2010 WIND GENERATOR buyer's guide", Home Power, Phoenix, OR, Richard and Karen Perez,* [Online], Access date: Jul. 2012, Available: http://nsac.ca/fens/wind/Buyers_GuideHP137_pg44_Woofenden.pdf

[149] D. Corbus, Newcomb, C., Baring-Gould, E. I., and S. Friedly. *"Battery Voltage Stability Effects on Small Wind Turbine Energy Capture", American Wind Energy Association (AWEA) WINDPOWER 2002*, [Online], Access date: Jul., 2012, Available: http://www.nrel.gov/docs/fy02osti/32511.pdf

[150] W. Short, D. Packey, and T. Holt, *A Manual for the Economic Evaluation of Energy Efficiency and Renewable Energy Technologies*. Golden, CL: NREL, 1995. ISBN: 978-1410221056

[151] R. Hunter and G. Elliot, *Wind-Diesel Systems*. Cambridge: University Press 1994. ISBN: 9780521020848

[152] P. Poonpun and W.T. Jewell, "Analysis of the Cost per Kilowatt Hour to Store Electricity," *IEEE Trans. Energy Convers.*, vol. 23, pp. 529-534, Jun. 2008, DOI: 10.1109/tec.2007.914157
[153] U. Sureshkumar, P.S. Manoharan, and A.P.S. Ramalakshmi, "Economic cost analysis of hybrid renewable energy system using HOMER," *Advances in Engineering, Science and Management (ICAESM), 2012 International Conference on*, Nagapattinam, 2012, pp. 94-99.
[154] A. Woodruff, "An Economic Assessment of Renewable Energy Options for Rural Electrification in Pacific Island Countries," Pacific Islands Applied Geoscience Commission (SOPAC), Suva, Fiji Islands2007.
[155] A. Saif, K.G. Elrab, H.H. Zeineldin, S. Kennedy, and J.L. Kirtley, "Multi-objective capacity planning of a PV-wind-diesel-battery hybrid power system," *Energy Conference and Exhibition (EnergyCon), 2010 IEEE International*, Manama, Bahrain, 2010, pp. 217-222.
[156] G. Hu, S. Duan, C. Tao, and C. Chen, "Techno-economical analysis of Vanadium redox and Lead-acid batteries in stand-alone photovoltaic systems," *Power Electronics for Distributed Generation Systems (PEDG), 2010 2nd IEEE International Symposium on*, New Brunswick, Canada 2010, pp. 868-872.
[157] G. Lijun, R.A. Dougal, and L. Shengyi, "Power enhancement of an actively controlled battery/ultracapacitor hybrid," *IEEE Trans. Power Electron.*, vol. 20, pp. 236-243, Jan. 2005, DOI: 10.1109/TPEL.2004.839784(410) 20
[158] L. Kuo-Yuan, C. Yaow-Ming, and C. Yung-Ruei, "MPPT Battery Charger for Stand-Alone Wind Power System," *IEEE Trans. Power Electron.*, vol. 26, pp. 1631-1638, Jun. 2011, DOI: 10.1109/tpel.2010.2088405
[159] Z.M. Salameh and A.B. Cultura, "Small scale distributed generation system at University of Massachusetts Lowell," *Power and Energy Society General Meeting, 2010 IEEE*, Minneapolis, MN, 2010, pp. 1-6.
[160] F. Giraud and Z.M. Salameh, "Steady-state performance of a grid-connected rooftop hybrid wind-photovoltaic power system with battery storage," *IEEE Trans. Energy Convers.*, vol. 16, pp. 1-7, Mar. 2001, DOI: 10.1109/60.911395
[161] F. Valenciaga and P.F. Puleston, "Supervisor control for a stand-alone hybrid generation system using wind and photovoltaic energy," *IEEE Trans. Energy Convers.*, vol. 20, pp. 398-405, Jun. 2005, DOI: 10.1109/tec.2005.845524
[162] J.F. Petit, G. Robles, and H. Amaris, "Current Reference Control for Shunt Active Power Filters Under Nonsinusoidal Voltage Conditions," *IEEE Trans. Power Del.*, vol. 22, pp. 2254-2261, Oct. 2007, DOI: 10.1109/tpwrd.2007.905811
[163] G.W. Chang and S. Tai-Chang, "A novel reference compensation current strategy for shunt active power filter control," *IEEE Trans. Power Del.*, vol. 19, pp. 1751-1758, Oct. 2004, DOI: 10.1109/tpwrd.2004.835430
[164] C. Lascu, L. Asiminoaei, I. Boldea, and F. Blaabjerg, "High Performance Current Controller for Selective Harmonic Compensation in Active Power Filters," *IEEE Trans. Power Electron.*, vol. 22, pp. 1826-1835, Sept. 2007, DOI: 10.1109/tpel.2007.904060
[165] S. Round, H. Laird, R. Duke, and A. Gardiner, "The transient and steady state performance of a shunt active filter using measured site data," *Harmonics and Quality of Power Proceedings, 1998. Proceedings. 8th International Conference On*, Athens, Greece, 1998, pp. 395-400 vol.1.
[166] *"Compact 1U Switch Mode Power Supply", ETPS Ltd, Unit 14, The Bridge, Beresford Way, Chesterfield, S41 9FG*, [Online], Access date: Jul. 2012,

Available: http://www.etps.co.uk/products/dc-sources/productinfo.aspx?ProdID=LAB-SMP
[167] *"Boostcap Series Datasheet," Maxwell Technologies, Maxwell Technologies, Inc., 5271 Viewridge Court, Suite 100, San Diego CA 92123*, [Online], Access date: Jul. 2012, Available: http://www.maxwell.com/products/ultracapacitors/docs/datasheet_bc_series_1017105.pdf
[168] *"PIC18F2420/2520/4420/4520 Data Sheet", Microchip Technology Inc.*, [Online], Access date: Jul. 2012, Available: http://ww1.microchip.com/downloads/en/devicedoc/39631e.pdf
[169] *"Current Transducer LA 100-P/SP13", LEM U.S.A., Inc., 11665 W. Bradley Road, Milwaukee, WI 53224 USA*, [Online], Access date: Jul. 2012, Available: http://www.lem.com/docs/products/la%20100-p%20sp13%20e.pdf
[170] C.M. Krishna, "Managing Battery and Supercapacitor Resources for Real-Time Sporadic Workloads," *IEEE Embedded Syst. Lett.*, vol. 3, pp. 32-36, Mar. 2011, DOI: 10.1109/les.2010.2098847
[171] D.B. Murray, J.G. Hayes, D.L. O'Sullivan, and M.G. Egan, "Supercapacitor Testing for Power Smoothing in a Variable Speed Offshore Wave Energy Converter," *IEEE J. Ocean. Eng.*, vol. 37, pp. 301-308, Apr. 2012, DOI: 10.1109/joe.2012.2188157
[172] E.H. El Brouji, O. Briat, J.M. Vinassa, N. Bertrand, and E. Woirgard, "Impact of Calendar Life and Cycling Ageing on Supercapacitor Performance," *IEEE Trans. Veh. Technol.*, vol. 58, pp. 3917-3929, Oct. 2009, DOI: 10.1109/tvt.2009.2028431
[173] R. Lu, C. Zhu, L. Tian, and Q. Wang, "Super-Capacitor Stacks Management System With Dynamic Equalization Techniques," *IEEE Trans. Magn*, vol. 43, pp. 254-258, Jan. 2007, DOI: 10.1109/tmag.2006.887652
[174] N.M.L. Tan, S. Inoue, A. Kobayashi, and H. Akagi, "Voltage Balancing of a 320-V, 12-F Electric Double-Layer Capacitor Bank Combined With a 10-kW Bidirectional Isolated DC--DC Converter," *IEEE Trans. Power Electron.*, vol. 23, pp. 2755-2765, Jan. 2008, DOI: 10.1109/tpel.2008.2005388
[175] B. Bae, J. Lee, J. Jeong, and B. Han, "Line-Interactive Single-Phase Dynamic Voltage Restorer With Novel Sag Detection Algorithm," *IEEE Trans. Power Del.*, vol. 25, pp. 2702-2709, Oct. 2010, DOI: 10.1109/tpwrd.2010.2044194
[176] R.W. Erickson, *Fundamentals of Power Electronics*: Chapman and Hall, 1997. ISBN: 978-0792372707
[177] R. Morici, C. Rossi, and A. Tonielli, "Variable structure controller for AC/DC boost converter," *Industrial Electronics, Control and Instrumentation, 1994. IECON '94., 20th Int. Conf.*, NY, USA, 1994, pp. 1449-1454 vol.3.
[178] J.C. Olivier, L. Loron, F. Auger, and J.C. Le Claire, "Improved linear model of self oscillating systems such as relay feedback current controllers," *Control Engineering Practice*, vol. 18, pp. 927-935, May 2010, DOI: 10.1016/j.conengprac.2010.03.016
[179] E. Sambatra, J. Raharijaona, G. Barakat, and B. Dakyo, "Modeling and Test of a PM Synchronous Generator Based Small Stand Alone Wind Energy Converter," *Power Electronics and Motion Control Conference, 2006. EPE-PEMC 2006. 12th International*, Portoroz, Slovenia, 2006, pp. 1591-1596.
[180] G. Papazov and D. Pavlov, "Influence of cycling current and power profiles on the cycle life of lead/acid batteries," *J. Power Sources*, vol. 62, pp. 193-199, Apr. 1996, DOI: 10.1016/s0378-7753(96)02422-6

[181] J.P. Barton and D.G. Infield, "Energy storage and its use with intermittent renewable energy," *IEEE Trans. Energy Convers.*, vol. 19, pp. 441-448, Jun. 2004, DOI: 10.1109/tec.2003.822305

[182] R. Ball. *"Supercapacitors see growth as costs fall", Electronics Weekley*, [Online], Access date: Jul. 2012, Available: http://www.electronicsweekly.com/Articles/03/03/2006/37810/Supercapacitors-see-growth-as-costs-fall.htm

[183] M. Arifujjaman, M.T. Iqbal, J.E. Ouaicoe, and M.J. Khan, "Modeling and control of a small wind turbine," *Electrical and Computer Engineering, 2005. Canadian Conference on*, Saskatoon, Canada, 2005, pp. 778-781.

[184] M.J. Khan and M.T. Iqbal, "Analysis of a small wind-hydrogen stand-alone hybrid energy system," *Applied Energy*, vol. 86, pp. 2429-2442, Feb. 2009, DOI: 10.1016/j.apenergy.2008.10.024

[185] L. Ha Thu, S. Santoso, and W.M. Grady, "Development and analysis of an ESS-based application for regulating wind farm power output variation," *Power & Energy Society General Meeting, 2009. PES '09. IEEE*, Calgary, AB, 2009, pp. 1-8.

[186] L. Ha Thu and N. Thang Quang, "Sizing energy storage systems for wind power firming: An analytical approach and a cost-benefit analysis," *Power and Energy Society General Meeting - Conversion and Delivery of Electrical Energy in the 21st Century, 2008 IEEE*, Pittsburgh, PA, 2008, pp. 1-8.

[187] E. Koutroulis, D. Kolokotsa, A. Potirakis, and K. Kalaitzakis, "Methodology for optimal sizing of stand-alone photovoltaic/wind-generator systems using genetic algorithms," *Solar Energy*, vol. 80, pp. 1072-1088, 2006, DOI: DOI: 10.1016/j.solener.2005.11.002

[188] D.S. Oliveira, A.R. Rangel, D.L. Queiroz, E.F. de Oliveira, G.J.M. de Sousa, L.P.C. dos Santos, L.F.A. Fontenele, and P.A.M. Bezerra, "Low cost and high efficiency static converter for small wind systems," *IECON '09. 35th Annual Conference of IEEE*, Porto, Portugal, 2009, pp. 601-608.

[189] A.L. Allegre, A. Bouscayrol, P. Delarue, P. Barrade, E. Chattot, and S. El-Fassi, "Energy Storage System with Supercapacitor for an Innovative Subway," *IEEE Trans. Ind. Electron.*, vol. 57, pp. 4001-4012, Dec. 2010, DOI: 10.1109/TIE.2010.2044124

[190] J. Dunlop, W. Bower, and S. Harrington, "Performance of battery charge controllers: first year test report," *Photovoltaic Specialists Conference, 1991., Conference Record of the Twenty Second IEEE*, Las Vegas, NV, 1991, pp. 640-645 vol.1.

[191] M. Arifujjaman, Iqbal, M. T., and J.E. Quaicoe, "Maximum Power Extraction from a Small Wind Turbine Emulator using a DC - DC Converter Controlled by a Microcontroller," *Electrical and Computer Engineering, 2006. ICECE '06. International Conference on*, Dhaka, Bangladesh 2006, pp. 213-216.

[192] E.I. Baring-Gould, Newcomb, C., Corbus, D. and R. Kalidas. *"Field Performance of Hybrid Power Systems", American Wind Energy Association's WINDPOWER 2001 Conference*, [Online], Access date: Jul., 2012, Available: http://www.nrel.gov/docs/fy01osti/30566.pdf

[193] C.N. Bhende, S. Mishra, and S.G. Malla, "Permanent Magnet Synchronous Generator-Based Standalone Wind Energy Supply System," *IEEE Trans. Sustain. Energy*, vol. 2, pp. 361-373, Oct. 2011, DOI: 10.1109/tste.2011.2159253

[194] A.J. Bowen, M. Cowie, and N. Zakay, "The performance of a remote wind-diesel power system," *Renewable Energy*, vol. 22, pp. 429-445, 2001, DOI: Doi: 10.1016/s0960-1481(00)00100-2

[195] A.M.O. Haruni, A. Gargoom, M.E. Haque, and M. Negnevitsky, "Dynamic operation and control of a hybrid wind-diesel stand alone power systems," *Applied Power Electronics Conference and Exposition (APEC), 2010 Twenty-Fifth Annual IEEE*, Long Beach, CA, 2010, pp. 162-169.

[196] N. Mendis, K.M. Muttaqi, S. Perera, and M.N. Uddin, "A novel control strategy for stand-alone operation of a wind dominated RAPS system," *Industry Applications Society Annual Meeting (IAS), 2011 IEEE*, Orlando, FL, 2011, pp. 1-8.

[197] M. Narayana, "Demand and supply analysis of community type wind power system at Gurugoda Village in Sri Lanka," *Industrial and Information Systems, 2007. ICIIS 2007. International Conference on*, Peadeniya , Sri lanka, 2007, pp. 117-122.

[198] S.A. Pourmousavi, M.H. Nehrir, C.M. Colson, and W. Caisheng, "Real-Time Energy Management of a Stand-Alone Hybrid Wind-Microturbine Energy System Using Particle Swarm Optimization," *IEEE Trans. Sustain. Energy*, vol. 1, pp. 193-201, Oct. 2010, DOI: 10.1109/tste.2010.2061881

[199] Y.S. Wong, Hurley, W. G. and W.H. Wölfle, "Charge regimes for valve-regulated lead-acid batteries: Performance overview inclusive of temperature compensation," *J. Power Sources*, vol. 183, pp. 783-791, 2008, DOI: 10.1016/j.jpowsour.2008.05.069

[200] R.L. Hammond, S. Everingham, and D. Srinivasan, "Batteries for stationary standby and for stationary cycling applications part 1: standby vs. cycling - definitions and concepts," *Power Engineering Society General Meeting, 2003, IEEE*, Toronto, Canada 2003, p. 145 Vol. 1.

[201] G.J. May, "Standby battery requirements for telecommunications power," *J. Power Sources*, vol. 158, pp. 1117-1123, Aug. 2006, DOI: 10.1016/j.jpowsour.2006.02.083

[202] S. Armstrong, M.E. Glavin, and W.G. Hurley, "Comparison of battery charging algorithms for stand alone photovoltaic systems," *Power Electronics Specialists Conference, 2008. PESC 2008. IEEE*, 2008, pp. 1469-1475.

[203] M. Bhatt, W.G. Hurley, and W.H. Wolfle, "A new approach to intermittent charging of valve-regulated lead-acid batteries in standby applications," *IEEE Trans. Ind. Electron.*, vol. 52, pp. 1337-1342, Oct. 2005, DOI: 10.1109/tie.2005.855665

[204] R.P.T. Bascope, H.M. de Oliveira Filho, L.D.S. Bezerra, C.M.T. Cruz, F.K.A. Lima, and D.S. Oliveira, "Electronic circuit for stand-alone wind energy conversion system," *Power Electronics Conference (COBEP), 2011 Brazilian*, Natal, Brazil, 2011, pp. 977-983.

[205] B.S. Manju, R. Ramaprabha, and B.L. Mathur, "Modelling and control of standalone solar photovoltaic charging system," *Emerging Trends in Electrical and Computer Technology (ICETECT), 2011 International Conference on*, Nagercoil, India, 2011, pp. 78-81.

[206] R.H. Newnham and W.G.A. Baldsing, "Benefits of partial-state-of-charge operation in remote-area power-supply systems," *J. Power Sources*, vol. 107, pp. 273-279, 2002, DOI: 10.1016/s0378-7753(01)01007-2

[207] Z. Shi-cheng and W. Liang-yu, "Research on charging control for battery in photovoltaic system," *Industrial Electronics and Applications (ICIEA), 2011 6th IEEE Conference on*, Singapore 2011, pp. 2321-2325.
[208] H. Murai, T. Takeda, K. Hirose, Y. Okui, Y. Iwase, K. Yukita, and K. Ichiyanagi, "A study on charge patterns for uninterruptible power supply system with distributed generators," *Telecommunications Energy Conference, 2009. INTELEC 2009. 31st International*, Orlando, FL, 2009, pp. 1-5.
[209] I. Serban and C. Marinescu, "A look at the role and main topologies of battery energy storage systems for integration in autonomous microgrids," *Optimization of Electrical and Electronic Equipment (OPTIM), 2010 12th International Conference on*, Brasov, Romania, 2010, pp. 1186-1191.
[210] "IEEE Guide for Application and Management of Stationary Batteries Used in Cycling Service," *IEEE Std 1660-2008*, pp. C1-31, Nov. 2008, DOI: 10.1109/ieeestd.2008.4690900
[211] P.C. Symons, "Batteries for stationary standby and for stationary cycling applications part 4: charge management," *Power Engineering Society General Meeting, 2003, IEEE*, Toronto, Canada 2003, p. 157 Vol. 1.
[212] C. Huang-Jen, L. Yu-Kang, Y. Chun-Jen, L. Ting-Peng, W. Jian-Min, and L. Jian-Xing, "A Modular Self-Controlled Photovoltaic Charger With InterIntegrated Circuit (<formula formulatype="inline"> <img src="/images/tex/19598.gif" alt="\hbox {I}^{2}\hbox {C}"> </formula>) Interface," *IEEE Trans. Energy Convers.*, vol. 26, pp. 281-289, Mar. 2011, DOI: 10.1109/tec.2010.2068548
[213] X. Muneret, M. Coux, and P. Lenain, "Analysis of the partial charge reactions within a standby VRLA battery leading to an understanding of intermittent charging techniques," *Telecommunications Energy Conference, 2000. INTELEC. Twenty-second International*, 2000, pp. 293-298.
[214] Handbook for Gel-VRLA-Batteries Part 2: Installation, Commissioning and Operation. Available: http://www.sonnenschein.org/PDF%20files/GelHandbookPart2.pdf
[215] M. Baheshti, "Chemistry-independent charge management in portable products," *Battery Conference on Applications and Advances, 1999. The Fourteenth Annual*, Long Beach, CA, 1999, pp. 241-245.
[216] T.T. Sack, J.C. Tice, and R. Reynolds, "Segmented battery charger for high energy 28 V lithium ion battery," *Applications and Advances, 2001. The Sixteenth Annual Battery Conference on*, Long Beach, CA, 2001, pp. 157-159.
[217] A. Gee and R.W. Dunn, "Design and analysis of a sliding-mode power electronic controlled battery / supercapacitor hybrid energy storage system for remote wind power," presented at the Universities' Power Engineering Conference (UPEC), Proceedings of 2011 46th International, Soest, Germany, 2011.
[218] A. Gee, F.V.P. Robinson, and R.W. Dunn, "Sliding-mode control, dynamic assessment and practical implementation of a bidirectional buck/boost DC-to-DC converter," *Power Electronics and Applications (EPE 2011), Proceedings of the 2011-14th European Conference on*, Birmingham, UK, 2011, pp. 1-10.
[219] A. Sabanovic, L. Fridman, and S. Spurgeon, *Variable Structure Systems: From Principles to Implementation*. Stevenage, UK: Institution of Engineering and Technology (IET), 2004, ch.1 pp. 9., ISBN: 978-0863413506
[220] S.C. Chung, S.R. Huang, and C.I. Ln, "Applications of describing functions to estimate the continuous and discontinuous conduction mode for a DC-to-DC

buck converter," *Electric Power Applications, IEE Proceedings* -, vol. 147, pp. 513-519, Nov. 2000, DOI: 10.1049/ip-epa:20000589
[221] H. Peng, A. Prodic, E. Alarcon, and D. Maksimovic, "Modeling of Quantization Effects in Digitally Controlled DC/DC Converters," *IEEE Trans. Power Electron.*, vol. 22, pp. 208-215, Jan. 2007, DOI: 10.1109/tpel.2006.886602
[222] L. Yu-Cheng, C. Ching-Jan, C. Dan, and B. Wang, "A Ripple-Based Constant On-Time Control With Virtual Inductor Current and Offset Cancellation for DC Power Converters," *IEEE Trans. Power Electron.*, vol. 27, pp. 4301-4310, Oct. 2012, DOI: 10.1109/tpel.2012.2191799
[223] J.A. Barrado, A.E. Aroudi, H. Valderrama-Blavi, J. Calvente, and L. Martinez-Salamero, "Analysis of a Self-Oscillating Bidirectional DC/DC Converter in Battery Energy Storage Applications," *IEEE Trans. Power Del.*, vol. 27, pp. 1292-1300, Jul. 2012, DOI: 10.1109/tpwrd.2012.2192455
[224] D.P. Atherton, *Non Linear Control Engineering*. Wokingham, UK: Van Noslrand Reinhold, 1975. ISBN: 9780442304867 - 1982
[225] R. Middleton and S. Cuk, "A general unified approach to modelling switching-converter power stages.," *Int. J. of Electronics*, vol. 42, p. 521—550, Jun. 1977, DOI: 10.1080/00207217708900678
[226] R.C. Dorf and R.H. Bishop, *Modern Control Systems (10th Edition)*. London: Pearson Prentice Hall, 2005. ISBN: 9780131457331
[227] *"CSB Battery: GPL1272 datasheet," CSB Battery Co. Ltd, 11F, No. 150, Sec. 4, Chengde Rd., Shilin Dist., Taipei City 11167, Taiwan.*, [Online], Access date, Available: http://www.csb-battery.com/english/01_product/02_detail.php?fid=5&pid=11
[228] R.F. Nelson and M.A. Kepros, "AC ripple effects on VRLA batteries in float applications," *Battery Conference on Applications and Advances, 1999. The Fourteenth Annual*, Long Beach, CA, 1999, pp. 281-289.
[229] S. Misak and L. Prokop, "Off-grid power systems," *Environment and Electrical Engineering (EEEIC), 2010 9th International Conference on*, Prague, Czech Republic, 2010, pp. 14-17.
[230] S. Tanezaki, T. Matsushima, and S. Muroyama, "Stand-alone hybrid power supply system composed of wind turbines and photovoltaic modules for powering radio relay stations," *Telecommunications Energy Conference, 2003. INTELEC '03. The 25th International*, Yokohama, Japan 2003, pp. 457-462.
[231] "IEEE Recommended Practice for Testing the Performance of Stand-Alone Photovoltaic Systems," *IEEE Std 1526-2003*, pp. 0_1-18, 2004, DOI: 10.1109/ieeestd.2004.94418
[232] M.A. Casacca, M.R. Capobianco, and Z.M. Salameh, "Lead acid battery storage configurations for improved available capacity," *IEEE Trans. Energy Convers.*, vol. 11, pp. 139-145, Mar. 1996, DOI: 10.1109/60.486588
[233] T. Jen-Chieh, C. Chi-Lin, L. Yu-Huei, Y. Hong-Yuan, H. Ming-Shen, and C. Ke-Horng, "Modified Hysteretic Current Control (MHCC) for Improving Transient Response of Boost Converter," *IEEE Trans. Circuits Syst.* , vol. 58, pp. 1967-1979, Aug. 2011, DOI: 10.1109/tcsi.2011.2106231
[234] L. Yan-Fei and P.C. Sen, "Large-signal modeling of hysteretic current-programmed converters," *IEEE Trans. Power Electron.*, vol. 11, pp. 423-430, May. 1996, DOI: 10.1109/63.491635
[235] S. Kapat, A. Patra, and S. Banerjee, "RHP zero elimination with near optimum regulation in a current controlled tri-state boost converter through inductor

current filtering," *Power and Energy Conf. at Illinois (PECI), 2010*, Illinois, IL, 2010, pp. 83-87.

[236] A. Gupta, R.P. Saini, and M.P. Sharma, "Hybrid energy system sizing incorporating battery storage: An analysis via simulation calculation," *Power Systems, 2009. ICPS '09. International Conference on*, London, UK, 2009, pp. 1-6.

Appendices

Appendix 1: Inductor Current Slew-rate-Control Bandwidth Limit

The bandwidth limitation is imposed on a system by a current slew-rate limit such as a power inductor in the synchronous buck converter's output filter circuit can be determined as follows.

The control system can be drawn to include the inductor current slew-rate:

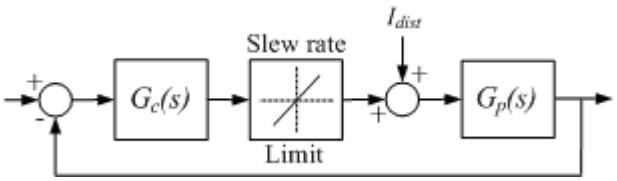

Fig. A1.1 Effective control system block diagram with current slew-rate limit

Let V_L denote the minimum voltage across the inductor during either switching interval. The inductor current slew-rate is then:

$$\frac{dI_L}{dt} = \frac{V_L}{L} \tag{A1.1}$$

Let the disturbance signal, I_{dist}, be sinusoidal and defined as follows:

$$I_{dist}(t) = I_{peak} \cdot Sin(2\pi f_c t) \tag{A1.2}$$

To reject the disturbance effectively, the control system output must accurately reproduce an equal and opposite sine wave according to the control action. The control slew-rate (*di/dt*) required to reproduce a sine wave of frequency f_c can be found by evaluating the maximum rate of change of the sine wave, which occurs at $t = 0$:

$$\frac{di}{dt} = \frac{d}{dt}\left[I_{peak} \cdot Sin(2\pi \cdot f_c t)\right]\Big|_{t=0} \tag{A1.3}$$

$$= I_{peak} \cdot 2\pi \cdot f_c$$

From this, the maximum achievable control bandwidth, f_c, can be determined for a given inductor current slew-rate limit (di_L/dt) and peak disturbance current, I_{peak}, as follows:

$$f_c = \frac{di_L}{dt} \cdot \frac{1}{2\pi \cdot I_{peak}} \tag{A1.4}$$

Substituting in Eq. (A1.1) in Eq. (A1.4) gives the following relationship:

$$f_c = \frac{V_L}{L} \cdot \frac{1}{2\pi \cdot I_{peak}} \tag{A1.5}$$

Eq. (A1.5) shows how the maximum achievable control bandwidth is proportional to the disturbance signal magnitude, inversely proportional to the inductance and the peak current amplitude. This was used in the control loop design process to ensure that the slew-rate limit imposed by the power inductance would not prevent the control system from functioning under worst case conditions for V_L and I_{peak}.

Appendix 2: Equivalent Linear Transfer-function

To verify the global stability of the system, the switching operation of the DC/DC converter was modelled as a relay with hysteresis and the describing function technique was used to verify the overall stability of the system.

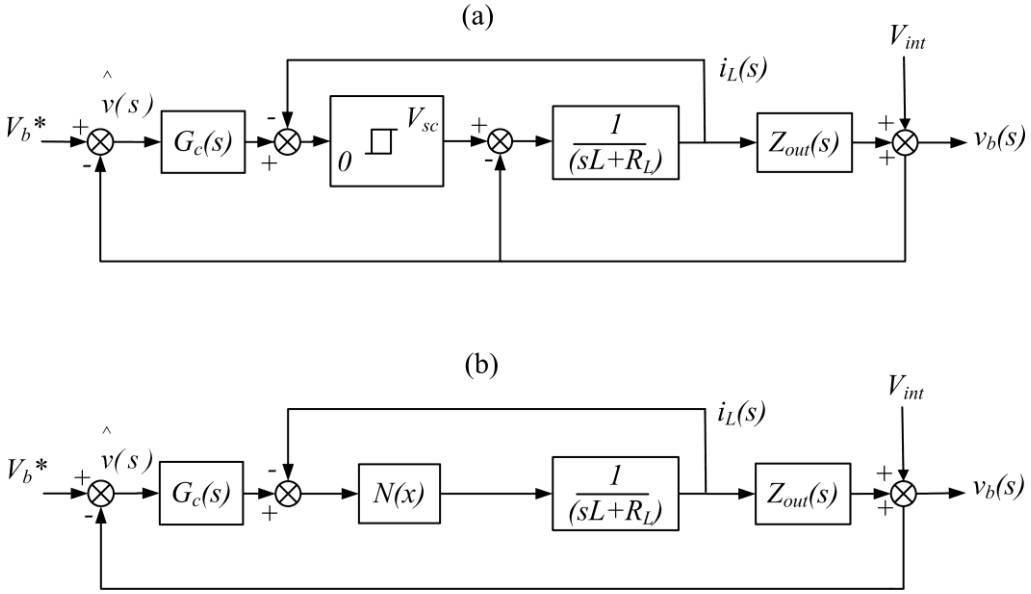

Fig. A2.1 (a) System block diagram including non-linear hysteresis representation of the converter. (b) System block diagram with relay hysteresis shown in describing function form.

The forward path transfer-function of the system in Fig. A2.1 was determined as follows:

$$G_{ol}(s) = \frac{As^2 + Bs + C}{Ds^4 + Es^3 + Fs^2 + Gs} \tag{A2.1}$$

where (A2.2)

$$A = k_p k_b N(x)$$
$$B = k_p k_b N(x) z + k_i N(x) k_b$$
$$C = k_i k_b N(x) z$$
$$D = L k_b C_{out}$$
$$E = N(x) k_b C_{out} + (k_b C_{out} z + 1) L + R_L k_b C_{out}$$
$$F = (k_b C_{out} z + 1) N(x) + Lp + (k_b C_{out} z + 1) R_L$$
$$G = N(x) p + R_L p$$

The unity feedback, closed loop transfer-function describing the system in Fig. 9.9(b) is then:

$$G_{cl}(s) = \frac{Num(s)}{Den(s)} = \frac{As^2 + Bs + C}{Ds^4 + Es^3 + (F + A)s^2 + (G + B)s + C} \tag{A2.3}$$

Since the system Fig A2.1 contains nested loops, an equivalent non-nested transfer-function can be defined as G_{linear}(s), having the same characteristic polynomial as Eq. (A2.1) when cascaded with the non-linear term, N(x), in a single, unity feedback loop as shown in Fig (A2.2)

$$G_{linear}(s) = \frac{terms\,in\ Den(s)\ containing N(x)}{terms\,in\ Den(s)\ not\ containing N(x)} \tag{A2.5}$$

$$= \frac{k_b C_{out} s^3 + (k_b C_{out} z + 1 + k_p k_b)s^2 + (k_p k_b z + k_i k_b + p)s + k_i k_b z}{L k_b C_{out} s^4 + \left[(k_b C_{out} z + 1)L + R_L k_b C_{out}\right]s^3 + \left[Lp + (k_b C_{out} z + 1)R_L\right]s^2 + R_L ps}$$

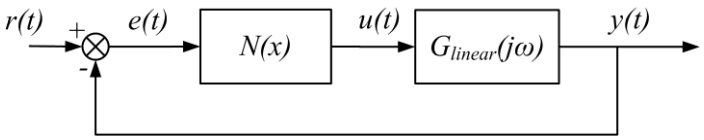

Fig. A2.2 Non-linear term cascaded with linear system

As the transfer-function G_{linear}(s) has the same characteristic polynomial as the system of Fig. A2.2, the stability of the system can be inferred from the stability of the equivalent system, G_{linear}(s).

Appendix 3: Synchronous Buck Converter Specifications

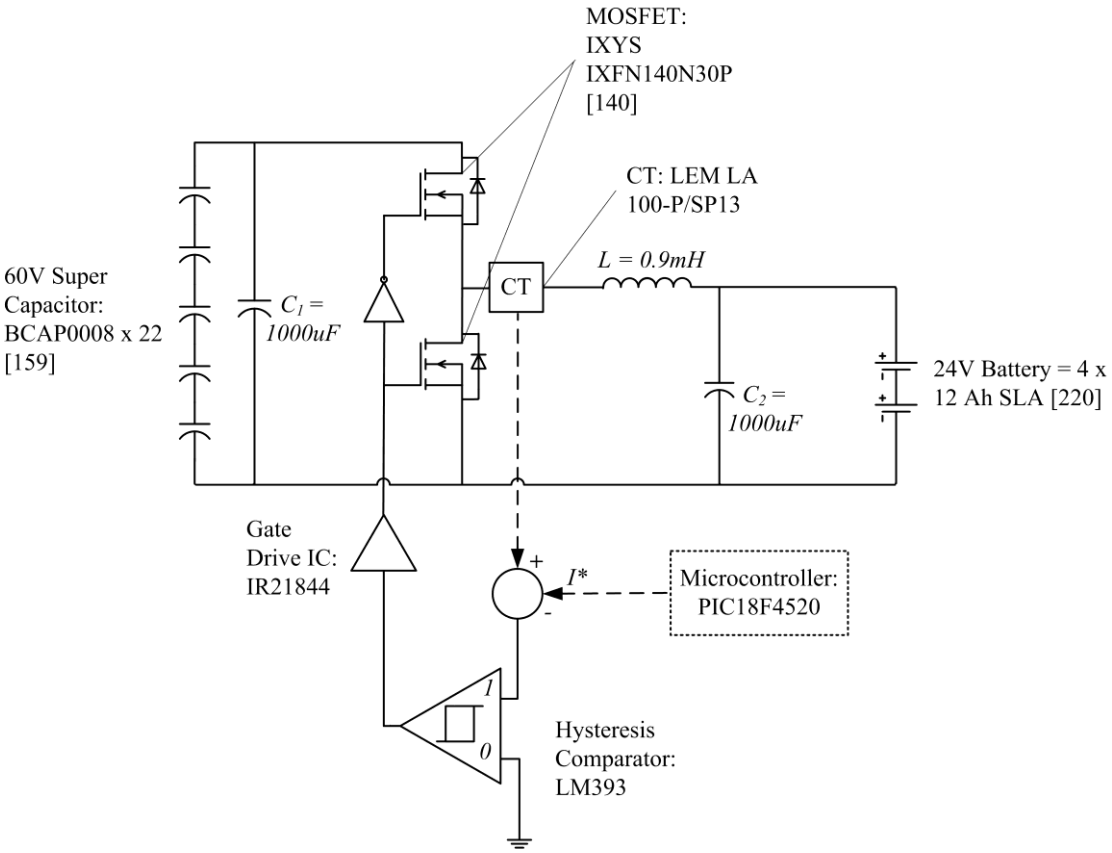

Appendix 4: Analogue-PI Voltage Control System

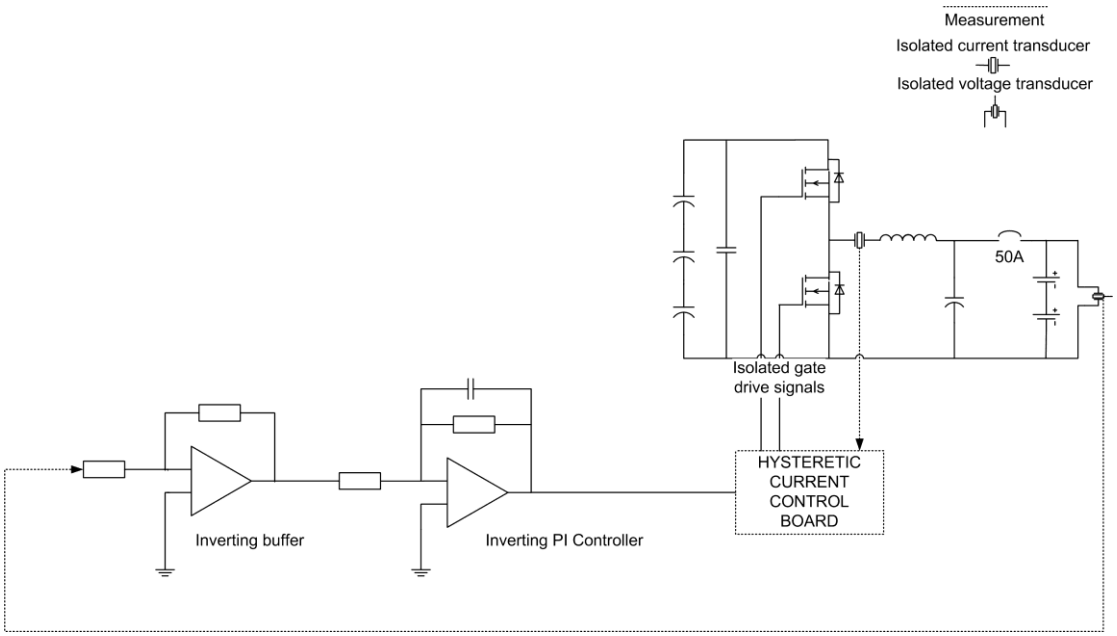

Appendix 5: Active Current Filter real-time control code

```
#include <p18cxxx.h> // Allows use of names like TRISC, PORTC …
#include <adc.h> // Lets us use ADC functions
#include <stdlib.h>
#include <delays.h>
#include <i2c.h>
#include <usart.h>
#include <string.h>
#include <stdio.h>
#include <math.h>
#include "esmanagement.h"
#include <timers.h>

/** C O N S T A N T S
******************************************************/
#define    threshold        =     307;       // threshold defaults
to 1.5V
//#define abs(n)    ( ((n) >= 0) ? (n) : -(n) ) ;
//#define fabs(n)   ( ((n) >= 0.0) ? (n) : -(n) );
const char  dac_i2c_address =0b01000000; // I2C address of DAC
const char  dac_0_select     =     0b00000000; // I2C commend byte
for max519 to selecet DAC0
const char  dac_1_select     =     0b01000001; // I2C commend byte
for max519 to selecet DAC1
const unsigned long int TASK0_COUNTER_MAX   = 2000;         //low
frequency task coutner


/** V A R I A B L E S
******************************************************/
long int counter; // used to generate delay
unsigned long int adc_result0, adc_result1, adc_0, adc_1 ;
int state; int toggle; float alpha;
long int task0_counter=0;


/** CONTROLLER VARIABLES
*************************************************/
long vbatref;
unsigned long kp;
unsigned long ki;
unsigned long imax;
long imaxneg ;
long errintmax;
long errintmaxneg;
long err;
long err_int;

long u0, u1, u;
char new_sample_flag; //** Be carefull chars are set to signed
***************/
int i, j, k;
long int acc; int a, b;
int window;
float lpf_out;
int lpf, vloop, vcap_high, vcap_low;
```

```
/** FUNCTION TO ENABLE INTERRUPT ON TIMER O
*********************************/

void set_timer(void)
{
     OpenTimer0(TIMER_INT_ON & T0_8BIT & T0_SOURCE_INT &
T0_PS_1_16); // NOTE: If writing 2 channels to I2C bus post scale 8
is minimum.
     INTCONbits.GIEH = 1; //enable interrupts
}

//*****************************************************************
***********/
// High priority interrupt routine

#pragma code
#pragma interrupt InterruptHandlerHigh

void
InterruptHandlerHigh ()
{ //Every 0.026 secs

   if (INTCONbits.TMR0IF)
   { //check for TMR0 overflow
      INTCONbits.TMR0IF = 0; //clear interrupt flag
      WriteTimer0(0);

      PORTDbits.RD7 = 1;     //for debugging timings

    //****************Read ADC and start new conversion

      // Toggle between ADCO and ADC1
      if (toggle == 1)
      {
            PORTDbits.RD2 = 1;
            //Take reading
            adc_1 = ( ADRESH * 256  ) | ADRESL ; //ADRESH needs
bitwise shift << 8. NOTE can also use ReadADC()
            Delay10TCYx(5);
            ConvertADC(); // Start conversion
            PORTDbits.RD2 = 0;
            SetChanADC( ADC_CH0 );
      }
      if (toggle == 0)
      {
            PORTDbits.RD3 = 1;
            //Take reading
            adc_0 = ( ADRESH * 256  ) | ADRESL ; //ADRESH needs
bitwise shift << 8. NOTE can also use ReadADC()
            Delay10TCYx(5);
            ConvertADC(); // Start conversion
            PORTDbits.RD3 = 0;
            SetChanADC( ADC_CH1 );
      }

      adc_result0 = adc_0 / 4;  //SCALE ADC RESULT to an 8 bit
number
```

```
      adc_result1 = adc_1 / 4;  //SCALE ADC RESULT to an 8 bit
number

      if ( lpf == 1 )
      {

            u0 = adc_result0 - (int)( lpf_out ) + 128;
//adc_result0; ----------------->>>>>>> 128 ;  // 128 equates to
zero current reference as the command signal is 8 bit centered on
128


            //if (     u1 < 132 & u1 > 126    ) {   u1 = 128 ; }
//Disable converter if current reference v small

            u1 = (int)( lpf_out );

            PORTBbits.RB0 = 1;     //Enable converter
            StartI2C(); // begin I2C communication
            IdleI2C();
            WriteI2C( dac_i2c_address );      // sends 0000 address
to the
            WriteI2C( dac_0_select );         //Write command byte
to selct DAC1. This is the negative analogue out via op amp
inverter
            WriteI2C( u0 );                           //Write command
byte for output value
            //WriteI2C( dac_1_select );       //Write command byts
to selct DAC0. Positive analogue output
            //WriteI2C( u1 );
            StopI2C();                        // stop all I2C
communications
            IdleI2C();

      }

            PORTBbits.RB0 = 1; //Enable converter
            StartI2C(); // begin I2C communication
            IdleI2C();
            WriteI2C( dac_i2c_address );      // sends 0000 address
to the
            WriteI2C( dac_0_select );         //Write command byte
to selct DAC1. This is the negative analogue out via op amp
inverter
            WriteI2C( u0 );                           //Write command
byte for output value
            //WriteI2C( dac_1_select );       //Write command byts
to selct DAC0. Positive analogue output
            //WriteI2C( u1 );
            StopI2C();                        // stop all I2C
communications
            IdleI2C();
      }

      if ( vcap_low || vcap_high )
      {
            PORTBbits.RB0 = 0; //Disable converter
            StartI2C(); // begin I2C communication
```

```
            IdleI2C();
            WriteI2C( dac_i2c_address );      // sends 0000 address
to the
            WriteI2C( dac_0_select );         //Write 128 midpoint
is zero to DAC0.
            WriteI2C( 128 );                        //Write command
byte for output value
            //WriteI2C( dac_1_select );       //Write 128 midpoint
is zero to DAC1.
            //WriteI2C( 128 );
            StopI2C();                        // stop all I2C
communications
            IdleI2C();
      }

      //***increment and poll counter to schedule low frequency
moving average task

      task0_counter++;
       if (task0_counter >= TASK0_COUNTER_MAX)     //low frequency
task
      {
            task0_counter=0;
            new_sample_flag = 1;
      }
      toggle = !toggle;
      PORTDbits.RD7 = 0;     //for debugging timings
      }

}

#pragma code InterruptVectorHigh = 0x08
void
InterruptVectorHigh (void)
{
  _asm
   goto InterruptHandlerHigh //jump to interrupt routine
  _endasm
}

//*****************************************************************
***********/
// Main program //

void main()
      {

/*************** Configure ports
*******************************************/
      //LATD = 0x00;
      TRISA = 0xFF;
      TRISD = 0b11110000; //Set PORTs as digital outputs
      TRISC = 0xFF;
      TRISB = 0x00;

            PORTDbits.RD0 = 1; //POWER ON LED
            PORTDbits.RD1 = 1; //Flash other leds
            PORTDbits.RD2 = 1;
```

```
            PORTDbits.RD3 = 1;

            Delay10KTCYx( 0 );
            Delay10KTCYx( 0 );
            Delay10KTCYx( 0 );
            Delay10KTCYx( 0 );
            Delay10KTCYx( 0 );
            Delay10KTCYx( 0 );
            PORTDbits.RD0 = 0; //POWER ON LED
            PORTDbits.RD1 = 0; //Flash other leds
            PORTDbits.RD2 = 0;
            PORTDbits.RD3 = 0;
            PORTBbits.RB0 = 1; //Enable converter

// INITIALISE ADC AND TAKE FIRST READING
*********************************/

            Initialize_ADC();
            initialize_i2c();
            ADCON0 = ADCON0 | 0b00000001; //set bit 0 to enable the
adc
            Delay10TCYx( 1 );
            ConvertADC(); // Start conversion

// INITIALISE VARIABLES
************************************************/

            //task0_counter = 10;  // initialise variables
            acc = 0;     i=0; lpf_out = 0;
            adc_result0 = 0;
            new_sample_flag = 0;
            alpha = 0.01;
            toggle = 1;
            set_timer(); // timer interrupt not used here
            WriteTimer0(0);

            lpf = 0;    //initialise states to 0
            vloop = 0;
            vcap_low = 0;
            vcap_high = 0;

            if ( !PORTDbits.RD7 && !PORTDbits.RD6 ) { lpf = 1; }


            PORTBbits.RB0 = 1;  // initialise converter

// INITIALISE CONTROLLER VARIABLES
************************************************/

            vbatref = 425;
            err = err_int = u1 = 0;
            kp = 1 ;
            ki = 0.1;
            imax = 250 ;   imaxneg = -50; // out of 256 for max 510
            errintmax = 50;
            errintmaxneg = -50;

while (1)
```

```
      {
                  PORTDbits.RD6 = 1;     //for debugging timings
                  //state machine logic

                  //RD7 = SC HIGH
                  //RD6 = BATTERY HIGH
                  //RD5 = SC SC QUITE LOW
                  //RD4 = SC VERY LOW

                  if          ( ( !PORTDbits.RD7 && !PORTDbits.RD4 )
&& !PORTDbits.RD6 )    { lpf = 1; vloop = 0; PORTDbits.RD1 = 1;
PORTDbits.RD0 = 0; }
                  //  if Vcap < Vcapmax AND battery voltage < V*...
enable lpf state

                  if ( PORTDbits.RD5 && !PORTDbits.RD4 )  { lpf = 1;
vloop = 0; PORTDbits.RD1 = 1; PORTDbits.RD0 = 0;  }
                  // For testing purposes - if SC is quite low: go
back to current filter.

                  if          ( ( !PORTDbits.RD7 && !PORTDbits.RD5 )
&& PORTDbits.RD6 )     { lpf = 0;  vloop = 1;  PORTDbits.RD0 = 1;
PORTDbits.RD1 = 0; }
                  // if Vcap < Vcapmax AND battery voltage > V*...
enable vloop state

                  //else if  ( vloop == 0 ) { PORTDbits.RD0 = 0; }
                  if          ( PORTDbits.RD7 )      { lpf = 0; vloop
= 0; vcap_high = 1;  PORTDbits.RD0 = 0; PORTDbits.RD1 = 0; }

                  // Vcap > Vcapmax... enable supercap overvoltage
state
                  else { vcap_high = 0; }

                  if          ( PORTDbits.RD4 )      { lpf = 0; vloop
= 0; vcap_low = 1; PORTDbits.RD0 = 0; PORTDbits.RD1 = 0; }

                  // Vcap > Vcapmax... enable supercap overvoltage
state
                  else { vcap_low = 0;}

                  if (  new_sample_flag == 1   )
                  {

                        lpf_out = lpf_out +
alpha*((float)adc_result0 - lpf_out);

                        new_sample_flag = 0;  // new sample stored
in ma algorithm -> clear new sample flag
                  }     //    end if

                  PORTDbits.RD6 = 0;     //for debugging timings
                  //else { PORTDbits.RD1 = 0; }
      }//end while


}// end main
```

Appendix 6: Resulting Publications.